Numerical Modeling of Fluid-Structure Interaction with Rheologically Complex Fluids

Numerische Modellierung der Fluid-Struktur-Interaktion mit rheologisch komplexen Fluiden
Vom Fachbereich Maschinenbau an der Technischen Universität Darmstadt
zur Erlangung des akademischen Grades Doktor-Ingenieur (Dr.-Ing.)
genehmigte Dissertation von M.Sc. Xingyuan Chen aus Guangdong, China
Oktober 2014 — Darmstadt — D 17

TECHNISCHE
UNIVERSITÄT
DARMSTADT

Center of
Smart Interfaces

Numerical Modeling of Fluid-Structure Interaction with Rheologically Complex Fluids
Numerische Modellierung der Fluid-Struktur-Interaktion mit rheologisch komplexen Fluiden

Genehmigte Dissertation von M.Sc. Xingyuan Chen aus Guangdong, China

1. Gutachten: Prof. Dr. rer. nat. Dieter Bothe
2. Gutachten: Prof. Dr. rer. nat. Michael Schäfer

Tag der Einreichung: 01. Juli 2014
Tag der Prüfung: 01. Oktober 2014

Darmstadt — D 17

Bitte zitieren Sie dieses Dokument als:
URN: urn:nbn:de:tuda-tuprints-42160
URL: http://tuprints.ulb.tu-darmstadt.de/4216

Abstract

In the present work the interaction between rheologically complex fluids and elastic solids is studied by means of numerical modeling. The investigated complex fluids are non-Newtonian viscoelastic fluids. The fluid-structure interaction (FSI) of this kind is frequently encountered in injection molding, food processing, pharmaceutical engineering and biomedicine. The investigation via experiments is costly, difficult or in some cases, even impossible. Therefore, research is increasingly aided by numerical modeling. FSI with non-Newtonian fluids has been studied for years, but not many works are concerned with viscoelastic fluids. The aims of the present work are: *1*) developing a numerical solver for viscoelastic fluid-structure interaction (VFSI) problems; *2*) investigating the behaviour of a VFSI system; *3*) using the developed numerical solver to study a valveless micropump as a potential application.

In order to reach these goals, a viscoelastic fluid flow solver is developed based on a collocated finite-volume code FASTEST for the Navier-Stokes equations. In the simulation of viscoelastic fluid flow the so-called *High Weissenberg Number Problem* (HWNP) occurs, which is a major challenge for the simulations. This problem refers to the difficulty of convergence of iterative algorithms, when the Weissenberg number is above a certain critical value. In order to cope with this numerical stability problem, various stabilization approaches, such as log-conformation representation, square-root-conformation representation, among others, are implemented. In order to achieve accurate and oscillation-free results, high-resolution schemes for advection are implemented as well. The flow solver is then embedded in an FSI solver, where an implicit partitioned coupling algorithm is employed for the fluid-solid coupling.

The thesis starts with the description of a mathematical model for VFSI problems and constitutive modeling of viscoelastic fluids. Then, numerical methods for the simulation of viscoelastic fluid flow are presented and simulation results for benchmark problems are discussed. Afterwards, the algorithm of numerical modeling of VFSI is described. The VFSI problems are investigated both via numerical simulation and via a mass-spring-dashpot mechanical model. Finally, the output flow rate of a valveless micropump is studied by means of numerical simulation.

The contribution of the thesis consists of three parts. The first part deals with the numerical modeling of viscoelastic fluid flow. The question of how to choose suitable stable and accurate numerical schemes for the simulation of viscoelastic fluid flow is discussed. In the second part, we focus on the numerical modeling of VFSI. The present work is the first attempt to apply stabilization approaches to cope with the HWNP in simulations of VFSI problems. In addition, a mass-spring-dashpot mechanical model is developed to assist the analysis of VFSI problems. During the investigation, different behaviours between VFSI and Newtonian FSI are found. In the third part, we show the applicability of the developed solver and use a valveless micropump as a relevant example of potential application. In particular, the volumetric flow rate with a Newtonian and a viscoelastic pumping medium, respectively, is investigated.

Keywords: Viscoelastic fluid flow, Oldroyd-B, Finite-volume method, High Weissenberg Number Problem, Log-conformation representation, Square-root-conformation representation, High resolution scheme, Fluid-structure interaction, Implicit partitioned coupling, Valveless micropump.

Kurzfassung

In der vorliegenden Arbeit wird die Wechselwirkung zwischen rheologisch komplexen Fluiden und elastischen Festköpern mit Hilfe numerischer Modellierung untersucht. Die untersuchten komplexen Fluide sind nichtnewtonsche viskoelastische Fluide. Eine derartige Fluid-Struktur-Interaktion (FSI) wird häufig in Spritzgießverfahren, in der Lebensmittelindustrie, der Pharmatechnik und der Biomedizin angetroffen. In diesen Fällen ist die Untersuchung durch Experimente teuer, schwierig und zum Teil sogar unmöglich. Daher werden Untersuchungen zunehmend mittels numerischer Modellierung durchgeführt. FSI mit nichtnewtonschen Fluiden ist bereits seit einigen Jahren Gegenstand der Forschung, wobei sich allerdings nur ein geringer Anteil der Arbeiten mit viskoelastischen Fluiden befasst. Die vorliegende Arbeit zielt darauf ab, *1*) einen numerischen Löser für viskoelastische Fluid-Struktur-Interaktion (VFSI) zu entwickeln, *2*) Verhaltensweisen eines VFSI-Systems zu untersuchen und *3*) mittels des entwickelten Lösers, als eine potenzielle Anwendung, eine ventillose Mikropumpe zu untersuchen.

Um diese Ziele zu erreichen, wird ein Löser für viskoelastische Fluidströmung auf Grundlage eines nichtversetzten Finite-Volumen-Lösers FASTEST für die Navier-Stokes-Gleichungen entwickelt. Bei der Simulation viskoelastischer Strömungen tritt das so genannte *High Weissenberg Number Problem* (HWNP) auf, welches eine große Herausforderung für numerische Verfahren darstellt. Dieses Problem bezieht sich auf die Schwierigkeit der Konvergenz iterativer Algorithmen, falls die Weissenberg-Zahl größer als ein bestimmter kritischer Wert ist. Um das numerische Stabilitätsproblem zu bewältigen, werden verschiedene Stabilisierungsansätze implementiert, z.B. der Log-Konformation-Ansatz, der Quadratwurzel-Konformation-Ansatz, usw. Um genaue und oszillationsfreie Ergebnisse zu erhalten, werden hochauflösende Schemata für die Advektion implementiert. Der Löser für viskoelastische Strömung wird in den FSI-Löser eingebettet, wobei ein implizit partitionierter Kopplungsalgorithmus für die Fluid-Festköper-Kopplung verwendet wird.

Die Arbeit beginnt mit der Beschreibung eines mathematischen Models für VFSI-Probleme und mit der konstitutiven Modellierung viskoelastischer Fluiden. Danach werden numerische Verfahren zur Simulation der viskoelastischen Fluidströmung vorgestellt und Simulationsergebnisse für Benchmark-Problemen diskutiert. Darauf folgend wird der Algorithmus zur Simulation der VFSI beschrieben. Die VFSI-Probleme werden sowohl mittels numerischer Simulationen, als auch mit Hilfe eines mechanischen Masse-Feder-Dämpfer-Modells untersucht. Schließlich wird die volumetrische Flussrate einer ventillosen Mikropumpe durch numerische Simulationen untersucht.

Der Beitrag der vorliegenden Arbeit besteht aus drei Teilen. Der erste Teil befasst sich mit der numerischen Modellierung viskoelastischer Fluidströmungen. Es wird die Frage diskutiert, wie geeignete stabile und genaue numerische Verfahren zur Simulation viskoelastischer Fluidströmungen ausgewählt werden können. Im zweiten Teil liegt der Schwerpunkt auf der numerischen Modellierung der VFSI. Die vorliegende Arbeit ist der erste Versuch, Stabilisierungsansätze für HWNP in Simulationen der VFSI-Probleme anzuwenden. Darüber hinaus wird ein mechanisches-Masse-Feder-Dämpfer-Modell entwickelt, um die Analyse von VFSI-Problemen zu unterstützen. Unterschiedliche Verhaltensweisen zwischen viskoelastischer FSI und newtonscher FSI werden aufgezeigt. Im dritten Teil wird das Anwendungspotenzial der entwickelten Löser gezeigt. Als ein relevantes Beispiel wird eine ventillose Mikropumpe verwendet. Insbesondere wird die volumetrische Flussrate sowohl mit einem newtonschen als auch mit einem viskoelastischen Medium untersucht.

Stichworte: Viskoelastische Fluidströmung, Oldroyd-B, Finite-Volumen-Methode, Log-Konformation-Ansatz, Quadratwurzel-Konformation-Ansatz, Hochauflösende Schemata, Fluid-Struktur-Interaktion, Implizit partitionierte Kopplung, Ventillose Mikropumpe.

Acknowledgement

The research in this thesis could not have been performed without the support of many individuals. I take this opportunity to offer my regards and blessing to all of them.

First and foremost, I would like to express my deepest gratitude to my supervisor Prof. Dr. rer. nat. Dieter Bothe for his encouragement, guidance and support from the initial to the final level. He has guided me into the world of science. From him, I learned the true meaning of scientific research. I am greatly indebted for his patience, inspiration and sharing his after-work time for discussion. Without his help I could not overcome numerous difficulties encountered in the research. He is not only my teacher but also my mentor in these years.

I would like to express my special appreciation to my co-supervisor Prof. Dr. rer. nat. Michael Schäfer who has introduced me to the world of computational engineering. He is always to willing share his ideas and experience with me. I especially thank for his useful suggestions and efficient feedback with detailed correction for my publications.

I thank all my colleagues at the institute of Mathematical Modeling and Analysis (MMA) for their support and help. Special thanks to Dr. Holger Marschall for his useful discussion with me about computation fluid dynamics and patient advising my academic writing and presentation skills. Many thanks to Kerstin Schmitt for her enthusiastic help in non-scientific matters. Without her help I cannot concentrate on my research. Thanks to Stefan Fleckenstein for his patient discussion with me about the mathematical and programming problems and for his useful advise in my thesis. He is also my teacher in learning German. Thanks to Christoph Albert. He is always willing to share his experience and knowledge in mathematical and programming problems. It was happy time when we watched football matches and drank beers. Thanks to my office mates Daniel Deising, Matthias Niethammer in Lichtwiese and Paul Weber in Dolivo Street. They have given me a conformable environment for academic discussion and fun. They have also helped to improve my thesis. Thanks to other MMA colleagues: Chen Ma, Matthias Köhne, Abdulaziz Ali, Dominik Weirich, Christian Focke, Prof. Dr. Jürgen Saal, André Fischer, Kathrin Dieter-Kissling, Tomislav Maric, Siegfried Maier, Anja Fath, Muyuan Liu and Johannes Kromer.

I am thankful to the colleagues at the institute of Numerical methods in Mechanical Engineering (FNB) who support my work. Special thanks to Dr. Dörte Sternel for her helping me in the code FASTEST. Thanks to Thorsten Reimann. I enjoyed our discussion and cooperation. Thanks to Michael Fladerer for helping me to solve numerous technical problems. Thanks to Stephen Sachs, Christine Baur, Stefanie Nowak, Frank Flitz, Dominik Staab and Julian Michaelis for sharing their experience in FASTEST.

I am also grateful to my colleagues at the Graduate School of Computation Engineering (GSC CE). Thanks to Markus Lazanowski, Melanie Gattermayer, Christian Schmitt, Carina Schuster, and Birgit Seibert for their support for my Ph.D. Study. Thanks to Jian Cui, Xiao Wang and Ying Zhao. Our fruitful discussion in mathematical problems helps me a lot in this thesis.

Next I would like to extend my deepest gratitude to my mother and father for their great love, encouragement and incredible support for everything.

Finally, I am thankful to the financial support by the Excellence Initiative of the German Federal and State Governments, the Cluster of Excellence “Smart Interfaces - Understanding and Designing Fluid Boundaries” (EXC 259) and the Graduate School of Excellence of Computational Engineering (GSC 233) at Technische Universität Darmstadt.

Darmstadt, June 2014 Xingyuan Chen

Contents

List of Figures

List of Tables

Nomenclature

Upper-case Roman		**Unit**
A	Area	m^2
$\mathbf{A}$	Square-root of conformation tensor	–
$\mathbf{B}$	Left Cauchy-Green strain tensor	–
$\mathbf{C}$	Right Cauchy-Green strain tensor	–
$\mathbf{D}$	Rate of deformation tensor	$1/\mathrm{s}$
$\mathbf{E}$	Green-Lagrange strain tensor	–
E	Young's modulus	Pa
F	Force	$\mathrm{kg} \cdot \mathrm{m}/\mathrm{s}^2$
$\mathbf{F}$	Deformation gradient tensor	–
$\mathbf{I}$	Unit tensor	–
J	Jacobian determinant	–
$\mathbf{J}$	Transformation matrix	–
$\mathbf{L}$	Velocity gradient	$1/\mathrm{s}$
L	Characteristic length	m
M	Momentum	$\mathrm{kg} \cdot \mathrm{m}/\mathrm{s}$
$\mathbf{M}$	Mass matrix	kg
N	Shape function	–
$\mathbf{P}$	First Piola-Kirchhoff stress tensor	Pa
Q	Volumetric flow rate	m^3/s
$\mathbf{R}$	Eigenvector tensor	–
$\mathbf{S}$	Second Piola-Kirchhoff stress tensor	Pa
T	Period	s
U	Characteristic velocity	m/s
V	Volume	m^3
$\mathbf{W}$	Spin tensor of velocity gradient	$1/\mathrm{s}$
W	Plate displacement	m
$\mathbf{X}$	Material coordinate	m

Lower-case Roman		**Unit**
$\mathbf{b}$	Density of volume force	$\mathrm{kg}/(\mathrm{m}^2 \cdot \mathrm{s}^2)$
$\mathbf{c}$	Conformation tensor	–
$\mathbf{d}$	Displacement	m
$\mathbf{e}$	Euler-Almansi strain tensor	–
f	frequency	Hz
h	Height	m

k	Stiffness of a spring	$\mathrm{kg/s^2}$
m	Mass	kg
$\mathbf{n}$	Normal vector of a surface	–
p	Pressure	Pa
r	Radius	m
$\mathbf{s}$	Logarithm of conformation tensor	–
t	Time	s
$\mathbf{t}$	Traction vector	Pa
$\mathbf{u}$	Velocity	m/s
$\mathbf{x}$	Current configuration coordinate	m

Upper-case Greek		**Unit**
Δ	Difference	–
Γ	Boundary	–
Λ	Eigenvalue tensor	–
Φ	Arbitrary scalar	–
Ψ	Limiter function	–
Ω	Domain	–

Lower-case Greek		**Unit**
α_m	Mass ratio	–
β	Viscosity ratio	–
$\dot{\gamma}$	Shear rate	1/s
ε	permutation tensor	–
η	Viscosity	$\mathrm{Pa \cdot s}$
η_{nd}	Diffuser efficiency	–
λ	Fluid relaxation time	s
ν	Poisson's ratio	–
ξ	Pressure loss coefficient	–
ρ	Density	$\mathrm{kg/m^3}$
σ	Cauchy stress tensor	Pa
τ	Extra stress tensor	Pa
φ	Lagrangian-to-Eulerian map	–
$\hat{\varphi}$	Referential-to-Eulerian map	–
$\tilde{\varphi}$	Lagrangian-to-Referential map	–
ω	Rad frequency	rad/s

Superscript	
f	Fluid domain
g	Grid movement
n	Time level

s	Solid domain

Subscript

C	Center point
D	Downwind point
d	Diffuser
E	East control volume
e	East side of the control volume
f	Cell face
i	Inlet
n	Nozzle
o	Outlet
P	Center control volume
p	Polymer contribution
s	Solvent contribution
U	Upwind point
X	With respect to Lagrangian coordinate
x	With respect to Eulerian coordinate
χ	With respect to referential coordinate

Dimensionless number

De	Deborah number
E	Elasticity number
Re	Reynolds number
Wi	Weissenberg number

Abbreviation

BSD	Both-Sides Diffusion
CBC	Convective Boundedness Criterion
CDS	Central Differencing Scheme
CFD	Computational Fluid Dynamics
CSM	Computational Structural Mechanics
CUBISTA	Convergent and Universally Bounded Interpolation Scheme
EVSS	Elastic-Viscous Stress Splitting
FEM	Fluid-Element Method
FSI	Fluid-Structure Interaction
FVM	Fluid-Volume Method
FENE	Finitely Extensible Non-linear Elastic
HOS	High-Order Scheme
HRS	High Resolution Scheme
HWNP	High Weissenberg Number Problem
LCR	Log-Conformation Representation
LUDS	Linear Upwind Differencing Scheme
MpCCI	Mesh-Based Parallel Code Coupling Interfaces

MSD	Mass-Spring-Dashpot
NFSI	Newtonian Fluid-Structure Interaction
NVD	Normalized Variable Diagram
PDPS	Positive Definiteness Preserving Scheme
PTT	Phan-Thien-Tanner
QUICK	Quadratic Upstream Interpolation for Convective Kinematics
SIMPLE	Semi-Implicit Method for Pressure Linked Equations
SIP	Strongly Implicit Procedure
SPSS	Solvent-Polymer Stress Splitting
SRCR	Square-Root Conformation Representation
TV	Total Variation
TVD	Total Variation Diminishing
VFSI	Viscoelastic Fluid-Structure Interaction
UDS	Upwind Differencing Scheme
UCM	Upper Convected Maxwell

1 Introduction

1.1 Motivation

Fluid-structure interaction (FSI) problems have received increasing attention in recent years. They occur in many fields of engineering and applied science. In some FSI problems, fluids have complex rheological, especially viscoelastic properties, e.g. deflection of solid cores in injection molding, deformation of the anchor impeller in a stirred-tank reactor in food and chemical industries, blood flow in arteries, micro-organisms swimming in body fluids, etc. Considering the influence of the complex rheological fluid properties is important in design and manufacture of products as well as in research of biomedicine. However, the investigation via experiments is costly, difficult or in some cases, even impossible. Therefore, the attention on numerical modeling of FSI with complex rheological fluids has been grown in the past few years. Yet difficulties have also been found, in particular, in the simulation of viscoelastic fluid flow, a number of advanced techniques have been developed to deal with these difficulties. These techniques help us to make further development in the research of FSI with complex fluids and gain deeper insight into the problem.

In the present work, numerical modeling of FSI with complex fluids is investigated, which is related to the subjects of complex fluids and fluid-structure interaction. As a relevant application of the FSI with complex fluids, a valveless micropump is also studied in this work. An introduction, as well as an overview of the current simulation techniques of these three topics, is given in the following sections. The presentation is based on the works [15, 115, 64, 34, 124, 97, 63].

1.2 Complex fluids

Complex fluids are referred to as non-Newtonian fluids and more generally as viscoelastic fluids which do not follow the law of the classical Newtonian fluids.

The Cauchy stress tensor σ of a fluid can be written as

$$\sigma = -p\mathbf{I} + \tau, \tag{1.1}$$

where p is the hydrostatic pressure, $\mathbf{I}$ is the unit tensor and τ is the extra stress tensor. Newtonian and non-Newtonian fluids have different extra stress tensors. For incompressible Newtonian fluids with viscosity η, the extra stress tensor is given by

$$\tau = 2\eta\mathbf{D}, \tag{1.2}$$

where $\mathbf{D}$ is the rate of deformation tensor defined by

$$\mathbf{D} = \frac{1}{2}\left(\nabla\mathbf{u} + \nabla\mathbf{u}^{\mathrm{T}}\right). \tag{1.3}$$

Equation (1.2) is called a constitutive equation, giving the relationship between the stress and the kinematic quantity. For Newtonian fluids, the constitutive equation is based only on the first power of $\mathbf{D}$, thus the relation between the stress tensor and the rate of deformation tensor is linear.

A first class of non-Newtonian fluids, called the generalized Newtonian fluids, is concerned with the case when viscosity η is a function of the shear rate $\dot{\gamma}$, which is defined as the second invariant of the rate of deformation tensor $\mathbf{D}$ according to

$$\dot{\gamma} = \sqrt{2\mathbf{D}:\mathbf{D}}. \tag{1.4}$$

With this expression of viscosity, the extra stress for generalized Newtonian fluids has the form

$$\tau = 2\eta(\dot{\gamma})\mathbf{D}. \tag{1.5}$$

One can obtain different non-Newtonian behaviours (see figure 1.1) with different functional forms of $\eta(\dot{\gamma})$. A commonly used function of viscosity is the power law [121]

$$\eta(\dot{\gamma}) = K\dot{\gamma}^{n-1}, \tag{1.6}$$

where K is the consistency factor and n is the power law index. For $n = 1$ the Newtonian case is recovered. Shear-thinning or pseudo-plastic fluids have $n < 1$, while shear-thickening or dilating fluids have $n > 1$.

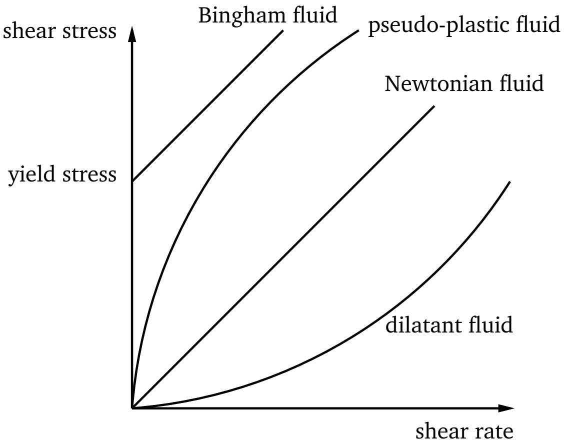

Figure 1.1.: Different behaviours of generalized Newtonian fluids. In the style of [115].

When the fluids have memory, they usually have some properties of both solids and liquids. Such materials are classified as the so-called viscoelastic materials. A typical example is silly putty which is a silicone material. If one puts it on the ground for a very long time, the material behaves like a liquid spreading out onto a flat surface. In contrary, if one throws it onto the ground, it bounds like an elastic solid. These two phenomena occur at large time scale and small time scale, respectively. At moderate time scale, the silly putty can be stretched like a plastic solid. The constitutive equation (1.5) is not able to describe such viscoelastic behaviours.

In the present work, the viscoelastic fluids are investigated. They are ubiquitous not only in industry, such as oil, food and rubber industries, but also in nature, such as blood or other body fluids. These fluids show striking visual phenomena:

Weissenberg (rod climbing) effect

If a rotating rod is inserted into a pool of Newtonian fluid, the rotating of the rod generates a centrifugal force which pushes the liquid outward, and near the rod the free surface forms a dip, see figure 1.2 (a). However, if the fluid is a viscoelastic fluid, such as polymer solutions, there is an alignment of polymer molecules with the flow direction. It causes a tension force in the flow direction which is referred to as normal stress. Therefore, in the experiment, the normal stresses cause a tension along the concentric streamlines. The resulting force pushes the fluid inward. Hence, the free surface rises and the fluid climbs up the rod, see figure 1.2 (b).

Die swell

Another significant effect caused by normal stress is the so-called die swell. When a fluid exits from a pipe, the diameter of the free jet and the diameter of the pipe are usually not equal. If the fluid is Newtonian, the change of diameter depends on the Reynolds number. At low Reynolds numbers, there is a slight increase in diameter. When the inertial effects become stronger, the diameter decreases, see figure 1.3 (a). If the fluid

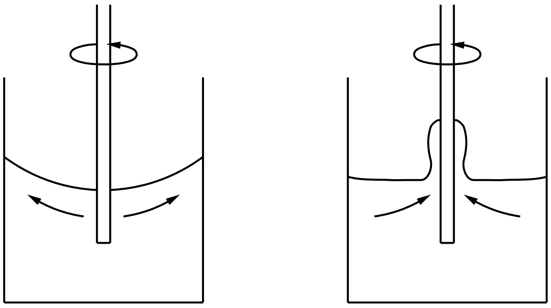

(a) Newtonian (b) Viscoelastic

Figure 1.2.: Weissenberg (rod climbing) effect

is viscoelastic, the fluid tends to show a strong increase in diameter which can be a few times the diameter of the pipe, see figure 1.3 (b). The reason is that the tension along streamlines is generated by the shear motion inside the pipe. As soon as the fluid exits the pipe, the tension is relieved, thus the jet shrinks in the longitudinal direction and expands in the transverse direction.

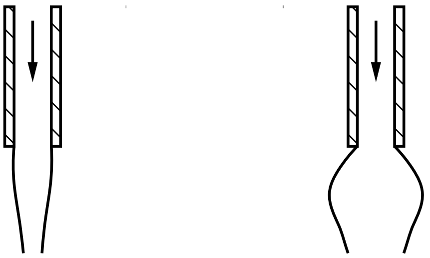

(a) Newtonian (b) Viscoelastic

Figure 1.3.: Die swell. In the style of [16].

Contraction flow

Sudden contraction in the geometry can lead to different streamline patterns in polymeric liquids from in Newtonian fluids. In polymeric liquids secondary flow can be observed, while in Newtonian liquids at low Reynolds numbers the secondary flow is not found. These flows are undesirable in many applications in polymer processing, because they can lead to stagnation and improper mixing of the fluid in the vortices.

Open siphon

Tilting a beaker to a small angle, the liquid inside is drawn over the side. If the liquid is Newtonian, the flow will stop when the level of the liquid surface is equal to the edge of the beaker, see figure 1.4 (a). If the fluid is viscoelastic, the flow will continue to empty the beaker partially or completely, see figure 1.4 (b).

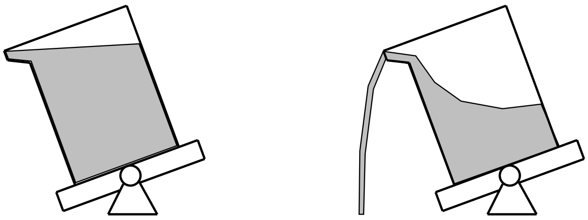

(a) Newtonian (b) Viscoelastic

Figure 1.4.: Open siphon

Elastic recoil

A dramatic phenomenon is the elastic recoil. If a sheet of a viscoelastic liquid is pouring down from a vessel, it can be cut with a pair of scissors. The process is very similar to a sheet of a elastic solid. The top part of the cut liquid recoils back into the vessel.

Numerical simulation gains increasing importance in industry dealing with complex fluid flow. Experiments involving complex fluids are normally expensive and time consuming. They may even interrupt a production line operation. However, the effect of design and improvement of a flow operation can be predicted with less effort via numerical methods. In the past decades there has been notable progress in the field of Computation Fluid Dynamics (CFD). However, it was found that numerical computation of viscoelastic fluid flow is a much more complex problem than for Newtonian fluid flow. A significant problem is the so-called *High Weissenberg Number Problem* (HWNP). The Weissenberg number is a dimensionless measure of the fluid elasticity. According to the HWNP, the loss of convergence of numerical algorithms occurs at relatively low Weissenberg numbers. How to effectively cope with the problem continues to be an important topic in current research. A number of advanced techniques have been developed to deal with the HWNP. How to choose suitable approaches for computation of practical interest in one of the main concerns in the present work.

1.3 Fluid-structure interaction

Fluid-structure interaction (FSI) is an interdisciplinary subject related to fluid dynamics and structural dynamics. In the process of FSI, on one hand, the solid deforms or moves, forced by the load of the surrounding fluid. On the other hand, the flow domain varies according to the deformed or moved solid, which in turn changes the flow field.

There are one-way and two-way interactions within different FSI problems. An FSI problem is a one-way coupling problem, if the solid is rigid, i.e. if no deformations of the solid are possible. The change of the flow domain is only caused by the change of position and configuration of the solid, see figure 1.5.

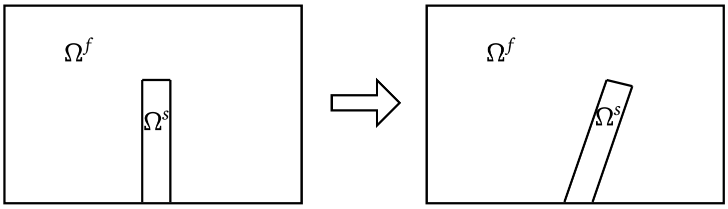

Figure 1.5.: One-way fluid-structure interaction problem. In the style of [124].

If the solid is elastic, the fluid flow acts on the surface of the structure and causes the deformation of the solid. At the same time, due to the deformation, the flow domain is altered, which forms a two-way interaction, as illustrated in figure 1.6.

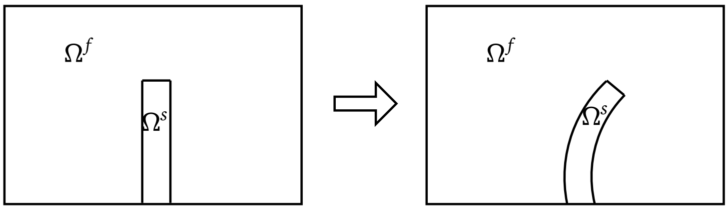

Figure 1.6.: Two-way fluid-structure interaction problem. In the style of [124].

FSI problems are frequently encountered in many applications. In biomedical research, for instance, a well-known case is the blood flow in arteries or veins, where information generated by investigation of blood vessel-wall interaction is required for medical evaluation. Another example involves micro-organisms, such as bacteria, algae or sperm, swimming in body fluids. Locomotion and transport of micro-organisms in fluids is an essential aspect of life. Here, understanding the propulsion mechanisms opens an avenue for the control of biological systems and the design of artificial micro-machines, e.g. micro-valves, micro-pumps or micro-robots which are employed to carry out very local and small-scale micro-operations such as minimally invasive surgery, highly localized drug delivery, and screening for diseases at their very early stages. For such micro-devices FSI plays an important role.

In the mentioned FSI problems, fluids usually have non-Newtonian, especially viscoelastic fluid properties. For such viscoelastic fluid-structure interaction (VFSI) problems the effect of the rheology may play a crucial role when it is comparable to or even dominates inertia effects. For instance, due to this fact the swimming of micro-organisms requires swimming strategies different from those in the macroscopic world.

Since studying FSI problems in biomedical research via experiments is of high difficulty and cost, the research is increasingly aided through numerical modeling. Techniques for numerical modeling of FSI with Newtonian fluids have been developed for many years. They serve well as a guide in both industrial and scientific applications. FSI with generalized Newtonian fluids, such as fluids with shear-dependent viscosity has been studied via numerical modeling in the recent years. Representative works are, e.g. [90, 89]. However, not much effort is made so far for viscoelastic fluids. Two relevant works are done by Chakraborty et al. [19, 20]. In both papers the simulations are carried out for fluid flowing in a two-dimensional deformable channel. The stationary deformation of the solid wall for different fluid relaxation times is investigated, but no transient behaviour of the VFSI system is studied. It is addressed by Chakraborty et al. [19] that one of the difficulties in simulation of VFSI is again the HWNP in simulation of viscoelastic fluid flow.

Therefore, applying advanced approaches on coping with the HWNP to investigate the transient two-way VFSI problems is another objective of the present work.

1.4 Valveless micropump

As emphasized in the previous section, knowing and understanding the VFSI behaviours is important for designing and manufacturing micro-fluid devices. Among a wide variety of devices employed in the micro-fluidic system, micropumps are indispensable. In industry they are used for dosing lubricants, hydraulic actuation. In medical fields, they are employed for diagnostic and infusion. The micropumps ensure reliable fluid supply and provide an ideal solution for both portable and stationary devices.

Among different types of micropumps, the valveless type is of particular interest, because there are no movable parts for the valves, which reduces the risk of valve failure and simplifies the fabrication process.

A typical valveless micropump consists of a large chamber with an oscillating diaphragm, which is also the FSI part of the pump, and two diffuser/nozzle elements at inlet and outlet, which control the flow directing. A diffuser is an expanding duct and a nozzle is a converging one. The flow directing action in the pump is based on the fact that in a diffuser/nozzle element lower pressure loss occurs in the diffuser direction than in the nozzle direction for the same flow velocity.

In the supply mode, as shown in figure 1.7 (a), the chamber volume increases, so the fluid flows into the chamber through both inlet and outlet. However, the inlet element acts as a diffuser, which has lower pressure loss, while the outlet element acts as a nozzle having higher pressure loss. Thus the overall volume flux flows from inlet to outlet. Analogously, in the pump mode the chamber volume decreases, inlet acts as a nozzle, outlet acts as a diffuser and larger volume flux is transported through the outlet than the inlet, see figure 1.7 (b). As a result, for a complete pump cycle, a net volume is transported from the inlet side to the outlet side, although the diffuser/nozzle elements conveys fluid in both directions.

Up to now, several semi-analytical models, e.g. [107, 108, 10], have been developed to aid the design and manufacture of valveless micropumps. However, these models are typical for pumping Newtonian fluids. In the applications in medicine and biotechnology, the transported liquid medium is usually non-Newtonian, in particular viscoelastic. This raises two questions: How does the pumping efficiency change when the pumping medium is viscoelastic? How to modify the available analytical models for pumping viscoelastic fluids? These questions become the third main concern in the present work.

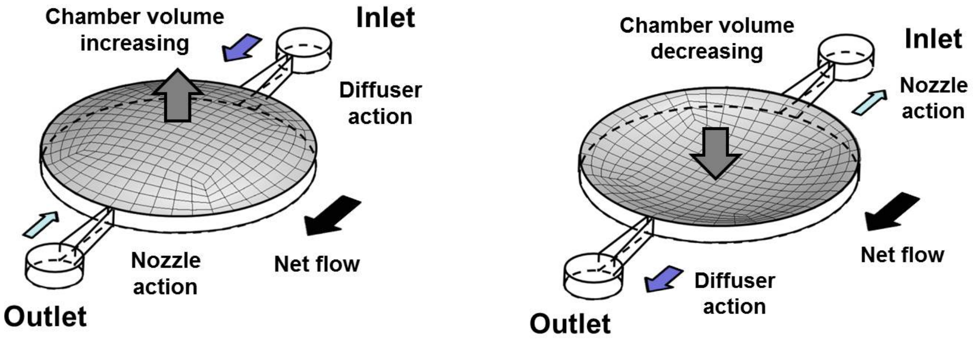

(a) Supply mode (b) Pump mode

Figure 1.7.: Principle of a valveless micropump

1.5 Objective and organisation of the work

The present work aims to shed light on the above mentioned problems which are summarized in the following three categories:

1. Numerical modeling of viscoelastic fluid flow:

   How to choose suitable stable and accurate numerical schemes to simulate viscoelastic fluid flow within the finite-volume method (FVM) framework?

2. Numerical modeling of viscoelastic fluid-structure interaction:

   What are the different behaviours between VFSI and NFSI?

3. Direct numerical simulation of a valveless micropump pumping viscoelastic fluid:

   How does the volumetric flow rate of a valveless micropump change when the pumping medium is a viscoelastic fluid?

With these aims in mind, a stable framework for numerical modeling of VFSI is developed and implemented. The development and implementation is based on an implicit partitioned coupling framework for NFSI. For the fluid solver, the in-house FVM program FASTEST [136] from institute of Numerical Methods in Mechanical Engineering is used. The finite-element method (FEM) program FEAP [140] is employed as the solid solver. The coupling and communication of the two solvers is realized by the software Mesh-Based Parallel Code coupling Interfaces (MpCCI) [46].

The remainder of this thesis is organised as follows:

In chapter 2, the necessary knowledge of continuum mechanics for FSI is reviewed, where kinematics and governing equations for fluid and structure are presented followed by the reformulation of the fluid equations in an Arbitrary-Lagrangian-Eulerian (ALE) framework.

Constitutive modeling of viscoelastic fluids is illustrated in chapter 3. Two routes to the differential constitutive equations are presented, namely the continuum and the micro-structure approach. Two dimensionless numbers in the constitutive equations, i.e. the Deborah and Weissenberg numbers, are introduced, followed by a summary of different formulations of the Oldroyd-B model. The Oldroyd-B model is chosen as the investigated model in the present work. This model has the simplest form among the others, but it also poses the most severe numerical difficulties. Once the developed numerical schemes can be successfully applied for this model, they can be used for other models without difficulties.

Numerical methods and discussion of simulation results for the simulation of viscoelastic fluid flow are presented in chapter 4. After the introduction of the general collocated FVM, special numerical treatments for viscoelastic fluids are explained. These include the high-resolution schemes for advection and the approaches for coping with the HWNP. At the end of the chapter three groups of simulation results are discussed. The first group is concerned with the effect of high-resolution schemes for advection. The second group aims to verify and validate the implemented viscoelastic fluid solver. In the last group different modern approaches to cope with the HWNP are investigated by comparison. The presented results and the discussion in this chapter are based on our published article [21].

FSI is mainly discussed in chapter 5. The numerical methods, such as FEM for structural dynamics, grid movement methods and coupling algorithm, are shown in the first part of the chapter. Investigation of VFSI problems begins by study of a mass-spring-dashpot model, a prototype model for a VFSI problem. The conclusion drawn from the study is verified in the simulations in two test cases: a collapsible channel flow and a lid driven cavity flow with deformable bottom. The presented results and the discussion in this chapter are based on our submitted article [22] and accepted article [23].

Modeling and simulation of a prototype valveless micropump is shown in chapter 6. First the available semi-analytical models for pumping Newtonian fluids are presented and extended for pumping viscoelastic fluids. Investigation begins with simulation of viscoelastic fluid flows in diffuser/nozzle elements. Subsequently, simulation of the whole micropump is shown and the flow rate for pumping viscoelastic fluids is presented. The presented results and the discussion in this chapter are based on our accepted article [23].

Finally, summary and outlook are given in chapter 7.

The aforementioned articles, which are written in the course of this thesis, are listed as follows:

- Xingyuan Chen, Holger Marschall, Michael Schäfer and Dieter Bothe: *A comparison of stabilisation approaches for finite-volume simulation of viscoelastic fluid flow*. International Journal of Computational Fluid Dynamics, 27(6-7): 229-250, 2013.

- Xingyuan Chen, Michael Schäfer and Dieter Bothe: *Numerical modeling and investigation of viscoelastic fluid-structure interaction applying an implicit partitioned coupling algorithm*. Journal of Fluids and Structures. Submitted.

- Xingyuan Chen, Michael Schäfer and Dieter Bothe: *Numerical modeling of viscoelastic fluid-structure interaction and its application for a valveless micropump*, In Proceeding of European Conference on Numerical Mathematics and Advanced Applications 2013, Lecture Notes in Computational Science and Engineering. Accepted.

2 Fundamentals of continuum mechanics

In this chapter the necessary basic knowledge of continuum mechanics is reviewed. In section 2.1 kinematics is introduced. It is followed by the governing equations for fluid and structural dynamics in section 2.2 and section 2.3, respectively. Arbitrary-Lagrangian-Eulerian formation and the whole equation system of a fluid-structure interaction problem are given in section 2.4. The definitions, theorems, physical laws and governing equations given in this chapter are presented based on [52, 133, 36].

2.1 Kinematics

The subject of kinematics is to express the deformation and motion of materials in a mathematical form. In the following, quantities such as velocity, deformation gradient and rate of deformation tensor are introduced. These quantities can be employed to describe a particular aspect of a deforming or moving material.

Physical materials are modeled employing an abstract mathematical entity called a "*body*". A body consists of an infinite number of material particles. A material particle $\mathbf{X}$ moves to a new position $\mathbf{x}$ after time t. This motion of a deformable body can be traced in terms of the deformation, see figure 2.1, a family of diffeomorphic maps, parametrized by the time coordinate $t \in \mathbb{R}^+$:

$$\varphi(\cdot, t) : \Omega_X \to \Omega_x = \varphi(\Omega_X, t), \quad \forall t \geqslant 0, \tag{2.1}$$

$$\mathbf{X} \mapsto \mathbf{x} = \varphi(\mathbf{X}, t), \quad \forall \mathbf{X} \in \Omega_X, \tag{2.2}$$

where $\mathbf{x}$ is the current position of an infinitesimal material particle located at $\mathbf{X}$ for $t = 0$. $\Omega_x(t)$ and $\Omega_X = \Omega_x(t = 0)$ are the *current configuration* and *original configuration* of the body, respectively.

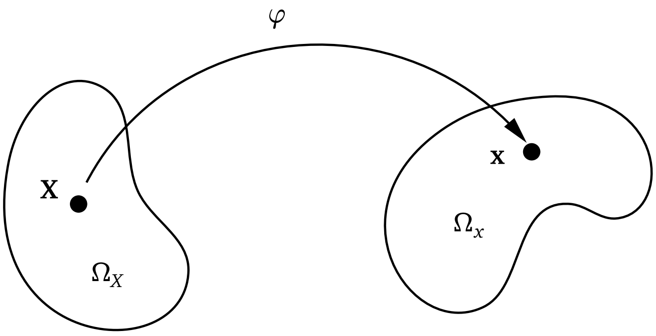

Figure 2.1.: Sketch of map φ

Because any point $\mathbf{x} \in \Omega_x$ can be traced back to its original position $\mathbf{X} = \varphi^{-1}(\mathbf{x}, t) \in \Omega_X$, the vector $\mathbf{X}$ represents also the original configuration coordinate for the point identified at time t by the current configuration coordinate $\mathbf{x}$. Therefore, the motion of a deformable body can be described either from the current configuration coordinate $\mathbf{x}$ or the original configuration coordinate $\mathbf{X}$. If the motion described in equation (2.2) is expressed with original configuration coordinates, then we call

$$\mathbf{x} = \varphi(\mathbf{X}, t), \quad x_i = \varphi_i(X_1, X_2, X_3, t) \tag{2.3}$$

the *material* or *Lagrangian description* and the coordinates $\mathbf{X} = (X_1, X_2, X_3)^{\mathsf{T}}$ are called material or Lagrangian coordinates. If the motion is expressed with current configuration coordinates, we call

$$\mathbf{X} = \varphi^{-1}(\mathbf{x}, t), \quad X_i = \varphi_i^{-1}(x_1, x_2, x_3, t) \tag{2.4}$$

the *spatial* or *Eulerian description* and the coordinates $\mathbf{x} = (x_1, x_2, x_3)^\mathsf{T}$ are called spatial or Eulerian coordinates. Any physical property or kinematic property of a body can be described in terms of either of these coordinates. The spatial description focuses on a fixed location in space. Material can pass through this location during the motion. It is often used in fluid mechanics. The material description concerns on the deformation of the body. The piece of matter may change its physical properties, but it is the same piece of material. This description is usually used in solid mechanics.

To describe the deformation, a number of useful tensors can be employed which are introduced next.

A line element $\mathrm{d}\mathbf{X}$, emanating from position $\mathbf{X}$ in the original configuration, becomes $\mathrm{d}\mathbf{x}$ in the current configuration. The expression of $\mathrm{d}\mathbf{x}$ is given by

$$\mathrm{d}\mathbf{x} = \varphi(\mathbf{X} + \mathrm{d}\mathbf{X}) - \varphi(\mathbf{X}) = (\nabla_X \varphi)^\mathsf{T} \mathrm{d}\mathbf{X} =: \mathbf{F}\, \mathrm{d}\mathbf{X}, \tag{2.5}$$

where the $\nabla_X(\cdot)$ denotes the gradient with respect to the material coordinates, whereas, in the rest of the thesis, the gradient with respect to the current coordinates is written as $\nabla(\cdot)$. The *deformation gradient* is therefore defined by

$$\mathbf{F} = (\nabla_X \varphi)^\mathsf{T} = \left(\frac{\partial \varphi}{\partial \mathbf{X}}\right)^\mathsf{T} = \left(\frac{\partial \mathbf{x}}{\partial \mathbf{X}}\right)^\mathsf{T}, \quad \text{with components} \quad F_{ij} = \frac{\partial x_i}{\partial X_j}. \tag{2.6}$$

This tensor maps the line elements in the original configuration onto line elements in the current configuration.

Other measures of deformation are the *left Cauchy-Green strain tensor* and the *right Cauchy-Green strain tensor*. They give the information about how the lengths of line elements and angles between line elements (determined through the vector inner product) change between configurations.

Consider two line elements $\mathrm{d}\mathbf{x}^{(1)}$ and $\mathrm{d}\mathbf{x}^{(2)}$ in the current configuration. The inner product of these two elements is

$$\mathrm{d}\mathbf{x}^{(1)} \cdot \mathrm{d}\mathbf{x}^{(2)} = \left(\mathbf{F}\mathrm{d}\mathbf{X}^{(1)}\right) \cdot \left(\mathbf{F}\mathrm{d}\mathbf{X}^{(2)}\right) = \left(\mathrm{d}\mathbf{X}^{(1)}\right)^\mathsf{T} \mathbf{F}^\mathsf{T}\mathbf{F}\mathrm{d}\mathbf{X}^{(2)} =: \left(\mathrm{d}\mathbf{X}^{(1)}\right)^\mathsf{T} \mathbf{C}\, \mathrm{d}\mathbf{X}^{(2)}, \tag{2.7}$$

where $\mathrm{d}\mathbf{X}^{(1)}$ and $\mathrm{d}\mathbf{X}^{(2)}$ are two line elements in the reference configuration. The right Cauchy-Green strain tensor is then defined by

$$\mathbf{C} = \mathbf{F}^\mathsf{T}\mathbf{F}. \tag{2.8}$$

Similarly, considering the two line elements in the original configuration, we have

$$\mathrm{d}\mathbf{X}^{(1)} \cdot \mathrm{d}\mathbf{X}^{(2)} = \left(\mathbf{F}^{-1}\mathrm{d}\mathbf{x}^{(1)}\right) \cdot \left(\mathbf{F}^{-1}\mathrm{d}\mathbf{x}^{(2)}\right) = \left(\mathrm{d}\mathbf{x}^{(1)}\right)^\mathsf{T} \mathbf{F}^{-\mathsf{T}}\mathbf{F}^{-1}\mathrm{d}\mathbf{x}^{(2)} = \left(\mathrm{d}\mathbf{x}^{(1)}\right)^\mathsf{T} \mathbf{B}^{-1}\, \mathrm{d}\mathbf{x}^{(2)}, \tag{2.9}$$

where the left Cauchy-Green strain tensor is defined by

$$\mathbf{B} = \mathbf{F}\mathbf{F}^\mathsf{T}. \tag{2.10}$$

Two further tensors give directly the information about the change in the squared length of elements. They are the *Green-Lagrange strain tensor* and the *Euler-Almansi strain tensor*.

When the Green-Lagrange strain tensor operates on a line element $\mathrm{d}\mathbf{X}$, it gives the change in the squares of the undeformed and deformed lengths:

$$\frac{1}{2}\left(|\mathrm{d}\mathbf{x}|^2 - |\mathrm{d}\mathbf{X}|^2\right) = \frac{1}{2}((\mathrm{d}\mathbf{X})^\mathsf{T}\mathbf{C}\mathrm{d}\mathbf{X} - \mathrm{d}\mathbf{X} \cdot \mathrm{d}\mathbf{X}) = \frac{1}{2}(\mathrm{d}\mathbf{X})^\mathsf{T}(\mathbf{C} - \mathbf{I})\mathrm{d}\mathbf{X}. \tag{2.11}$$

Therefore, the Green-Lagrange strain tensor $\mathbf{E}$ is defined by

$$\mathbf{E} = \frac{1}{2}(\mathbf{C} - \mathbf{I}) = \frac{1}{2}(\mathbf{F}^\mathsf{T}\mathbf{F} - \mathbf{I}). \tag{2.12}$$

Similarly, the Euler-Almansi strain tensor is defined by

$$\mathbf{e} = \frac{1}{2}(\mathbf{I} - \mathbf{B}^{-1}) = \frac{1}{2}(\mathbf{I} - \mathbf{F}^{-\mathsf{T}}\mathbf{F}^{-1}). \tag{2.13}$$

The *displacement* of a material particle is investigated in structural dynamics. It is defined by

$$\mathbf{d}'(\mathbf{X},t) = \mathbf{x}(\mathbf{X},t) - \mathbf{X} \tag{2.14}$$

in the material description or

$$\mathbf{d}(\mathbf{x},t) = \mathbf{x} - \mathbf{X}(\mathbf{x},t) \tag{2.15}$$

in the spatial description. The vectors $\mathbf{d}'$ and $\mathbf{d}$ have the same values but different arguments.

The *velocity* of a moving particle is

$$\mathbf{u}'(\mathbf{X},t) = \left.\frac{\partial \varphi(\mathbf{X},t)}{\partial t}\right|_X, \tag{2.16}$$

with $(.)|_X$ meaning that the material coordinate X is kept fixed. The spatial description of the velocity can be obtained by

$$\mathbf{u}(\mathbf{x},t) = \mathbf{u}'(\varphi^{-1}(\mathbf{x},t),t). \tag{2.17}$$

These two velocities have the same value, i.e. $\mathbf{u}'(\mathbf{X},t) = \mathbf{u}(\mathbf{x},t)$ for $\mathbf{x} = \varphi(\mathbf{X},t)$.

Consider two fixed neighbouring points $\mathbf{x}$ and $\mathbf{x} + \mathrm{d}\mathbf{x}$. The velocities of these two particles are related to each other according to

$$\mathbf{u}(\mathbf{x} + \mathrm{d}\mathbf{x}) = \mathbf{u}(\mathbf{x}) + \nabla\mathbf{u}^{\mathsf{T}}\mathrm{d}\mathbf{x}. \tag{2.18}$$

The *velocity gradient* is here defined by

$$\mathbf{L} = \nabla\mathbf{u}, \quad \text{with components} \quad L_{ij} = \frac{\partial u_j}{\partial x_i}. \tag{2.19}$$

This gradient can be decomposed into a symmetric part $\mathbf{D}$ and an anti-symmetric part $\mathbf{W}$ according to

$$\mathbf{L} = \mathbf{D} + \mathbf{W}, \tag{2.20}$$

where

$$\mathbf{D} = \frac{1}{2}(\mathbf{L} + \mathbf{L}^{\mathsf{T}}) \tag{2.21}$$

is the *rate of deformation tensor* and

$$\mathbf{W} = \frac{1}{2}(\mathbf{L} - \mathbf{L}^{\mathsf{T}}) \tag{2.22}$$

is the *spin tensor*.

The volume and area between the original and current configurations are related to each other by the *Jacobian determinant* of the deformation gradient defined by

$$J = \det\mathbf{F}. \tag{2.23}$$

It gives the ratio between the volume $\mathrm{d}V_X$ in the original configuration and the volume $\mathrm{d}V_x$ in the current configuration, i.e

$$\mathrm{d}V_x = J\,\mathrm{d}V_X. \tag{2.24}$$

The Jacobian determinant is also used in *Nanson's formula*. Let us consider the oriented infinitesimal surface $\mathbf{n}_x\mathrm{d}A_x$ lying on the tangent plane to the surface $\partial\Omega_x$ and the oriented infinitesimal surface $\mathbf{n}_X\mathrm{d}A_X$ lying on the tangent plane to the surface $\partial\Omega_X$. Nanson's formula shows how the vector element of $\mathbf{n}_x\mathrm{d}A_x$ in the current configuration is related to the vector element of $\mathbf{n}_X\mathrm{d}A_X$ in the original configuration:

$$\mathbf{n}_x\mathrm{d}A_x = J\mathbf{F}^{-\mathsf{T}}\mathbf{n}_X\mathrm{d}A_X. \tag{2.25}$$

2.2 Fluid dynamics

The governing equations of continuum mechanics are derived from the following physical conservation principles

- conservation of mass,
- conservation of momentum,
- conservation of energy.

In the present work, only isothermal problems are considered, where the temperature is assumed to be constant.

Transport theorem

Theorem (Reynolds Transport Theorem)**.** *Let $\Omega_x(t)$ be a material domain deforming according to the diffeomorphism φ with velocity $\mathbf{u}$. Let $\partial\Omega_x(t)$ be the boundary of $\Omega_x(t)$ with outward normal $\mathbf{n}_x$. Let Ω_X be the inverse image of $\Omega_x(t)$ fulfilling $\Omega_x(t) = \varphi(\Omega_X, t)$. Let Φ be a smooth scalar function. Then*

$$\frac{\mathrm{d}}{\mathrm{d}t} \int\limits_{\Omega_x(t)=\varphi(\Omega_X,t)} \Phi \,\mathrm{d}V_x = \int\limits_{\Omega_x(t)} \left(\frac{\partial \Phi}{\partial t} + \nabla \cdot (\Phi \mathbf{u}) \right) \mathrm{d}V_x. \tag{2.26}$$

The term on the right-hand side of equation (2.26) can be also reformulated as

$$\frac{\partial \Phi}{\partial t} + \nabla \cdot (\Phi \mathbf{u}) = \frac{\mathrm{d}\Phi}{\mathrm{d}t} + \Phi \nabla \cdot \mathbf{u}, \tag{2.27}$$

where

$$\frac{\mathrm{d}\Phi}{\mathrm{d}t} = \frac{\partial \Phi}{\partial t} + \mathbf{u} \cdot \nabla \Phi \tag{2.28}$$

is the material or Lagrangian time derivative of the scalar Φ. It can be alternatively derived by

$$\frac{\mathrm{d}\Phi}{\mathrm{d}t} = \left. \frac{\partial \Phi(\mathbf{x}, t)}{\partial t} \right|_X = \left. \frac{\partial \Phi(\varphi(\mathbf{X}, t), t)}{\partial t} \right|_X = \frac{\partial \Phi}{\partial t} + \nabla \Phi \cdot \left. \frac{\partial \varphi}{\partial t} \right|_X = \frac{\partial \Phi}{\partial t} + \mathbf{u} \cdot \nabla \Phi. \tag{2.29}$$

Conservation of mass

Mass is a physical property of matter which quantifies its resistance to acceleration. The mass over a volume $\Omega_x(t)$ is given by

$$m(t) = \int\limits_{\Omega_x(t)} \rho(\mathbf{x}, t) \mathrm{d}V_x, \tag{2.30}$$

where ρ is the *density*. The law of conservation of mass states that mass cannot be created or destroyed, i.e.

$$\frac{\mathrm{d}m}{\mathrm{d}t} = \frac{\mathrm{d}}{\mathrm{d}t} \int\limits_{\Omega_x(t)} \rho \mathrm{d}V_x = 0. \tag{2.31}$$

Applying the Reynolds transport theorem by substituting $\Phi = \rho$ in equation (2.26), we obtain

$$\int\limits_{\Omega_x(t)} \left(\frac{\partial \rho}{\partial t} + \nabla \cdot (\rho \mathbf{u}) \right) \mathrm{d}V_x = 0. \tag{2.32}$$

Since the integrand is continuous by assumption, we obtain the continuity equation

$$\frac{\partial \rho}{\partial t} + \nabla \cdot (\rho \mathbf{u}) = 0. \tag{2.33}$$

If the material is incompressible with constant density ρ, the continuity equation (2.33) reduces to

$$\nabla \cdot \mathbf{u} = 0. \tag{2.34}$$

Conservation of momentum

The *momentum* over a volume $\Omega_x(t)$ is given by

$$M(t) = \int\limits_{\Omega_x(t)} \rho\mathbf{u}\,\mathrm{d}V_x. \tag{2.35}$$

The forces acting on Ω_x are of two types: first, volume forces in Ω_x, and second, surface forces on $\partial\Omega_x$. Volume forces can be expressed by a distributed function $\mathbf{b}$. According to *Cauchy's stress theorem* (see [52] for proof), surface forces can be described with the *Cauchy stress tensor* σ. The force density per unit area (the traction) acting on a surface with normal $\mathbf{n}_x$ is equal to $\sigma \cdot \mathbf{n}_x$.

Therefore, the total force acting on Ω_x is

$$F = \int\limits_{\partial\Omega_x(t)} \sigma \cdot \mathbf{n_x}\,\mathrm{d}A_x + \int\limits_{\Omega_x(t)} \rho\mathbf{b}\mathrm{d}V_x = \int\limits_{\Omega_x(t)} (\nabla\cdot\sigma + \rho\mathbf{b})\,\mathrm{d}V_x, \tag{2.36}$$

where the divergence theorem is applied to convert the surface integral onto a volume integral.

The Cauchy stress tensor σ is related to the kinematic variables by constitutive equations. These constitutive equations will be presented in the next chapter.

Newton's second law requires that the change in momentum is equal to the acting force. Hence we have

$$\frac{\mathrm{d}}{\mathrm{d}t}\int\limits_{\Omega_x(t)} \rho\mathbf{u}\,\mathrm{d}V_x = \int\limits_{\Omega_x(t)} (\nabla\cdot\sigma + \rho\mathbf{b})\,\mathrm{d}V_x. \tag{2.37}$$

Applying the Reynolds transport theorem by substituting $\Phi = \rho u_i$ for $i = 1, 2, 3$, we have

$$\frac{\mathrm{d}}{\mathrm{d}t}\int\limits_{\Omega_x(t)} \rho u_i\,\mathrm{d}V_x = \int\limits_{\Omega_x(t)} \left(\frac{\partial(\rho u_i)}{\partial t} + \nabla\cdot(\rho u_i\mathbf{u})\right)\mathrm{d}V_x. \tag{2.38}$$

Since this equation holds for all choices of the material volume and the integrands are continuous in space, we therefore have

$$\frac{\partial(\rho u_i)}{\partial t} + \nabla\cdot(\rho u_i\mathbf{u}) = (\nabla\cdot\sigma)_i + \rho b_i. \tag{2.39}$$

Written in more compact form, the equations read

$$\frac{\partial(\rho\mathbf{u})}{\partial t} + \nabla\cdot(\rho\mathbf{u}\mathbf{u}) = \nabla\cdot\sigma + \rho\mathbf{b}. \tag{2.40}$$

With the conservation of mass (2.33), we get the *Cauchy equation of motion*

$$\rho\frac{\partial\mathbf{u}}{\partial t} + \rho\mathbf{u}\cdot\nabla\mathbf{u} = \nabla\cdot\sigma + \rho\mathbf{b}. \tag{2.41}$$

Conservation of angular momentum

In the present work, non-polar fluids are considered. The *angular momentum* of a volume with regard to the origin is given by

$$L = \int\limits_{\Omega_x(t)} \mathbf{x}\times(\rho\mathbf{u})\,\mathrm{d}V_x, \tag{2.42}$$

and the torque produced by the forces is

$$T = \int\limits_{\Omega_x(t)} \mathbf{x} \times (\rho \mathbf{b})\, \mathrm{d}V_x + \int\limits_{\partial\Omega_x(t)} \mathbf{x} \times (\sigma \cdot \mathbf{n})\, \mathrm{d}A_x. \tag{2.43}$$

Conservation of angular momentum tells us $\frac{\mathrm{dL}}{\mathrm{d}t} = T$. Applying the Reynolds transport theorem we get the change of angular momentum as

$$\frac{\mathrm{d}L}{\mathrm{d}t} = \int\limits_{\Omega_x(t)} \mathbf{x} \times \left(\rho \frac{\partial \mathbf{u}}{\partial t} + \rho \mathbf{u} \cdot \nabla \mathbf{u}\right) \mathrm{d}A_x. \tag{2.44}$$

Therefore the conservation of angular momentum reads

$$\mathbf{x} \times \left(\rho \frac{\partial \mathbf{u}}{\partial t} + \rho \mathbf{u} \cdot \nabla \mathbf{u} - \nabla \cdot \sigma - \rho \mathbf{b}\right) = \epsilon : \sigma, \tag{2.45}$$

where ϵ is the permutation tensor given by

$$\epsilon_{ijk} = \begin{cases} 1 & \text{if } (i,j,k) \text{ is an even permutation of } (1,2,3), \\ -1 & \text{if } (i,j,k) \text{ is an odd permutation of } (1,2,3), \\ 0 & \text{if any symbol is repeated, } i=j, i=k, j=k. \end{cases} \tag{2.46}$$

Since the left part in equation (2.45) is given by the momentum conservation, the conservation of angular momentum equation implies

$$\epsilon : \sigma = 0 \quad \Leftrightarrow \quad \sigma = \sigma^{\mathsf{T}}. \tag{2.47}$$

Thus, conservation of angular momentum is an additional condition requiring the symmetry of the stress tensor σ for non-polar fluids.

The conservation equations are derived from basic principles and hold for all materials considered in the present work. However, the four equations have ten physical quantities, namely the density, three components of velocity vector, and six components of symmetric tensor σ. To close the gap, constitutive equations for the dependence of the stress tensor on the kinematic variables are needed. They will be discussed in chapter 3.

2.3 Structural dynamics

In structural dynamics, the material description is preferred, i.e. the motion is described in the material configuration Ω_X.

Balance equations

Let $\rho_0(\mathbf{X})$ be the density in the material configuration. Using the transformation (2.24), the conservation of mass reads

$$\int\limits_{\Omega_X} \rho_0 \mathrm{d}V_X = \int\limits_{\Omega_x(t)} \rho \mathrm{d}V_x = \int\limits_{\Omega_X} \rho J \mathrm{d}V_X.$$

Thus

$$\rho_0 = J\rho. \tag{2.48}$$

Momentum conservation is formulated according to the Newton's second law:

$$\frac{\mathrm{d}}{\mathrm{d}t}\int\limits_{\Omega_X} \rho_0 \dot{\mathbf{d}}\,\mathrm{d}V_X = \int\limits_{\partial\Omega_X} \mathbf{t}_0\,\mathrm{d}A_X + \int\limits_{\Omega_X} \rho_0 \mathbf{b}\,\mathrm{d}V_X, \tag{2.49}$$

where $\mathbf{t}_0$ is the traction on $\partial\Omega_X$ and $\dot{\mathbf{d}}$ denotes the total time derivative of the displacement $\mathbf{d}$. Because Ω_X is fixed in time, the left-hand side of equation (2.49) can be written as

$$\frac{\mathrm{d}}{\mathrm{d}t}\int\limits_{\Omega_X} \rho_0 \dot{\mathbf{d}}\,\mathrm{d}V_X = \int\limits_{\Omega_X} \rho_0 \ddot{\mathbf{d}}\,\mathrm{d}V_X. \tag{2.50}$$

The vector $\mathbf{t}_0$ is calculated by

$$\mathbf{t}_0 = \mathbf{P}\,\mathbf{n}_X, \tag{2.51}$$

where $\mathbf{P}$ is the *first Piola-Kirschhoff stress tensor* and $\mathbf{n}_X$ is the unit outward pointing normal to $\partial\Omega_X$. Let us also consider the traction on $\partial\Omega_x$ in the current configuration

$$\mathbf{t} = \sigma\mathbf{n}_x, \tag{2.52}$$

where $\mathbf{n}_x$ is the unit outward pointing normal to the current surface $\partial\Omega_x$. The forces on the surface calculated by the first Piola-Kirchhoff stress tensor and Cauchy stress tensor must be equal, i.e.

$$\sigma\,\mathbf{n}_x\,\mathrm{d}A_x = \mathbf{P}\,\mathbf{n}_X\,\mathrm{d}A_X. \tag{2.53}$$

Applying Nanson's formula (2.25) to equation (2.53), we obtain the relation between the first Piola-Kirchhoff stress tensor and the Cauchy stress tensor:

$$\mathbf{P} = J\sigma\mathbf{F}^{-\mathsf{T}}. \tag{2.54}$$

One of the difficulties with application of the first Piola-Kirchhoff stress tensor is that it is not symmetric, which makes it difficult to form constitutive models. Therefore, the *second Piola-Kirchhoff stress tensor* is introduced which is defined by

$$\mathbf{S} = J\mathbf{F}^{-1}\,\sigma\,\mathbf{F}^{-\mathsf{T}} = \mathbf{F}^{-1}\mathbf{P}. \tag{2.55}$$

Applying the Gauss theorem we can rewrite the first term on the right-hand side of equation (2.49) as

$$\int\limits_{\partial\Omega_X} \mathbf{P}\mathbf{n}_X\,\mathrm{d}A_X = \int\limits_{\Omega_X} \nabla_X \cdot \mathbf{P}\,\mathrm{d}V_X = \int\limits_{\Omega_X} \nabla_X \cdot (\mathbf{F}\,\mathbf{S})\,\mathrm{d}V_X. \tag{2.56}$$

The final form of the momentum conservation therefore reads

$$\rho_0\ddot{\mathbf{d}} - \nabla_X \cdot (\mathbf{F}\,\mathbf{S}) - \rho_0\mathbf{b} = 0. \tag{2.57}$$

Constitutive equation

In the present work only elastic solids are considered. For a linear, homogeneous and isotropic material, the second Piola-Kirchhoff stress tensor $\mathbf{S}$ is related to the Green-Lagrangian strain tensor $\mathbf{E}$ by

$$\mathbf{S} = \lambda^s \mathrm{tr}(\mathbf{E})\mathbf{I} + 2\mu^s\mathbf{E}, \tag{2.58}$$

where λ^s and μ^s are two *Laḿe constants*. They can be expressed with *Poisson's ratio* ν and *Young's modulus* E according to

$$\nu = \frac{\lambda^s}{2(\lambda^s + \nu)}, \quad E = \frac{\mu(3\lambda^s + 2\mu^s)}{\lambda^s + \mu^s}. \tag{2.59}$$

Materials governed by this linear material law are called *Saint Venant-Kirchhoff materials*.

2.4 Fluid-structure interaction

From the above description we know that fluid motion is described in the current (Eulerian) configuration, whereas structural motion is described in the material (Lagrangian) configuration. For an FSI problem a difficulty exists: Due to the force exerted by the fluid, the structure deforms and the fluid domain is no longer fixed but varies in consequence. In order to overcome this difficulty, the *Arbitrary-Lagrangian-Eulerian* (ALE) formulation is employed.

Arbitrary-Lagrangian-Eulerian formulation

Besides the current configuration Ω_x and the material configuration Ω_X, a *referential configuration* Ω_χ is introduced. The configuration Ω_χ is neither fixed nor attached to the material. It moves with, in principle, arbitrary motion. The relation between these three configurations is illustrated in figure 2.2. The configuration can be regarded as the mesh configuration in numerical computation. In an abstract sense, we can think of the mesh as a virtual material which deforms according to a law different from the real material.

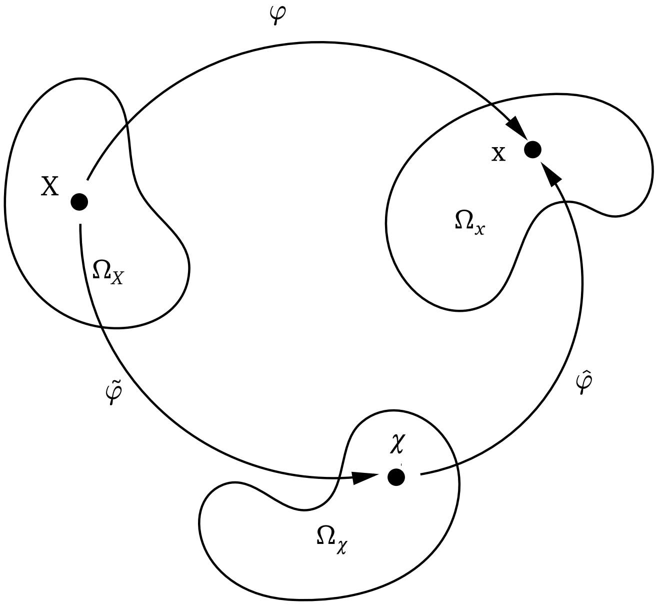

Figure 2.2.: Sketch of maps φ, $\tilde{\varphi}$ and $\hat{\varphi}$. In the style of [133].

Therefore, making a close analogy with the Lagrangian-to-Eulerian transformation, we can define a parametrized family of diffeomorphisms relating the referential frame to the Eulerian frame, such that

$$\hat{\varphi}(\cdot,t):\Omega_\chi \rightarrow \Omega_x = \hat{\varphi}(\Omega_\chi,t), \quad \forall t \geqslant 0, \tag{2.60}$$

$$\chi \mapsto \mathbf{x} = \hat{\varphi}(\chi,t), \quad \forall \chi \in \Omega_\chi, \tag{2.61}$$

where χ is the position vector in the referential frame Ω_χ.

Displacement $\hat{\mathbf{d}}$, velocity $\hat{\mathbf{u}}$ as well as deformation gradient $\hat{\mathbf{F}}$ are then defined by

$$\hat{\mathbf{d}} = \hat{\varphi}(\chi,t) - \chi, \tag{2.62}$$

$$\hat{\mathbf{u}} = \left.\frac{\partial \hat{\mathbf{d}}}{\partial t}\right|_\chi, \tag{2.63}$$

$$\hat{\mathbf{F}} = \nabla_\chi \mathbf{x} = \frac{\partial \mathbf{x}}{\partial \chi}. \tag{2.64}$$

Drawing an analogy with the material derivative, we define the referential time derivative of a scalar function with respect to the χ coordinate by

$$\left.\frac{\partial \Phi(\mathbf{x},t)}{\partial t}\right|_{\chi} = \left.\frac{\partial \Phi(\hat{\varphi}(\chi,t),t)}{\partial t}\right|_{\chi} = \frac{\partial \Phi}{\partial t} + \nabla\Phi\cdot\left.\frac{\partial \hat{\varphi}}{\partial t}\right|_{\chi} = \frac{\partial \Phi}{\partial t} + \hat{\mathbf{u}}\cdot\nabla\Phi. \tag{2.65}$$

In addition, it is important to introduce the Lagrangian-to-Referential transformation

$$\tilde{\varphi}(\cdot,t):\Omega_X \rightarrow \Omega_\chi = \tilde{\varphi}(\Omega_X,t), \quad \forall t \geqslant 0, \tag{2.66}$$

$$\mathbf{X} \mapsto \chi = \tilde{\varphi}(\mathbf{X},t), \quad \forall \mathbf{X} \in \Omega_X, \tag{2.67}$$

which tracks the motion of the referential frame observed from the Lagrangian frame. This map is given as

$$\tilde{\varphi} = \hat{\varphi}^{-1}\circ\varphi. \tag{2.68}$$

Displacement $\tilde{\mathbf{d}}$, velocity $\tilde{\mathbf{u}}$ and deformation gradient $\tilde{\mathbf{F}}$ undergone by the mesh, observed from the Lagrangian reference frame, are defined by

$$\tilde{\mathbf{d}} = \tilde{\varphi}(\mathbf{X},t) - \mathbf{X}, \tag{2.69}$$

$$\tilde{\mathbf{u}} = \left.\frac{\partial \tilde{\mathbf{d}}}{\partial t}\right|_{X}, \tag{2.70}$$

$$\tilde{\mathbf{F}} = \nabla_X \chi = \frac{\partial \chi}{\partial \mathbf{X}}. \tag{2.71}$$

Correspondingly, the material time derivative of a scalar function with respect to the χ coordinate has the form

$$\frac{\mathrm{d}\Phi}{\mathrm{d}t}(\chi,t) = \left.\frac{\partial \Phi}{\partial t}\right|_{\chi} + \tilde{\mathbf{u}}\cdot\nabla_{\chi}\Phi. \tag{2.72}$$

Using equation (2.72) to calculate the time derivative of vector $\mathbf{x} = \hat{\varphi}(\chi,t)$, we obtain the relationship between the velocities $\mathbf{u}$, $\hat{\mathbf{u}}$ and $\tilde{\mathbf{u}}$ in different configurations:

$$\mathbf{u} = \hat{\mathbf{u}} + \hat{\mathbf{F}}\,\tilde{\mathbf{u}}. \tag{2.73}$$

The difference between the material and mesh velocities,

$$\mathbf{u} - \hat{\mathbf{u}} = \hat{\mathbf{F}}\,\tilde{\mathbf{u}}, \tag{2.74}$$

is called the *convective velocity*. Employing the convective velocity and equation (2.28) and (2.65) we obtain another expression of the material derivative according to

$$\frac{\mathrm{d}\Phi}{\mathrm{d}t}(\mathbf{x},t) = \frac{\partial \Phi}{\partial t} + \mathbf{u}\cdot\nabla\Phi = \left.\frac{\partial \Phi}{\partial t}\right|_{\chi} - \hat{\mathbf{u}}\cdot\nabla\Phi + \mathbf{u}\cdot\nabla\Phi = \left.\frac{\partial \Phi}{\partial t}\right|_{\chi} + (\mathbf{u}-\hat{\mathbf{u}})\cdot\nabla\Phi \tag{2.75}$$

Applying the material derivative (2.75), we can rewrite the mass conservation (2.33) and momentum conservation (2.41) in the ALE formulation:

$$\left.\frac{\partial \rho}{\partial t}\right|_{\chi} + (\mathbf{u}-\hat{\mathbf{u}})\cdot\nabla\rho + \rho\nabla\cdot\mathbf{u} = 0, \tag{2.76}$$

$$\rho\left.\frac{\partial \mathbf{u}}{\partial t}\right|_{\chi} + \rho(\mathbf{u}-\hat{\mathbf{u}})\cdot\nabla\mathbf{u} = \nabla\cdot\sigma + \rho\mathbf{b}. \tag{2.77}$$

The ALE form of the transport equation for volume integrals of a scalar quantity Φ reads

$$\frac{\mathrm{d}}{\mathrm{d}t}\int\limits_{\Omega_x=\varphi(\Omega_X)} \Phi\,\mathrm{d}V_x = \frac{\mathrm{d}}{\mathrm{d}t}\int\limits_{\Omega_x=\hat{\varphi}(\Omega_\chi)} \Phi\,\mathrm{d}V_x + \int\limits_{\partial\Omega_x} \Phi(\mathbf{u}-\hat{\mathbf{u}})\cdot\mathbf{n}_x\,\mathrm{d}A_x, \tag{2.78}$$

which is used in finite-volume discretization.

Fluid-structure interaction problem

Let Ω be the domain of an FSI problem consisting of the fluid subdomain Ω^f and the solid subdomains Ω^s, i.e.

$$\Omega = \Omega^f \cup \Omega^s, \tag{2.79}$$

as described in figure 2.3. The superscripts f and s denote the parameter and variables in the fluid and solid domain, respectively. The subdomains have their own boundaries Γ^f and Γ^s. The interface between the two subdomains is Γ^i, having unit normal $\mathbf{n}_x$ with respect to the current configuration pointing from the fluid side to the solid side. Volume forces, such as gravity, are not considered in the present work.

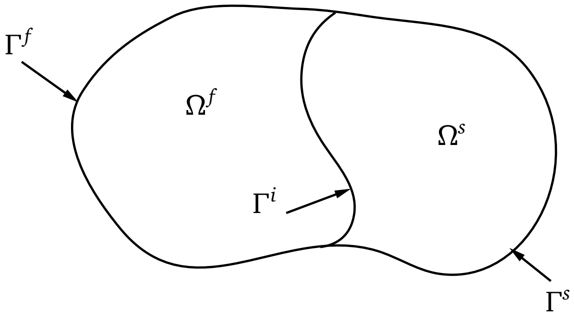

Figure 2.3.: Sketch of a general fluid-structure interaction problem

Fluid part:

$$\begin{aligned}
\rho^f \left.\frac{\partial \mathbf{u}}{\partial t}\right|_\chi + \rho^f (\mathbf{u} - \hat{\mathbf{u}}) \cdot \nabla \mathbf{u} &= \nabla \cdot \sigma \quad \text{in } \Omega^f \times (0,T), \\
\nabla \cdot \mathbf{u} &= 0 \quad \text{in } \Omega^f \times (0,T) \\
&+ \text{boundary conditions on } \Gamma^f \\
&+ \text{initial conditions}
\end{aligned}$$

Solid part:

$$\begin{aligned}
\rho^s \ddot{\mathbf{d}} - \nabla_X \cdot (\mathbf{F}\,\mathbf{S}) &= 0 \quad \text{in } \Omega^s \times (0,T) \\
&+ \text{boundary conditions on } \Gamma^s \\
&+ \text{initial conditions}
\end{aligned}$$

Coupling condition:

$$\begin{aligned}
\mathbf{u} = \hat{\mathbf{u}} = \dot{\mathbf{d}} &\quad \text{on } \Gamma^i, \\
\sigma \mathbf{n}_x = \frac{1}{J} \mathbf{F}\,\mathbf{S}\,\mathbf{F}^{\mathrm{T}} \mathbf{n}_x &\quad \text{on } \Gamma^i
\end{aligned}$$

3 Constitutive equations for viscoelastic fluids

As mentioned in the previous chapter, the relation between the stress tensor and the kinematic variables is so far missing in the problem description for viscoelastic fluids. This relation is mathematically given by the constitutive equation. To find the constitutive equations for specific material, particularly for non-Newtonian fluids, is the main concern in the field of rheology.

Rheology is "the study of the flow and deformation of all forms of matter" [32]. Its origin can be traced back to an exact date: April 29th, 1929, cf. [37]. The pioneers of rheology, including E. C. Bingham, W. H. Herschel, M. Brillouin, H. Freundlich, W. Ostwald, L. Prandtl and M. Reiner, met on this day in Columbus, Ohio. In the event, Bingham and Reiner proposed the word "*Rheology*", which describes the "study of the flow and deformation of all forms of matter". Heraclitus' quote "*Panta rhei*" (everything flows) was taken to be the motto of rheology, cf. [120].

In the 85 years old history of rheology, various approaches for constructing constitutive equations have been developed. These approaches can be roughly classified into two branches: the *continuum approach* and the *microstructure approach*. In the first part of this chapter (section 3.1), these two approaches are briefly reviewed, followed by the introduction of the principles for constitutive modeling. In the second part (section 3.2 and 3.3), the derivation of the Oldroyd-B model is given via both approaches. It will be shown that the two routes lead eventually to the same macroscopic differential constitutive equation for the Oldroyd-B fluid. In the final part of the chapter, the generic form of the constitutive models, two dimensionless numbers (the Deborah and the Weissenberg number) in the constitutive equations and different formulations of the Oldroyd-B model are given in section 3.4, 3.5 and 3.6, respectively. The models, equations and their derivations given in this chapter are summarized from [144, 16, 64, 122, 34, 115, 25]. More details can be found in those works.

3.1 Approaches and principles for constitutive modeling

To achieve the goal of modeling viscoelastic fluids, one route starts from continuum mechanics, the other starts from molecular dynamics.

Since the publication of Oldroyd [101] in 1950, a rigorous theoretical framework has been set up in continuum approaches. In this approach the modeled material is assumed to be a continuum, i.e. no micro-inertial features are considered. The relevant variables are related in a framework which guarantees the material frame indifference. Different restrictions are then imposed on the constitutive equation for practical application. The models developed with this approach fall into two categories: differential and integral models.

Differential models

A starting point for the differential models is, e.g., a non-linear modification of *Maxwell's linear model*

$$\tau + \lambda \frac{\partial \tau}{\partial t} = 2\eta \mathbf{D}, \tag{3.1}$$

taking material frame-indifference into account. It yields the *Upper Convected Maxwell (UCM) model*:

$$\tau + \lambda \overset{\triangledown}{\tau} = 2\eta \mathbf{D}, \tag{3.2}$$

where λ is the relaxation time of the fluid and $\overset{\triangledown}{\tau}$ is the upper convected derivative of the stress tensor which will be explained later. Similarly, the derivation of the Oldroyd-B model starts with the Jeffrey model, see section 3.2. It has a Newtonian contribution in addition to the UCM model. More complicated models of this type can be constructed by adding terms to equation (3.2). They have the form

$$\tau + \lambda \overset{\triangledown}{\tau} + \mathbf{f}(\tau, \mathbf{D}) = 2\eta \mathbf{D}, \tag{3.3}$$

where $\mathbf{f}$ is a tensor function of τ and $\mathbf{D}$. Actually, these models are motivated by molecular ideas and originally derived from micro-structure aspects. Popular models include the *Giesekus model*, which adds a term proportional to τ^2 on the left-hand side of equation (3.2), the *Phan-Thien-Tanner (PTT) model*, which adds a term proportional to $\tau \operatorname{tr}(\tau)$, and the *Johnson-Segalman model*, which adds a term proportional to $\tau\mathbf{D} + \mathbf{D}\tau$. The major reason for adding these terms is to overcome the drawback of the UCM and Oldroyd-B model which over-predict stress at large deformation rates.

Integral models

In an integral model the stress has the form of integrals of the deformation history. One of the popular integral models derived with the continuum approach is the so-called *K-BKZ model* (named after Kaye [75], Bernstein, Kearsley and Zapas [14]). It is formulated in terms of a stored energy function $W(I_1, I_2, t-s)$, where I_1 and I_2 are two principal invariants of the relative right Cauchy-Green strain tensor $\mathbf{C}_t$, i.e.

$$I_1 = \operatorname{tr}\mathbf{C}_t^{-1}(s), \quad I_2 = \operatorname{tr}\mathbf{C}_t(s). \tag{3.4}$$

The model has the form

$$\tau = \int_{-\infty}^{t} \frac{\partial W(I_1, I_2, t-s)}{\partial I_1}(\mathbf{C}_t^{-1}(s) - \mathbf{I})\,\mathrm{d}s - \int_{-\infty}^{t} \frac{\partial W(I_1, I_2, t-s)}{\partial I_2}(\mathbf{C}_t(s) - \mathbf{I})\,\mathrm{d}s. \tag{3.5}$$

The idea behind K-BKZ is that every prior configuration of the material can be viewed as a “temporary” equilibrium configuration. The stress is found by superposition of the elastic stresses resulting from all the deformations relative to these temporary equilibrium states, cf. [122]. The UCM model can be regarded as a special case of the K-BKZ model, which has the form

$$\tau = \int_{-\infty}^{t} \frac{\eta}{\lambda^2} e^{-(t-s)/\lambda}(\mathbf{C}_t^{-1}(s) - \mathbf{I})\,\mathrm{d}s. \tag{3.6}$$

Despite of their more difficult implementation in a numerical algorithm compared to the differential models, integral models are relatively easy to use when one wants to match them with experimental data, cf. [64].

In later developments, the trend in constitutive modeling has shifted from using the continuum approach to the more physical micro-structure approach. In this approach, constitutive models are constructed with the assumption on the behaviour of polymer molecules and their interaction with the flow. The advantage of this approach is that the constitutive equations are more relevant to the material in question, i.e. if a particular physical phenomenon cannot be predicted by the developed model due to the missing considered physical factor, the model can be corrected at the micro-structural level by adding the relevant details. Three groups of basic theories are employed in the micro-structure approach: *dilute solution theories*, *network theories* and *reptation theories*.

Dilute solution theories

Kuhn [78] was the first to address the characterization of the configuration of polymer molecules using a random coil model. Starting with this work and progressing with the landmark kinetic theory, it has become more and more evident that material equations should reflect the polymer structure to facilitate processing and development of new materials. This approach culminated in the major work by Bird and co-workers [15, 16] which also summarized the state-of-the-art in the field.

In dilute solution theories the polymer molecules are treated individually, i.e. the interaction between different polymers are neglected. Therefore, two forces are considered: the hydrodynamic forces and the Brownian forces exerted on the polymer by the surrounding solvent molecules. A molecule is modelled as a chain of beads and springs, which form a “dumbbell”. Models such as UCM, Oldroyd B, finitely extensible non-linear elastic (FENE) and Giesekus can be derived from this dumbbell model.

Network theories

Since polymer interactions are neglected in the dilute solution theories, the derived models are limited to flows with small concentration. Thus one needs different theories taking the interaction between polymers into account. The work by Green and Tobolsky [53] belonged to one of the first attempts to describe relaxation processes in networked polymers, cf. [37]. The network theory for rubber-like fluids developed independently by Lodge [88] and Yamamoto [154] brought major advance in the field.

By this approach, the polymer is treated as a network of molecular chains which are linked at junction points, see figure 3.1. The junctions are not permanent, i.e. they form and decay following certain statistical laws. The motion of junctions results in the interaction between the polymer molecule and the flow. Models derived via this approach are, e.g. the Phan-Thien-Tanner (PTT) and the Johnson-Segalman models [73].

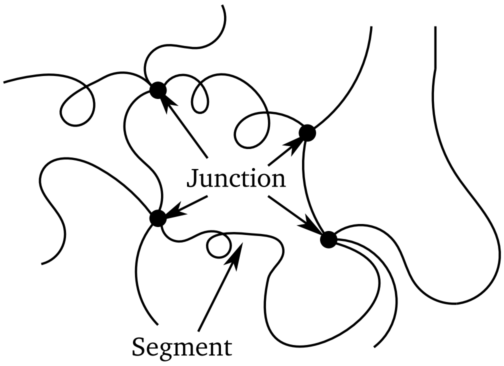

Figure 3.1.: An example of a network with temporary junctions formed by segments. In the style of [16].

Reptation theories

A theory somehow in between the dilute solution and network theories is the reptation theory. The polymer molecules are treated individually but constrained by a tube, see figure 3.2. A tube model was first proposed by Edwards [40] for rubbers. The Doi-Edwards model [35] based on the reptation theory of de Gennes [48] was another significant advancement in the field whereby the tube model was extended to melts and concentrated solutions.

With this approach, the transverse motion of each chain is strongly reduced by the surrounding polymers, but each chain has the freedom to diffuse along its own length by reptations, a random snakelike motion. Models like "Doi-Edwards" and "Pom-Pom" are representative models derived with this theory.

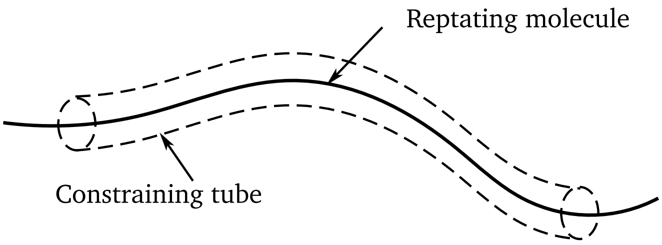

Figure 3.2.: An example of the Doi-Edwards reptating tube model

As a summary of this brief review, the classification and the representative models of the various approaches for constitutive modeling are listed in table 3.1.

Approach		Representative model
Continuum	Differential models	UCM and Oldroyd-B [101]
	Integral models	K-BKZ [75, 14]
Micro-structural	Dilute solution theories	FENE-P [114], FENE-CR [24], Giesekus [49]
	Network theories	PTT [141], Johnson-Segalman [73]
	Reptation theories	Doi-Edwards [35], Pom-Pom [94]

Table 3.1.: Classification of approaches for constitutive modeling and the representative models

Principles for constitutive modeling

Despite so many routes leading to the goal of constitutive modeling, there should also be rules which guide to derive constitutive equations that are admissible from rational and physical standpoints. The methodological principles have been proposed by different people and these principles have been the subject of long debates. Nevertheless, the following three general principles for building constitutive equations can be summarized, cf. [143]:

Principle of local action
: The stress of a material point should be determined by the history of the deformation in an arbitrarily small neighbourhood of that point.

Principle of determinism
: The current stress state in the material is determined by the past history of the motion. Future states of the motion are not related to the current state.

Principle of material frame-indifference
: The constitutive function of an objective constitutive quantity must be independent of the frame.

The first two are easy to understand, while the third one is here explained in more details.

Let φ and φ^* be two frames of references, $(\mathbf{x}, t)$ and $(\mathbf{x}^*, t^*)$ be the position and time of the same event observed by φ and φ^* simultaneously. a change of frame from φ to φ^* is a usually a *Euclidean transformation* given by

$$\mathbf{x}^*(t^*) = \mathbf{Q}(t)\mathbf{x} + \mathbf{a}(t) \quad \text{and} \quad t^* = t - t_s, \tag{3.7}$$

where $\mathbf{Q}(t)$ is a proper orthogonal tensor, hence fulfilling $\mathbf{Q}(t)^{-1} = \mathbf{Q}(t)^{\mathsf{T}}$, $\mathbf{Q}(t)\mathbf{Q}(t)^{\mathsf{T}} = \mathbf{I}$, $\mathbf{a}(t)$ is a translational vector and t_s is a constant time shift.

Relative to a change of frame from φ to φ^*, a scalar ϕ, a vector $\mathbf{u}$ or a second-order tensor σ is said to be *objective* if they meet the following requirements:

$$\begin{aligned} \phi^* &= \phi, \\ \mathbf{u}^* &= \mathbf{Q}(t)\mathbf{u}, \\ \sigma^* &= \mathbf{Q}(t)\sigma\mathbf{Q}(t)^{\mathsf{T}}. \end{aligned} \tag{3.8}$$

It can be shown that kinematic quantities such as velocity and velocity gradient are not objective quantities, while the surface normal and the rate of deformation tensor are objective. Physical quantities such as mass density, body forces, surface traction and temperature are postulated to be objective physical quantities.

Let us consider a motion χ relative to the frame φ and let $\sigma(\mathbf{X}, t)$ be the value of the Cauchy stress tensor at the material point $\mathbf{X}$ and time t in the frame φ. The constitutive equation is postulated in the form

$$\sigma(\mathbf{X}, t) = \mathscr{F}_{\varphi}(\chi^t, \mathbf{X}), \tag{3.9}$$

where $\mathscr{F}$ is called the constitutive functional and χ^t is the past history of the motion up to instant t. Similarly, the constitutive equation can be written relative to the frame φ^* as

$$\sigma^*(\mathbf{X}, t^*) = \mathscr{F}_{\varphi^*}((\chi^t)^*, \mathbf{X}). \tag{3.10}$$

The Cauchy stress tensor is an objective tensor due to the fact that the surface traction and surface normal are objective vectors. Hence the constitutive equations (3.9) and (3.10) should fulfil

$$\mathscr{F}_{\varphi^*}((\chi^t)^*, \mathbf{X}) = \mathbf{Q}(t)\mathscr{F}_{\varphi}(\chi^t, \mathbf{X})\mathbf{Q}^{\mathsf{T}}. \tag{3.11}$$

Equation (3.11) is referred to as the *condition of Euclidean objectivity*, cf. [86].

The principle of material frame-indifference requires that the constitutive function of an objective quantity must be independent of the frame, i.e.

$$\mathscr{F}_{\varphi}(\cdot, \mathbf{X}) = \mathscr{F}_{\varphi^*}(\cdot, \mathbf{X}) \tag{3.12}$$

for all frames of reference φ and φ^*, cf. [86].

Combining the condition (3.11) and (3.12), we obtain the so-called *condition of material objectivity*

$$\mathscr{F}((\chi^t)^*, \mathbf{X}) = \mathbf{Q}(t)\mathscr{F}(\chi^t, \mathbf{X})\mathbf{Q}^{\mathsf{T}}. \tag{3.13}$$

Because this condition involves only the function $\mathscr{F} = \mathscr{F}_{\varphi} = \mathscr{F}_{\varphi^*}$, it imposes restrictions on the constitutive equation for a legitimate material model, cf. [86].

The time derivative of the stress tensor plays a pivotal role in development of constitutive equations for viscoelastic fluids. As we will see later, an objective time derivative of the stress tensor is required in the constitutive equation. However, neither the partial time derivative nor the material time derivative of the stress tensor is objective. As it was first proposed by Oldroyd [101], a proper objective tensor rate can be obtained if we employ a rate operator as the time derivative $\partial/\partial t$ with respect to a reference frame suitably fixed to the body. Different choices of body-fixed frames yield different objective time derivatives of a tensor, e.g.

- *upper convected derivative*

$$\overset{\triangledown}{\sigma} = \frac{\partial \sigma}{\partial t} + (\mathbf{u} \cdot \nabla)\sigma - \sigma \nabla \mathbf{u} - \nabla \mathbf{u}^{\mathsf{T}} \sigma, \tag{3.14}$$

- *lower convected derivative*

$$\overset{\vartriangle}{\sigma} = \frac{\partial \sigma}{\partial t} + (\mathbf{u} \cdot \nabla)\sigma + \sigma \nabla \mathbf{u}^{\mathsf{T}} + \nabla \mathbf{u}\, \sigma, \tag{3.15}$$

- *co-rotational derivative*

$$\overset{\circ}{\sigma} = \frac{\partial \sigma}{\partial t} + (\mathbf{u} \cdot \nabla)\sigma - \sigma \mathbf{W} + \mathbf{W}\sigma. \tag{3.16}$$

A detailed derivation for the above invariant derivatives is provided in appendix A.

These three objective time derivatives can be combined in a general form given by

$$\frac{\mathrm{D}\sigma}{\mathrm{D}t} = \frac{\partial \sigma}{\partial t} + (\mathbf{u} \cdot \nabla)\sigma - \sigma \mathbf{W} + \mathbf{W}\sigma - a(\mathbf{D}\sigma + \sigma \mathbf{D}), \quad \text{with} \quad -1 \leqslant a \leqslant 1. \tag{3.17}$$

Substituting $a = 1, -1$ or 0 into equation (3.17), we recover the upper convected, lower convected and co-rotational derivatives, respectively. With other values of a, other objective time derivatives can be obtained. Among these objective time derivatives, the upper convected derivative is widely preferred, because it can well predict the physical phenomena (e.g. the Weissenberg effect) and this derivative can also be derived from molecular theories, as shown later in section 3.3.

3.2 Continuum approach

The Cauchy stress tensor has the form

$$\sigma = -p\mathbf{I} + \tau, \tag{3.18}$$

where p is the hydrostatic pressure and τ is the extra stress tensor. From chapter 1 it is known that it has the form

$$\tau = 2\eta(\dot{\gamma})\mathbf{D}$$

for generalized Newtonian fluid. For viscoelastic fluids the starting point of modeling with the continuum approach is to derive the stress-strain relation with the aid of prototype models which are the combinations of mechanical elements of spring and dashpot. We can associate the spring with the elastic effect of the fluid and the dashpot with the viscous effect. The produced linear viscoelastic models are then extended to material objective forms.

In what follows we illustrate *a*) the Upper Convected Maxwell (UCM) model and its mechanical prototype, the Maxwell model; *b*) the Oldroyd-B model and its mechanical prototype, the Jeffrey model.

Maxwell and Upper Convected Maxwell (UCM) model

As a first attempt to obtain a viscoelastic constitutive equation, we consider the Maxwell element which is a spring with stiffness k and a dashpot with viscosity η combined in series, see figure 3.3.

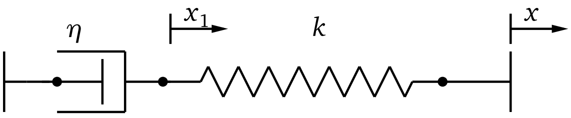

Figure 3.3.: Maxwell element

The restoring force of the spring is calculated by Hooke's law according to

$$F_1 = k\,(x - x_1), \tag{3.19}$$

where $x - x_1$ is the displacement of the spring. The friction force F_2 in the dashpot is given by

$$F_2 = \eta \dot{x}_1, \tag{3.20}$$

where $\dot{x}_1 = \partial x_1 / \partial t$ is the velocity. Because the spring and the dashpot are in series, the forces must be equal across the element, i.e. $F_1 = F_2 = F$. Therefore, the Maxwell model is obtained, i.e.

$$F + \frac{\eta}{k}\dot{F} = \eta \dot{x}. \tag{3.21}$$

We can regard F as the stress and $\dot{x}$ as the strain in the fluid. Replacing F with τ and $\dot{x}$ with $2\mathbf{D}$ in equation (3.21) and defining

$$\lambda = \frac{\eta}{k} \tag{3.22}$$

as the relaxation time, we obtain the evolution equation for the extra stress tensor,

$$\tau + \lambda \frac{\partial \tau}{\partial t} = 2\eta \mathbf{D}. \tag{3.23}$$

The relaxation time fulfils the restriction $\lambda > 0$. A large relaxation time means that the elastic effect of the fluid is strong and the fluid remembers a longer flow history. When $\lambda = 0$, the Newtonian fluid model is recovered.

Obviously, we cannot use equation (3.23) as a constitutive equation, since it does not meet the condition of material objectivity (3.13), i.e.

$$\tau^* + \lambda \frac{\partial \tau^*}{\partial t^*} - 2\eta \mathbf{D}^* \neq \mathbf{Q}(t) \left(\tau + \lambda \frac{\partial \tau}{\partial t} - 2\eta \mathbf{D} \right) \mathbf{Q}(t)^{\mathsf{T}}.$$

The problem can be remedied if we choose one of the objective time derivatives to replace the partial time derivative in equation (3.23). If we choose the upper convected derivative among the others, the Upper Convected Maxwell (UCM) model,

$$\tau + \lambda \overset{\triangledown}{\tau} = 2\eta \mathbf{D}, \tag{3.24}$$

is obtained.

Jeffrey and Oldroyd-B model

As a second attempt, we extend the Maxwell element to the Jeffrey element by adding a dashpot with viscosity η_2 parallel to the spring, see figure 3.4. The parallel combination of the spring and dashpot builds the so-called Voigt element.

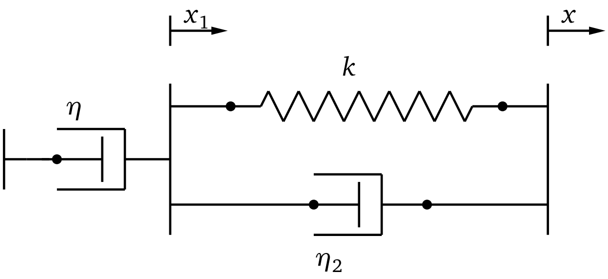

Figure 3.4.: Jeffrey element

The total displacement x in a Jeffrey element is the sum of the displacement of the dashpot with viscosity η and the displacement of the Voigt element. Therefore, the displacement of the Voigt element is

$$x_2 = x - x_1. \tag{3.25}$$

Because the dashpot with viscosity η and the Voigt element are in series, the forces are equal, i.e.

$$F = \eta \dot{x}_1 = k x_2 + \eta_2 \dot{x}_2. \tag{3.26}$$

With equations (3.25) and (3.26), the Jeffrey model is obtained, i.e.

$$F + \frac{\eta + \eta_2}{k} \dot{F} = \eta \left(\dot{x} + \frac{\eta_2}{k} \ddot{x} \right). \tag{3.27}$$

We define the relaxation time as

$$\lambda = \frac{\eta + \eta_2}{k} \tag{3.28}$$

and the retardation time as

$$\lambda_2 = \frac{\eta_2}{k}. \tag{3.29}$$

Replacing F with τ and $\dot{x}$ with $2\mathbf{D}$, replacing the partial time derivative with the upper convected derivative in equation (3.27), we obtain the Oldroyd-B model

$$\tau + \lambda \overset{\triangledown}{\tau} = 2\eta (\mathbf{D} + \lambda_2 \overset{\triangledown}{\mathbf{D}}). \tag{3.30}$$

The relaxation time λ and the retardation time λ_2 fulfil the restriction $0 \leqslant \lambda_2 \leqslant \lambda$. If $\lambda = \lambda_2 = 0$, the model reduces to a Newtonian fluid model. If $\lambda > 0$ and $\lambda_2 = 0$, the UCM model is recovered.

In numerical simulations the extra stress tensor is usually split into a solvent contribution τ_s and a polymer contribution τ_p according to

$$\tau = \tau_s + \tau_p. \tag{3.31}$$

Therefore, it is convenient to define a solvent viscosity

$$\eta_s = \eta \frac{\lambda_2}{\lambda} \tag{3.32}$$

and a polymer viscosity

$$\eta_p = \eta \left(1 - \frac{\lambda_2}{\lambda}\right). \tag{3.33}$$

Thus the solvent contribution is

$$\tau_s = 2\eta_s \mathbf{D}, \tag{3.34}$$

and the polymer contribution fulfils the equation

$$\tau_p + \lambda \overset{\triangledown}{\tau}_p = 2\eta_p \mathbf{D}. \tag{3.35}$$

The Oldroyd-B fluid is able to represent the characteristic feature of the so-called Boger fluid, a viscoelastic fluid with constant viscosity. The Boger fluid allows one to study the influence of elasticity on the fluid behaviour. This is one the of reasons why the Oldroyd-B model has been extensively investigated in numerical simulations.

Other rate type models

The UCM as well as the Oldroyd-B model have several drawbacks, such as lack of shear-dependent behaviour and unbounded extensional viscosity. In order to remedy these defects, an extra term can be added to the Oldroyd-B fluid, which results in a generic form of many constitutive equations:

$$\tau_p + \lambda \overset{\triangledown}{\tau}_p + \mathbf{f}(\tau_p, \mathbf{D}) = 2\eta_p \mathbf{D}. \tag{3.36}$$

Examples are

- Giesekus model
  It introduces a quadratic non-linearity which represents a drag force. It aims to keep the extensional viscosity finite when the extensional rate increases. The tensor function has the form

  $$\mathbf{f} = \alpha \frac{\lambda}{\eta_p} \tau_p \cdot \tau_p, \tag{3.37}$$

  where $0 \leqslant \alpha \leqslant 1$.

- Phan-Thien-Tanner model (PTT)
  For this model, the tensor function has the form

  $$\mathbf{f} = (\mathbf{Y}(\tau_p) - \mathbf{I})\tau_p + \lambda\xi(\tau_p \mathbf{D} + \mathbf{D}\tau_p), \tag{3.38}$$

  where $\mathbf{Y}$ either has the exponential form

  $$\mathbf{Y} = \exp\left(\frac{\epsilon\lambda}{\eta_p} \mathrm{tr}(\tau_p)\right), \tag{3.39}$$

  or the linearised form

  $$\mathbf{Y} = 1 + \frac{\epsilon\lambda}{\eta_p} \mathrm{tr}(\tau_p) \tag{3.40}$$

  which forms the LPPT model. The parameters ξ and ϵ regulate the shear-thinning effect and ϵ removes the singularity of the extensional viscosity.

3.3 Micro-structure approach

In the micro-structure approach the constitutive models are derived from assumptions on the behaviour of polymer molecules and their interaction with the flow. The dilute solution theory with the dumbbell model is illustrated in this section by derivation of the Oldroyd-B model. The derivation follows the works of Bird and Hassager [16], Owens and Phillips [105] and Renardy [122]. The same constitutive equation as derived from the continuum approach will be obtained. In addition, an important form of the Oldroyd-B model, the conformation tensor form, will be presented.

Bead-spring dumbbell model

We assume that the viscoelastic fluid consists of a suspension of dumbbells in a Newtonian solvent. A dumbbell possesses two identical beads (spheres) connected by a spring as shown in figure 3.5. Each of the two beads has mass m and position vectors $\mathbf{r}_1$ and $\mathbf{r}_2$ with respect to a fixed coordinate frame. The connector vector of the dumbbell is denoted as $\mathbf{R} = \mathbf{r}_2 - \mathbf{r}_1$.

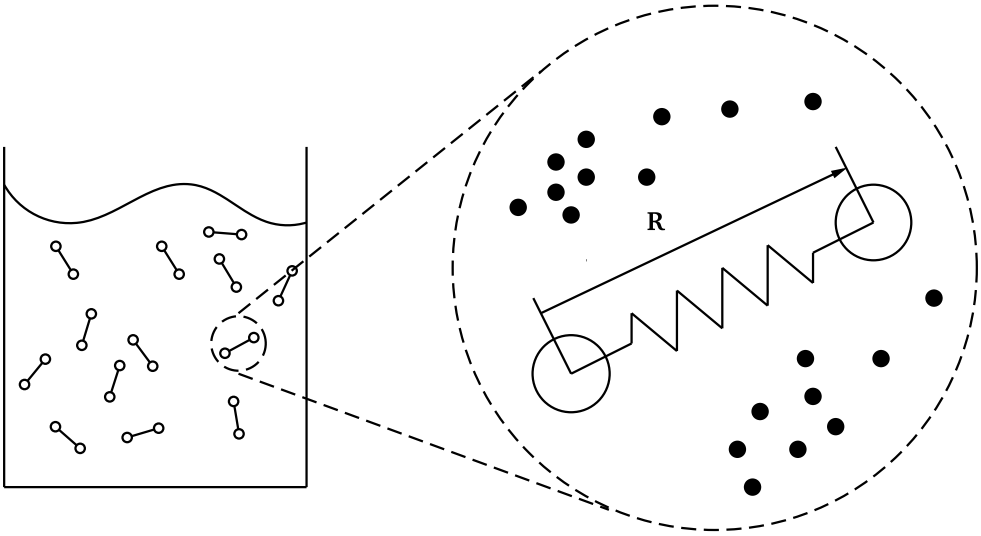

Figure 3.5.: Illustration of suspension of dumbbells in a Newtonian solvent. In the style of [25].

During the derivation, the following assumptions are made: *a*) external forces, such as gravity on the beads, are neglected; *b*) inertial forces at the molecular level are also neglected, cf. [132]. Therefore, the equation of motion for each sphere of the dumbbell according to Newton's second law now reduces to the force balance

$$\mathbf{F}_i^{(d)} + \mathbf{F}_i^{(s)} + \mathbf{F}_i^{(b)} = 0, \quad \text{with } i = 1, 2, \tag{3.41}$$

where $\mathbf{F}_i^{(d)}$, $\mathbf{F}_i^{(s)}$ and $\mathbf{F}_i^{(b)}$ stand for the friction force, spring force and Brownian force imposed on the i-th bead, respectively. These forces are calculated as follows:

- Drag force
  When the bead moves through the solution, a frictional force acts on it. According to Stokes' law, the drag force is given by

  $$\mathbf{F}_i^{(d)} = -\zeta \left(\frac{\mathrm{d}\mathbf{r}_i}{\mathrm{d}t} - \mathbf{u}(\mathbf{r}_i) \right), \tag{3.42}$$

  where ζ is the friction coefficient, $\mathbf{u}(\mathbf{r}_i)$ is the velocity of the surrounding fluid at position $\mathbf{r}_i$. The term $\mathrm{d}\mathbf{r}_i/\mathrm{d}t - \mathbf{u}(\mathbf{r}_i)$ gives the relative velocity of the i-th bead in the surrounding fluid. The friction coefficient has the form

  $$\zeta = 6\pi\eta_s a, \tag{3.43}$$

where η_s is the solvent viscosity, a is the radius of the sphere.

- Spring force
  With the assumption that the spring is a Hookean spring with the spring constant H, the spring force on the i-th sphere is

$$\mathbf{F}_1^{(s)} = -H(\mathbf{r}_1 - \mathbf{r}_2) = H\mathbf{R}, \tag{3.44}$$
$$\mathbf{F}_2^{(s)} = -H(\mathbf{r}_2 - \mathbf{r}_1) = -H\mathbf{R}. \tag{3.45}$$

- Brownian force
  The beads experience a highly random Brownian force due to the impacts of the solvent molecules. Mathematically, this random motion can be described via a multi-dimensional Wiener process $\mathbf{W}_i(t)$ $(i = 1, 2)$, which is a Gaussian stochastic process characterized by the mean and autocorrelation of its components $W_{i,j}$:

$$\langle \mathbf{W}_{i,j}(t)\rangle = 0, \quad \langle \mathbf{W}_{i,j}(t)\mathbf{W}_{i,j}(t')\rangle = \min(t, t')\mathbf{I}. \tag{3.46}$$

  We assume that the bead is large compared to the solvent molecules. Then the Brownian force can be written with the Wiener process according to

$$\mathbf{F}_i^{(b)} \mathrm{d}t = \sqrt{2kT\zeta}\,\mathrm{d}\mathbf{W}_i, \tag{3.47}$$

  where k is the Boltzmann constant, T is the absolute temperature; the coefficient $\sqrt{2kT\zeta}$ can be derived from the principle of equipartition of energy, see, e.g.,[64].

Knowing these three types of forces, we now rewrite the force balance equation (3.41) for each bead as

$$-\zeta\left(\frac{\mathrm{d}\mathbf{r}_1}{\mathrm{d}t} - \mathbf{u}(\mathbf{r}_1)\right) + H\mathbf{R} + \sqrt{2kT\zeta}\frac{\mathrm{d}\mathbf{W}_1}{\mathrm{d}t} = 0, \tag{3.48}$$
$$-\zeta\left(\frac{\mathrm{d}\mathbf{r}_2}{\mathrm{d}t} - \mathbf{u}(\mathbf{r}_2)\right) - H\mathbf{R} + \sqrt{2kT\zeta}\frac{\mathrm{d}\mathbf{W}_2}{\mathrm{d}t} = 0. \tag{3.49}$$

We want to rewrite equations (3.48) and (3.49) in terms of the connector vector $\mathbf{R}$. Truncating the Taylor expansion of $\mathbf{u}(\mathbf{r}_2)$ with respect to $\mathbf{r}_1$ at second-order, we have the following expression for $\mathbf{u}(\mathbf{r}_2)$:

$$\mathbf{u}(\mathbf{r}_2) = \mathbf{u}(\mathbf{r}_1) + \nabla\mathbf{u}^{\mathrm{T}} \cdot (\mathbf{r}_2 - \mathbf{r}_1) = \mathbf{u}(\mathbf{r}_1) + \nabla\mathbf{u}^{\mathrm{T}} \cdot \mathbf{R}. \tag{3.50}$$

Defining $\mathbf{W} = (\mathbf{W}_2 - \mathbf{W}_1)/\sqrt{2}$ and subtracting the equation (3.49) from (3.48), the following equation regarding the end-to-end vector of the dumbbell is obtained

$$\frac{\mathrm{d}\mathbf{R}}{\mathrm{d}t} = \nabla\mathbf{u}^{\mathrm{T}} \cdot \mathbf{R} - \frac{2H}{\zeta}\mathbf{R} + \sqrt{\frac{4kT}{\zeta}}\frac{\mathrm{d}\mathbf{W}}{\mathrm{d}t}. \tag{3.51}$$

Fokker-Plank equation of the dumbbell

Equation (3.51) is a stochastic differential equation, the treatment of which requires additional mathematical tools. Assume that each macroscopic volume element in space contains numerous polymer molecules. A probability density $\psi(\mathbf{R}, t)$ describes the distribution of dumbbells having the orientation $\mathbf{R}$. Equation (3.51) can be converted to the Fokker-Planck equation

$$\frac{\partial \psi(\mathbf{R}, t)}{\partial t} = -\frac{\partial}{\partial \mathbf{R}}\left((\nabla\mathbf{u}^{\mathrm{T}} \cdot \mathbf{R} - \frac{2H}{\zeta}\mathbf{R})\psi(\mathbf{R}, t) - \frac{2kT}{\zeta}\frac{\partial \psi(\mathbf{R}, t)}{\partial \mathbf{R}} \right). \tag{3.52}$$

As mentioned by Renardy [122], it is not necessary to solve equation (3.52). Instead, only a system of equations involving some moments of $\psi(\mathbf{R}, t)$ has to be solved. We define g as a function of the connector vector $\mathbf{R}$. The expectation of g is

$$\langle g(\mathbf{R})\rangle = \int_{\mathbb{R}^3} g(\mathbf{R})\psi(\mathbf{R}, t)\,\mathrm{d}\mathbf{R}. \tag{3.53}$$

We then multiply the Fokker-Planck equation (3.52) by $g(\mathbf{R})$ and integrate over $\mathbb{R}^3$. Applying the partial integration and using the fact that $\psi = 0$ for $|\mathbf{R}| \to \infty$, the equation of change for $\langle g(\mathbf{R})\rangle$ is obtained as

$$\frac{\mathrm{d}}{\mathrm{d}t}\langle g(\mathbf{R})\rangle = \left\langle (\nabla\mathbf{u}^{\mathrm{T}} \cdot \mathbf{R})\frac{\partial}{\partial \mathbf{R}} g(\mathbf{R})\right\rangle + \frac{2kT}{\zeta}\left\langle \frac{\partial}{\partial \mathbf{R}}\frac{\partial}{\partial \mathbf{R}} g(\mathbf{R})\right\rangle - \frac{2H}{\zeta}\left\langle \mathbf{R}\frac{\partial}{\partial \mathbf{R}} g(\mathbf{R})\right\rangle. \tag{3.54}$$

A similar relation to (3.54) holds for a tensor function $\mathbf{g}(\mathbf{R})$. In particular, we are interested in $\mathbf{g}(\mathbf{R}) = \mathbf{RR}$, since we will see later that $\langle \mathbf{RR}\rangle$ is related to the conformation tensor $\mathbf{c}$ and to the stress tensor τ_p. Therefore, we have the equation for $\langle \mathbf{RR}\rangle$:

$$\frac{\mathrm{d}}{\mathrm{d}t}\langle \mathbf{RR}\rangle - \langle \mathbf{RR}\rangle\nabla\mathbf{u} - \nabla\mathbf{u}^{\mathrm{T}}\langle \mathbf{RR}\rangle = \frac{4kT}{\zeta}\mathbf{I} - \frac{4H}{\zeta}\langle \mathbf{RR}\rangle. \tag{3.55}$$

The terms on the left-hand side of equation (3.55) are equal to the upper convected derivative of $\langle \mathbf{RR}\rangle$. When the system is in equilibrium, i.e. $\nabla\mathbf{u} = 0$ and $\mathrm{d}\langle \mathbf{RR}\rangle/\mathrm{d}t = 0$, from equation (3.55) we obtain

$$\langle \mathbf{RR}\rangle_{eq} = \frac{kT}{H}\mathbf{I}. \tag{3.56}$$

Extra stress tensor and conformation tensor

The next step is to find the relation between $\langle \mathbf{RR}\rangle$ and the extra stress tensor. We split the total stress tensor σ into a solvent part σ_s and a polymer part σ_p according to

$$\begin{aligned} \sigma &= \sigma_s + \sigma_p \\ &= (-p_s\mathbf{I} + \tau_s) + (-p_p\mathbf{I} + \tau_p) \\ &= -p\mathbf{I} + \tau, \end{aligned} \tag{3.57}$$

where $p = p_s + p_p$, $\tau = \tau_s + \tau_p = 2\eta_s\mathbf{D} + \tau_p$. Following the elementary physical derivation by Kramer [77], the dumbbell contributes to the stress for two principal reasons: *a*) an arbitrary plane in the suspension may at any moment be straddled by the two beads of the dumbbell, and there will be a force of tension or compression transmitted through the connector; *b*) the beads themselves may cross the arbitrary plane and bring with them a certain amount of momentum. Therefore, we separate the polymer contribution of the extra stress into these two contributions $\tau_p^{(s)}$ and $\tau_p^{(b)}$ according to

$$\tau_p = \tau_p^{(s)} + \tau_p^{(b)}. \tag{3.58}$$

- Contribution from the spring force
  Let an arbitrary plane in the suspension have unit normal $\mathbf{n}$. The average force is exerted by all springs of all dumbbells from the negative side of the oriented plane on the positive side. The positive side has the same direction as the plane normal, see figure 3.6. For every dumbbell straddling the plane, we denote the force as $\mathbf{F}_1^{(s)}$, if bead 1 is on the negative side, i.e. $\mathbf{R}\cdot\mathbf{n} > 0$, and the force as $\mathbf{F}_2^{(s)}$, if bead 2 is on the negative side, i.e. $\mathbf{R}\cdot\mathbf{n} < 0$. Let $\mathbf{F}^{(s)} = \mathbf{F}_1^{(s)} = -\mathbf{F}_2^{(s)}$. The average force exerted by all dumbbells of all orientations for which the connector vector $\mathbf{R}$ intersects the plane in the direction $\mathbf{n}$ is

$$\langle \mathrm{sgn}(\mathbf{R}\cdot\mathbf{n})\mathbf{F}^{(s)}\rangle = \int \mathrm{sgn}(\mathbf{R}\cdot\mathbf{n})\mathbf{F}^{(s)}\psi(\mathbf{R}, t)\,\mathrm{d}\mathbf{R}. \tag{3.59}$$

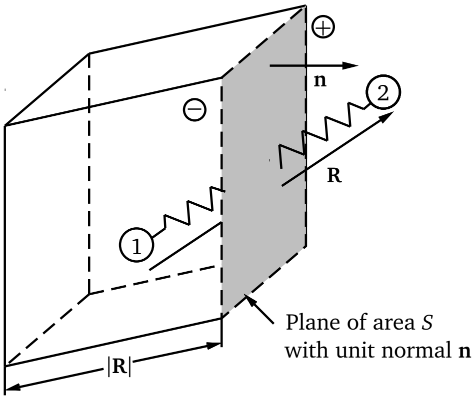

Figure 3.6.: Illustration of contribution from spring force. In the style of [16].

Assume that we have N_p elastic dumbbells in the system. The connector $\mathbf{R}$ intersects the plane if and only if either $\mathbf{r_1}$ or $\mathbf{r_2}$ is contained in the box with volume $S|\mathbf{R}\cdot\mathbf{n}|$, where S is the area of the plane. The probability of finding $\mathbf{r}_i$ $(i = 1,2)$ in this box is given by $S|\mathbf{R}\cdot\mathbf{n}|/V$, where V is the volume of the system. The total average force on the plane $\mathbf{F}$ can be calculated by

$$\mathbf{F} = N_p \int \operatorname{sgn}(\mathbf{R}\cdot\mathbf{n})\mathbf{F}^{(s)}\psi(\mathbf{R},t)\frac{1}{V}S|\mathbf{R}\cdot\mathbf{n}|\,\mathrm{d}\mathbf{R} = n\int \mathbf{F}^{(s)}\mathbf{R}\psi(\mathbf{R},t)\mathrm{d}\mathbf{R}\cdot S\mathbf{n}, \tag{3.60}$$

where $n = N_p/V$ is the number of dumbbells per unit volume. Since $\mathbf{F} = \sigma_p^{(c)}\cdot S\mathbf{n}$, the contribution of the dumbbell spring connectors to the stress in the solution is

$$\sigma_p^{(s)} = n\int \mathbf{F}^{(s)}\mathbf{R}\psi(\mathbf{R},t)\mathrm{d}\mathbf{R} = n\langle\mathbf{F}^{(s)}\mathbf{R}\rangle = nH\langle\mathbf{R}\mathbf{R}\rangle, \tag{3.61}$$

where the expression of $\mathbf{F}^{(s)} = H\mathbf{R}$ is obtained from equation (3.44).

- Contribution from bead motion
  The beads crossing an arbitrary plane will contribute to the stress tensor because of the momentum transported by the beads. In a time interval Δt the beads in volume $(\mathrm{d}\mathbf{r}_1/\mathrm{d}t - \mathbf{u})S\Delta t$ cross the plane of area S. Every bead transports the momentum $m(\mathrm{d}\mathbf{r}_1/\mathrm{d}t - \mathbf{u})$. The probability of having $\mathbf{r}_1$ within this volume is $\frac{1}{V}(\mathrm{d}\mathbf{r}_1/\mathrm{d}t - \mathbf{u})S\Delta t$. Then the amount of momentum transported across the plane is

$$nm\left(\frac{\mathrm{d}\mathbf{r}_1}{\mathrm{d}t} - \mathbf{u}\right)\left(\left(\frac{\mathrm{d}\mathbf{r}_1}{\mathrm{d}t} - \mathbf{u}\right)\cdot\mathbf{n}S\right)\Delta t, \tag{3.62}$$

  where n is again the number of dumbbells per unit volume and m the mass of the beads.

  In most publications on kinetic theory, the velocity distribution is assumed to be Maxwellian, cf. [16]. The Maxwell-Boltzmann distribution is a Gaussian distribution given by

$$\langle\mathbf{X}\rangle = 0, \tag{3.63}$$

$$\langle\mathbf{X}^2\rangle = \frac{kT}{m}\mathbf{I}, \tag{3.64}$$

  where $\mathbf{X}$ is a random variable. Consequently, we obtain

$$\left\langle nm\left(\frac{\mathrm{d}\mathbf{r}_1}{\mathrm{d}t} - \mathbf{u}\right)^2 S\Delta t\cdot\mathbf{n}\right\rangle = nm\left\langle\left(\frac{\mathrm{d}\mathbf{r}_1}{\mathrm{d}t} - \mathbf{u}\right)^2\right\rangle\cdot\mathbf{n}S\Delta t = nkT\mathbf{I}\cdot\mathbf{n}S\Delta t. \tag{3.65}$$

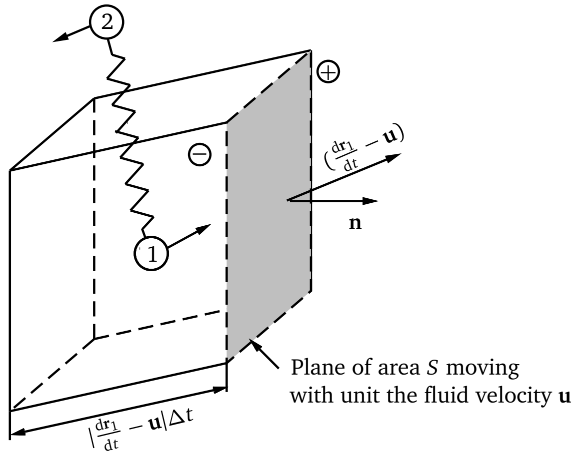

Figure 3.7.: Illustration of the contribution from bead motion. In the style of [16].

Therefore, the average value of the momentum flux resulting from bead 1 with all possible velocities and dumbbells of all possible configurations is given by

$$n \int kT\mathbf{I}\psi(\mathbf{R},t)\mathrm{d}\mathbf{R} \cdot \mathbf{n}S\Delta t = nkT\mathbf{I} \int \psi(\mathbf{R},t)\mathrm{d}\mathbf{R} \cdot \mathbf{n}S\Delta t = nkT\mathbf{I} \cdot \mathbf{n}S\Delta t. \tag{3.66}$$

The above result is also valid for bead 2. Hence we have

$$\sigma_p^{(b)} \cdot \mathbf{n}S\Delta t = 2nkT\mathbf{I} \cdot \mathbf{n}S\Delta t, \tag{3.67}$$

which yields

$$\sigma_p^{(b)} = 2nkT\mathbf{I}. \tag{3.68}$$

Summarizing the above two contributions, according to equations (3.61) and (3.68), the total polymer stress is then given by

$$\sigma_p = \sigma_p^{(b)} + \sigma_p^{(s)} = -p_p\mathbf{I} + \tau_p = 2nkT\mathbf{I} + nH\langle \mathbf{RR} \rangle. \tag{3.69}$$

The corresponding equation in equilibrium (i.e. $\tau_p = 0$) gives the polymeric contribution to the pressure. From equation (3.56) we know $\langle \mathbf{RR} \rangle_{eq} = \frac{kT}{H}\mathbf{I}$ and thus obtain

$$p_p\mathbf{I} = -nH\langle \mathbf{RR} \rangle_{eq} - 2nkT\mathbf{I} = -3nkT\mathbf{I}. \tag{3.70}$$

According to equation (3.69) we obtain

$$\tau_p = 2nkT\mathbf{I} + nH\langle \mathbf{RR} \rangle + p_p\mathbf{I} = nH\langle \mathbf{RR} \rangle - nkT\mathbf{I}. \tag{3.71}$$

Then, on the one hand, the so-called Kramers expression for the extra stress tensor is obtained:

$$\tau = \tau_s + \tau_p = 2\eta_s\mathbf{D} + nH\langle \mathbf{RR} \rangle - nkT\mathbf{I}. \tag{3.72}$$

On the other hand, using the information from equations (3.55) and (3.71), we obtain the so-called Giesekus expression

$$\tau = 2\eta_s\mathbf{D} - \frac{n\zeta}{4}\overset{\triangledown}{\langle \mathbf{RR} \rangle}. \tag{3.73}$$

The term with $\langle \mathbf{RR} \rangle$ in (3.72) and (3.73) can be eliminated by taking the upper convected derivative of (3.72) and using the equation

$$\overset{\triangledown}{\mathbf{I}} = -2\mathbf{D}. \tag{3.74}$$

The final form of the extra stress tensor then reads

$$\tau - 2\eta_s \mathbf{D} = -\frac{\zeta}{4H}(\overset{\triangledown}{\tau} - nkT2\mathbf{D} - 2\eta_s \overset{\triangledown}{\mathbf{D}}). \tag{3.75}$$

The relaxation time λ, the polymer viscosity η_p and the retardation time λ_2 are defined by

$$\lambda = \frac{\zeta}{4H}, \quad \eta_p = \frac{nkT\zeta}{4H} \quad \text{and} \quad \lambda_2 = \frac{\eta_s}{\eta}\lambda, \tag{3.76}$$

where $\eta = \eta_s + \eta_p$. We obtain the final form

$$\tau + \lambda \overset{\triangledown}{\tau} = 2\eta(\mathbf{D} + \lambda_2 \overset{\triangledown}{\mathbf{D}}), \tag{3.77}$$

which is the same as equation (3.30) as it is derived from the continuum approach. Written in solvent-polymer contribution form, they read

$$\tau = \tau_s + \tau_p, \tag{3.78}$$

$$\tau_s = 2\eta_s \mathbf{D}, \tag{3.79}$$

$$\tau_p + \lambda \overset{\triangledown}{\tau}_p = 2\eta_p \mathbf{D}. \tag{3.80}$$

The tensor $\langle \mathbf{RR} \rangle$ is related to the conformation tensor by

$$\mathbf{c} = \frac{\langle \mathbf{RR} \rangle}{\langle \mathbf{RR} \rangle_{eq}}, \tag{3.81}$$

where $\langle \mathbf{RR} \rangle_{eq}$ is known from equation (3.56). Therefore, we easily obtain the relation between the polymer contribution of the extra stress tensor and the conformation tensor according to

$$\tau_p = \frac{\eta_p}{\lambda}(\mathbf{c} - \mathbf{I}). \tag{3.82}$$

The evolution equation of the conformation tensor for the Oldroyd-B model can be obtained either by substituting (3.81) into (3.55) or substituting (3.82) into (3.80). It reads

$$\frac{\partial \mathbf{c}}{\partial t} + \mathbf{u} \cdot \nabla \mathbf{c} - \mathbf{c} \nabla \mathbf{u} - \nabla \mathbf{u}^{\mathrm{T}} \mathbf{c} = \frac{1}{\lambda}(\mathbf{I} - \mathbf{c}). \tag{3.83}$$

Non-linear Dumbbells

The Oldroyd-B model has drawbacks such as infinite extensional viscosity for finite extension rate. The problem comes from the fact that the dumbbells are infinitely extensible. To remedy this problem, non-linear dumbbells can be applied. These models are called Finitely Extensible Non-linear Elastic (FENE) models.

- FENE-P model
  This model has been proposed by Peterlin [114], hence the model is called “-P” model. The spring force in the model is obtained from

$$\mathbf{F}^{(s)} = \frac{H\mathbf{R}}{1 - \langle R^2/R_0^2 \rangle}, \tag{3.84}$$

  where $R^2 = \mathrm{tr}(\mathbf{RR})$ and R_0 is the maximum spring length. The evolution equation for the conformation tensor reads

$$\mathbf{c} + \frac{\lambda}{f^{(s)}(\mathbf{c})} \overset{\triangledown}{\mathbf{c}} = \frac{1}{f^{(s)}(\mathbf{c})}\mathbf{I}, \tag{3.85}$$

  where

$$f^{(s)}(\mathbf{c}) = \frac{1}{1 - \mathrm{tr}(\mathbf{c})/R_0^2}. \tag{3.86}$$

  The FENE-P model is able to predict a finite extensional viscosity for all extensional rates and to describe shear-shinning effects.

- FENE-CR model
  A modification of the FENE-P model has been performed by Chiloctt and Rallison [24], thus “CR”, to enable the model to reproduce constant shear viscosity and, therefore, to predict the behaviour of Boger fluids. The equation for the conformation tensor reads

$$\mathbf{c} + \frac{\lambda}{f^{(s)}(\mathbf{c})} \overset{\triangledown}{\mathbf{c}} = \mathbf{I}, \tag{3.87}$$

  where the function $f^{(s)}(\mathbf{c})$ is given by (3.86)

3.4 The generic form of the conformation tensor transport equation

The presented models derived from continuum and micro-structure approaches can be written in a generic differential equation in terms of the conformation tensor as

$$\overset{\triangledown}{\mathbf{c}} = \frac{f(\mathbf{c})}{\lambda}\mathcal{H}(\mathbf{c}), \tag{3.88}$$

where the function $f(\mathbf{c})$ is a scalar and $\mathcal{H}(\mathbf{c})$ is a tensor-valued function of the tensorial variable $\mathbf{c}$. The models are explicitly displayed in table 3.2. With this generic form, it is convenient to implement different models in a CFD code.

Model name	$f(\mathbf{c})$	$\mathcal{H}(\mathbf{c})$
Oldroyd-B	1	$\mathbf{I} - \mathbf{c}$
Linear PTT	$(1 + \epsilon(\mathrm{tr}(\mathbf{c}) - 3))$	$\mathbf{I} - \mathbf{c}$
PTT	$\epsilon(\mathrm{tr}(\mathbf{c}) - 3)$	$\mathbf{I} - \mathbf{c}$
FENE-CR	$\frac{1}{1-\mathrm{tr}(\mathbf{c})/R_0^2}$	$\mathbf{I} - \mathbf{c}$
FENE-P	1	$\mathbf{I} - \frac{\mathbf{c}}{1-\mathrm{tr}(\mathbf{c})/R_0^2}$
Giesekus	1	$\mathbf{I} - \mathbf{c} - \alpha(\mathbf{I} - \mathbf{c})^2$

Table 3.2.: Function $f(\mathbf{c})$ and $\mathcal{H}(\mathbf{c})$ for different viscoelastic fluid models

3.5 Dimensionless numbers in viscoelastic fluid flow

Dimensionless groups are usually used in engineering to facilitate correlation and interpretation of experimental data. They significantly reduce the amount of experimental work to determine the effect of a parameter variation on the dependent parameter of the experiment. The group used for Newtonian fluids is the *Reynolds number*

$$\mathrm{Re} = \frac{\rho U L}{\eta}, \tag{3.89}$$

where U and L are the characteristic flow velocity and length, respectively. This number represents the ratio of inertial forces to viscous forces.

In the class for viscoelastic fluids, there are two dimensionless numbers: the *Deborah number* (De) and the *Weissenberg number* (Wi). Although they have different origins and quantify different effects, they are frequently used as synonyms. The difference between these two numbers and their application is briefly presented here. Details can be read in [30] and [118].

Deborah number

The Deborah number owes its name to the prophetess Deborah who proclaimed "The mountains flowed before the lord" (Judges 5:5). This number is defined by M. Reiner [120] in his after-dinner talk at the Fourth International Congress of Rheology. The Deborah number is originally defined as $\mathrm{De} = \frac{\text{time of relaxation}}{\text{time of observation}}$. Thus, if the time of observation is long or the relaxation time is short, i.e. at a small Deborah number, the material behaves like a fluid. In contrast, at large Deborah number, the material is solid-like. One can compare such a material with a silly putty, which can be both fluid-like and solid-like.

Since the definition of "time of observation" is not precise, shortly after Reiner's work, the significance of the Deborah number was discussed by Metzner, White and Denn [96]. The definition was slightly altered by using "time scale of the process" or "fluid residence time" instead of "time of observation". Therefore, the Deborah number is defined by

$$\mathrm{De} = \frac{\lambda}{T}, \tag{3.90}$$

where T is a characteristic time for the deformation process, cf. [118].

According to the definition, the Deborah number is a dimensionless measure of the rate of change of flow conditions and related to flow unsteadiness from a Lagrangian point of view. In slowly changing and steady flows, e.g. in fully developed duct flows or steady simple shear flow, the characteristic time for the deformation process is infinite, and hence the Deborah number is zero.

Weissenberg number

The Weissenberg number was introduced by White [150] who used dimensional analysis to make the equation of motion for the steady flow of a second order fluid dimensionless. The Weissenberg number is defined by

$$\mathrm{Wi} = \lambda \frac{U}{L}, \tag{3.91}$$

where U/L represents the strain rate. To avoid confusion with the Weber number (We), the Weissenberg number is usually written as Wi.

This number is interpreted as the ratio of elastic forces to viscous forces, cf. [150]. This can be illustrated, e.g. in steady simple shear flow. The dominant elastic force is due to the first normal stress difference $\tau_{xx} - \tau_{yy}$. The viscous force is the shear stress τ_{xy}. For a UCM model, $\tau_{xx} - \tau_{yy} = 2\lambda\eta\dot{\gamma}^2$ and $\tau_{xy} = \eta\dot{\gamma}$ are valid. The Weissenberg number is then $\mathrm{Wi} = 2\lambda\eta\dot{\gamma}^2/\eta\dot{\gamma}$, where the characteristic deformation rate $\dot{\gamma}$ can be estimated via U/L.

The Deborah and Weissenberg number are different but related to each other. In engineering applications, the flow in complex geometries is usually not steady. Therefore, the Deborah number is not zero. In these geometries, if one length scale determines the dynamics of the problem, the Deborah number and the Weissenberg number can coincide. For instance, in the lid-driven cavity flow an appropriate characteristic time would be $T = L/U$ where L and U are the length and the velocity of the lid, respectively. A suitable estimate for the deformation rate is $\dot{\gamma} = U/H$, where H is the height of the cavity. If $L = H$ then the Deborah and Weissenberg number are equal, i.e. $\mathrm{De} = \mathrm{Wi}$. If not, then the two numbers are related through a geometric factor.

In the rest of the present work the Weissenberg number will be used to characterize the viscoelastic flow regime.

With the Weissenberg number, the constitutive equation (3.35) for the Oldroyd-B model reads

$$\tau_p + \mathrm{Wi}\left(\frac{\partial \tau_p}{\partial t} + \mathbf{u}\cdot\nabla\tau_p - \tau_p\nabla\mathbf{u} - \nabla\mathbf{u}^{\mathrm{T}}\tau_p\right) = 2(1-\beta)\mathbf{D}, \tag{3.92}$$

where all the variables are dimensionless. The dimensionless parameter β is the viscosity ratio defined by

$$\beta = \frac{\eta_s}{\eta}. \tag{3.93}$$

The corresponding conformation tensor (3.83) is transformed to

$$\mathrm{Wi}\left(\frac{\partial \mathbf{c}}{\partial t} + \mathbf{u}\cdot\nabla\mathbf{c} - \mathbf{c}\nabla\mathbf{u} - \nabla\mathbf{u}^{\mathrm{T}}\mathbf{c}\right) = \mathbf{I} - \mathbf{c}. \tag{3.94}$$

3.6 Different forms of the differential Oldroyd-B model

In the previous sections, various forms of the Oldroyd-B model have been presented. Since the Oldroyd-B model is the mainly investigated model in the present work, its different forms will be summarised here. All these forms are often used in the literature. Some of them have concrete physical meaning, while some of them are only designed for the purpose of numerical simulation. In these different forms, the momentum and constitutive equations differ, while the continuity equation remains unchanged.

- Basic form
  This form is formulated in terms of the total extra stress tensor τ:

$$\begin{aligned} &\rho\frac{\partial \mathbf{u}}{\partial t} + \rho\mathbf{u}\cdot\nabla\mathbf{u} = -\nabla p + \nabla\cdot\tau, \\ &\tau + \lambda\overset{\triangledown}{\tau} = 2\eta(\mathbf{D} + \lambda\frac{\eta_s}{\eta}\overset{\triangledown}{\mathbf{D}}). \end{aligned} \tag{3.95}$$

- Solvent-polymer stress splitting form
  This is the most popular form in numerical simulation. It formulates the equation in terms of the polymeric contribution τ_p of the extra stress:

$$\begin{aligned} &\rho\frac{\partial \mathbf{u}}{\partial t} + \rho\mathbf{u}\cdot\nabla\mathbf{u} = -\nabla p + \nabla\cdot(2\eta_s\mathbf{D}) + \nabla\cdot\tau_p, \\ &\tau_p + \lambda\overset{\triangledown}{\tau}_p = 2\eta_p\mathbf{D}. \end{aligned} \tag{3.96}$$

- Conformation tensor form
  Based on the solvent-polymer stress splitting form, the equations can be directly written in terms of the conformation tensor:

$$\begin{aligned} &\rho\frac{\partial \mathbf{u}}{\partial t} + \rho\mathbf{u}\cdot\nabla\mathbf{u} = -\nabla p + \nabla\cdot(2\eta_s\mathbf{D}) + \frac{\eta_p}{\lambda}\nabla\cdot(\mathbf{c}-\mathbf{I}), \\ &\mathbf{c} + \lambda\overset{\triangledown}{\mathbf{c}} = \mathbf{I}, \end{aligned} \tag{3.97}$$

  where $\mathbf{c}$ and τ_p are related by

$$\tau_p = \frac{\eta_p}{\lambda}(\mathbf{c}-\mathbf{I}). \tag{3.98}$$

- Elastic-viscous stress splitting (EVSS) form
  This form is neither derived from the continuum nor from the micro-structure approach. It is designed for stable numerical simulation in order to remedy the problem of the absence of an explicit diffusive term in the basic Oldroyd-B model. A detailed discussion of this form is given in section 4.3. The governing equations read:

$$\begin{aligned} &\rho\frac{\partial \mathbf{u}}{\partial t} + \rho\mathbf{u}\cdot\nabla\mathbf{u} = -\nabla p + \nabla\cdot(2\eta\mathbf{D}) + \nabla\cdot\tau_e, \\ &\tau_e + \lambda\overset{\triangledown}{\tau}_e = -2\lambda\frac{\eta_s}{\eta}\overset{\triangledown}{\mathbf{D}}. \end{aligned} \tag{3.99}$$

  The elastic stress τ_e is related to the total extra stress according to

$$\tau = \tau_e + 2\eta\mathbf{D}. \tag{3.100}$$

4 Numerical modeling of viscoelastic fluid flow

This chapter is concerned with numerical modeling of viscoelastic fluid flow via the finite-volume method (FVM). The collocated FVM for viscoelastic fluid flow is presented in the section 4.1, where the discretization is illustrated for a generic transport equation. Afterwards, specific numerical treatments for viscoelastic fluids are discussed. These include the high-resolution schemes (HRS) for advection in section 4.2 and stabilization approaches to cope with the High Weissenberg Number Problem (HWNP) in section 4.3. At the end of the chapter three groups of simulation results are discussed. In the first group (section 4.4.1) we aim to show the effect of HRS. The simulations in the second group (section 4.4.2) have the aim to verify and validate the implemented viscoelastic fluid flow solver. In the last group (section 4.4.3) different advanced approaches to cope with the HWNP are investigated by comparison.

4.1 Finite-volume method for viscoelastic fluid flow

In this section, the FVM is presented based on the works [130, 60, 45, 136]. The governing equations for the fluid motion presented in section 2.2 and the constitutive equations shown in section 3.6 are transformed into a generic transport equation having the form

$$\underbrace{\frac{\partial \phi}{\partial t}}_{\text{accumulation term}} + \underbrace{\nabla \cdot (\mathbf{u}\phi)}_{\text{advective term}} = \underbrace{\nabla \cdot (\Gamma \nabla \phi)}_{\text{diffusive term}} + \underbrace{S^{\phi}}_{\text{source term}} \, , \tag{4.1}$$

where ϕ, which can be a scalar, a vector or a tensor, denotes a transport quantity. The vector $\mathbf{u}$ is the velocity. The scalar Γ is the diffusion coefficient. S^{ϕ} is the source term. The specific forms of ϕ, Γ and S^{ϕ} are listed in table 4.1.

Equation	ϕ	Γ	S^{ϕ}
Mass conservation	1	0	0
Momentum conservation	$\rho\mathbf{u}$	η_s/ρ	$-\nabla p + \nabla \cdot \tau_p$
Constitutive equation of Oldroyd-B model	τ_p	0	$\tau_p \nabla \mathbf{u} + \nabla \mathbf{u}^{\mathsf{T}} \tau_p + \frac{1}{\lambda}(2\eta_p \mathbf{D} - \tau_p)$
Equation for the conformation tensor	$\mathbf{c}$	0	$\mathbf{c}\nabla \mathbf{u} + \nabla \mathbf{u}^{\mathsf{T}} \mathbf{c} + \frac{1}{\lambda}(\mathbf{I} - \mathbf{c})$

Table 4.1.: Definition of the variables and constants in equation (4.1)

The starting point for finite-volume discretization is a decomposition of the spatial domain Ω into a finite number of subdomains V called control volumes (CVs), and related nodes where the unknown variables are to be computed. The collocated variable arrangement is employed, i.e. all the variables are stored at the volume center. For illustration, a two-dimensional case is discussed. The node notation for two dimensional finite-volumes is shown in figure 4.1.

After having defined the CVs, the balance equations describing the problem are formulated in the integral form for each CV. Thus, equation (4.1) is integrated over a respective control volume V and a time interval Δt, which has the form

$$\int\limits_{\Delta t}\int\limits_{V} \frac{\partial \phi}{\partial t} \mathrm{d}V \mathrm{d}t + \int\limits_{\Delta t}\int\limits_{V} \nabla \cdot (\mathbf{u}\phi) \mathrm{d}V \mathrm{d}t = \int\limits_{\Delta t}\int\limits_{V} \nabla \cdot (\Gamma \nabla \phi) \mathrm{d}V \mathrm{d}t + \int\limits_{\Delta t}\int\limits_{V} S^{\phi} \mathrm{d}V \mathrm{d}t \, . \tag{4.2}$$

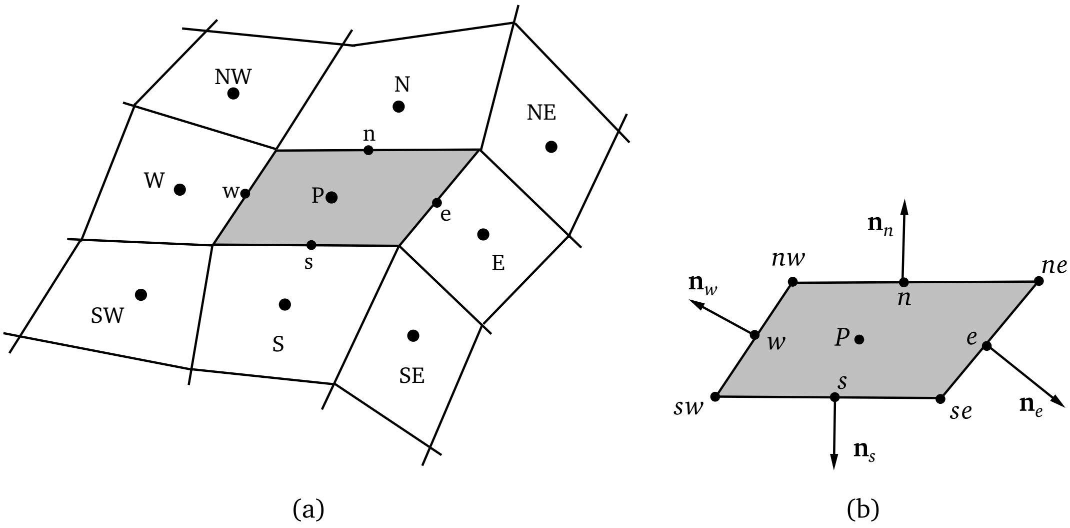

Figure 4.1.: Node notation for two-dimensional finite-volumes. In the style of [130].

- Spacial discretization of advective term

  The divergence theorem is applied to the advective term. The produced surface integrals over surface A are approximated by the mid-point rule, i.e.

$$\int_V \nabla \cdot (\mathbf{u}\phi)\,\mathrm{d}V = \int_A (\mathbf{u}\phi) \cdot \mathbf{n}\,\mathrm{d}A \approx \textstyle\sum_f (\mathbf{u}\phi)_f \cdot \mathbf{n}_f\, \delta A_f =: \sum_f F_f^C, \tag{4.3}$$

where $\mathbf{n}$ is the outer normal of the cell face, see figure 4.1. F_f^C denotes the convective flux though the face. The quantities with index f denote the value at the cell face center for the corresponding face $f = e, w, n, s$. As a standard choice, these values are calculated with first order upwind differential scheme (UDS). Without loss of generality, the example of the e side of control volume P is taken to illustrate this scheme. The value of ϕ_e depends on the direction of the mass flux $\dot{m}_e$, i.e.

$$\begin{aligned} \phi_e &= \phi_P, \quad \text{if } \dot{m}_e > 0, \\ \phi_e &= \phi_E, \quad \text{if } \dot{m}_e < 0. \end{aligned} \tag{4.4}$$

Another standard choice, the central differencing scheme (CDS), which is of second order, is employed. The face value is approximated by linear interpolation with the values in the neighbours P and E, according to

$$\phi_e = \gamma_e \phi_E + (1 - \gamma_e)\phi_P, \tag{4.5}$$

where

$$\gamma_e = \frac{|\mathbf{x}_e - \mathbf{x}_P|}{|\mathbf{x}_E - \mathbf{x}_P|}. \tag{4.6}$$

It is known that with UDS one can perform stable computations but have solution with low accuracy due to numerical diffusion, while CDS and other higher-order schemes are accurate but non-physical oscillation can be produced in the numerical solution. Since these two schemes have complementary properties, we can combine their advantages, which results the idea of high resolution schemes. The topic of high resolution schemes is discussed separately in section 4.2.

The face area δA_e and normal vector $\mathbf{n}_e$ in this two-dimensional case are

$$\delta A_e = \sqrt{(x_{ne} - x_{se})^2 + (y_{ne} - y_{se})^2},$$

$$\mathbf{n}_e = \frac{1}{\delta A_e}(y_{ne} - y_{se}, -(x_{ne} - x_{se}))^{\mathsf{T}}.$$

- Spatial discretization of diffusive term
  The divergence theorem is also applied to the diffusive term, which yields

$$\int\limits_V \nabla\cdot(\Gamma\nabla\phi)\,\mathrm{d}V = \textstyle\sum_f (\Gamma\nabla\phi)_f\cdot\mathbf{n}_f\,\delta A_f =: \textstyle\sum_f F_f^D, \tag{4.7}$$

where F_f^D denotes the diffusive flux though the face. For orthogonal grids, the gradient at the cell face can be approximated by CDS. For non-orthogonal grids, modification is required. Here we make a coordinate transformation $(x,y)\rightarrow(\xi_1,\eta_1)$. The gradient can be therefore computed by

$$\nabla\phi = \mathbf{J}^{-1}\tilde{\nabla}\phi, \tag{4.8}$$

where $\tilde{\nabla}$ denote the derivative with respect to the local coordinate (ξ_1,η_1) for the cell face. Considering exemplary the E face of the CV, the direction of ξ_1 is determined by the connecting line between P and E, while the direction of η_1 is along the face e, see figure 4.2. The transformation matrix $\mathbf{J}$ is calculated explicitly by

$$\mathbf{J} = \begin{pmatrix} \frac{\partial x}{\partial \xi_1} & \frac{\partial y}{\partial \xi_1} \\ \frac{\partial x}{\partial \eta_1} & \frac{\partial y}{\partial \eta_1} \end{pmatrix} = \begin{pmatrix} \frac{x_E-x_P}{|\mathbf{x}_E-\mathbf{x}_P|} & \frac{y_E-y_P}{|\mathbf{x}_E-\mathbf{x}_P|} \\ \frac{x_{ne}-x_{se}}{\delta A_e} & \frac{y_{ne}-y_{se}}{\delta A_e} \end{pmatrix}. \tag{4.9}$$

The determinant of the transformation matrix is

$$\det(\mathbf{J}) = \frac{(x_E-x_P)(y_{ne}-y_{se})-(y_E-y_P)(x_{ne}-x_{se})}{|\mathbf{x}_E-\mathbf{x}_P|\delta A_e}. \tag{4.10}$$

The components of $\tilde{\nabla}\phi$ are approximated by

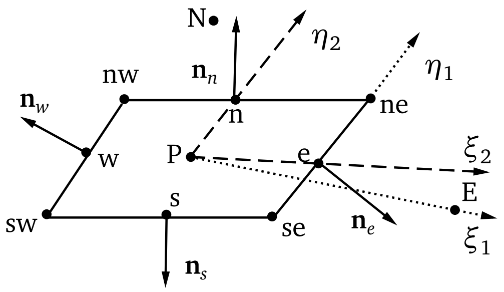

Figure 4.2.: Local coordinates (ξ_1,η_1) for point P and (ξ_2,η_2) for face e in a control volume. In the style of [130].

$$\frac{\partial\phi}{\partial\xi_1} \approx \frac{\phi_E-\phi_P}{|\mathbf{x}_E-\mathbf{x}_P|} \quad \text{and} \quad \frac{\partial\phi}{\partial\eta_1} \approx \frac{\phi_{ne}-\phi_{se}}{\delta A_e}, \tag{4.11}$$

where $\frac{\partial\phi}{\partial\xi_1}$ and $\frac{\partial\phi}{\partial\eta_1}$ are the so-called direct gradient and cross-diffusion, respectively. Therefore, the diffusion flux for the face e has the form

$$F_e^D = \underbrace{D_e(\phi_E-\phi_P)}_{\text{direct gradient term}} + \underbrace{C_e(\phi_{ne}-\phi_{se})}_{\text{cross-diffusion term}} \tag{4.12}$$

with

$$D_e = \frac{\Gamma((y_{ne}-y_{se})^2+(x_{ne}-x_{se})^2)}{(x_{ne}-x_{se})(y_E-y_P)-(y_{ne}-y_{se})(x_E-x_P)},$$
$$C_e = \frac{\Gamma((y_{ne}-y_{se})(y_E-y_P)+(x_{ne}-x_{se})(x_E-x_P))}{(y_{ne}-y_{se})(x_E-x_P)-(x_{ne}-x_{se})(y_E-y_P)}.$$

In equation (4.12) the values of ϕ_{ne} and ϕ_{se} are calculated by interpolation of the values of the neighbouring nodes N, NE, E and P. It can be shown that equation (4.12) has the same form as the decomposition with over-relaxed approach [67] which is usually used in unstructured FVM.

- Spatial discretization of accumulation and source terms
  The accumulation and source terms are evaluated in the cell center, i.e.

$$\int_V \frac{\partial \phi}{\partial t} \mathrm{d}V = \frac{\partial \phi_P}{\partial t} \delta V \quad \text{and} \quad \int_V S^\phi \mathrm{d}V = S_P^\phi \delta V, \tag{4.13}$$

  where ϕ_P and S_P^ϕ represent the average value over the CV. δV denotes the volume of the CV, which is computed in this two-dimensional as

$$\delta V = \frac{1}{2} |(x_{se} - x_{nw})(y_{ne} - y_{sw}) - (x_{ne} - x_{sw})(y_{se} - y_{nw})|.$$

  The gradient in the source terms, e.g. ∇p in the momentum equation, is computed analogously to the diffusive term. However, the local coordinate is now (ξ_2, η_2). The direction of ξ_2 is the connecting lines of P and face center e, while the direction of η_2 is the connecting lines of P and face center n, see figure 4.2. Therefore, the components of ∇p are calculated as

$$\begin{aligned} \left(\frac{\partial p}{\partial x}\right)_P &\approx \frac{(p_e - p_w)(y_n - y_s) - (p_n - p_s)(y_e - y_w)}{(x_e - x_w)(y_n - y_s) - (x_n - x_s)(y_e - y_w)}, \\ \left(\frac{\partial p}{\partial y}\right)_P &\approx \frac{(p_n - p_s)(x_e - x_w) - (p_e - p_w)(x_n - x_s)}{(x_e - x_w)(y_n - y_s) - (x_n - x_s)(y_e - y_w)}. \end{aligned} \tag{4.14}$$

  The denominators in the above equations are equal to the CV volume δV.

- Time discretization
  After spatial discretization, the approximation of equation (4.2) reads

$$\int_{\Delta t} \frac{\partial \phi_P}{\partial t} \mathrm{d}t + \frac{1}{\delta V} \int_{\Delta t} \sum\nolimits_f F_f^{tot} \mathrm{d}t = \int_{\Delta t} S_P^\phi \mathrm{d}t \ , \tag{4.15}$$

  where $F_f^{tot} = F_f^C + F_f^D$ denotes the sum of the convective and diffusive flux terms over the cell face f. Using an implicit Euler scheme, equation (4.15) is approximated by

$$\frac{1}{\Delta t} \left(\phi^n - \phi^{n-1}\right) = \frac{1}{\delta V} \left(\sum\nolimits_f F_f^{tot}\right)^n - \left(S^\phi\right)^n \ , \tag{4.16}$$

  where the superscript n and $n-1$ denote the values at current time level n and previous time level $n-1$.

Finally, the discretized equations can be written as a coupled system of linear equations having the form

$$a_P^\phi \phi_P = \sum_{nb} a_{nb}^\phi \phi_{nb} + b^\phi \ , \tag{4.17}$$

where a_P^ϕ is the central coefficient, a_{nb}^ϕ are the off-diagonal coefficients and b^ϕ includes source terms, explicitly treated parts of the convective, diffusive and temporary terms, as well as the correction terms for non-orthogonal grids. The linear equations are solved with the Strongly Implicit Procedure (SIP) by Stone [138]. The pressure-velocity coupled system is solved with the Semi-Implicit Method for Pressure Linked Equations (SIMPLE) algorithm by Patankar and Spalding [111]. This algorithm is briefly outlined in the following. More detailed description can be found in [45, 130].

After discretization, the momentum equations can be written in the form

$$\begin{aligned} a_P^u u_P &= \sum_{nb} a_{nb}^u u_{nb} + b^{u*} - (y_n - y_s)(p_e - p_w) + (y_e - y_w)(p_n - p_s), \\ a_P^v v_P &= \sum_{nb} a_{nb}^v v_{nb} + b^{v*} + (x_n - x_s)(p_e - p_w) - (x_e - x_w)(p_n - p_s), \end{aligned} \tag{4.18}$$

where u and v are the components of the velocity $\mathbf{u}$. The pressure terms are excluded form b^u and b^v, which results the rest of the source terms b^{u*} and b^{v*}. Using equation (4.18) we can express the velocity at the cell center as

$$\begin{aligned} u_P &= \frac{1}{a_P^u}\left(\sum_{nb} a_{nb}^u u_{nb} + b^{u*} - (y_n - y_s)(p_e - p_w) + (y_e - y_w)(p_n - p_s)\right), \\ v_P &= \frac{1}{a_P^v}\left(\sum_{nb} a_{nb}^v v_{nb} + b^{v*} + (x_n - x_s)(p_e - p_w) - (x_e - x_w)(p_n - p_s)\right), \end{aligned} \tag{4.19}$$

In the first step we compute the provisional velocity components u^* and v^* in equation (4.18) with an estimated pressure field p^*. The mass fluxes $\dot{m}_f^*$ computed with the provisional velocity do not fulfil the continuity equation

$$\sum_f \dot{m}_f = 0 \tag{4.20}$$

but leave a mass source b_m, i.e.

$$\sum_f \dot{m}_f^* = b_m. \tag{4.21}$$

In the next step we introduce the corrections

$$u' = u - u^*, \quad v' = v - v^* \quad \text{and} \quad p' = p - p^*.$$

Subtracting equation (4.21) from equation (4.20) yields the equation for the mass flux correction

$$\sum_f \dot{m}_f' = -b_m. \tag{4.22}$$

In the spirit of the SIMPLE algorithm, it is assumed that

$$\sum_c a_{nb}^u u_{nb}' \approx 0 \quad \text{and} \quad \sum_c a_{nb}^v v_{nb}' \approx 0.$$

Therefore, the velocity corrections are calculated according to equation (4.19) which have the forms

$$\begin{aligned} u_P' &= \frac{1}{a_P^u}\left(-(y_n - y_s)(p_e' - p_w') + (y_e - y_w)(p_n' - p_s')\right), \\ v_P' &= \frac{1}{a_P^v}\left((x_n - x_s)(p_e' - p_w') - (x_e - x_w)(p_n' - p_s')\right), \end{aligned} \tag{4.23}$$

In order to obtain the velocity correction at the cell faces without introducing oscillatory pressure field, the interpolation technique of Rhie and Chow [123] is employed. The components of velocity correction, e.g. at cell face e, are calculated by

$$u_e' = -\overline{\left(\frac{y_n - y_s}{a_P^u}\right)_e}(p_E' - p_P') \quad \text{and} \quad v_e' = \overline{\left(\frac{x_n - x_s}{a_P^v}\right)_e}(p_E' - p_P'), \tag{4.24}$$

where the overbar denotes the linear interpolation from values at neighbouring CV centers. In the above expressions (4.24), the cross-derivatives (the term related to $p_{ne}' - p_{se}'$) due to the non-orthogonality is neglected. This treatment makes the computation more efficient if the computational grid is not severely non-orthogonal (i.e. angle between grid lines is in the range 45°to 135°), cf. [113]. The velocity components at other cell faces are calculated analogously.

With the velocity correction at cell faces, equation (4.22) can be written in terms of the pressure correction, which has the form

$$a_P p_P' = \sum_{nb} a_{nb} p_{nb}' - b_m. \tag{4.25}$$

The pressure correction p' is obtained by solving equation (4.25). Afterwards, the pressure and velocity are corrected. Since the pressure correction is derived from the continuity constraint, the corrected pressure and velocity do not fulfil the momentum equation. Therefore, the procedure is repeated until both the momentum and the continuity restriction are fulfilled within a given tolerance.

In order to stabilize the solution procedure, under-relaxation is used, i.e.

$$p = p^* + \alpha_p p', \tag{4.26}$$

where α_p is the under-relaxation factor having the value between 0 and 1. This under-relaxation factor is necessary, when the sum terms in the SIMPLE method or the terms due to grid non-orthogonality are neglected, cf. [130]. It should be pointed out that the under-relaxation technique does not influence the final solution.

The calculation in each iteration within a time step proceeds as shown in figure 4.3.

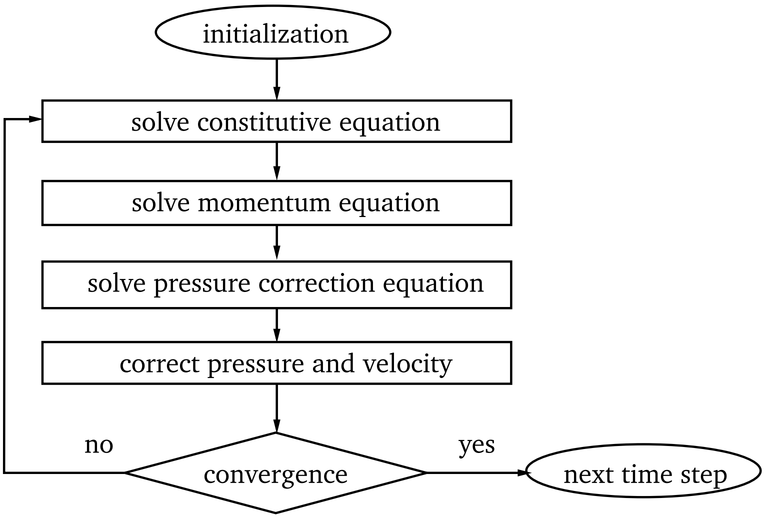

Figure 4.3.: Schematic diagram of the solution process

4.2 High resolution schemes for computation of viscoelastic fluid flow

In the Oldroyd-B and other viscoelastic fluid models the constitutive equation is advection dominated. Therefore, the treatment of advective term is of great importance. For advection dominated problems, UDS may be applied to ensure the boundedness. However, the major drawback of UDS is that it is so diffusive, that it causes the distribution of transported properties to become smeared. An possible solution is using High-Order Schemes (HOS), e.g. Linear Upwind Differencing Scheme (LUDS) or Quadratic Upstream Interpolation for Convective Kinetics (QUICK) scheme. These schemes can improved accuracy but fails to converge at rather low values of Weissenberg number when the computational meshed are fine, cf. [102]. The reason of the failure of convergence is that LUDS is lack of delimiters in the regions where high stress gradients appear. Thus the interpolated stress values at the cell face can be much higher than the values at the neighbouring nodes.

This is a well-known phenomenon in computing advection equations: first-order schemes result in a low accuracy, particularly at a shock. The solution, however, does not oscillate; Higher-order schemes capture shocks better but produce oscillatory solutions. Therefore, accurate schemes, which also do not allow an oscillatory behaviour in the solution to occur, are required.

An analysis of the conditions required by a scheme to satisfy this requirement has been initiated by Godunov [51]. He has introduced the monotonicity preserving requirement for a numerical scheme which states that no extrema is created by the numerical scheme, other than those present in the initial solution. Unfortunately, any higher-order linear scheme cannot be monotonicity preserving due to Godunov's theorem.

Theorem (Godunov)**.** *A linear monotonicity preserving scheme is at most first-order accurate.*

The proof and detailed discussions of this theorem can be found in e.g. [51, 85, 60].

Thus the only way to circumvent the theorem is to move away from the linearity property of the schemes. Consequently, only non-linear schemes can be made to be monotonicity preserving, while being essentially of higher order accuracy simultaneously. This idea builds the basic principle of the High Resolution Schemes (HRS).

To construct the HRS, there are two basic approaches: flux limiters and normalized variables. Correspondingly, two boundedness criteria are designed for these two approaches: Total Variation Diminishing (TVD) criterion for flux limiters and Convection Boundedness Criterion (CBC) for normalized variables. These two approaches and criteria have a closed relationship: *a*) flux limiters can be formulated in normalized variables; *b*) TVD is a stronger criterion than CBC, i.e. if TVD criterion is fulfilled CBC is automatically satisfied. In this section these two approaches and criteria are briefly reviewed. The illustration is done for uniform grids. Thereafter, the scheme CUBISTA [5] is presented. This scheme is applied in the simulation of viscoelastic fluid flow in the present work. The implementation of the HRS in FASTEST is discussed in the final part of this section, where the extension of HRS to non-uniform grids, treatment of block boundaries and deferred correction representation are presented.

Flux limiters and total variation diminishing criterion

The idea of introducing flux limiter can be tracked back to formulation of a generalized form of upwind-biased high-order schemes. To illustrate the problem in a simply way, we consider a one-dimensional flow with positive velocity $u > 0$. We compute the face value of the transported quantity ϕ at center cell C. As mentioned, uniform grids are considered. The face value computed with the basic schemes UD, LUDS, CDS and QUICK can be written as

$$\begin{aligned}
\text{UDS:} \quad & \phi_f = \phi_C, \\
\text{CDS:} \quad & \phi_f = \phi_C + \frac{1}{2}(\phi_D - \phi_C), \\
\text{LUDS:} \quad & \phi_f = \phi_C + \frac{1}{2}\left(\frac{\phi_C - \phi_U}{\phi_D - \phi_C}\right)(\phi_D - \phi_C), \\
\text{QUICK:} \quad & \phi_f = \phi_C + \frac{1}{2}\cdot\frac{1}{4}\left(3 + \frac{\phi_C - \phi_U}{\phi_D - \phi_C}\right)(\phi_D - \phi_C).
\end{aligned}$$

The indices U, C and D are the upwind, center and downwind points, respectively, as defined in figure 4.4. The above formulations can be written in a compact form if we define a *limiter* function $\Psi(r)$. The face value is then given by

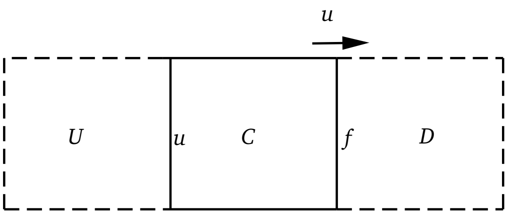

Figure 4.4.: Definition of upwind, center and downwind points

$$\phi_f = \phi_C + \frac{1}{2}\Psi(r)(\phi_D - \phi_C), \tag{4.27}$$

where

$$r = \frac{\left(\frac{\partial \phi}{\partial x}\right)_u}{\left(\frac{\partial \phi}{\partial x}\right)_f}, \tag{4.28}$$

which can be transformed, in the case of uniform grids, to

$$r = \frac{\phi_C - \phi_U}{\phi_D - \phi_C}. \tag{4.29}$$

The variable r represents the ratio of the gradients of ϕ at the face u and f. It should be remarked that in some references the authors define r as the reciprocal of the above expression. With the compact formulation (4.27), we can choose different values for the limiter function, such that different basic schemes are recovered. The values of limiter function for the basic schemes are shown in table 4.2.

Scheme	UDS	CDS	LUDS	QUICK
$\Psi(r)$	0	1	r	$(3+r)/4$

Table 4.2.: Limiter function for different linear schemes

Since changing schemes can be realised by changing the limiter function, UDS and HOS can be easily switched for computation of the cell face value. The task of the limiter function is to control the limiter, such that HOS is applied in the smooth regions while UDS is employed near shocks. It raises the question of how to distinguish smooth field to shocks. The variable r, which is the only one variable in the limiter function, can be used to identify various region. In smooth filed we expect $r \approx 1$, while near shocks we expect that r is far from 1. Then we can set criterion in term of r and Ψ.

One possible way to measure oscillations in the solution is using *total variation* of the discrete solution ϕ which is defined as

$$TV(\phi) = \sum_{i=-\infty}^{\infty} \left|\phi_{i+1} - \phi_i\right|. \tag{4.30}$$

Figure 4.5 summarizes the cases in which total variation increases, cf.[80].

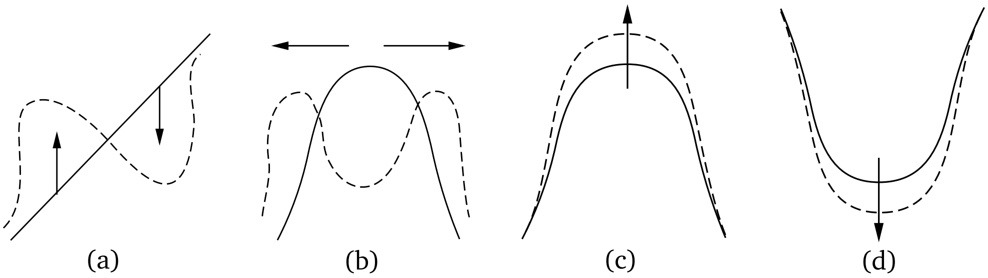

Figure 4.5.: Cases of total variation increasing [80]: (a) Monotone region becomes a maximum and a minimum; (b) Maximum splits into two maxima and a minimum; (c) Maximum increases; (d) Minimum Decreases

A numerical solution to the advection equation might not have constant total variation. However, if the oscillation appears in the solution, we would expect that the total variation of ϕ to increase. Therefore, we attempt to avoid oscillation by requiring that the scheme does not increase the total variation.

Definition. *A two-level scheme is called Total Variation Diminishing (TVD), if ϕ^n computed by the scheme satisfies*

$$TV(\phi^{n+1}) \leqslant TV(\phi^n). \tag{4.31}$$

TVD schemes has an important property that any TVD scheme is monotonicity preserving, cf. [56]. Harten [56] has devised the general condition for construction explicit three-point TVD schemes.

Theorem (Harten). *Consider a general explicit scheme of the form*

$$\phi_i^{n+1} = \phi_i^n - C_{i-1}^n(\phi_i^n - \phi_{i-1}^n) + D_i^n(\phi_{i+1}^n - \phi_i^n) \tag{4.32}$$

over one time step, where the coefficients C_{i-1}^o *and* D_i^o *are arbitrary values (which may depend on values of* ϕ^n*). Then*

$$TV(\phi^n) \leqslant TV(\phi^o)$$

provided the following conditions are satisfied:

$$\begin{aligned} C_{i-1}^n &\geqslant 0 \quad \forall i, \\ D_i^n &\geqslant 0 \quad \forall i, \\ C_i^n + D_i^o &\leqslant 1 \quad \forall i. \end{aligned} \tag{4.33}$$

Harten [56], Harten and Lax [57], Yee et al. [157] and Yee and Harten [156] have extended the theorem for implicit schemes. The extension for multipoint explicit, implicit and semi-discrete TVD schemes has been done by Jameson and Lax [66]. Wang and Widhopf [146] and Glaster [50] have given the modification for non-uniform grids. Harten's theorem and its variation give us a simple and general way to design limiter functions.

Sweby [139] has proposed a sufficient condition for a scheme to be TVD in term of the $r - \Psi$ relationship:

$$\begin{aligned} &0 \leqslant \Psi(r) \leqslant 2r, &&\text{for} \quad 0 < r < 1 \\ &0 \leqslant \Psi(r) \leqslant 2, &&\text{for} \quad r \geqslant 1 \\ &\Psi(r) = 0, &&\text{for} \quad r \leqslant 0, \end{aligned} \tag{4.34}$$

which is the grey-colour area in the $r - \Psi$ diagram shown in figure 4.6. This diagram is the so-called Sweby diagram. Plotting different basic schemes in the $r - \Psi$ diagram it is clear that all the basic schemes in table 4.2 do not fulfil TVD criterion except UDS.

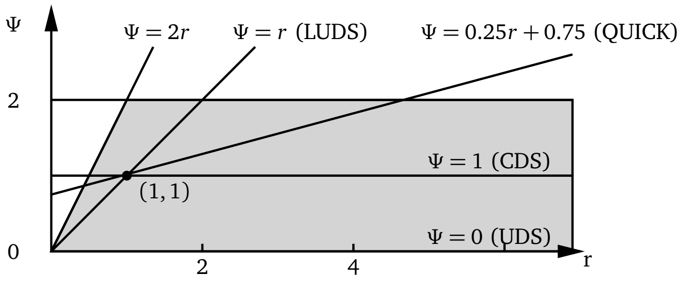

Figure 4.6.: TVD and the different linear schemes

Sweby has also introduced additional conditions which is necessary for the scheme to be second order: the limiter function should pass through the point $(1, 1)$ in the $r - \Psi$ diagram; and the range of possible second order schemes is bounded by the CDS and LUDS. These conditions results in the grey-colour area in the $r - \Psi$ diagram shown in figure 4.7. The reason why the limiter function should pass through the point $(1, 1)$ is clear. In the region of $r = 1$ the field is smooth. In this case the second order schemes should be satisfied, which implies that the limiter function Ψ should be equal to 1.

Usually, the limiter function is required to be symmetric, which is written mathematically as

$$\frac{\Psi(r)}{r} = \Psi\left(\frac{1}{r}\right). \tag{4.35}$$

This requirement ensures that the backward and forward facing gradients are treated in the same manner without need for special coding.

A number of TVD flux limiter functions have been designed which fulfil the TVD criterion (4.34) and requirement of second order accuracy and symmetry. They have the form either of piecewise-linear functions, ratios of equal-order polynomials or combinations of the two, e.g.

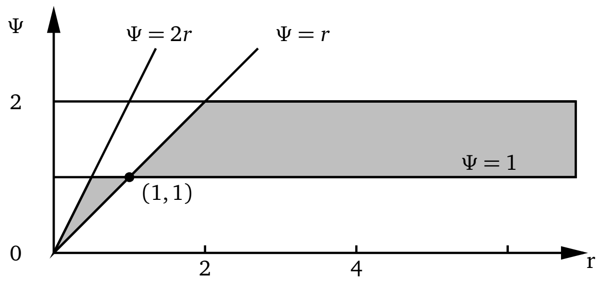

Figure 4.7.: Region for a second order TVD scheme

- Minmod [126]

$$\Psi(r) = \max[0, \min(r, 1)] \tag{4.36}$$

- Superbee [125]

$$\Psi(r) = \max[0, \min(2r, 1), \min(r, 2)] \tag{4.37}$$

- MUSCLE [83]

$$\Psi(r) = \max[0, \min(2r, \frac{r+1}{2}, 2)] \tag{4.38}$$

Normalized variables and convective boundedness criterion

Another approach to construct HRS is applying *normalized variables* introduced by Gaskell and Lau [47] and Leonard [84]. In this approach any differencing scheme, which evaluates a cell face value ϕ_f as a function of the neighbour cell values (U, C and D), i.e. $\phi_f = f(\phi_U, \phi_C, \phi_D)$, can be written as a simplified functional form

$$\tilde{\phi} = f(\tilde{\phi}_C), \tag{4.39}$$

where the advected variable ϕ is normalized by

$$\tilde{\phi} = \frac{\phi - \phi_U}{\phi_D - \phi_U}. \tag{4.40}$$

With this normalization the normalized values at upwind and downwind points are $\tilde{\phi}_U = 0$ and $\tilde{\phi}_U = 1$, respectively. When an extrema exits at center point, we have $\tilde{\phi}_C \leqslant 0$ or $\tilde{\phi}_C \geqslant 1$. When the profile of ϕ is monotonic, we have $0 < \tilde{\phi}_C < 1$. These cases are shown in form of non-normalized and normalized forms in figure 4.3.

Therefore, the basic schemes can be written in normalized variables form. They have the forms as shown in table 4.4 for the problem discretized with uniform grid.

Gaskell and Lau [47] have shown the requirement for a bounded scheme: it must possess both convective stability and interpolative boundedness, i.e. the scheme should be upwind bias and the face value must be bounded by the local cell-center values. This *Convective Boundedness Criterion* (CBC) is written mathematically written in the normalized variable formulation as

$$\begin{aligned}
&\tilde{\phi}_C \leqslant \tilde{\phi}_f, && \text{if} \quad 0 < \tilde{\phi}_C < 1, \\
&\tilde{\phi}_f = \tilde{\phi}_C, && \text{if} \quad \tilde{\phi}_C \geqslant 1 \\
&\tilde{\phi}_f = \tilde{\phi}_C, && \text{if} \quad \tilde{\phi}_C \leqslant 0.
\end{aligned} \tag{4.41}$$

Case	Non-normalized profile	Normalized profile
$\tilde{\phi}_C \leqslant 0$	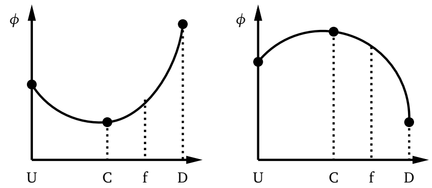	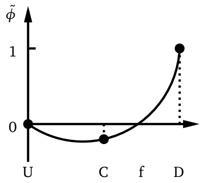
$\tilde{\phi}_C \geqslant 1$	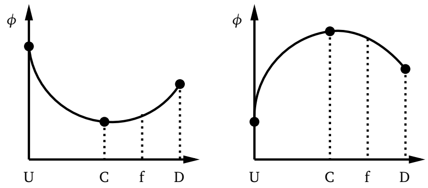	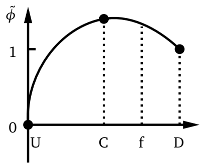
$0 < \tilde{\phi}_C < 1$	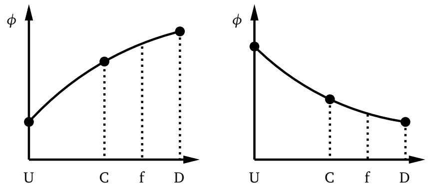	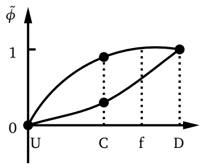

Table 4.3.: Non-normalized and normalized profiles of ϕ across three successive grid points. In style of [28].

Scheme	UDS	CDS	LUDS	QUICK
$\tilde{\phi}_f = f(\tilde{\phi}_C)$	$\tilde{\phi}_C$	$0.75 + 0.5(\tilde{\phi}_C - 0.5)$	$1.5\tilde{\phi}_C$	$0.75 + 0.75(\tilde{\phi}_C - 0.5)$

Table 4.4.: Normalized variable form for different linear schemes

According to the CBC: *a*) When ϕ_C is in a monotonic profile, the interpolation value at the cell surface should not yield any new extrema. *b*) When the value of ϕ_C is extrema, i.e. $\tilde{\phi}_C \geqslant 1$ or $\tilde{\phi}_C \leqslant 1$, ϕ_f is assigned the upwind value.

These conditions can be transformed into the Normalized Variable Diagram (NVD), as shown in figure 4.8, where the grey-colour region and the line $\tilde{\phi}_f = \tilde{\phi}_C$ correspond to the CBC region. In the figure different basic schemes are also presented in the NVD, which shows that all the schemes except for UDS do not fulfil the CBC. Leonard [84] has also concluded that if the function $\tilde{\phi}_f = f(\tilde{\phi}_C)$ passes through the point $(0.5, 0.75)$, the scheme is at least second order accuracy. Since any function $\tilde{\phi}_f$, which passes through point $(0.5, 0.75)$ can be written as

$$\tilde{\phi}_f = 0.5(1+\tilde{\phi}_C) - \mathscr{F}(1-2\tilde{\phi}_C),$$

or in non-normalized form as

$$\phi_f = 0.5(\phi_D + \phi_C) - \mathscr{F}(\phi_D - 2\phi_C + \phi_U),$$

where $\mathscr{F}$ is a function of $\tilde{\phi}_C$. Making a Taylor series expansion at the face

$$\phi_f = 0.5(\phi_D + \phi_C) - \mathscr{F}\left(\frac{\partial^2 \phi}{\partial x^2}\right)\Bigg|_f \Delta x^2 + \cdots,$$

the conclusion can be directly shown.

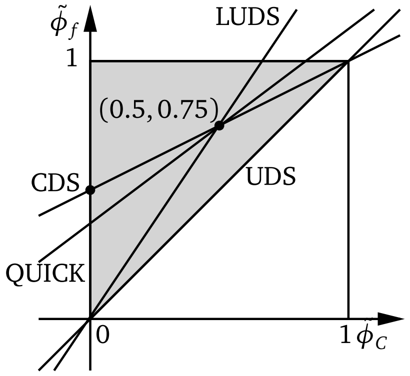

Figure 4.8.: Convection Boundedness Criterion(CBC) in Normalized Variable Diagram (NVD)

A number of schemes have developed applying the normalized variable approach and using CBC as a design principle. The typical approaches are e.g.

- SMART [47]

$$\tilde{\phi}_f = \begin{cases} 3\tilde{\phi}_C & \text{, if } 0 < \tilde{\phi}_C < \frac{1}{6} \\ \frac{3}{4}\tilde{\phi}_C + \frac{3}{8} & \text{, if } \frac{1}{6} \leqslant \tilde{\phi}_C \leqslant \frac{5}{6} \\ 1 & \text{, if } \frac{5}{6} < \tilde{\phi}_C < 1 \\ \tilde{\phi}_C & \text{, elsewhere.} \end{cases} \tag{4.42}$$

- GAMMA [68]

$$\tilde{\phi}_f = \begin{cases} \tilde{\phi}_C\left(1 + \frac{1}{2\beta_m}(1-\tilde{\phi}_C)\right) & \text{, if } 0 < \tilde{\phi}_C < \beta_m \\ \frac{1}{2}\tilde{\phi}_C + \frac{1}{2} & \text{, if } \beta_m \leqslant \tilde{\phi}_C < 1 \\ \tilde{\phi}_C & \text{, elsewhere,} \end{cases} \tag{4.43}$$

where β_m is a constant in the rage $\frac{1}{10} \leqslant \beta_m \leqslant \frac{1}{2}$.

Relation between flux limiters and normalized variables

The two approaches have different forms, but they are related to each other. It can be shown without difficulty that the cell face value function in flux limiter form can be transformed to the normalized variable form according to

$$\tilde{\phi}_f = \tilde{\phi}_C + \frac{1}{2}\Psi(r)(1-\tilde{\phi}_C), \tag{4.44}$$

where r is also a function of $\tilde{\phi}_C$, i.e.

$$r(\tilde{\phi}_C) = \frac{\tilde{\phi}_C}{1-\tilde{\phi}_C}. \tag{4.45}$$

Similarly, the flux limiter can be transferred to

$$\Psi(r) = \frac{2\tilde{\phi}_f}{1-\tilde{\phi}_C} - 2r = \frac{2(\tilde{\phi}_f - \tilde{\phi}_C)}{1-\tilde{\phi}_C}. \tag{4.46}$$

Therefore, the face value function is turned to a function $\tilde{\phi}_f = f(\tilde{\phi}_C)$ with a limiter $\Psi(\tilde{\phi}_C)$. In addition, the TVD criterion represented in $r-\Psi$ diagram can also be transformed into NVD. The grey-colour region in the NVD shown in figure 4.9 represents the TVD region. We can clearly see that TVD criterion is stronger than CBC.

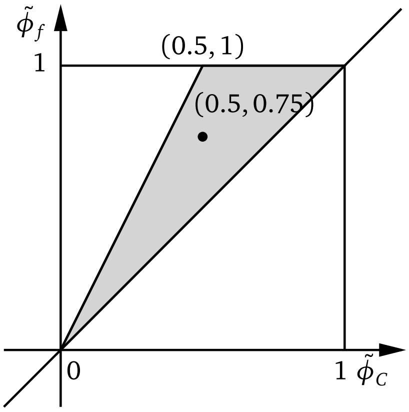

Figure 4.9.: Total variation diminishing (TVD) criterion in normalized variable diagram (NVD)

High resolution scheme CUBISTA

The boundedness criterion is one of the two essential design principles for reconstruction of HRS, cf. [148]. The other essential principle is the linearity preserving. It requires that the changes of slope of the schemes representation in the NVD should be avoided in the region near $\tilde{\phi}_C = 0.5$. There are, in addition, four optional principles which are summarized in [148]. The scheme CUBISTA (*Convergent and Universally Bounded Interpolation Scheme for the Treatment of Advection*) proposed by Alves et al. [5] are constructed according to these principles. CUBISTA uses QUICK as the basic scheme in the smooth region (near $\tilde{\phi}_C = 0.5$) and fulfils the TVD constrain.

For uniform grids the scheme CUBISTA is given by

$$\tilde{\phi}_f = \begin{cases} 1.75\tilde{\phi}_C & \text{, if} \quad 0 < \tilde{\phi}_C < 0.375, \\ 0.75\tilde{\phi}_C + 0.375 & \text{, if} \quad 0.375 \leqslant \tilde{\phi}_C \leqslant 0.75, \\ 0.25\tilde{\phi}_C + 0.75 & \text{, if} \quad 0.75 < \tilde{\phi}_C < 1, \\ \tilde{\phi}_C & , \quad \text{elsewhere.} \end{cases} \tag{4.47}$$

which corresponds the curve in NVD as shown in figure 4.10. This scheme has been shown to be suitable for computation of viscoelastic fluid flow, cf. [5]. The computation for viscoelastic fluid flow in the present work are accomplished with this scheme.

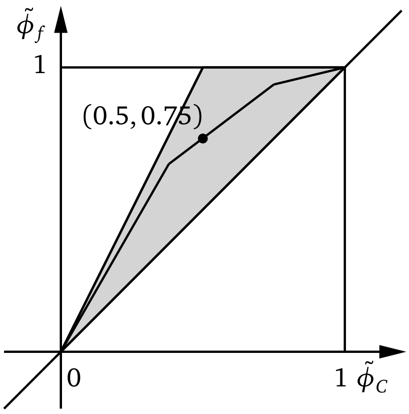

Figure 4.10.: CUBISTA in normalized variable diagram

Implementation of high resolution schemes

The previous presented HRSs are given for uniform grids. Thus the question raises: how to deal with non-uniform grids? Moreover, the values of the transported variables in the further upwind point are required in the schemes. However, there is only one layer of ghost cells at the block boundaries in the present code. How to apply the HRS at these block boundaries without large change of the code? Finally, it is important to know how to implement the scheme based on the current treatment of the convection term in FASTEST in an effective way. The following three subsections are concerned with the above questions.

High resolution schemes for non-uniform grids

The way to formulate HRS for non-uniform grids has been pointed out by Darwish and Moukalled [27]. This formulation is called *Normalized Variable and Space Formulation* (NVSF). In this formulation the normalized cell face value of any variable becomes a function of besides its closest normalized upwind neighbour value, also the corresponding normalized cell center and face locations, i.e.

$$\tilde{\phi}_f = f(\tilde{\phi}_C, \tilde{x}_C, \tilde{x}_f) \tag{4.48}$$

where the normalized coordinates are calculated as

$$\tilde{x}_C = \frac{x_C - x_U}{x_D - x_U} \quad \text{and} \quad \tilde{x}_f = \frac{x_f - x_U}{x_D - x_U}. \tag{4.49}$$

Since HRS are combinations of various basic schemes, once the derivation of the NVSF for these basic schemes is finished, the transformation of HRS is direct forward. As for an example, the basic scheme QUICK, the core scheme in CUBISTA, is presented.

In QUICK scheme, a parabolic profile is applied to describe the variation of the variable. It is written mathematically by

$$\phi = ax^2 + bx + c \tag{4.50}$$

subject to

$$\phi = \phi_U \quad \text{for } x = x_U, \tag{4.51}$$

$$\phi = \phi_C \quad \text{for } x = x_C, \tag{4.52}$$

$$\phi = \phi_D \quad \text{for } x = x_D. \tag{4.53}$$

The coefficient a, b and c can be determined from equations (4.50)-(4.53). After rearrangement and normalization the NVSF form of QUICK scheme is obtained:

$$\tilde{\phi}_f = \frac{\tilde{x}_f(\tilde{x}_f - 1)}{\tilde{x}_C(\tilde{x}_C - 1)}\tilde{\phi}_C + \frac{\tilde{x}_f(\tilde{x}_f - \tilde{x}_C)}{1 - \tilde{x}_C}. \tag{4.54}$$

Similarly, we can obtain the NVSF of the other basic schemes:

- UDS

$$\tilde{\phi}_f = \tilde{\phi}_C, \tag{4.55}$$

- CDS

$$\tilde{\phi}_f = \frac{\tilde{x}_f - \tilde{x}_C}{1 - \tilde{x}_C} + \frac{\tilde{x}_f - 1}{\tilde{x}_C - 1}\tilde{\phi}_C, \tag{4.56}$$

- LUDS

$$\tilde{\phi}_f = \frac{\tilde{x}_f}{\tilde{x}_C}\tilde{\phi}_C. \tag{4.57}$$

All second- and third-order schemes can be represented by

$$\tilde{\phi}_f = \tilde{x}_f + \mathscr{M}(\tilde{\phi}_C - \tilde{x}_C),$$

where $\mathscr{M}$ is the slope of the linear function. Based on this fact, Darwish and Moukalled [27] proposed the necessary and sufficient condition for a scheme in NVSF to be second order accurate: the normalized function passes through the point $(\tilde{x}_C, \tilde{x}_f)$.

Following the above conclusions, the HRS developed for a uniform grid can be extended to non-uniform grid. The NVSF of CUBISTA reads

$$\tilde{\phi}_f = \begin{cases} \left(1 + \dfrac{\tilde{x}_f \tilde{x}_C}{3(1 - \tilde{x}_C)}\right)\dfrac{\tilde{x}_f}{\tilde{x}_C}\tilde{\phi}_C, & \text{if} \quad 0 < \tilde{\phi}_C < \dfrac{3}{4}\tilde{x}_C, \\ \dfrac{\tilde{x}_f(1 - \tilde{x}_f)}{\tilde{x}_C(1 - \tilde{x}_C)}\tilde{x}_C + \dfrac{\tilde{x}_f(\tilde{x}_f - \tilde{x}_C)}{1 - \tilde{x}_C}, & \text{if} \quad \dfrac{3}{4}\tilde{x}_C \leqslant \tilde{\phi}_C \leqslant \dfrac{1 + 2(\tilde{x}_f - \tilde{x}_C)}{2\tilde{x}_f - \tilde{x}_C}\tilde{x}_C, \\ 1 - \dfrac{1 - \tilde{x}_f}{2(1 - \tilde{x}_C)}(1 - \tilde{x}_C), & \text{if} \quad \dfrac{1 + 2(\tilde{x}_f - \tilde{x}_C)}{2\tilde{x}_f - \tilde{x}_C}\tilde{x}_C < \tilde{\phi}_C < 1, \\ \tilde{\phi}_C, & \text{elsewhere}. \end{cases} \tag{4.58}$$

Construction of virtual upwind point

The solution to deal with the block boundary problem is construction of virtual upwind point. In order to understand the necessaries for using virtual upwind point, the block structured technique in FASTEST is first reviewed. For parallel computation the computed spatial problem domain is divided into non-overlapping blocks. These blocks are assigned to different processors for simultaneous computation. The coupling of these blocks is realised by data exchange between adjacent block boundaries. To keep the communication effort between processors small, the ghost cells is introduced. The data in the adjacent boundary layer of the neighbour block is stored in these ghost cells, see figure 4.11. It is obvious that if higher-order schemes are applied, farther neighbouring points are involved and one layer of ghost cells is not enough. For instance, consider the right boundary cell faces in the left block A in figure 4.11. If velocity directs from left to right, the upwind points locate at the second left layer in block B. The information of the cells in this layer is not known by block A. To remedy the problem, one can add one more layer of ghost cells, which is programming-expensive. Alternatively, the concept of virtual upwind point, can be introduced.

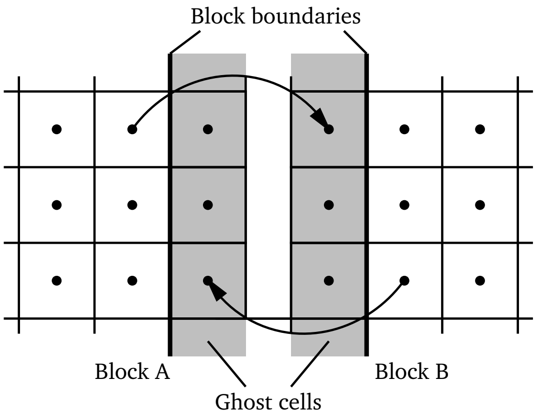

Figure 4.11.: Block boundaries and ghost cells. In style of [130].

The idea of introducing virtual upwind points has been proposed by Jasak et al. [68]. The motivation of introducing virtual upwind point is to solve the problem in unstructured meshes. Because an unstructured mesh does not have clear directionality, it is not clear how to determine the neighbour cells. Thus we want to approximate the value at upwind point according to

$$\phi_U = \phi_D - (\nabla\phi)_C \cdot \mathbf{d}_{UD}, \tag{4.59}$$

where $\mathbf{d}_{UD}$ is the distance between points U and D. Since we do not know the exact position of the upwind point, we choose the virtual upwind node such that the center point C locates at the center between point U and point D, see figure 4.12. Then we have $\mathbf{d}_{UD} = 2\mathbf{d}_{CD}$. The value of the virtual upwind point is, therefore, computed as

$$\phi_U = \phi_D - 2(\nabla\phi)_C \cdot \mathbf{d}_{CD}. \tag{4.60}$$

Consequently, the effort on programming is only to compute the gradients at the cell center and to store them in the ghost cells in the same way as other variables. Since the virtual upwind point is assumed to be at the middle between upwind and downwind points, it is required that the variation of the size of cells should not be large at the block boundaries.

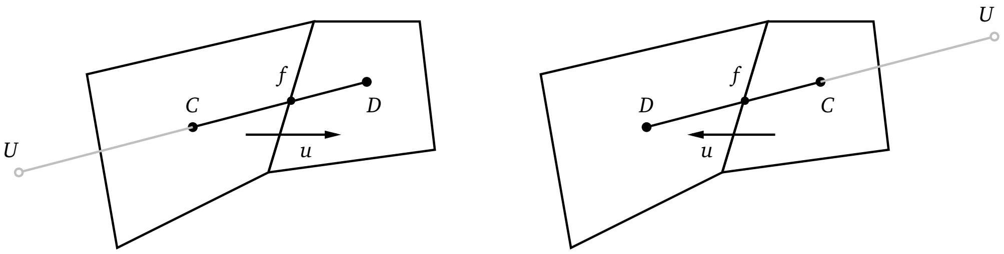

Figure 4.12.: Illustration of virtual upwind point. In style of [29].

Deferred correction representation of high resolution schemes

Most of the high resolution schemes are piece-wise functions. In different regions of $\tilde{\phi}_C$ they have different forms, which makes the implementation of various schemes complicated. Consequently, it is worth writing all the schemes in a consistent form.

Khosla and Rubin [76] has introduced the *deferred correction* (also known as flux-blending) procedure to combine the lower-order and higher-order schemes. An additional advantage of deferred correction is that it ensures the coefficient matrix to be tridiagonal and always diagonally dominant.

Let us denote the normalised cell face value ϕ_f computed with lower-order scheme as ϕ_f^{LOS} and with higher-order scheme as ϕ_f^{HOS}. The deferred correction representation is given by

$$\phi_f = \phi_f^{LOS} + \alpha(\phi_f^{HOS} - \phi_f^{LOS}) \quad \text{with } 0 \leqslant \alpha \leqslant 1. \tag{4.61}$$

Changing the value of α the portions of the corresponding schemes can be controlled. The lower-order scheme is referred to as UDS and $\tilde{\phi}_f^{UDS} = \tilde{\phi}_C$. Therefore, we write equation (4.61) in the NV form as

$$\tilde{\phi}_f = \tilde{\phi}_C + \alpha(\tilde{\phi}_f^{HOS} - \tilde{\phi}_C). \tag{4.62}$$

Equation (4.62) shows how the cell face value computation is implemented in FASTEST. In particular, the higher-order scheme is CDS in FASTEST. Therefore, we are inspired to reform the schemes in a similar form

$$\tilde{\phi}_f = \tilde{\phi}_C + \gamma(\tilde{\phi}_f^{CDS} - \tilde{\phi}_C), \tag{4.63}$$

where γ is the function which determines the chosen schemes. With different functions of γ, different schemes are recovered. This formulation is also called the γ-formulation of HRS, cf. [100]. The functions of γ is obtained by

$$\gamma = \frac{\tilde{\phi}_f^{HRS} - \tilde{\phi}_C}{\tilde{\phi}_f^{CDS} - \tilde{\phi}_C}, \tag{4.64}$$

where $\tilde{\phi}_f^{HRS}$ is the NV form of the chosen HRS. For example, the γ function of the CUBISTA scheme reads

$$\gamma = \begin{cases} \dfrac{3}{2}\dfrac{\tilde{\phi}_C}{1-\tilde{\phi}_C}\,, & \text{if} \quad 0 < \tilde{\phi}_C < \dfrac{3}{8}, \\ \dfrac{3-2\tilde{\phi}_C}{4-4\tilde{\phi}_C}\,, & \text{if} \quad \dfrac{3}{8} \leqslant \tilde{\phi}_C \leqslant \dfrac{3}{4}, \\ \dfrac{3}{2}\,, & \text{if} \quad \dfrac{3}{4} < \tilde{\phi}_C < 1, \\ 0\,, & \quad \text{otherwise.} \end{cases} \tag{4.65}$$

4.3 Coping with the High Weissenberg Number Problem

In the past decades there have been significant progress and developments for the simulation of viscoelastic fluid flow. However, numerical stability problems were found during the developments, in particular the so-called *High Weissenberg Number Problem* (HWNP). It occurs regardless the choice of the discretization method, i.e. for finite-difference, finite-volume or finite-element methods. People are hindered to perform numerical simulations of complex flows of complex fluids. The problem is identified by the difficulty of convergence of iterative algorithms in numerical simulation when the Weissenberg number is above certain limit values. The failure at these frustrating low Weissenberg numbers (Wi $\sim$ 1) is accompanied by numerical inaccuracy and lack of mesh-convergence. It is more prominent when geometrical corners (e.g. by the flow in contraction geometry) or stagnation point singularities (e.g. by the flow past a cylinder) appear.

4.3.1 Understanding the High Weissenberg Number Problem

The problem continues to be a major challenge in simulation of viscoelastic fluid flow since the 1970’s, cf. [105]. So far the reason of the problem is not yet clearly identified and no complete solution is found. Nevertheless, several plausible explanations have been made and effective solutions have been developed in the past decades. These explanations and solutions concern two aspects: constitutive models and numerical methods.

Aspect of constitutive models

The chosen constitutive model for simulation should correctly describe the fluid rheological properties of the real working fluid. It has been presented in many works that the models of UCM and Oldroyd-B suffer more severe HWNP in the simulation. It is no wonder, because, as mentioned in chapter 3, these models have drawbacks, such as lack of shear-dependent behaviour and unbounded extensional viscosity. A more concrete reason why UCM and Oldroyd-B models have lower critical Weissenberg numbers than other models has been pointed out by Renardy [122]: the disability to resolve the large stress gradients near solid boundaries and corner singularities sets the limitation on numerical simulation. The cause for the steep stress gradients is the existence of boundary layers. The memory of the fluids is the reason of the appearance of boundary layers. Due the no-slip condition, the fluid particles do not move. Hence the stress is completely determined by the local shear rate. However, at a small distance (of order Wi within one relaxation time) from the boundary , these upper convected derivative terms enter the dominant balance. Consequently, the stress behaviour in a thin layer close to the solid boundaries differs form the behaviour in the domain where is far away from these boundaries. The thickness of the boundary layers decreases with increasing Weissenberg number, cf. [122] and the thickness of the boundary layer is different for different models: for the model of UCM model, PTT and Giesekus, the thickness is of order Wi^{-1}, $\mathrm{Wi}^{-1/3}$ and $\mathrm{Wi}^{-1/2}$, respectively. Therefore, the UCM model has boundary layer which sharpen much more rapidly as the Weissenberg number increase than the PTT and Giesekus models. As a consequence, UCM model suffers more severe HWNP than other models in numerical simulations. Other advanced models help in simulation at higher Weissenberg numbers, as they are demonstrated in many numerical works. Nevertheless, the models of UCM and Oldroyd-B, the most simple models, can already approximate the rheological behaviour of many viscoelastic fluids, e.g. Boger fluids. Moreover, they present the common mathematical difficulties to most of the viscoelastic fluid models. Therefore, they are popular for mathematical analysis and investigation of numerical methods.

Aspect of numerical methods

From numerical point of view, an opinion about the reason for HWNP is that the absence of an explicit diffusive term in the momentum equation of the Oldroyd-B and related models makes the convergence of iterative algorithms in numerical simulation difficult, cf. [9]. Therefore, a common practice to stabilize the computation is to include additional diffusive terms in the momentum equation. This can be realized either by separating pure viscous components from the stress tensor or by decomposing into solvent and polymer contributions. The former method is known as the *elastic-viscous stress splitting* (EVSS) introduced by Perera and Walters [112], while the latter is known as the *solvent-polymer stress splitting* (SPSS) presented by Bird and Hassager [16]. These two splitting forms are shown in equation (3.99) and (3.96) in section 3.6. Both methods allow preserving the elliptic nature of the problem and thus enhance stability as reported by Sarkar et al. [129]. While EVSS is devised from purely numerical point of view, with the objective of enlarging the diffusive term in the momentum equations, SPSS can be derived from dilute solution theory and is related to viscoelastic fluids being composed by an elastic polymeric solute in a Newtonian solvent. Regarding the implementation effort, the advantage of SPSS compared to EVSS is that one does not need to compute the convective time derivative of the rate of deformation tensor in the constitutive equation. Taking the advantage of SPSS and simultaneously using the stabilizing effect of diffusion, a numerical diffusive term can be added on both sides of the momentum equation, where one is treated explicitly like a source and the other one implicitly. The latter gives rise to the algebraic coefficients that regulate convergence of the iterative algorithm, cf. [129]. This method is known as the *Both Side Diffusion* (BSD). Recent application of this approach can be found in [103] and [152]. In [152] the authors have also concluded that BSD is not suitable as a stabilization approach for transient simulation due to over diffusion. It is worth mentioning another widely used method in the context of finite-element method introduced by Guénette et al. [55], the *Discrete Elastic-Viscous Split Stress* (DEVSS). Although derived from EVSS, it uses different contribution of the extra stress as unknowns. The advantage of changing unknowns is keeping the constitutive equation unchanged such that calculation of the upper convective derivative of the rate of deformation tensor is avoided. In addition, the governing momentum equation of DEVSS results from adding diffusive terms on both sides. It is called a Discrete EVSS approach, because the added diffusive terms are approximated in a different manner in the discretized form. Comparing their governing equations and the treatment of the discrete added diffusion, DEVSS is the same as BSD.

Another opinion about the reason for the HWNP is that the problem is related to the positive definiteness of the conformation tensor. Stability problem occurs when the positive definiteness of the conformation tensor is destroyed during the simulation. As shown in the chapter 3, the conformation tensor is a second-order internal structural tensor associated with the second moment of a suitably defined chain end-to-end distribution function. The eigenvalues of the conformation tensor and their corresponding eigenvectors have the physical meaning of the square of the average macromolecular size along the principal three directions and the orientation of those directions in space, respectively, cf. [13]. All those eigenvalues are positive, i.e. the conformation tensor are positive definite. Although on the continuum level the conformation tensor remains positive definite while it evolves in time, on the discretized level this need not always be the case. In fact, an improper discretization of the constitutive equation may destroy this property, which gives rise to the loss of evolution, an instability of Hadamard type. In such instability the growth rates of short waves increase without bound as the wavelength tends to zero. It then poses a severe problem in numerical simulation, since the convergence of the discrete solution is worse as the mesh is refined, cf. [105]. A analysis of the loss of evolution in the flow of an Oldroyd-B fluid is briefly shown in appendix B and detailed in [105]. Therefore, preserving the positive definiteness of the conformation tensor is crucial in the simulation.

A number of approaches have been developed with the aim to preserve the positive definiteness of the conformation tensor. These approaches can be classified into two subclasses. The approaches in the first subclass aim at designing a discretization scheme for the original constitutive equation without modification of it, such that the positive definiteness of the conformation tensor is guaranteed during the computation. One example is the *Positive Definiteness Preserving Scheme* (PDPS) proposed by Stewart et al. [137], which has been successfully applied in finite-volume simulation of viscoelastic two-phase flow. They derived a restriction for the time step size by discrete the constitutive equation using a semi-Lagrangian approach, which ensures the positivity of the conformation tensor during the time stepping. Another example is the PDPS presented by Lee and Xu [82]. They also use semi-Lagrangian approach but within the FEM. Their approach is based on the observation that the constitutive equation can be cast into the formulation of Riccati Differential Equations, cf. [82].

In the second subclass, the positive definiteness of the conformation tensor is preserved by design. Moreover, the approaches in this subclass are capable to resolve the large gradient of the stress in boundary layers. It has been shown that failing to resolve large gradients in stress is one of the factors that destroy the positive definiteness of the conformation tensor. Important representatives in this subclass are the *Log-Conformation Representation* (LCR) proposed by Fattal and Kupferman [43] and the *Square-Root-Conformation Representation* (SRCR) proposed by Balci et al. [11].

The motivation behind LCR is that the stress suffers a combination of deformation and convection, which produces steep exponential profiles [43]. Numerical schemes based on polynomial interpolation would always underestimate this exponential growth. To remedy this problem, Fattal and Kupferman have proposed to reformulate the constitutive equation in the form of the logarithm of the conformation tensor. This idea can be nicely explained with the help of a one-dimensional toy problem as given in [43]: assume the velocity is constant and the conformation tensor is replaced by a scalar $c(x,t)$ in the one-dimensional constitutive equation. Find $c(x,t)$ with x in the interval $(0,L)$ and time $t>0$ such that

$$\frac{\partial c}{\partial t}+u\frac{\partial c}{\partial x}=bc, \tag{4.66}$$

where u, b are constants and $u,b>0$. In addition, we assume $c(x,t=0)=1$ as initial condition and $c(x=0,t)=1$ as boundary condition. The equation has the analytical solution

$$c(x,t)=\begin{cases}\exp\left(\dfrac{b}{u}x\right) & \text{for} \quad x\leqslant ut,\\[2ex] \exp(bt) & \text{for} \quad ut<x\leqslant L.\end{cases} \tag{4.67}$$

As emphasized in [43, 65], the numerical difficulty of solving equation (4.66) is that the standard discretization based on polynomial interpolation of such an equation always fails to balance the exponential growth. Using higher order discretization schemes can ease the problem to some extent but can not solve it. If we transform equation (4.66) to the equations in terms of $s = \log c$, the equation turns out to be

$$\frac{\partial s}{\partial t} + u\frac{\partial s}{\partial x} = b, \tag{4.68}$$

which has the solution

$$s(x,t) = \begin{cases} \dfrac{b}{u}x & \text{for} \quad x \leqslant ut, \\ bt & \text{for} \quad ut < x \leqslant L \end{cases} \tag{4.69}$$

We clearly see that equation (4.68) linearises the exponential growth of c. Hence the error can be greatly reduced. An additional important consequence of LCR is that it guarantees the positive definiteness of the conformation tensor. The approach has been widely applied in different numerical studies, e.g. [43, 65, 2].

Similarly, we can also, e.g., transform equation (4.66) to the equations in terms of $a = \sqrt{c}$:

$$\frac{\partial a}{\partial t} + u\frac{\partial a}{\partial x} = \frac{1}{2}ba \tag{4.70}$$

which has the solution

$$a(x,t) = \begin{cases} \exp\left(\dfrac{b}{2u}x\right) & \text{for} \quad x \leqslant ut, \\ \exp\left(\dfrac{b}{2}t\right) & \text{for} \quad ut < x \leqslant L. \end{cases} \tag{4.71}$$

Equation (4.70) does not linearise the exponential growth but reduces it by a factor 2, which can also significantly help in the computation.

Naturally, besides the logarithm and square-root transformation, it is possible to obtain other logarithm based, root based or more general transformations for the evolution equation of the conformation tensor, which also help for resolving the exponential growth of the stress. Afonso et al. [4] have presented a generic kernel-conformation tensor transformation for a large class of differential constitutive models. The square root-conformation representation can also be described in this way. Nevertheless, there is another more attractive formulation of the square-root transformation which is proposed by Balci et al. [11]. Their method does not require the calculation of eigenvectors and eigenvalues of the conformation tensor at every iteration and location. Hence it results in significant practical advantages regarding reduction of computational cost and lower implementation complexity compared with the kernel-conformation transformation.

In summary, the understanding of the HWNP is still not complete. None of the above mentioned approaches can fully solve the HWNP. Nevertheless, the advance approaches can now be applied to simulate the specified situations at the Weissenberg number of practical interest.

4.3.2 Approaches to cope with the High Weissenberg Number Problem

In the literature a large number of approaches can be found, but only the approaches within the FVM framework are concerned in the present work. Four typical ones are chosen for illustration with the Oldroyd-B model: BSD, PDPS as defined by Stewart et al. [137], LCR and SRCR as explained by Balci et al. [11]. Their derivations and formulations are presented in the following sections, while their performances in simulation will be shown in section 4.4.3.

Both-sides diffusion (BSD)

In this approach the constitutive equation is not reformulated, but additional diffusions are added on both sides of the momentum equation (3.96):

$$\rho\left(\frac{\partial \mathbf{u}}{\partial t}+\mathbf{u}\cdot\nabla\mathbf{u}\right)-2(\eta_s+\kappa)\nabla\cdot\mathbf{D}=-\nabla p-2\kappa\nabla\cdot\mathbf{D}+\nabla\cdot\tau_p\ , \tag{4.72}$$

where κ is a positive constant. In the present work $\kappa=\eta_p$ is chosen. In discretization practice, the terms on the left-hand side of (4.72) are treated implicitly, while the terms on the right-hand side are evaluated explicitly. The implicitly treated additional diffusive term contributes to the "ellipticity" of the problem. Hence it helps in the stabilization of numerical iterative methods [9].

Positive definiteness preserving scheme (PDPS)

In this approach the constitutive equation is formulated using the conformation tensor form (3.97) of the model. The basic principle is a discretization of the Lie derivative using the semi-Lagrangian approach. Any objective stress rate is a specific case of the Lie derivative. In the form of a Lie derivative, the upper convected time derivative of the conformation tensor $\mathbf{c}$ is represented as

$$\overset{\triangledown}{\mathbf{c}}=\mathbf{F}\frac{\mathrm{d}}{\mathrm{d}t}\left(\mathbf{F}^{-1}\mathbf{c}\mathbf{F}^{-\mathsf{T}}\right)\mathbf{F}^{\mathsf{T}}, \tag{4.73}$$

where $\mathbf{F}$ is the deformation gradient tensor and $\mathrm{d}/\mathrm{d}t$ denotes the material derivative operator. Note that due to $\mathbf{F}\,\mathrm{d}(\mathbf{F}^{-1})/\mathrm{d}t=-\nabla\mathbf{u}^{\mathsf{T}}$ the upper convected derivative of $\mathbf{c}$ is recovered. With the help of the semi-Lagrangian approach, equation (4.73) can be approximated as

$$\overset{\triangledown}{\mathbf{c}}\approx\mathbf{F}^{n+1}\frac{\left(\mathbf{F}^{-1}\mathbf{c}\mathbf{F}^{-\mathsf{T}}\right)^{n+1}-\left(\mathbf{F}^{-1}\mathbf{c}\mathbf{F}^{-\mathsf{T}}\right)^{*}}{\Delta t}\left(\mathbf{F}^{\mathsf{T}}\right)^{n+1}, \tag{4.74}$$

where the superscript $*$ denotes the values of the material particle at the current position at the n-th time step, and Δt is the time step size. The configuration at the n-th time step being the reference configuration yields $\mathbf{F}^{*}=\mathbf{I}$. The tensor $\mathbf{c}^{*}$ is computed by interpolation of the values of the surrounding control volumes at the n-th time step according to

$$\mathbf{c}^{*}=\mathbf{c}^{n}-\Delta t\,\mathbf{u}\cdot\nabla\mathbf{c}^{n}. \tag{4.75}$$

According to [137], the first order upwind scheme is used to discretize the term $\mathbf{u}\cdot\nabla\mathbf{c}$. For example, in one space dimension and with positive velocity u, the conformation tensor at the i-th position is

$$\mathbf{c}_i^{*}=\mathbf{c}_i^{n}-\Delta t\,\mathbf{u}\cdot\nabla\mathbf{c}_i^{n}=\frac{u\Delta t}{\Delta x}\mathbf{c}_{i-1}^{n}+\left(1-\frac{u\Delta t}{\Delta x}\right)\mathbf{c}_i^{n}. \tag{4.76}$$

In order to preserve the property that the interpolated result $\mathbf{c}^{*}$ is positive, the interpolation factors need to be positive. According to [137] the time step size is required to fulfill the condition

$$\Delta t<\frac{1}{2d}\frac{\Delta x}{\max|\mathbf{u}|}, \tag{4.77}$$

where d is the number of dimensions of the problem and Δx is the mesh spacing.

Equation (4.74) is further approximated as

$$\overset{\triangledown}{\mathbf{c}}\approx\frac{\mathbf{c}^{n+1}-\mathbf{F}^{n+1}\mathbf{c}^{*}(\mathbf{F}^{\mathsf{T}})^{n+1}}{\Delta t}. \tag{4.78}$$

Substituting (4.78) into equation (3.97) yields

$$\mathbf{c}^{n+1} = \frac{1}{1+\frac{\lambda}{\Delta t}}\mathbf{I} + \frac{\frac{\lambda}{\Delta t}}{1+\frac{\lambda}{\Delta t}}\mathbf{F}^{n+1}\mathbf{c}^{*}(\mathbf{F}^{\mathsf{T}})^{n+1}. \tag{4.79}$$

Since $\mathbf{c}$ is initially positive definite and the coefficients are all positive, the positive definiteness of $\mathbf{c}^{n+1}$ is preserved. During the computation, the deformation tensor is approximated [62] according to

$$\mathbf{F}^{n+1} = \mathbf{I} + \Delta t(\nabla\mathbf{u})^{\mathsf{T}}\ . \tag{4.80}$$

To sum up, the steps for updating the conformation tensor are – cf. [137]:

1. Use linear interpolation to calculate the conformation tensor of the material particle at the previous time step:

$$\mathbf{c}^{*} = \mathbf{c}^{n} - \Delta t\,\mathbf{u}\cdot\nabla\mathbf{c}^{n}\ , \tag{4.81}$$

2. Calculate the deformation tensor:

$$\mathbf{F}^{n+1} = \mathbf{I} + \Delta t(\nabla\mathbf{u})^{\mathsf{T}}\ , \tag{4.82}$$

3. Update the conformation tensor:

$$\mathbf{c}^{n+1} = \frac{1}{1+\frac{\lambda}{\Delta t}}\mathbf{I} + \frac{\frac{\lambda}{\Delta t}}{1+\frac{\lambda}{\Delta t}}\mathbf{F}^{n+1}\mathbf{c}^{*}(\mathbf{F}^{\mathsf{T}})^{n+1}\ . \tag{4.83}$$

Log-conformation representation (LCR)

The constitutive equation (3.97) is formulated in the form of the logarithm of the conformation tensor $\mathbf{s} = \log\mathbf{c}$. The tensor $\mathbf{c}$ can be diagonalized as

$$\mathbf{c} = \mathbf{R}\Lambda\mathbf{R}^{\mathsf{T}}, \tag{4.84}$$

where $\mathbf{R}$ is an orthogonal tensor which consists of the eigenvectors of $\mathbf{c}$, and Λ is diagonal with the corresponding three eigenvalues Λ_i of $\mathbf{c}$. The logarithm of $\mathbf{c}$ is calculated as

$$\mathbf{s} = \mathbf{R}\log\Lambda\,\mathbf{R}^{\mathsf{T}}, \tag{4.85}$$

where $\log\Lambda$ is a diagonal matrix with entries $\log\Lambda_i$.

Let us denote the antisymmetric matrix $-\mathbf{R}(\mathrm{d}\mathbf{R}^{\mathsf{T}}/\mathrm{d}t)$ by Ω, where $\mathrm{d}\mathbf{R}^{\mathsf{T}}/\mathrm{d}t$ is the material derivative of $\mathbf{R}^{\mathsf{T}}$, and let $\mathbf{L} = \nabla\mathbf{u}$. Then the constitutive equation of conformation tensor form reads

$$\tilde{\Omega}\Lambda + \Lambda\tilde{\Omega}^{\mathsf{T}} + \frac{\mathrm{d}\Lambda}{\mathrm{d}t} = (\tilde{\mathbf{L}}\Lambda + \Lambda\tilde{\mathbf{L}}^{\mathsf{T}}) + \frac{1}{\lambda}(\mathbf{I}-\Lambda), \tag{4.86}$$

where the relations between the tensors $\tilde{\Omega}$, $\tilde{\mathbf{L}}$ and Ω, $\mathbf{L}$ are $\Omega = \mathbf{R}\tilde{\Omega}\mathbf{R}^{\mathsf{T}}$ and $\mathbf{L} = \mathbf{R}\tilde{\mathbf{L}}\mathbf{R}^{\mathsf{T}}$.

The evolution of $\mathbf{s} = \log\mathbf{c}$ is governed by

$$\frac{\mathrm{d}\mathbf{s}}{\mathrm{d}t} = \mathbf{R}\left(\frac{\mathrm{d}\Lambda}{\mathrm{d}t}\Lambda^{-1} + \tilde{\Omega}\,\log\Lambda + \log\Lambda\,\tilde{\Omega}^{\mathsf{T}}\right)\mathbf{R}^{\mathsf{T}}. \tag{4.87}$$

The key observation here is to express the terms $\frac{\mathrm{d}\Lambda}{\mathrm{d}t}\Lambda^{-1}$ and $\tilde{\Omega}$ in equation (4.87) with the help of Equation (4.86) in order to get the evolution of $\mathbf{s}$. The tensor $\frac{\mathrm{d}\Lambda}{\mathrm{d}t}\Lambda^{-1}$ is diagonal and is evaluated according to

$$\frac{\mathrm{d}\Lambda}{\mathrm{d}t}\Lambda^{-1} = 2\tilde{\mathbf{B}} + \frac{1}{\lambda\Lambda} - \frac{1}{\lambda}\mathbf{I}, \tag{4.88}$$

where the components of $\tilde{\mathbf{B}}$ are

$$\tilde{B}_{ij} = \begin{cases} \tilde{L}_{ij}\,,\ \text{if} \quad i = j, \\ 0\,,\ \text{if} \quad i \neq j. \end{cases} \tag{4.89}$$

The components of $\tilde{\Omega}$ are

$$\tilde{\Omega}_{ij} = \begin{cases} \dfrac{\Lambda_{ii}\tilde{L}_{ij} + \tilde{L}_{ji}\Lambda_{jj}}{\Lambda_{jj} - \Lambda_{ii}}\,,\ \text{if} \quad i \neq j, \\ 0\,,\ \text{if} \quad i = j. \end{cases} \tag{4.90}$$

Substituting equations (4.88) and (4.90) into equation (4.87) and defining $\mathbf{B} = \mathbf{R}\tilde{\mathbf{B}}\mathbf{R}^{\mathsf{T}}$, the final form of the evolution of $\mathbf{s}$ is obtained as

$$\frac{\partial \mathbf{s}}{\partial t} + \mathbf{u} \cdot \nabla \mathbf{s} = \Omega \mathbf{s} - \mathbf{s}\Omega + 2\mathbf{B} + \frac{1}{\lambda}(e^{-\mathbf{s}} - \mathbf{I})\,. \tag{4.91}$$

Additional details of the derivation are given in appendix D.

Square root-conformation representation (SRCR)

In this approach the conformation equation (3.97) is reformulated in the form of the square root of the conformation tensor $\mathbf{A} = \mathbf{c}^{\frac{1}{2}}$ with components a_{ij}. Using the fact that a positive definite tensor has a unique positive definite symmetric square root, the evolution of $\mathbf{A}$ can be derived. It is governed by

$$\frac{\partial \mathbf{A}}{\partial t} + \mathbf{u} \cdot \nabla \mathbf{A} = \mathbf{A}\nabla\mathbf{u} + \mathbf{M}\mathbf{A} + \frac{1}{2\lambda}\left(\mathbf{A}^{-\mathsf{T}} - \mathbf{A}\right)\,, \tag{4.92}$$

where $\mathbf{M}$ is an anti-symmetric tensor with components m_{ij}, satisfying $\mathbf{A}^{\mathsf{T}}\mathbf{A} = \mathbf{c}$ point wise in space and time with the initial condition $\mathbf{A}^{\mathsf{T}}(\mathbf{x}, 0)\mathbf{A}(\mathbf{x}, 0) = \mathbf{c}(\mathbf{x}, 0)$, cf. [11]. Because the conformation tensor is symmetric and positive definite, it has a unique positive symmetric square root. As emphasized by Balci et al. [11], the key point is to choose $\mathbf{M}$ properly, so that the symmetry of $\mathbf{A}$ is preserved. For this reason the matrix

$$\mathbf{K} = \mathbf{A}\nabla\mathbf{u} + \mathbf{M}\mathbf{A} \tag{4.93}$$

with components k_{ij} is required to be symmetric. The entries of the tensor $\mathbf{M}$ are depending on $\mathbf{L} = \nabla\mathbf{u}$ with components l_{ij} and the symmetric tensor $\mathbf{A}$. They are calculated by solving the equations $k_{ij} = k_{ji}$. For the three-dimensional case, this yields a system of three equations. In matrix notation, this system reads as

$$\begin{pmatrix} a_{11} + a_{22} & a_{23} & -a_{13} \\ a_{23} & a_{11} + a_{33} & a_{12} \\ -a_{13} & a_{12} & a_{22} + a_{33} \end{pmatrix} \begin{pmatrix} m_{12} \\ m_{13} \\ m_{23} \end{pmatrix} = \begin{pmatrix} r_1 \\ r_2 \\ r_3 \end{pmatrix}, \tag{4.94}$$

where

$$\begin{aligned} r_1 &= (a_{12}l_{11} - a_{11}l_{12}) + (a_{22}l_{21} - a_{12}l_{22}) + (a_{23}l_{31} - a_{13}l_{32})\,, \\ r_2 &= (a_{13}l_{11} - a_{11}l_{13}) + (a_{33}l_{31} - a_{13}l_{33}) + (a_{23}l_{21} - a_{12}l_{23})\,, \\ r_3 &= (a_{13}l_{12} - a_{12}l_{13}) + (a_{23}l_{22} - a_{22}l_{23}) + (a_{33}l_{32} - a_{23}l_{33})\,. \end{aligned} \tag{4.95}$$

Following the idea described in [11], it can be shown that the matrix $\mathbf{M}$ calculated in this way allows to preserve the symmetry of the matrix $\mathbf{K}$. Further details are given in appendix E.

4.4 Simulation of test cases and discussion of high resolution schemes and stabilization approaches

In this section three groups of simulation results are presented. In the first group we aim to assess the performance of the implemented high resolution schemes and show the importance of these schemes in simulation of the viscoelastic fluid flow. In the second group we show validation of the viscoelastic flow solver in the benchmark test cases. Typical numerical and mathematical problems within these test cases are discussed. In the last group we intend to shed light on choosing suitable approaches to cope with the HWNP for practical applications. It is realized by comprehensive comparison of the approaches mentioned in section 4.3.

4.4.1 Test cases for high resolution schemes

In this part the implemented high resolution schemes are investigated. Besides CUBISTA, the scheme GAMMA with $\beta_m = 0.5$ and MUSCL are tested. On the purpose of comparison, the basic schemes UDS and QUICK are included in the discussion. Firstly, the classical test of pure advection of a scalar is considered, with the aim to assess the basic properties of the HRS. Secondly, the test cases of lid-driven cavity and flow past a cylinder for viscoelastic fluid flow are employed to examine their properties in complex problems.

Pure advection of a scalar

This test aims to test the resolution properties of the high resolution schemes. A scalar ϕ is transported by a given uniform velocity field oblique to the mesh with angle $\theta = 45°$. The computed domain is square in two-dimension with inlet boundary at left and bottom sides and outlet boundary at top and right sides, see figure 4.13. The equation to be solved is

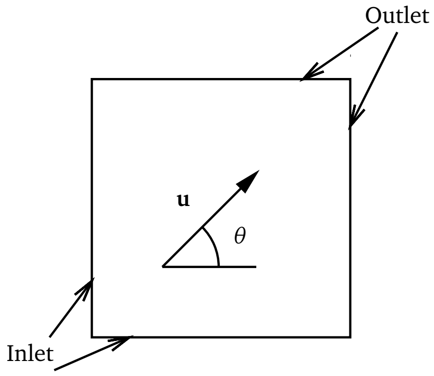

Figure 4.13.: Test case set-up for pure advection of a scalar

$$\nabla \cdot (\mathbf{u}\phi) = 0, \tag{4.96}$$

where $\mathbf{u}$ is a constant velocity. The values of its components are $u = v = \sqrt{2}/2$ for a mesh-to-flow angle of 45°. Three inlet boundary conditions are imposed in the test with different aims to assess the scheme in different aspects:

- Step profile

$$\begin{array}{ll} \phi(0,y) = 1 & \text{for } 0 \leqslant y \leqslant 1 \\ \phi(x,0) = 1 & \text{for } 0 \leqslant x \leqslant 1 \end{array} . \tag{4.97}$$

The step profile gives the severe gradient variation. The ability of the schemes to resolve sharp fronts, with least numerical diffusion and without oscillation, can be assessed.

- Sine-square profile

$$\begin{aligned} \phi(0,y) &= \begin{cases} \sin^2(\frac{10}{3}\pi y) & \text{for } 0 \leqslant y \leqslant \frac{3}{20} \\ 1 & \text{for } \frac{3}{20} < y \leqslant 1 \end{cases} \\ \phi(x,0) &= 0 \quad \text{for } 0 \leqslant x \leqslant 1 \end{aligned} \tag{4.98}$$

  The sine-square function provides a much smoothly changing profile than the step profile. It can be used to assess the schemes' order of accuracy.

- Semi-ellipse profile

$$\begin{aligned} \phi(0,y) &= \begin{cases} \sqrt{1-(6y)^2} & \text{for } y < \frac{1}{6} \\ \phi(0,y) = 0 & \text{for } y \geqslant \frac{1}{6} \end{cases} \\ \phi(x,0) &= \begin{cases} \sqrt{1-(6x)^2} & \text{for } x < \frac{1}{6} \\ \phi(x,0) = 0 & \text{for } x \geqslant \frac{1}{6} \end{cases} \end{aligned} \tag{4.99}$$

  The semi-ellipse profile is a combination of abrupt change in gradient at the base and a region of slowly varying curvature without sharp maximum. It is axis-symmetric. It can be therefore applied to check the property of symmetry in the schemes.

A uniform mesh with 59×59 cells are employed in the simulation. Figure 4.14 shows the ϕ field for the case of step profile. We can clearly see the character of diffusion of UDS, while QUICK scheme can well preserve the sharp front but over shoots and under shoots appear. The scheme CUBISTA can not only preserve the sharp front but also give a smooth field.

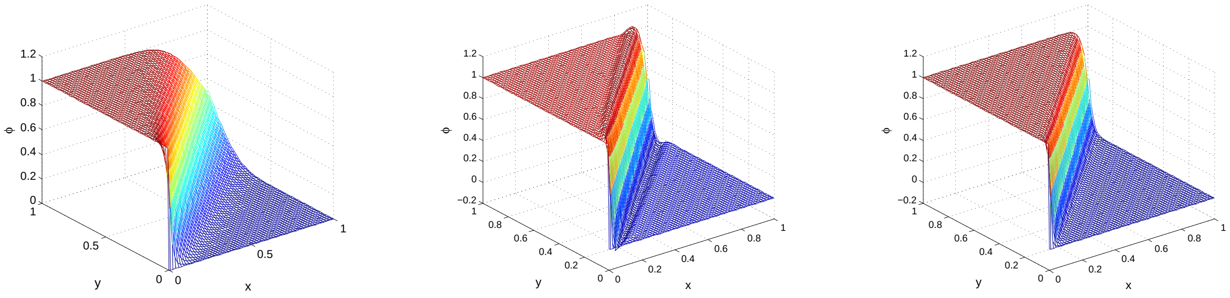

(a) UDS (b) QUICK (c) CUBISTA

Figure 4.14.: Three-dimensional representation of ϕ field with step profile at inlet

To compare them with the exact solution and the other two high resolution schemes, the profiles of ϕ along $x = 0.5$ are plotted in figure 4.15. It is clear that UDS smears out the solution due the its too diffusive property, while QUICK produces oscillation near the sharp font. The HRS can well balance the problems by UDS and QUICK. Among the three HRS, the schemes CUBISTA and MUSCL produce nearly the same results, while GAMMA is more diffusive than the other two. The reason is that the larger β_m can result in more numerical diffusion. The value of $\beta_m = 0.5$ is chosen in this test, which is the upper bound of β_m.

The results for the sine-square profile at inlet are plot in figure 4.16 (a). A similar phenomenon to the step profile is observed. In figure 4.16 (b) we plot the average absolute errors against different mesh sizes. The slope of the curve indicates the convergence rate of the scheme. We can see that all the high resolution schemes have higher convergence rate than UDS.

The ϕ field for the semi-ellipse profile at inlet is shown in figure 4.17. The ϕ profile along $x = 0.5$ is given in figure 4.18. UDS is not able to capture the peak, while QUICK scheme can well predict this local maximum but also produce undershoot at the bottom. All the high resolution schemes show the symmetry property.

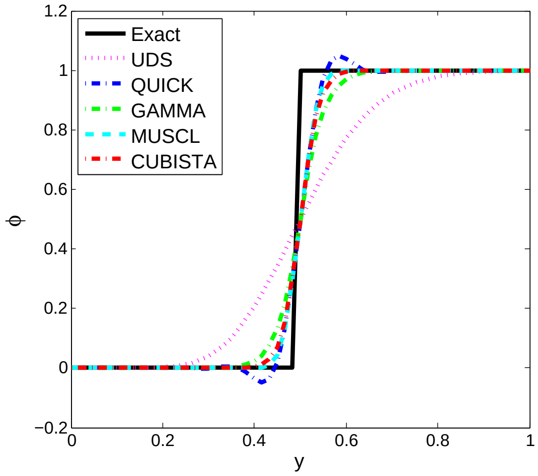

Figure 4.15.: Profile of $\phi(0.5, y)$ for step profile inlet boundary

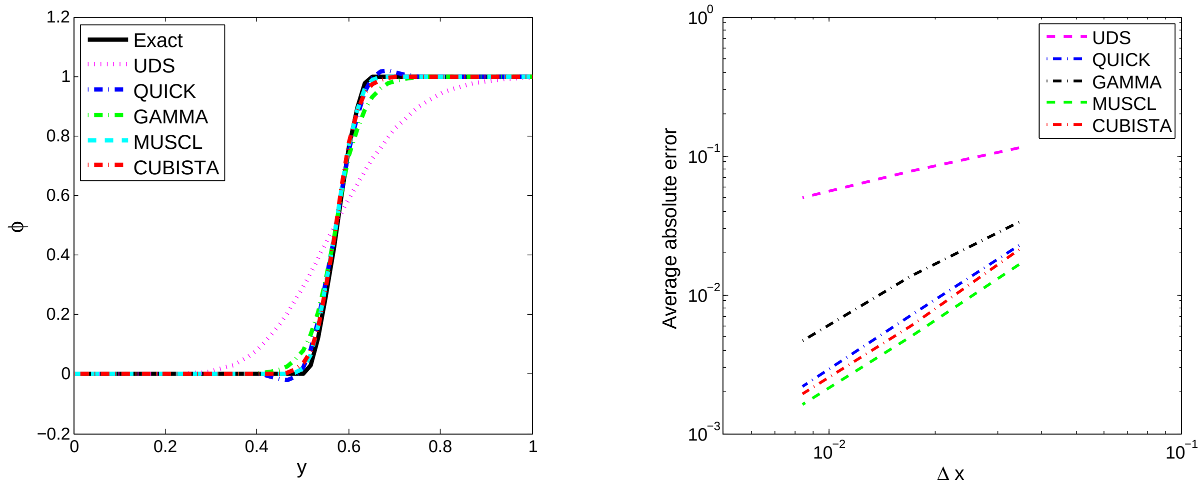

(a)

(b)

Figure 4.16.: Sine-square inlet boundary: (a) profile of $\phi(0.5, y)$ and (b) average absolute value against mesh size

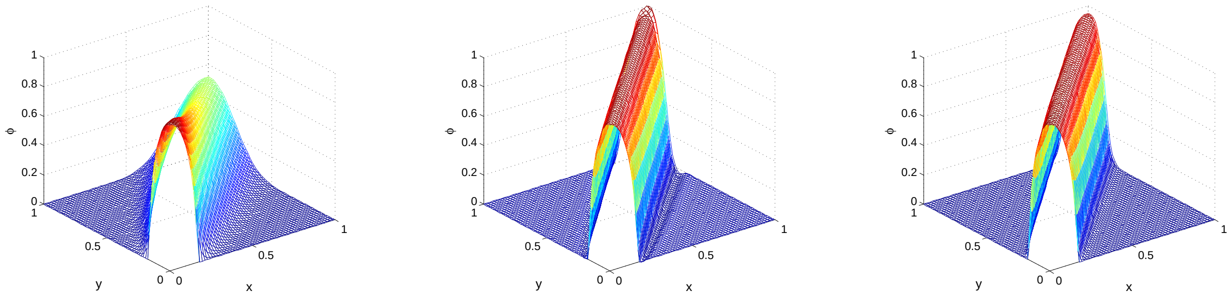

(a) UDS

(b) QUICK

(c) CUBISTA

Figure 4.17.: Three-dimensional representation of ϕ field with semi-ellipse profile at inlet

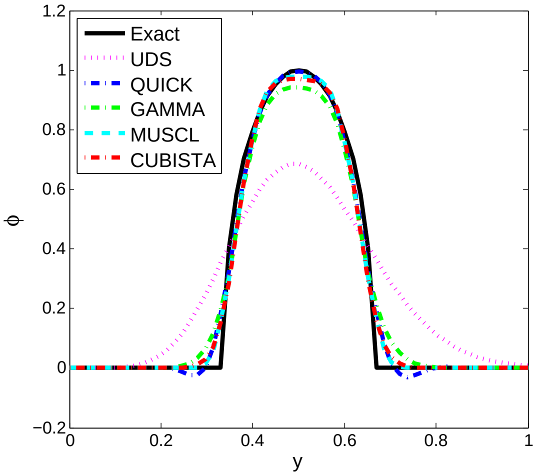

Figure 4.18.: Profile of $\phi(0.5, y)$ for semi-ellipse profile inlet boundary

Test cases for viscoelastic fluid flow

To test the effect of HRS in simulation of viscoelastic fluid flow, simulation for the test cases lid-driven cavity and flow past a cylinder are employed. The description and simulation set up for these test cases are given in section 4.4.2. The simulations are done with the LCR approach described in section 4.3.2. The simulation results produced with UDS and CUBISTA are compared.

In the test case lid-driven cavity, the normal stress component τ_{xx} on the lid is investigated. In this region τ_{xx} shows large gradient along x direction and the gradient becomes larger when the Weissenberg number increases. In this test the Weissenberg number is $\mathrm{Wi} = 1.0$. Figure 4.19 shows the stress profiles computed with UDS and CUBISTA with successive refined meshes.

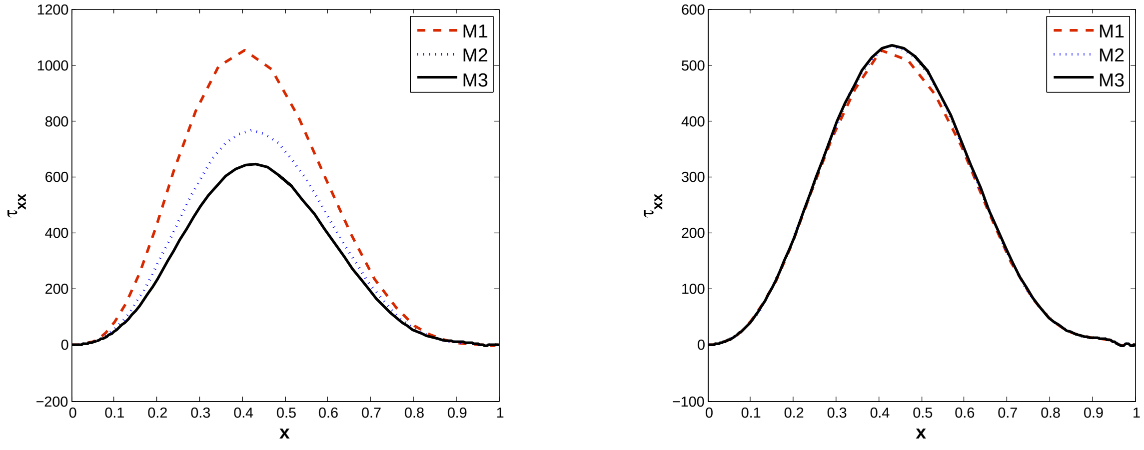

(a) UDS

(b) CUBISTA

Figure 4.19.: Profile of normal stress component τ_{xx} along $y = 1$ computed with UDS and CUBISTA for the case lid-driven cavity

We can see the great differences between the profiles produced with UDS and CUBISTA: the scheme CUBISTA provides higher convergence rate than UDS. With mesh M3, CUBISTA can already produce a mesh independent solution, while more refinement should be made if UDS is applied. It is also noticed that the directions towards to convergence are different by the two schemes. As the mesh is refined, the peaks of the stress profile reduce for UDS, while they increase for CUBISTA. This is due to the different signs of the truncation error by UDS and CUBISTA. Consider face value of the i-th cell. The face value approximated with UDS is

$$\phi_f = \phi_i + \frac{1}{2}\left.\frac{\partial \phi}{\partial x}\right|_i \Delta x + \mathcal{O}(\Delta x^2), \tag{4.100}$$

which has a positive coefficient by the dominated $\mathcal{O}(\Delta x)$ term. The value approximated with QUICK scheme (the core scheme of CUBISTA) is

$$\phi_f = \frac{6}{8}\phi_i + \frac{3}{8}\phi_{i+1} - \frac{1}{8}\phi_{i-1} - \frac{1}{16}\left.\frac{\partial^3 \phi}{\partial x^3}\right|_i \Delta x^3 + \mathcal{O}(\Delta x^4), \tag{4.101}$$

which has a negative coefficient by the dominated $\mathcal{O}(\Delta x^3)$ term.

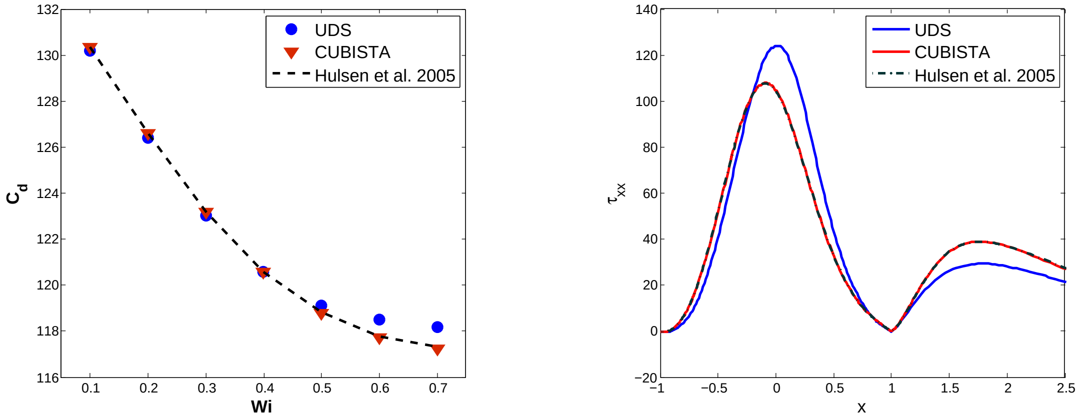

(a) Drag coeffiecient

(b) Normal stress

Figure 4.20.: Values computed with UDS and CUBISTA for (a) drag coefficients at different Weissenberg numbers and (b) the normal stress component profile τ_{xx} along the cylinder and the rear wake.

As for a second test case we consider the flow around cylinder. This is one of the benchmark test cases in simulation of viscoelastic fluid flow. One of the comparison quantity is the drag coefficients at various Weissenberg numbers. The computed values in the literature show consistence, see table 4.10 in section 4.4.2. The results computed with UDS and CUBISTA are shown in figure 4.20 (a), together with the data provided in [65]. The curve of UDS starts to deviate from the reference at Wi = 0.5. The the deviation becomes larger at higher Weissenberg numbers. Meanwhile the curve of CUBISTA is always on the track of the reference. The agreement between CUBISTA and the reference is reflected also on the local stress profile, as we can see in figure 4.20 (b), which shows the normal stress component τ_{xx} along the cylinder and in the rear wake at Wi = 0.7. However, the stress value computed with UDS is much higher at the cylinder top and lower in the rear wake.

4.4.2 Computation of benchmark problems for viscoelastic fluid flow

Five problems are here considered

- Two-dimensional Poiseuille flow
  A classical test case for validation, for which the analytical solutions for Oldroyd-B fluid are available for both steady and start-up states.

- Channel entry flow slip-stick geometry
  A prototype model of contraction flow. It is often applied to illustrate the different flow pattern with Newtonian and viscoelastic fluids.
- Lid-driven cavity flow
  A popular test case for testing the stabilization approaches for viscoelastic fluid flow.
- 4:1 contraction flow
  One of the standard benchmark test cases for viscoelastic fluid flow, cf. [17, 105], where a geometry singularity appears in the domain.
- Flow around cylinder
  Another standard benchmark test case for viscoelastic fluid flow, where no geometry singularity appear in the domain.

Without specifically mentioning, the presented results are computed with the LCR stabilization approach in the constitutive equation and CUBISTA discretization scheme for the convection term. The presented computation settings are applied also in section 4.4.3 for comparison of different stabilization approaches.

Two-dimensional Poiseuille flow

In this test case an Oldroyd-B fluid flows in a channel with height $H = 2h$ as shown in figure 4.21. The flow is driven by a constant pressure gradient. No-slip boundary conditions are set at the upper and bottom wall. The Reynolds number is fixed at $\mathrm{Re} = 0.1$. Weissenberg numbers $\mathrm{Wi} = \lambda U/h = 0.1, 1.0$ and 5.0 are employed. The variation of the Weissenberg number is realized by changing the relaxation time λ. The viscosity ratio has the value of $\beta = 1/10$. A uniform mesh with $\Delta y = h/80$ is used. Analytical solutions for steady and start-up states are presented in appendix C.

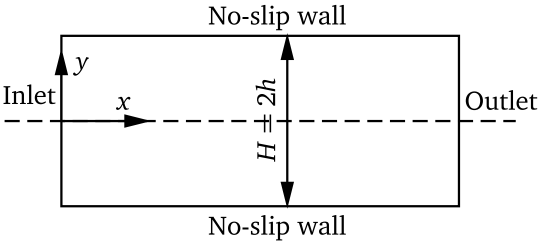

Figure 4.21.: Geometry of two-dimensional Poiseuille flow

The steady state solutions are first studied. The simulation results at different Weissenberg numbers are shown in figure 4.22. They show good agreement with the analytical solutions. Profiles of the velocity components u are identical at every Weissenberg number (actually, they are also identical with the solution for Newtonian fluids). It is the same case for the shear stress τ_{xy}. However, the profile for normal stress τ_{xx} exhibits significant change at different Weissenberg numbers. The normal stress has steep profile near the wall and the slope becomes larger as the Weissenberg number increases.

The transient solutions are shown in figure 4.23. We observe the evolution of the velocity near the center at position $y = 0.0125h$. The simulation results agree well with the analytical solution. As the Weissenberg number increases, the amplitude of the oscillation increases accompanied with changing of phase-shift and oscillation period.

Channel entry flow with slip-stick geometry

Due to the change of boundaries, the channel entry flow with slip-stick geometry shows significant difficulty in numerical simulation. A singularity exits at the boundary changing point, which causes theoretically an infinite

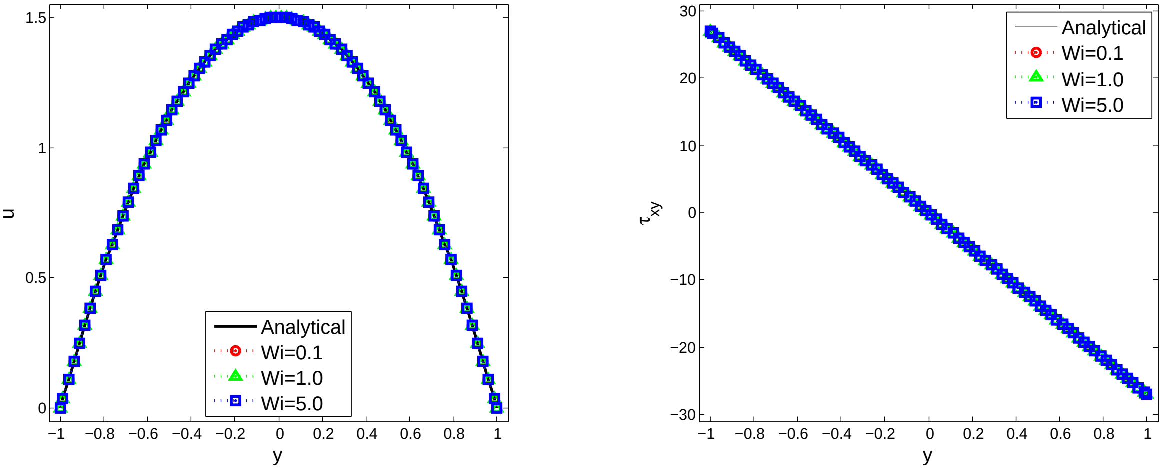

(a) u (b) τ_{xy}

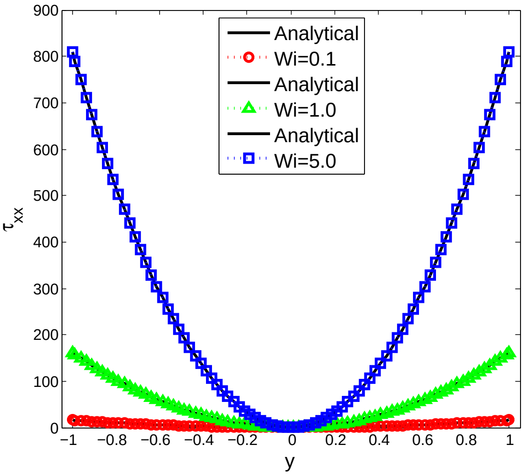

(c) τ_{xx}

Figure 4.22.: Profiles of velocity and extra stresses in steady two-dimensional Poiseuille flow

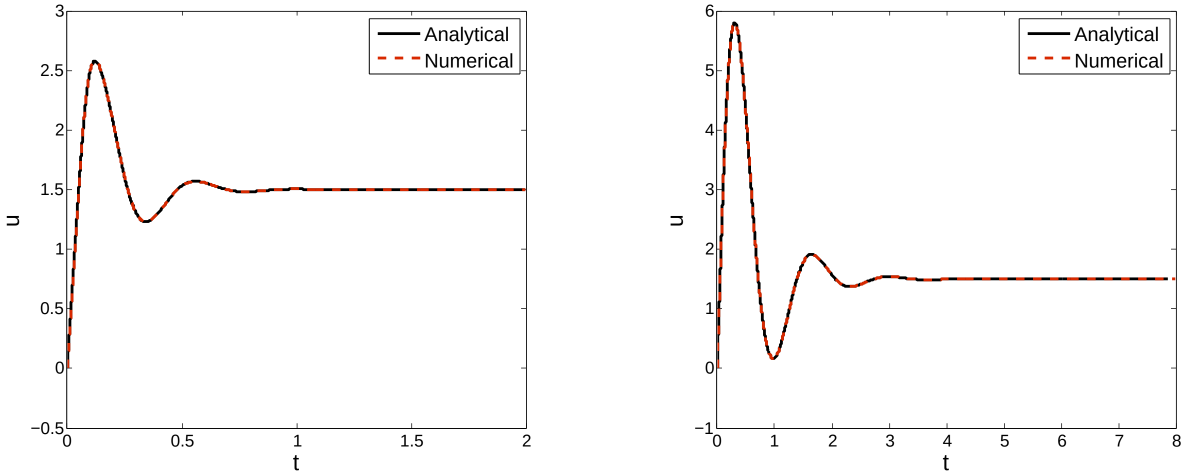

(a) Wi=0.1 (b) Wi=1.0

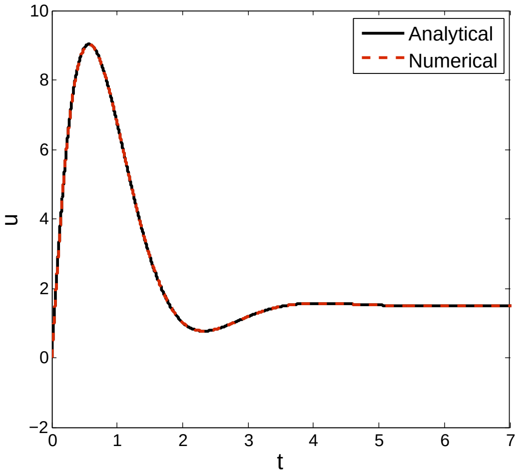

(c) Wi=5.0

Figure 4.23.: Evolution of velocity at point $y = 0.0125h$ in the start-up Poiseuille flow

stress and results in profiles of the stress with very sharp shape in this region. Despite of this difficulty, this test case has been used for examining the effect of fluid elasticity, see e.g. [41, 103, 98].

The geometry and boundary conditions of the test case are presented in figure 4.24 (a). A uniform velocity profile and zero stresses are imposed at the inlet. Zero stream wise gradients of velocity and stress are employed at the outlet, which is located far away from the singularity point. Symmetry planes are placed at the upper and lower boundary in front of the singularity. The dimensionless parameters are $\mathrm{Re} = \rho U_{in} H/(\eta_s + \eta_p) = 20$, $\mathrm{Wi} = \lambda U_{in}/H = 0.5, 1.0$ and 2.0 and $\beta = 1/10$. Three mesh sizes are used for the simulations as they are displayed in table 4.5. The mesh is divided into two blocks: one in front of the singularity, the other behind the singularity. The mesh is concentrated close to the wall and the singularity, see figure 4.24 (b).

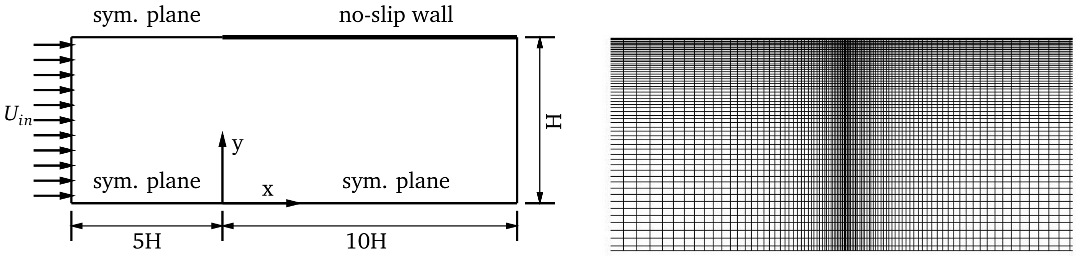

(a) Geometry (b) Mesh in the region near $(0, H)$

Figure 4.24.: Slip-stick geometry and its mesh near the singularity

Mesh	Number of CVs	Block 1	$\Delta x_{min}/H = \Delta y_{min}/H$	Block 2	$\Delta x_{min}/H = \Delta y_{min}/H$
M1	555	12×15	0.03	25×15	0.03
M2	2250	35×30	0.01	50×30	0.01
M3	10200	70×60	0.005	100×60	0.005

Table 4.5.: Mesh information for slip-stick geometry

With this test case the effects of increasing Weissenberg number are illustrated. They are shown by comparison of the streamline plots and profiles, contours of the velocity and stress in the region near the boundary changing point $(0, H)$.

The streamlines for $\mathrm{Wi} = 0.1$ and $\mathrm{Wi} = 2.0$ are shown in figure 4.26. The difference between these two Weissenberg numbers are obvious: The viscoelasticity causes the flow to strongly decelerate near the wall. Due to the continuity of the flow, the velocity near the axis of the channel increases. A more clear comparison can be seen in figure 4.25 where the profiles of velocity component u at $x = 0.6H$ are plotted for different Weissenberg numbers.

Significant difficulty has been met in predicting accurate stress field near the slip-stick boundary changing point even at very low Weissenberg numbers. Figure 4.27 shows the contours for stress tensor components at Wi=0.5. Even at such a low Weissenberg number large gradient of the stress exits near the boundary changing point. Difficulty appears in reaching mesh independent solution. Figure 4.28 shows the stress tensor components along y=0.98H near the boundary changing point with different meshes.

Lid-driven cavity flow

Viscoelastic fluids has been the subject of scientific studies of lid-driven cavity flow in recent years, see e.g [54, 43, 109, 155, 26]. In particular, this case has been applied to assess the performance of LCR in the simulations, see e.g. [43, 109, 26].

The cavity has equal width and height with $L = H = 1$, see figure 4.29 (a). The upper wall moves from left to right with a space and time dependent velocity profile given by

$$u(x,t) = 8[1 + \tanh 8(t - 0.5)]x^2(1-x)^2\,, \tag{4.102}$$

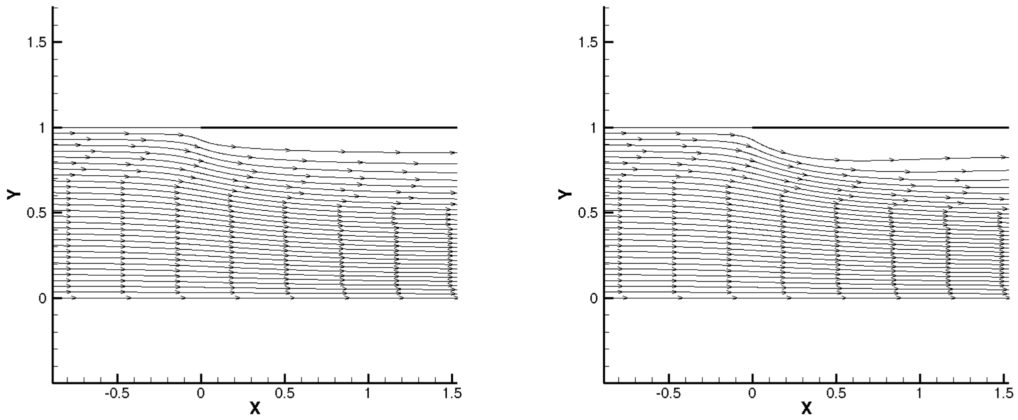

(a) Wi=0.1 (b) Wi=2.0

Figure 4.25.: Streamlines in channel entry flow with slip-stick geometry

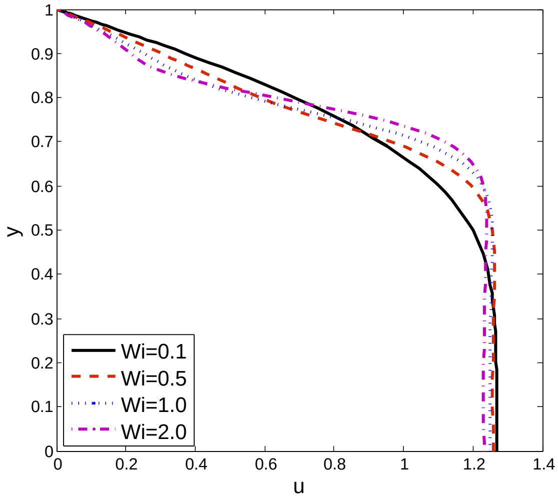

Figure 4.26.: Profile of u at $x = 0.6H$ in channel entry flow with slip-stick geometry

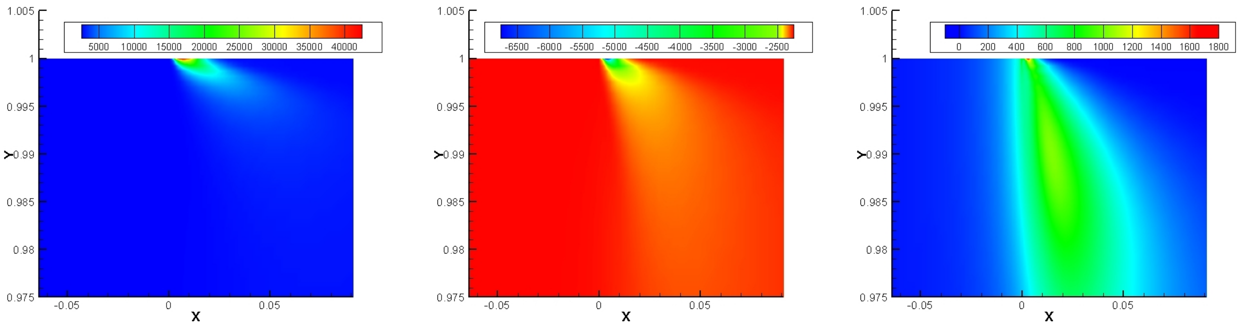

(a) τ_{xx} (b) τ_{xy} (c) τ_{yy}

Figure 4.27.: Stress field contour in channel entry flow with slip-stick geometry at Wi=0.5

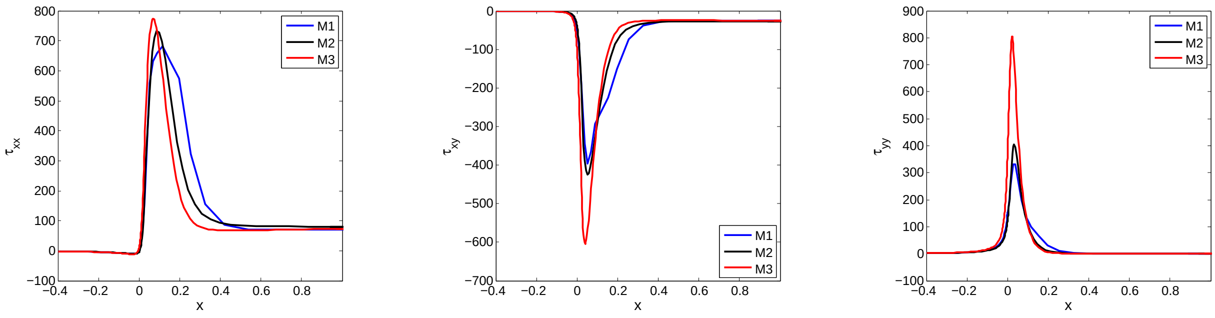

(a) τ_{xx} (b) τ_{xy} (c) τ_{yy}

Figure 4.28.: Stress profiles along y=0.98H in channel entry flow with slip-stick geometry at Wi=0.5

to eliminate the singularities at the corners. The lid velocity gradually increases until $t = 1$, when it reaches its maximum of $u = 1$ at the wall center $x = 0.5$. The other walls are fixed where no-slip boundary conditions are imposed on them. The creeping flow situation of $\mathrm{Re} \to 0$ is simulated, so the convective term in the momentum equation is neglected. The viscosity ratio is $\beta = 1/2$. The Weissenberg number is varied by changing the value of the relaxation time λ.

Figure 4.29 (b) shows the distribution of the mesh density. The mesh is denser near the walls and corners than in the central domain. Three successively refined meshes M1, M2 and M3 are used for the study. Detailed mesh information provided by table 4.6.

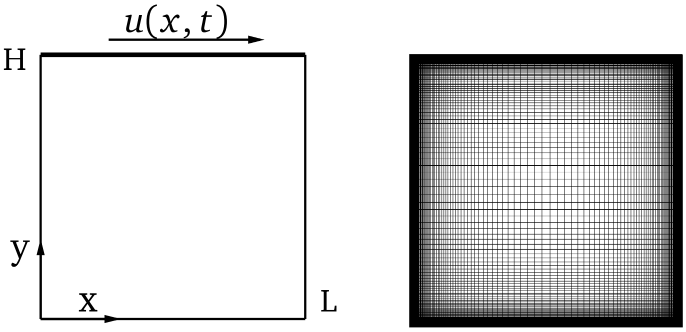

(a) Geometry (b) Mesh

Figure 4.29.: Geometry and mesh for lid-driven cavity

Mesh	Number of CVs	$\Delta x_{\min}/H = \Delta y_{\min}/H$
M1	6400	1.0 e-5
M2	25600	5.0 e-6
M3	102400	2.5 e-6

Table 4.6.: Mesh information for lid-driven cavity

For Newtonian fluid the main vortex center shifts in the positive direction of x-axis as the Reynolds number increases. Contrarily, it is observed in the experiment that the vortex center shifts in the opposite direction for viscoelastic fluids as the Weissenberg number becomes larger, cf. [106]. This phenomenon appears also in the simulations in the present work. Figure 4.30 shows the computed stream lines for the flow at Weissenberg number from 0.5 to 3. For higher Weissenberg numbers the flow is unsteady.

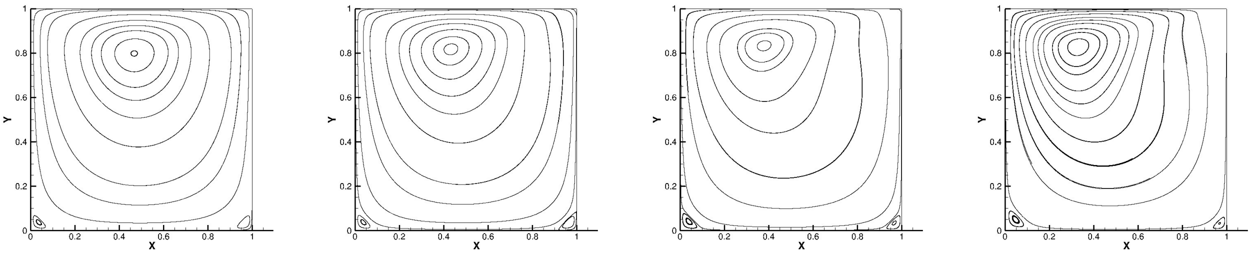

(a) Wi=0.5 (b) Wi=1.0 (c) Wi=2.0 (d) Wi=3.0

Figure 4.30.: Stream lines with different Weissenberg numbers for lid-driven cavity

The simulations are run until the flow reaches the steady state. During the flow evolution we monitor the change of the kinetic energy $\int_{\Omega} \frac{1}{2}\|\mathbf{u}\|_2^2 \, \mathrm{d}\Omega$ and the elastic energy $\int_{\Omega}(c_{xx} + c_{yy})\,\mathrm{d}\Omega$ in the whole domain, where c_{xx} and c_{yy} are the diagonal elements in the conformation tensor.

As for an example, the results for Wi=1.0 is presented. The evolutions of these two energies are shown in figure 4.32 (a) and (b). The kinetic energy grows at the first stage, reaches the maximum at the end stage of the lid acceleration, then decreases toward a steady state. The elastic energy increases gradually till steady state.

The contour of the velocity and stress fields at steady state are shown in figure 4.31. It is hard to see the change of value of τ_{xx} at different position in the domain in the contour. Actually, a very thin boundary layer of the normal stress component τ_{xx} is built along the upper wall, well large gradient exhibits. In order to display this thin boundary layer, the profiles of velocity component u and stress component τ_{xx} along $x = 0.5$ are plotted in figure 4.32 (c) and (d). In figure 4.32 (e) and (f) the profiles of velocity component v and stress component τ_{xy} along $y = 0.75$ are shown. We can also see a boundary layer of τ_{xy} exhibit on the right wall.

4:1 Contraction flow

In the contraction geometry the fluid flow exhibits strong shearing in the region near the wall and uni-axial extension along the center line. Non-Newtonian fluids exhibit significant different behaviour to Newtonian fluids e.g. the vortex behaviour, near the re-entrant corner and in the salient corner. In the benchmark test case the contraction ratio is set to 4:1, as displayed in figure 4.33 (a). The abrupt contraction produces a geometrical singularity at the re-entrant corner, where stresses are infinite leading to difficulties for the computation. Simulation studies of this problem can be found in a number of papers, e.g [6, 1, 8, 39, 26].

The computational domain in the present work is from $x = -20H$ to $x = 50H$, where H is the height of the outlet channel. The full computational domain is symmetric with respect to the x-axis so it is reasonable to consider half of it at the Weissenberg numbers considered in the present work. At the inlet, fully developed velocity and stress profiles are imposed. The length of the downstream part is large enough for the outlet flow to become fully developed. Zero normal derivatives for velocity and stress are applied at the outlet and the pressure value at the outlet boundary is extrapolated linearly from the two internal cells. A no-slip condition is imposed at the channel walls and inertial terms in the momentum balance are neglected. The relaxation time λ is changed to vary the Weissenberg number. The viscosity ratio is kept at the value of $\beta = 1/9$, the same as in the literature.

To resolve the stress field near the re-entrant corner, mesh density is concentrated there as shown in Figure 4.33 (b). Detailed information on the successively refined meshes is presented in table 4.7.

In this test a scalar target quantity characterising the flow and the local fields near the re-entrant corner are investigated.

The scalar target quantity is the recirculating corner vortex size X_R. Figure 4.34 presents this change of vortex size. The size of the vortex reduces with increasing Weissenberg numbers. In addition, it is found that a smaller

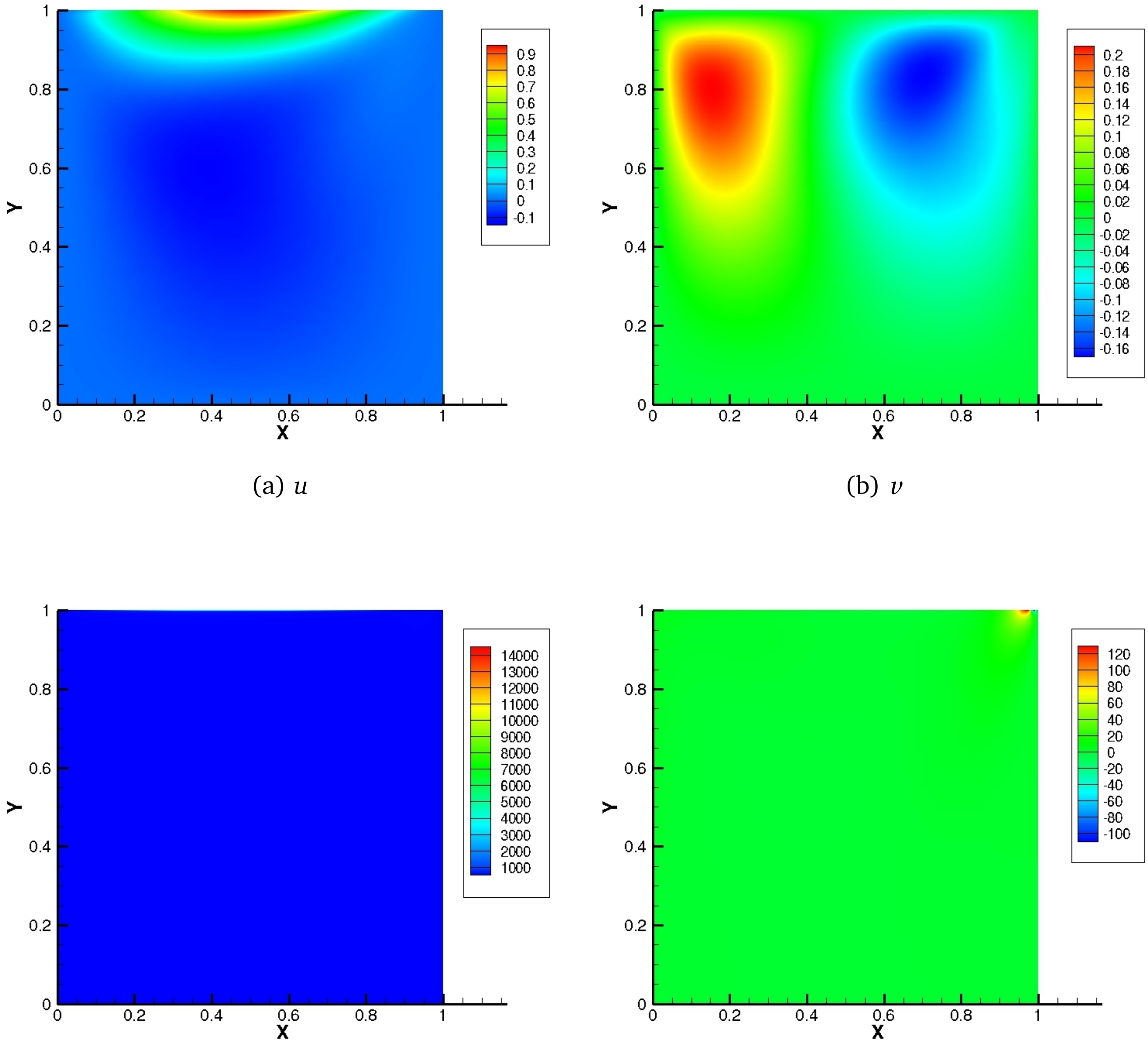

(a) u (b) v

(c) τ_{xx} (d) τ_{xy}

Figure 4.31.: Velocity and stress field at Wi $= 1.0$ for lid-driven cavity

Mesh	Number of CVs	$\Delta x_{\min}/H = \Delta y_{\min}/H$
M1	3846	0.02
M2	15384	0.01
M3	61536	0.005

Table 4.7.: Mesh information for 4:1 contraction flow

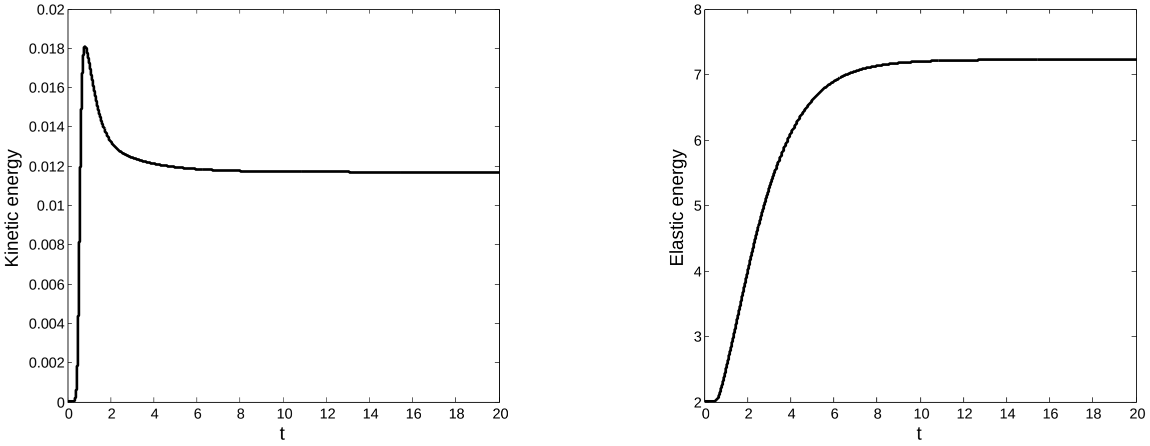

(a) Kinetic energy (b) Elastic energy

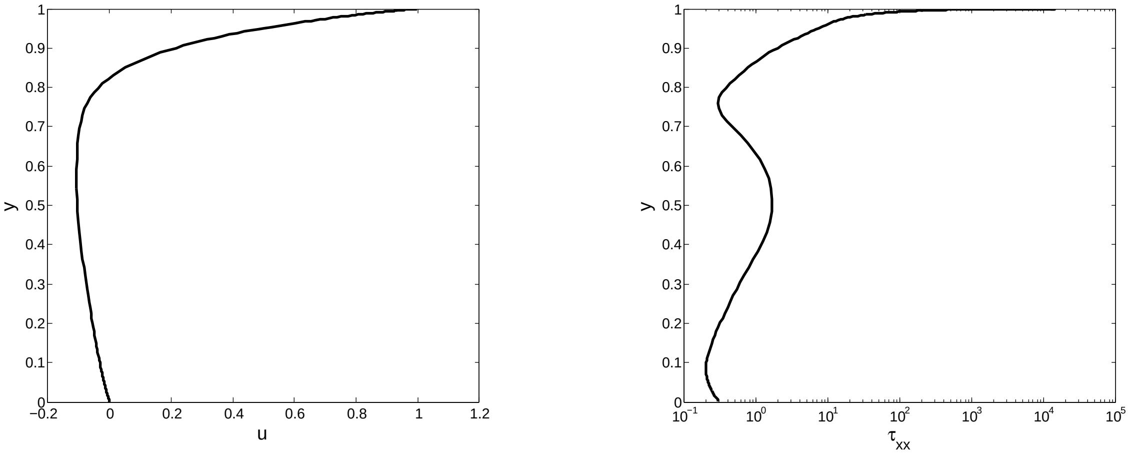

(c) $u(0.5, y)$ (d) $\tau_{xx}(0.5, y)$

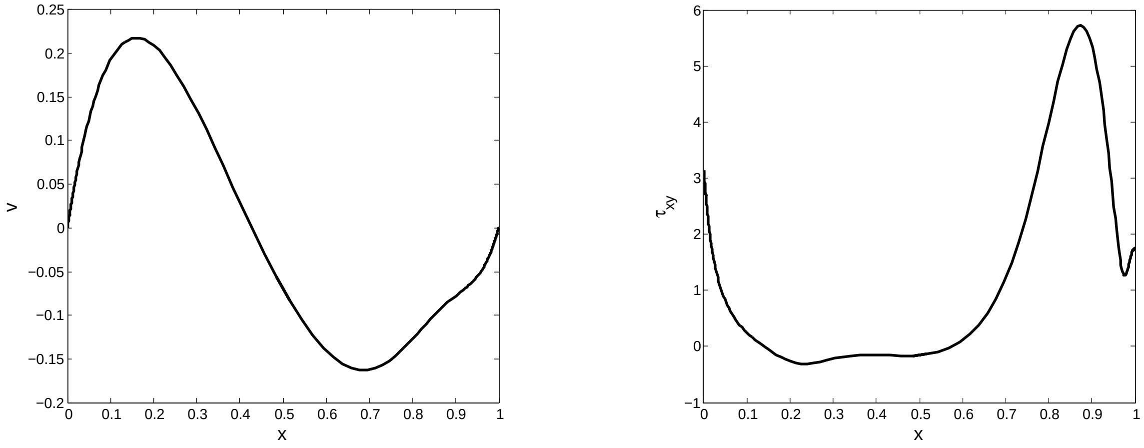

(e) $v(x, 0.75)$ (f) $\tau_{xy}(x, 0.75)$

Figure 4.32.: Evolution of kinetic and elastic energy and velocity and stress profiles at Wi $= 1.0$ for lid-driven cavity

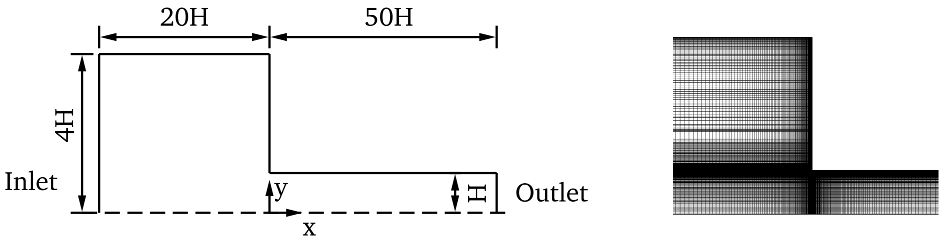

(a) Geometry (b) Mesh near corner

Figure 4.33.: Geometry and mesh for 4:1 contraction flow

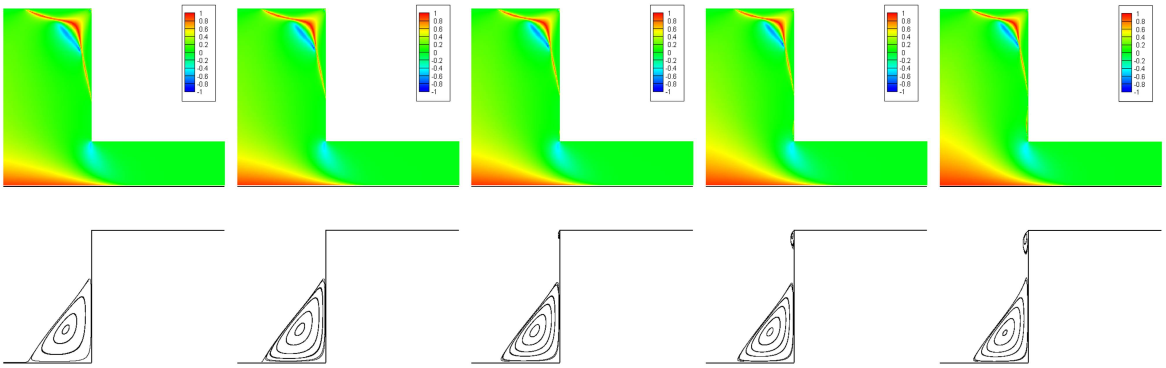

(a) Wi=0.5 (b) Wi=1.0 (c) Wi=1.5 (d) Wi=2.0 (e) Wi=2.5

Figure 4.34.: Contour of flow type parameter ξ (upper part) and corner Vortices (lower part) in the 4:1 contraction flow

vortex (lip vortex) near the re-entrance forms when the Wi > 1.0. This lip vortex grows with increasing Weissenberg numbers. In figure 4.34 the contour of the parameter

$$\xi = \frac{|\mathbf{D}| - |\mathbf{W}|}{|\mathbf{D}| + |\mathbf{W}|}$$

is also presented, which is a scalar employed to classify the local flow type, cf. [81], also see [3]. This parameter varies in the range form -1 to 1. When the $\xi = -1$ the flow is rotational, while $\xi = 1$ the flow is extensional. Pure shear flow occur when $\xi = 0$. These three regions are clear in this case. Rotation region locates near the re-entrance and the corner. Extension region in the upstream and near the corner. The shear region locates in the main domain of the inlet channel and near the walls especially in the outlet channel. The size of these regions varies with increasing Weissenberg numbers: the rotation region near the re-entrance increases, the extension region in the corner decreases.

The vortex sizes at various Weissenberg numbers together with the results in references are shown in figure 4.35 and part of them are explicitly shown in table 4.8. In the present work the vortex size is measured at Weissenberg number up to 2.5. For Wi > 2.5 the flow becomes unsteady. The reference values in the literature are the computed with *a*) unstructured collocated FVM with mesh 3 in their work and QUICK scheme by Edussuriya et al. [39]; *b*) structured collocated FVM with mesh 6 in their work and CUBISTA scheme by Alves et al. [8]; *c*) cell-vertex finite-volume/element method with mesh NM3 in their work by Aboubacar et al. [1] and *d*) spectral element method with mesh 1 in their work by Meng et al. [95].They are quite different from each other. The results in present work are between the lower bound and upper bound reported there.

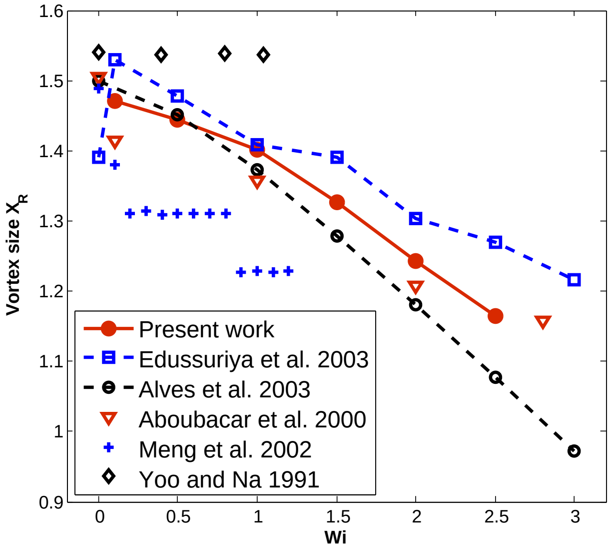

Figure 4.35.: Conner vortex size at various Weissenberg numbers

Wi	Present work	Edussuriya et al [39]	Alves et al. [8]	Aboubacar et al. [1]	Meng et al. [95]
0.0	-	1.391	1.5002	-	-
0.1	1.470	1.530	-	1.412	1.340
0.5	1.432	1.478	1.4520	-	1.309
1.0	1.385	1.408	1.373	1.358	1.229
1.5	1.320	1.391	1.279	-	-
2.0	1.265	1.304	1.181	1.203	-
2.5	1.232	1.269	1.077	-	-
3.0	-	1.217	0.973	-	

Table 4.8.: Corner vortex size at different Weissenberg numbers in 4:1 contraction flow

In the next step, the local field near the re-entrance is examined, in particular, the asymptotic behaviour in the vicinity of the re-entrant corner. Hinch [59] has shown that an Oldroyd-B fluid around a 270° re-entrant corner, the velocity vanishes like $r^{5/9}$ and the stress is singular like $r^{-2/3}$, i.e.

$$u_i \propto r^{5/9} \quad \text{and} \quad \tau_{ij} \propto r^{-2/3}, \tag{4.103}$$

where r is the distance from the re-entrant corner, u_i and τ_{ij} are the components of the velocity and stress tensor, respectively. The velocity and stress profiles along the line emanating from the corner at angle $\pi/2$ measured anti-clockwise from the inflow direction, which corresponds to the line $x = 0$, are compared. Figure 4.36 shows the profiles for Wi $= 1.0$. For higher Weissenberg numbers, a significant lip vortex develops and the conditions for the Hinch's asymptotic solutions are no longer valid. The present results show good agreement with the asymptotic solutions.

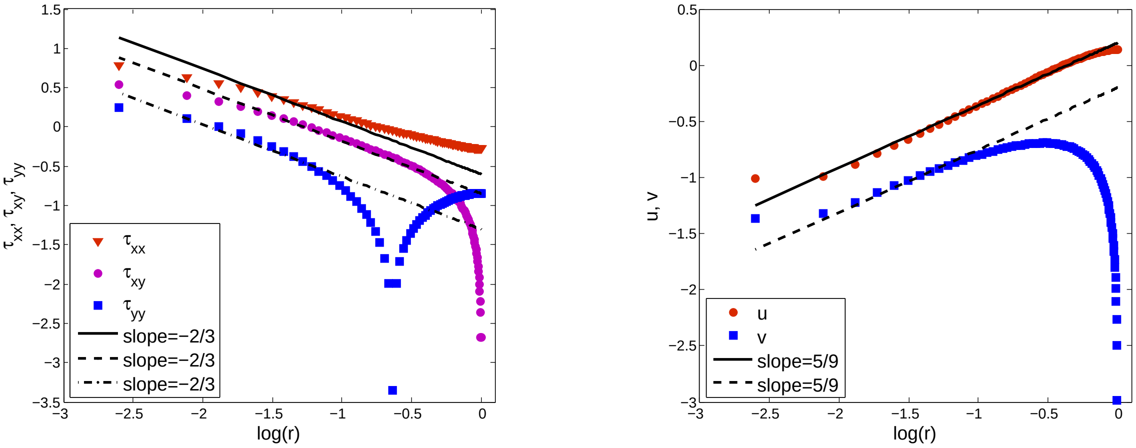

(a) Stress components

(b) Velocity components

Figure 4.36.: Asymptotic solution for velocity and stress components at the re-entrant corner at Wi $= 1.0$ in the 4:1 contraction flow

Flow past a cylinder

The interest in viscoelastic flow past cylinder arose in the instrument technology where hot-wire probes or sensors are placed in an elastic fluid flow and correlations made between drag and heat transfer coefficient data, cf. [105]. In this test case the cylinder is placed at the center line of a bounded channel, perpendicular to the main flow direction. Both shearing and extension effect can be seen in this case. The flow between the cylinder and the wall is mainly shear flow, while the flow near the symmetry plane and in the rear wake the flow is highly extensional. There is no geometry singularity in the domain. Yet, it is a difficult enough to produce accurate solution of the stress on the cylinder surface and along the center line in the cylinder rear wake. Therefore, this test case is chosen as a benchmark problem for the comparison of different codes. Much work has been devoted to this problem employing the finite-element method e.g. [116, 42, 26]. Studies applying finite-volume method can be found in e.g. [7, 4, 127]

The cylinder has radius R. The ratio of channel half-height to cylinder radius is 2:1. The computational domain is 80R long, with 19R upstream and 59R downstream of the forward and rear stagnation points of the cylinder, respectively. The full computational domain is symmetric, so it is reasonable to consider only half of it at least for moderate Weissenberg numbers. The geometry is shown in figure 4.37.

At the inlet, fully developed velocity and stress profiles are imposed. The downstream length is sufficient for the outlet flow to become fully developed, hence zero normal derivatives for velocity and stress are applied at the

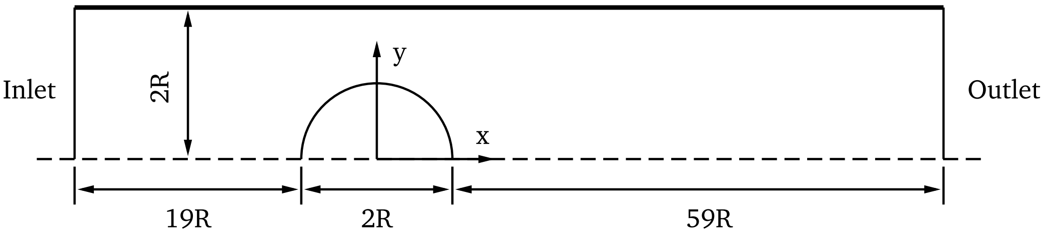

Figure 4.37.: Geometry for flow past a cylinder

outlet, and the pressure value at the outlet boundary is extrapolated linearly from the two internal cells. No-slip conditions are imposed at both the cylinder surface and channel wall. All computations are carried out for the case of creeping flow with Re → 0. In the simulations with different Weissenberg numbers the inlet velocity remains unchanged (parabolic inlet profile) while the Weissenberg number is varied by changing the value of the relaxation time λ. The viscosity ratio is set to the same value of $\beta = 0.59$ as in the literature.

The mesh is refined in the region along the cylinder surface and along the rear wake, in order to resolve the thin stress boundary layer, as it is shown in figure 4.38 (a). To clearly show this stress boundary layer, as for an example, the profiles of τ_{xx} along in these regions are shown figure 4.38 (b) for Wi=0.4 to 0.7. The large gradient of the stress can be clearly seen by these profiles. As the Weissenberg number increases, the gradient increases dramatically, particularly in the rear wake. Detailed mesh information is presented in table 4.9. The mesh is non-orthogonal so that it can fit the curved boundary.

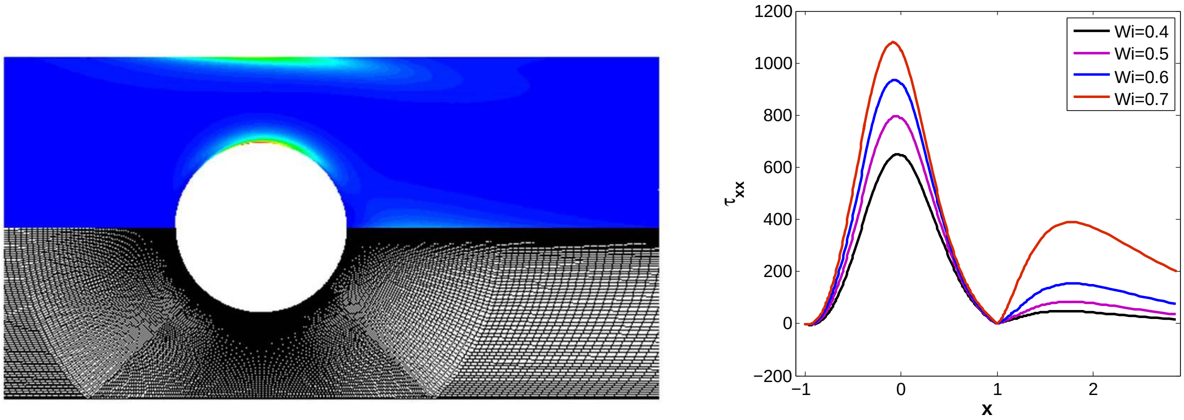

(a)

(b)

Figure 4.38.: (a)Mesh (upper part) and contour (lower part) of the τ_{xx} at Wi=0.7 for flow past a cylinder (b) Profiles of τ_{xx} along the cylinder surface and in the rear wake

Mesh	Number of CVs	Number of CVs along cylinder	$(\Delta r_{\min}/R)^a$	$(\Delta s_{\min}/R)^a$
M1	3050	97	0.016	0.0024
M2	11700	177	0.008	0.0012
M3	46800	342	0.004	0.0006

[a] Δr and Δs are the grid sizes in radial and tangential direction.

Table 4.9.: Mesh information for flow past a cylinder

Similar to the previous test case a scalar target quantity and the local field in the critical region are investigated.

The scalar target quantity is the dimensionless drag coefficient resulting from the stress and pressure on the cylinder surface:

$$C_d = \frac{1}{\eta U} \int_S (\tau - p\mathbf{I}) \cdot \mathbf{n} \cdot \mathbf{e}_x \, dS \, , \tag{4.104}$$

where $\mathbf{n}$ is the unit normal vector to the cylinder surface and $\mathbf{e}_x$ is the unit vector in the x-direction.

Results in the literature slightly differ from each other up to second decimal place. The comparison is shown in table 4.10 and figure 4.39. In these references Hulsen et al. [65] employ FEM using the DEVSS/DG formulation, while Fan et al. [42] apply FEM and their MIX1 formulation. Alves et al. [7] use collocated finite-volume method with the high resolution scheme SMART. Sahin and Wilson [128] apply semi-staggered dilation-free FVM with hexahedral elements.

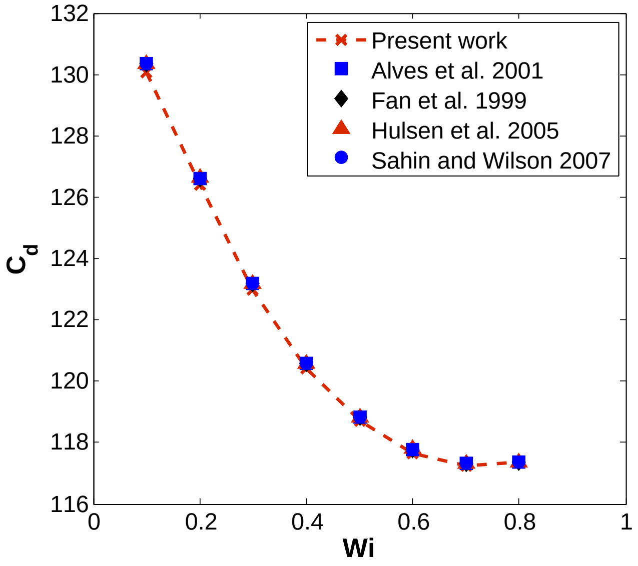

Figure 4.39.: Drag coefficient for different Weissenberg numbers in flow past a cylinder

Wi	Present work	Hulsen et al. [65]	Fan et al. [42]	Alves et al. [7]	Sahin and Wilson [128]
0.1	130.076	130.363	130.36	130.355	130.349
0.2	126.384	126.626	126.62	126.632	126.613
0.3	122.994	123.193	123.19	123.210	123.180
0.4	120.431	120.596	120.59	120.607	120.581
0.5	118.696	118.836	118.83	118.838	118.818
0.6	117.667	117.792	117.78	117.787	117.771
0.7	117.226	117.340	117.32	117.323	117.320
0.8	117.291	117.373	117.36	117.357	117.371

Table 4.10.: Drag coefficient in flow past a cylinder

The investigated local field is the normal stress along the cylinder surface and in the rear wake at Wi=0.7. Its profile is shown in figure 4.40. In the region on the cylinder surface the present result agrees well with the all the results in cited references. In the rear wake the present result agrees with the one in [65] but the peak is below the ones in [42] and [128].

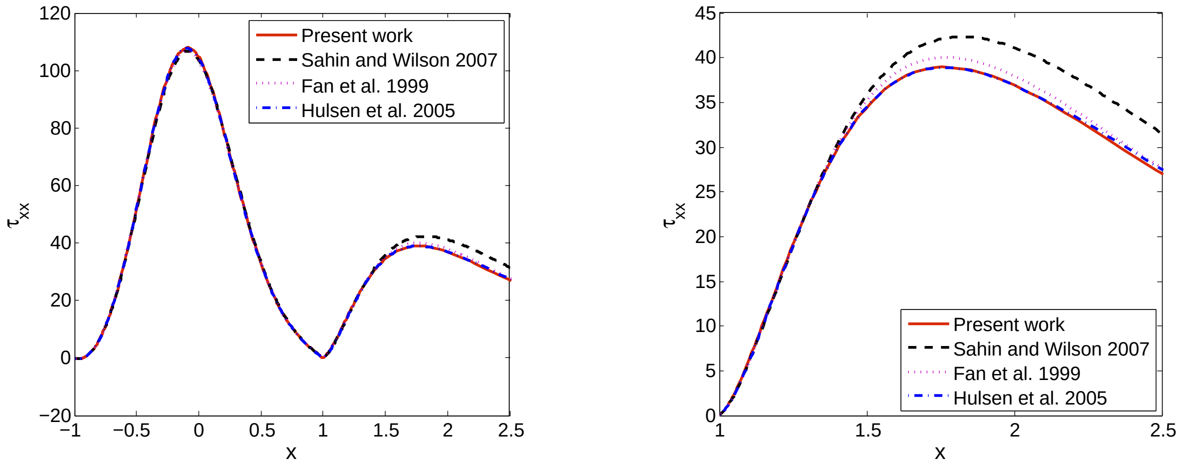

(a) Along cylinder and wake

(b) Zoom in along rear wake wake

Figure 4.40.: Profile of normal stress τ_{xx} (a) along the cylinder and rear wake and (b) zoom in along rear wake

4.4.3 Comparison of stabilization approaches for viscoelastic fluid flow

Since so many stabilization approaches are available, the question of suitability for practical applications arises naturally and is basically open. Knowing the advantages and disadvantages of these approaches and their difference is of high practical interest. This is helpful for choosing the appropriate approaches to cope with different kinds of stability problems caused by large Weissenberg number or by small viscosity ratios as well as to fulfil different requirements such as high accuracy, low computation cost etc. in the simulation. To shed light on the question, the performance of the four mentioned approaches are compared, namely BSD, PDPS as defined by Stewart et al. [137], LCR and SRCR as explained by Balci et al. [11].

Five aspects of the approaches are compared. Firstly, the implementation complexity is discussed. Secondly, comprehensively assess is done regarding their stability, accuracy, and efficiency for the test cases: lid-driven cavity flow, 4:1 contraction flow and flow past a cylinder – all for an Oldroyd-B fluid. Finally, the applicability of the approaches to complex problems is discussed.

During the comparison the approach devoid of any special stabilization technique is denoted as the standard approach. The results and the discussion are based on our published work [21].

Implementation complexity

Only the implementation of the stabilization approaches is considered here, hence we assume that the standard approach for computing an Oldroyd-B fluid flow is already available in a CFD code. This is also the case in the present work: The standard approach was first implemented in FASTEST and then various stabilization approaches were built based on the standard one. Therefore, the implementation complexity of code extension towards stabilization approaches is an important aspect.

We can divide the four stabilization approaches into two groups according to their formulation of the constitutive equation. It is clear that more effort must be made if a reformulation of the constitutive equation is required.

BSD and PDPS belong to the group which uses the original equation. As described in section 4.3.2, the implementation of BSD is adding diffusive terms simultaneously on both sides of the momentum equation and treating one term implicitly, the other explicitly. This is not a difficult task, since the treatment of the diffusive term is available if the solver for the Navier-Stokes equations is already implemented. The implementation of PDPS is devoid of modification of the momentum equation. Instead, the discretization of the constitutive equation needs to be modified. As shown in section 4.3.2, the implementation of the updating of the conformation is not complicated.

The other group of approaches reformulates the constitutive equation. This indicates that the working variables and constants in equation (4.1) should be changed correspondingly. The evolution equation of the conformation $\mathbf{c}$ is transformed to the evolution equation of $\log \mathbf{c}$ and $\mathbf{c}^{\frac{1}{2}}$ by LCR and SRCR, respectively. LCR requires several eigenvalues and eigenvectors calculations and matrix operations. This results in more effort in the implementation, whereas for SRCR the reformulated equation has a similar form to the original one, so effort must be made only for modification of working variables and constants. The implementation complexities are summarized in table 4.11.

Use the original constitutive equation		Reformulate the constitutive equation	
BSD	PDPS	LCR	SRCR
Adding two diffusive terms in the momentum equation, one to be treated implicitly, the other one explicitly	Changing the discretization in the constitutive equation according to section 4.3.2	Changing the working variable (from $\mathbf{c}$ to $\mathbf{s} = \log \mathbf{c}$) and constants in equation (4.1), calculating the eigenvalues and eigenvectors and implementing matrix operations	Changing the working variable (from $\mathbf{c}$ to $\mathbf{A} = \mathbf{c}^{\frac{1}{2}}$) and constants in equation (4.1)

Table 4.11.: Implementation complexity of each stabilization approach

Stability

Naturally, stability is the central aspect for the evaluation of the aforementioned approaches. The stability problem can be assessed by two dimensionless numbers in the simulation. One is the Weissenberg number and the other is the viscosity ratio.

When the Weissenberg number is above specific critical values, instability occurs. This problem is referred to as the HWNP. To assess the ability of the approaches to cope with this problem, we compare their critical Weissenberg numbers, which are defined according to the following two criteria: *a*) the computation does not converge *b*) the positive definiteness of the conformation tensor is destroyed. During the simulation the positive definiteness of the conformation tensor is examined by monitoring the sign of its determinant. Note that, starting with a positive definite matrix, the first sign change of one eigenvalue will result in a negative determinant The critical Weissenberg numbers are different for different cases and with different meshes or numerical parameters. Nevertheless, we can give the critical value of each approach for the same test case using the same settings.

Table 4.12 lists the critical Weissenberg numbers of each approach in the different test cases. The values are obtained using the mesh M1s, M2 and M3 for the cases lid-driven cavity, flow past a cylinder and 4:1 contraction flow, respectively. The mesh M1s in the lid-driven cavity flow has the same number of CVs as M1 in table 4.6 but larger cell size ($\Delta x_{min} = 6.\text{e-}3$). The reason for using a relatively coarse mesh in this case is the computational cost when employing PDPS. This will be discussed in detail in the next section. For the flow past a cylinder, PDPS in not involved due to non-orthogonal grid.

From the comparison we see that LCR and SRCR are suitable for higher critical values than the other approaches. When the Weissenberg numbers are larger than the values given in the table, simulations based on LCR and SRCR are still stable. Therefore, we can not give the critical Weissenberg numbers for both of the approaches. On the one hand, as the Weissenberg number increases the computation time increases dramatically. On the other hand, above certain Weissenberg numbers the flow becomes unsteady. BSD shows little improvement for such kind of instability, as we observe the same critical values for the standard approach and BSD.

It is worth mentioning that simulations with the standard approach and BSD can converge even when the conformation tensor looses its positive definiteness. For the lid-driven cavity the standard approach and BSD converge up to $\mathrm{Wi} = 1.0$, while for the 4:1 contraction flow these two approaches converge up to $\mathrm{Wi} = 2.0$. Those

Approach	Lid-driven cavity	Flow pasts a cylinder	4:1 contraction flow
Standard	0.75 (<0.5 [43])[b]	0.8 (0.88 [65])	1.5 (2.0 [3])
BSD	0.75	0.8	1.5
PDPS	0.75	–	2.0
LCR	>5.0 (>5.0 [43])	>1.0 (>1.4 [65])	>4.0 (>3.0 [3])
SRCR	>5.0	>1.0	>4.0

[b] values in brackets are the critical values given in the corresponding literature

Table 4.12.: Critical Weissenberg number of each approach in different test cases

Weissenberg numbers are all larger than the values given in the table. Therefore, we should carefully examine the results at high Weissenberg numbers when standard or BSD approaches are applied, in order to guarantee that physical results are obtained.

Since PDPS can preserve the positive definiteness of the conformation tensor, it is wondered why it can not obtain higher critical Weissenberg numbers. The key point lies in the fulfilment of the positive preserving condition (4.77). As shown in section 4.3.2, the positivity of the conformation tensor is only preserved under the condition (4.77). However, the numerical error introduced by PDPS in the constitutive equation eventually violates this condition, since the discretization scheme in PDPS has only first order accuracy. The error produced in the conformation tensor is introduced in the momentum equation which may produce an overestimated velocity. Before the simulation starts, the time step size is set according to the estimated maximum velocity. Therefore, it can happen that the velocity will exceed this estimated value during the simulation an then the condition (4.77) is not fulfilled any more. For example, in the test case of the lid-driven cavity, the maximum velocity is 1, which is the maximum velocity of the lid. During the simulation we have found that the maximum velocity exceeds 1, at physical time $t = 9.105$ in the region near the upper wall. In the simulation the time step size $\Delta t = 0.0005$ is employed which fulfils the positive preserving condition (4.77). However, the condition is violated shortly after the maximum velocity exceeds 1 at the physical time $t = 9.1065$. If we decrease the time step size, the computation blows up later. The approach may be more stable if the time step size is adaptive, but this case is not studied in the present work.

The second stability problem is caused by the viscosity ratio. The viscosity ratios in the test cases are $\beta > 0.1$. These values are large enough to prevent the instability caused by the viscosity ratio. A stability problem occurs when this ratio is small. If we use the values which were obtained by fitting the model to the experimental data reported in [119], namely $\eta_s = 0.002\,\mathrm{Pa\,s}$ and $\eta_p = 1.422\,\mathrm{Pa\,s}$, for which the viscosity ratio is $\beta = 0.0014$, the stability problem occurs for the standard approach at a very low Weissenberg number of $\mathrm{Wi} = 0.1$. Using these parameters and applying the stabilization approaches in all the test cases, we found that except BSD all approaches blow up also at a very low Weissenberg number $\mathrm{Wi} = 0.1$, whereas BSD can reach almost the same critical Weissenberg numbers as possible for large viscosity ratios. This fact shows that the additional implicitly treated diffusive term makes a contribution to the stabilization as explained in section 4.3. Considering the low implementation complexity (modification only has to be done in the momentum equation) BSD can accompany other stabilization approaches to cope with such kind of stabilization problem.

Accuracy

In principle, different approaches should obtain the same results when their solutions are mesh independent. At this point, two questions become relevant: Can all approaches obtain mesh independent solutions at tolerable computational cost? How expensive is it to obtain mesh independent solutions by a specific approach? To answer these two questions, we employ the lid-driven cavity for $\mathrm{Wi} = 0.5$ because it has a simple geometry and no singularity occurs in the flow field. During the comparison, the same spatial discretization schemes (CUBISTA for convective terms and CDS for diffusive terms) are employed in all approaches, except for the evolution equation of the conformation tensors in PDPS due to its special treatment as set out in section 4.3.2.

When we apply different approaches with the coarsest mesh M1s, we find that in the center of the domain, taking as an example the region along $x = 0.491$, all approaches predict almost the same velocity profiles as shown in figure 4.41 (a). As for the normal stress profile (figure 4.41 (b)), PDPS deviates a bit from the others in the region near $y = 0.73$, whereas the other approaches predict almost the same stress profiles.

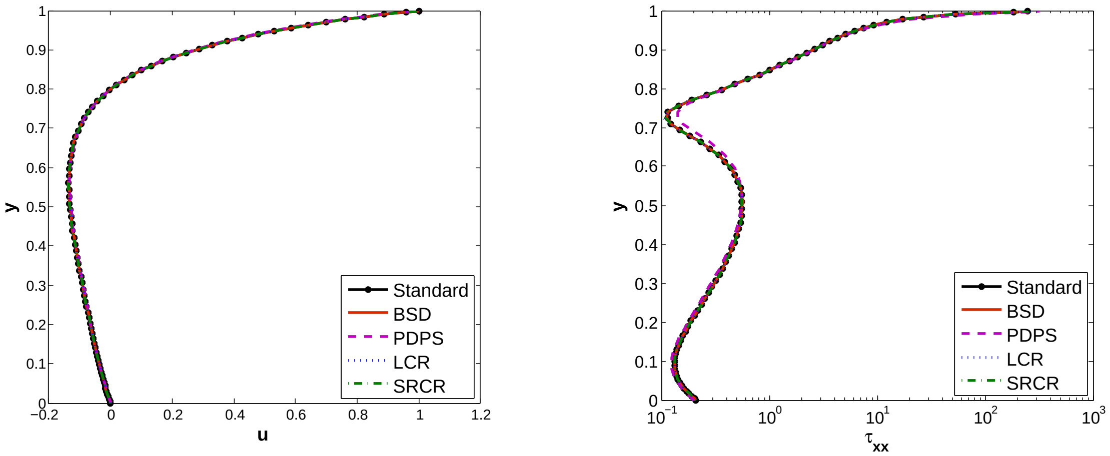

(a) $u(0.491, y)$ (b) $\tau_{xx}(0.491, y)$

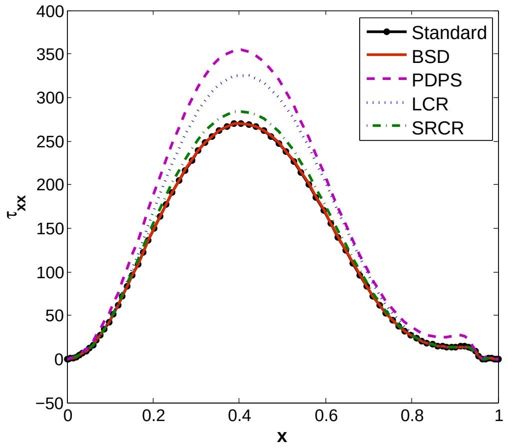

(c) $\tau_{xx}(x, 1.0)$

Figure 4.41.: Velocity component u and normal stress τ_{xx} along $x = 0.491$ and normal stress τ_{xx} along $y = 1.0$ at $\mathrm{Wi} = 0.5$ using mesh M1s in the case of the lid-driven cavity

However, a large difference appears along the upper wall as depicted in figure 4.41 (c). This shows that the mesh M1s is not fine enough to resolve the stress field in this region. It is reported in [109] that a stress boundary layer builds up at the upper wall, where very fine cells should be employed to resolve the large gradient of stress in this region. By a mesh study we find that the mesh M3 can be used to produce accurate solutions with the standard approach under the condition that high resolution schemes are employed. Let us note that using the first order upwind scheme, the mesh M3 is still not fine enough. A comparison of the effects of the schemes UDS and CUBISTA in predicting the normal stress profiles is shown in figure 4.42 for standard approach. The effect of these two schemes for LCR has been shown in section 4.4.1.

Since first order upwind scheme is used to calculate the advection term in PDPS, the above analysis gives us an indication that in order to get a mesh independent solution with PDPS, a much finer mesh than M3 is needed.

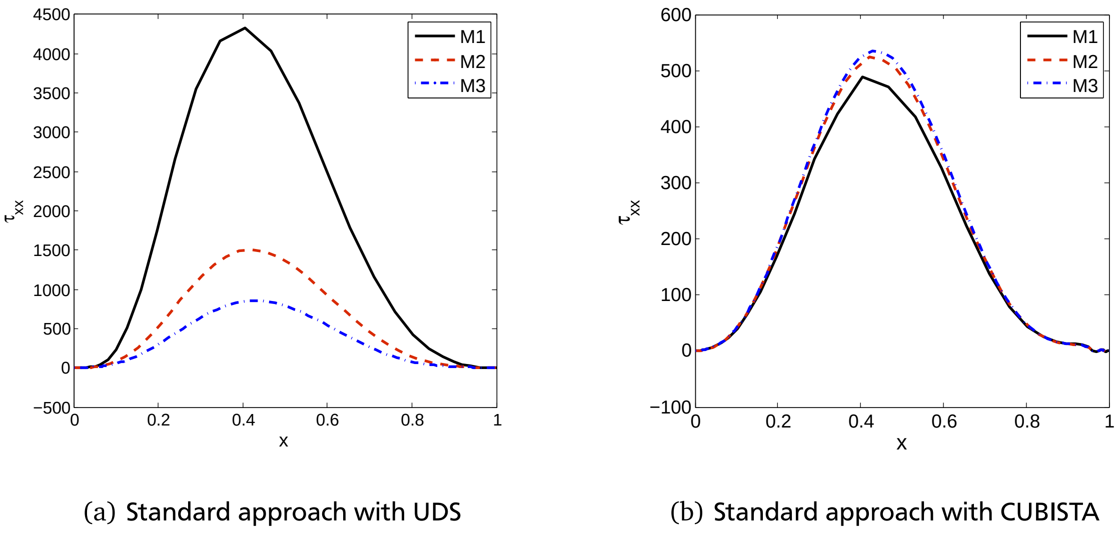

(a) Standard approach with UDS (b) Standard approach with CUBISTA

Figure 4.42.: Normal stresses τ_{xx} along the upper wall $y = 1.0$ at Wi = 0.5 using standard approach with UDS and CUBISTA in the case of the lid-driven cavity

Besides the requirement of spatial resolution, sufficient temporal resolution is required for PDPS as well. If we apply PDPS with the mesh M3, according to the positive preserving condition (4.77) the time step size should be

$$\Delta t < \frac{1}{2d} \frac{\Delta x}{\max|\mathbf{u}|} = 6.25 \times 10^{-7}, \tag{4.105}$$

where $d = 2$ and $\max|\mathbf{u}| = 1$. For a simulation at Wi = 0.5 the flow reaches steady state until $t = 10$. The total computation time is extraordinarily long under these conditions. As mentioned above, the mesh M3 is still not fine enough for this approach, so it is out of reach to get a mesh independent solution using PDPS.

Similarly, we perform a convergence study for BSD, LCR and SRCR. As expected, BSD predicts the same results as the standard approach, since the addition of the terms on both sides of the momentum equation should not influence the steady state solution. We find that LCR and SRCR converge faster than the standard approach and BSD. To compare them quantitatively we study the maximum value of the normal stress τ_{xx} along the upper wall. The results are shown in table 4.13. Since it predicts the same result as the standard approach, BSD is not involved in the table. Given the results shown in the table we confirm that LCR has a higher convergence rate than the other approaches.

Mesh	Standard	LCR	SRCR
M1	488.162 (9.427%)[a]	526.384 (1.815%)	513.929 (4.213%)
M2	523.942 (2.789%)	534.215 (0.355%)	530.501 (1.124%)
M3	534.526 (0.825%)	535.745 (0.069%)	534.923 (0.299%)
Extrapolated	538.972	536.117	536.532

[a] values in brackets are the relative errors compared with the extrapolated values.

Table 4.13.: Convergence study for maximum τ_{xx} along $y = 1.0$ in the lid-driven cavity flow

Using the same mesh size, the result predicted by LCR is closer to the mesh independent solution. It indicates that LCR allows the use of a larger grid spacing without loss of accuracy. SRCR has a lower convergence rate than LCR, yet it converges faster than the standard approach and BSD. The reason is that SRCR resolves the large stress gradient better than the standard approach. This can be explained analogously to the analysis of the "toy model" of the constitutive equation (4.66) introduced section 4.3.

As emphasized in [43, 65], the numerical difficulty of solving equation (4.66) is that the standard discretization based on polynomial interpolation of such an equation always fails to balance the exponential growth. Using higher order discretization schemes can ease the problem to some extent but can not solve it. If we transform equation (4.66) to the equations for $s = \log c$ and $a = \sqrt{c}$, the corresponding equations are (4.68) and (4.70), respectively. From the solutions of these two transformed equations we clearly see that equation (4.68) linearises the exponential growth of c. Hence the error can be greatly reduced. Equation (4.70) does not linearise the exponential growth but reduces it by a factor 2, which also can help significantly in the computation.

When the Weissenberg number is larger, a much finer mesh is required to resolve the stress boundary layer. For these cases LCR and SRCR show their great advantage in saving computational cost, because the requirement of the mesh refinement is less critical than for the other approaches.

Another way to assess the fidelity of the approaches and the quality of their results is to accomplish a code-to-code comparison with the benchmark cases. To see the effect of different approaches, we use the moderately fine meshes M2 in table 4.9 and 4.7. In each test case the results are compared in two ways: comparing a scalar target quantity characterising the flow and comparing the local profiles of velocity and stress.

In figure 4.43 (a) we plot our results together with the drag coefficient presented in [7]. BSD gives the same results as the standard approach. Hence we only show the values predicted by the standard approach. We see that our results are below all the reference values by a small amount with a maximum relative difference of 0.23%. Yet, according to the mesh study we have done, we find that if a finer mesh is used, the results are closer to the reference. Because of this fact and due to the comparison, we conclude that using a moderately fine mesh LCR predicts more accurate results than the other approaches in the test. At the same time SRCR is more accurate than the standard approach. A similar conclusion can also be drawn from comparison of the normal stress in the rear wake behind the cylinder shown in figure 4.43 (b). The profile of LCR is closer to the reference than the profile of SRCR, which is closer than the one of the standard approach. To see the effect of mesh refinement in the wake we plotted the profiles of LCR for different meshes in figure 4.43 (c). The peaks of the profiles approach the reference as the mesh is refined.

For the 4:1 contraction flow the scalar target quantity is the recirculating corner vortex size. Results together with the reference are shown in figure 4.44. They are quite different from each other. Our results are between the lower bound and upper bound reported there, hence we can not finally conclude which results are correct, so we can not judge the accuracy by this comparison. However, we have observed that all the approaches predict almost the same results until $\mathrm{Wi} = 1.5$. For $\mathrm{Wi} > 1.5$, PDPS deviates from the other approaches.

The deviation of PDPS is more obvious when we examine the local profile of the stress and velocity. Here the asymptotic behaviour in the vicinity of the re-entrant corner is considered. To be compared are the velocity and stress profiles along the line emanating from the corner at angle $\pi/2$ measured anti-clockwise from the inflow direction, which corresponds to the line $x = 0$, where the asymptotic solutions $u_i \propto r^{5/9}$ and $\tau_{ij} \propto r^{-2/3}$ are available. Figure 4.45 shows the profiles for $\mathrm{Wi} = 1.0$. From the figures we see that all the approaches are in good agreement with the asymptotic solutions except PDPS which deviates from the others, especially for the components u, v and τ_{xx}. We believe that the deviation of PDPS is caused by the lower accuracy of the scheme itself. This is examined by the mesh study of PDPS shown in figure 4.46. With finer mesh the profiles are significantly closer to the asymptotic solution.

Efficiency

Another important aspect is efficiency, where high efficiency means large ratio of accuracy to the cost of computation. The accuracy of the approaches has been discussed in the previous section. Therefore, we first discuss the cost of computation then set out the influence of accuracy on the efficiency of the approaches. A direct way to measure the cost of computation is examine the computation time of each approach for the same test case with the same mesh and parameter setting on a workstation using single CPU core. The parameter setting includes the under-relaxation factors $\alpha_u = 0.6$ for the velocity components, $\alpha_p = 0.4$ for pressure and $\alpha_s = 0.1$ for the conformation tensor components. Due to the formulation of PDPS there is no under-relaxation factors in the computation of the conformation tensor. The computations are stopped at the same physical time at which the field reaches steady

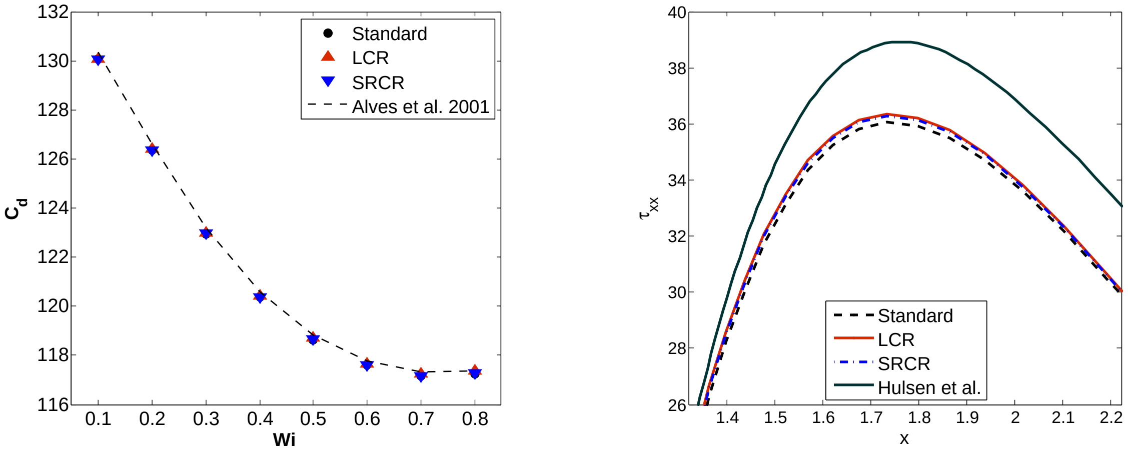

(a) Drag coefficient

(b) τ_{xx} in the rear wake with mesh M2

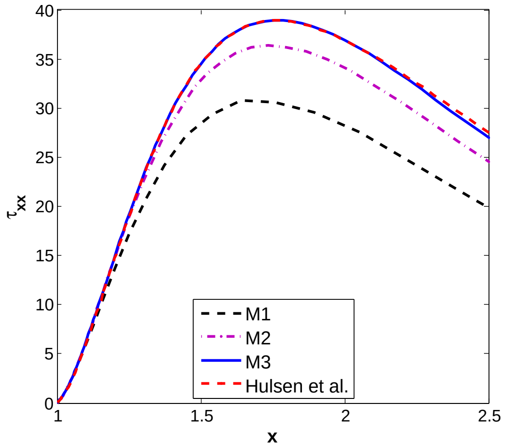

(c) τ_{xx} with LCR for different meshes

Figure 4.43.: Drag coefficient and the profile of normal stress τ_{xx} in the rear wake at Wi $= 0.7$ in the case of the flow past a cylinder

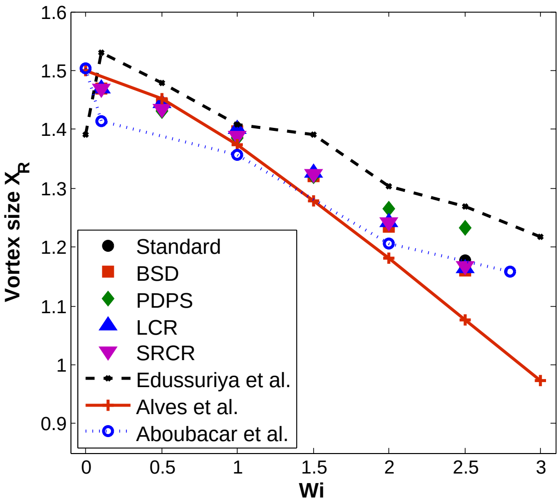

Figure 4.44.: Vortex size X_R in the case of the 4:1 contraction flow

state in the same test case. In order to reduce the computation time but without too big loss of accuracy, we use the moderate mesh size for the test, namely, the mesh M1s for lid-driven cavity, the mesh M2 for flow past a cylinder and 4:1 contraction flow. For the case of lid-driven cavity every simulation starts with a zero-value initial condition, whereas for the other two more complicated cases the simulation for a higher Weissenberg number starts with the solution of the lower Weissenberg number as the initial condition in order to save computation time. The CPU time for each approach in each case with increasing Weissenberg numbers is displayed in figure 4.47.

Evidently, the CPU time required by the approaches does not stay in the same order in different test cases. However, we see something in common:

Simulations with PDPS run the fastest. The explicit calculation of the conformation tensor takes less time (compared to implicit approach), because no linear equation solver is required.

SRCR is always faster than LCR. The reason lies in the formulation of the constitutive equation. As we have shown in section 4.3.2, several eigenvalue and -vector calculations and matrix operations are executed by LCR at every iteration. These calculations and operations are time-consuming. On the contrary, no such calculations are required by SRCR.

As mentioned, efficiency is closely related to the accuracy. For instance, PDPS offers the fastest simulation, but it provides low accuracy. Therefore, a much finer mesh is mandatory for accurate results, which slows down the simulation. LCR computes slower than SRCR, yet it predicts more accurate results, especially at high Weissenberg numbers. Consequently, it allows the use of a coarser mesh while reaching the same accuracy, which saves computation time.

Based on the above analysis, a final assessment of the efficiency of the approaches is not possible, in particular because it is problem dependent. Instead, we can only suggest to choose the most efficient approach on a case-by-case basis, taking into account the information given above.

Applicability to complex problems

In the previous sections we have compared performances of the stabilization approaches for problems with simple two-dimensional geometries using the simplest viscoelastic fluid model Oldroyd-B. However, complex three-dimensional domains and complex fluid models are encountered in real world applications. Therefore, it is useful to know the applicability of these approaches to more complex problems.

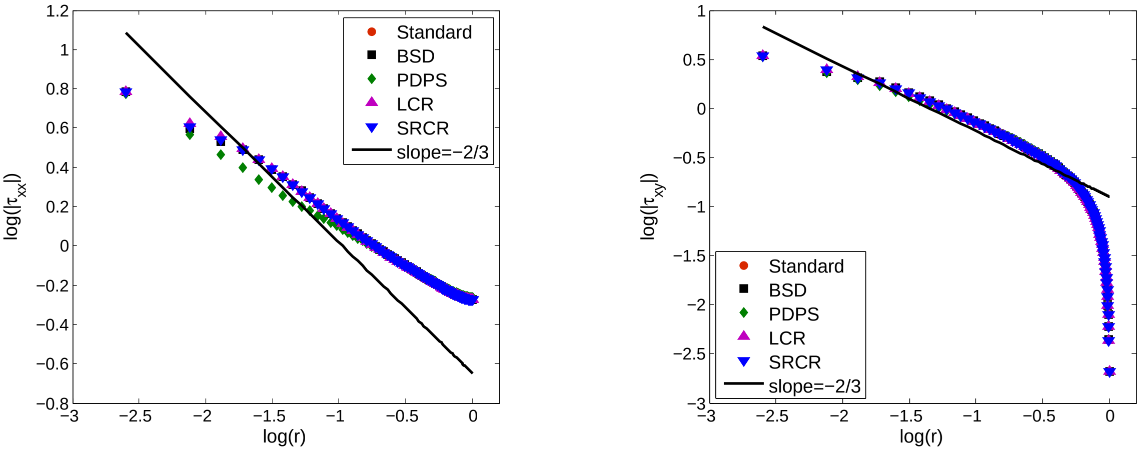

(a) τ_{xx} (b) τ_{xy}

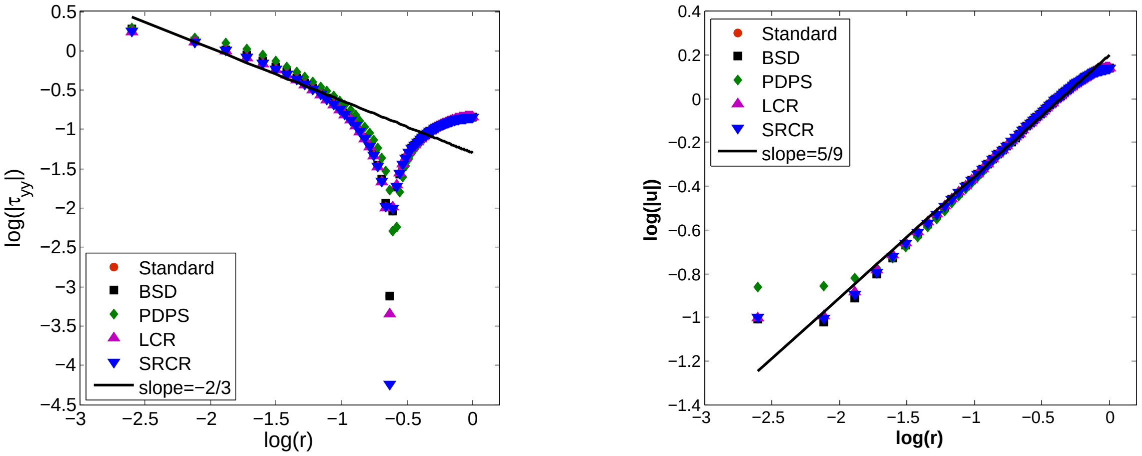

(c) τ_{yy} (d) u

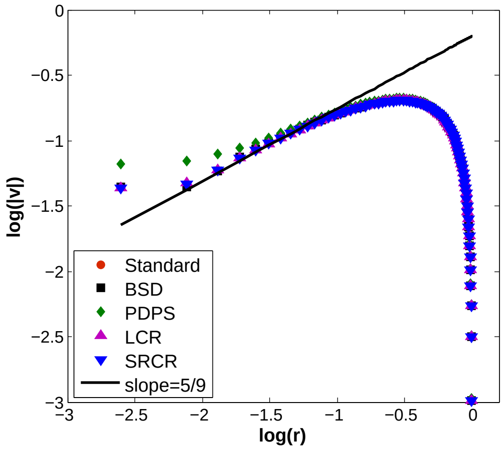

(e) v

Figure 4.45.: Asymptotic solution for velocity and stress fields at the re-entrant corner in the case of the 4:1 contraction flow

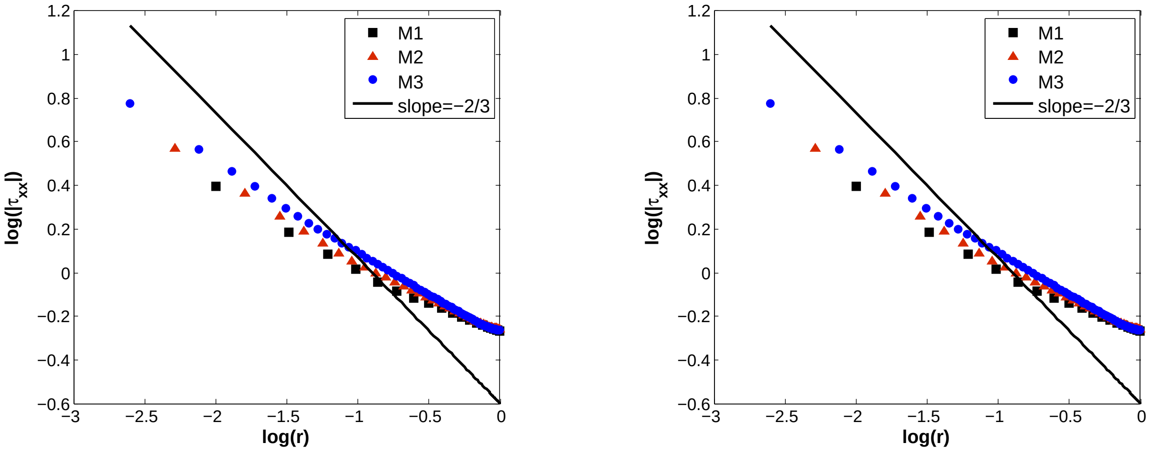

(a) τ_{xx} (b) τ_{xy}

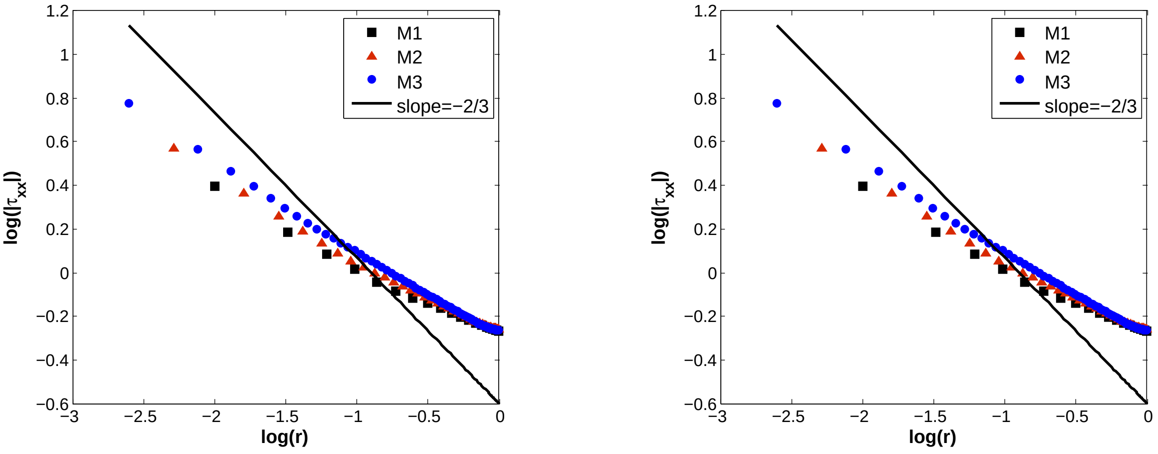

(c) τ_{yy} (d) u

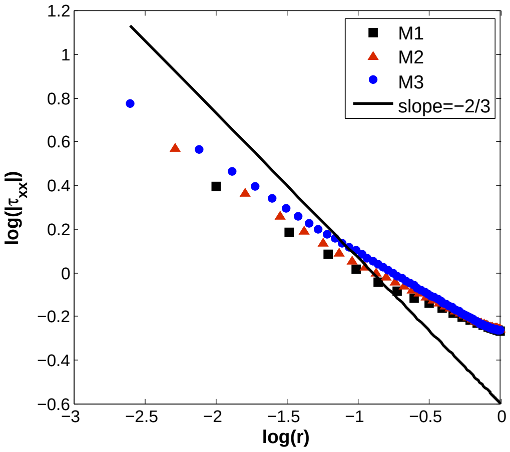

(e) v

Figure 4.46.: Asymptotic behaviour predicted by PDPS with different meshes in the case of the 4:1 contraction flow

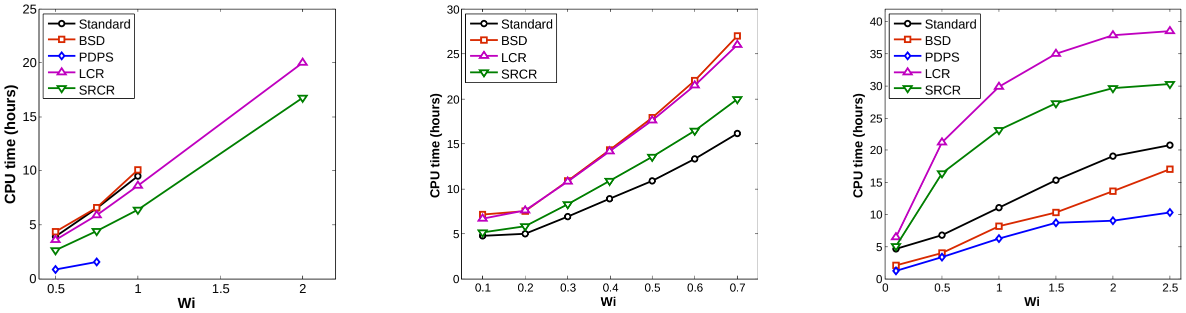

(a) Lid-driven cavity (b) Flow pasts a cylinder (c) 4:1 contraction flow

Figure 4.47.: CPU time for the test cases at various Weissenberg numbers

The first issue is related to applicability of the stabilization approaches in three-dimensional domains with complex geometries. All the approaches are able to compute three-dimensional problems. When the flows take place in complex geometries, a non-orthogonal block structured or unstructured mesh is required.

BSD, LCR and SRCR are derived independently from the employed discretization schemes. Therefore, they can be applied to non-orthogonal structured meshes as well as to unstructured meshes. In the literature we can find the application of these approaches to the three-dimensional complex flow domains. An example for application of BSD is found in [61], where a three-dimensional contraction flow is simulated. Applications of LCR in a three-dimensional contraction flow and in the flow past a three-dimensional cylinder can be found in [3] and [127], respectively. It is worth mentioning that in [61] and [127] the stabilization approaches BSD and LCR are applied for an unstructured finite-volume framework. We have not found any application of SRCR to complex geometries or unstructured meshes in published work.

Different from the above three approaches PDPS must be modified for non-orthogonal meshes. The modification is the approximation of $\mathbf{c}^*$ which is the conformation tensor of the material particle at the current position at the previous time step. It is computed according to equation (4.75), i.e.

$$\mathbf{c}^* = \mathbf{c}^n - \Delta t \mathbf{u} \cdot \nabla \mathbf{c}^n. \tag{4.106}$$

In order to keep the tensor $\mathbf{c}^*$ positive definite, the interpolation coefficients of Equation (4.106) should be positive which is the key step in the PDPS. This is easy to realize for orthogonal meshes when first order upwind scheme is employed to calculate $\mathbf{u} \cdot \nabla \mathbf{c}^n$, as illustrated in section 4.3.2. If non-orthogonality is encountered, the discretization of the term $\nabla \mathbf{c}$ accounts for the mesh non-orthogonality. As a result, additional terms for mesh non-orthogonality (see e.g. [130]) will appear in the interpolation coefficients and gives rise to the difficulty in keeping them positive.

The second issue is related to the applicability for complex constitutive models. BSD is independent from the constitutive models, since only the momentum equation is changed. Favero et al. [44] have shown the application of BSD in a wide range of differential models including Oldroyd-B/UCM, Giesekus, PTT, FENE-P, FENE-CR, and Pom-Pom based constitutive equations in single as well as multi mode forms.

As it is shown in section 3.4 we can write a generic equation (3.88) for the constitutive equation:

$$\overset{\triangledown}{\mathbf{c}} = \frac{f(\mathbf{c})}{\lambda}\mathscr{H}(\mathbf{c}) \, ,$$

Let us first consider PDPS. According to the derivation shown in section 4.3.2, it can be easily shown that if the tensor $\mathscr{H}(\mathbf{c})$ is a linear function of $\mathbf{c}$, say $\mathscr{H}(\mathbf{c}) = h_1\mathbf{c} + h_2\mathbf{I}$, then the updating of the conformation tensor by PDPS is

$$\mathbf{c}^{n+1} = \frac{f(\mathbf{c})h_2}{\frac{\lambda}{\Delta t} - f(\mathbf{c})h_1}\mathbf{I} + \frac{\frac{\lambda}{\Delta t}}{\frac{\lambda}{\Delta t} - f(\mathbf{c})h_1}\mathbf{F}\mathbf{c}^*\mathbf{F}^{\mathsf{T}} \, . \tag{4.107}$$

If the coefficients in the above equation is positive, then the positive definiteness of the conformation tensor is preserved. However, if $\mathscr{H}(\mathbf{c})$ is not a linear function of $\mathbf{c}$, e.g. in the Giesekus model, then PDPS is not applicable.

Fattal and Kupferman [43] have mentioned that LCR can be applied to large number of differential models as it is derived for a generic constitutive equation. Following the idea of LCR, Afonso et al. [4] have presented a generic kernel-conformation tensor transformation for a generic constitutive model. Based on the derivation shown in [4], we can rewrite the generic constitutive model (3.88) in the form of $\mathbf{s} = \log \mathbf{c}$ as

$$\frac{\partial \mathbf{s}}{\partial t} + \mathbf{u} \cdot \nabla \mathbf{s} = \Omega \mathbf{s} - \mathbf{s}\Omega + 2\mathbf{B} + \frac{1}{\lambda} f(e^{\mathbf{s}}) \mathbf{R} \mathscr{H}(\Lambda) \Lambda^{-1} \mathbf{R}^{\mathsf{T}} , \tag{4.108}$$

where Λ is diagonal with the corresponding three eigenvalues Λ_i of $\mathbf{c}$ and $\mathscr{H}(\Lambda)$ is calculated by substituting $\mathbf{c}$ by Λ in $\mathscr{H}(\mathbf{c})$. Many applications of LCR in the complex models can be found in the literature, e.g. Hulsen et al. [65] applied it to the Giesekus model and Afonso et al. [2] used it in the linear PTT model.

Balci et al. [11] have only shown SRCR with Oldroyd-B and FENE-P model. However, the approach can be extended to other models without difficulty. It has the following form for the generic model:

$$\frac{\partial \mathbf{A}}{\partial t} + \mathbf{u} \cdot \nabla \mathbf{A} = \mathbf{A} \nabla \mathbf{u} + \mathbf{M}\mathbf{A} + \frac{1}{2\lambda} f(\mathbf{A}^2) \mathbf{R} \mathscr{H}(\Lambda) \Lambda^{-\frac{1}{2}} \mathbf{R}^{\mathsf{T}} . \tag{4.109}$$

From the above discussion we conclude that BSD, LCR and SRCR can be well applied to the calculation of complex fluid models in complex flow domain, while PDPS is subject to restrictions when it comes to complex problems.

Summary of the comparison

According to the above discussion it is found:

- Based on the implemented standard approach for computing viscoelastic fluid flow, BSD and PDPS are more convenient to implement than LCR and SRCR. Comparing the last two approaches, SRCR is implemented with less effort.

- Considering the stability problem known as the high Weissenberg number problem, LCR and SRCR are more stable at high Weissenberg numbers. PDPS preserves the positive definiteness of the conformation tensor, while BSD can not. Yet, an attractive advantage of BSD is that it can well solve the stability problem caused by small viscosity ratios. In addition, because of its low implementation complexity this approach can be easily combined with the other stabilization approaches.

- By checking the accuracy, we found that LCR has a higher convergence rate than the other approaches. The reason is that it can well resolve the large gradient of the stress in the boundary layer. This feature makes it possible to pursue high accuracy with rather low computational cost. This has been checked by comparing the results computed with moderately fine mesh to the reference results in the benchmark test cases. On the contrary, PDPS has a low convergence rate due to the low order discretization scheme in this approach. Hence it is difficult to get an accurate solution in the boundary layer using PDPS.

- Having the second highest convergence rate, SRCR provides the advantage of shorter computation time compared to LCR. Considering its high accuracy, SRCR is an optimal choice in computation of flow at moderate Weissenberg numbers.

- Despite the fact that PDPS allows for fast computation (due to its explicit calculation of the conformation tensor), it should be developed further regarding several aspects including higher order accuracy, support for non-orthogonal meshes, adaptive time stepping.

Requirement	BSD	PDPS	LCR	SRCR
Low implementation complexity	√	√		
Stability at high Weissenberg number			√	√
Stability at low viscosity ratio	√			
Resolving stress boundary layer	√		√	√
Accuracy at moderate Weissenberg number			√	√
Accuracy at hight Weissenberg number			√	
Preserving positive definiteness of conformation tensor		√	√	√
Fast computation with coarse mesh		√		
Fast computation at high Weissenberg number				√
Applicability for complex flow domain	√		√	√
Applicability for complex constitutive models	√		√	√

Table 4.14.: Features and capabilities of the stabilization approaches

To give an overview of the different approaches their capability is listed in table 4.14, showing under which requirement the discussed approaches can be recommended.

According to table 4.14 we can see that LCR and SRCR have complementary advantages for high Weissenberg number flows, i.e. LCR has relatively high accuracy but low speed of computation, while SRCR has relatively low accuracy but high speed of computation. It is interesting to know whether it is possible to use their respective advantages for computation, e.g. switching the approaches during the computation when necessary. The reason for fast computation with SRCR is that due to its transformation of the conformation tensor transport equation, it does not require eigensystem calculation at every calculation step. However, this special transformation also makes it difficult to switch LCR and SRCR during the computation. Nevertheless, as mentioned in the previous sections, square-root transformation can also be performed with the generic kernel-conformation transformation [4]. This transformation makes the change of logarithm based or root based transformation more simple. Therefore, it is worth implementing the generic kernel-conformation transformation and evaluating various logarithm based and root based transformation approaches in the future work, in order to optimize the computation.

5 Numerical modeling of viscoelastic fluid-structure interaction

The viscoelastic fluid flow solver, which is presented in the previous chapter, is embedded into the fluid-structure interaction (FSI) framework. To simulate FSI problems, an implicit partitioned coupling algorithm is employed. Therefore, the solid part is solved by a separated solver. The finite-element method (FEM) solver FEAP [140], is employed for simulation of structural dynamics.

This chapter is organized as follows: In section 5.1 FEM for structural dynamics is introduced. Grid movement techniques and coupling algorithms are presented in section 5.2 and 5.3, respectively. In section 5.4 the mechanical mass-spring-dashpot model is employed for preliminary analysis of the phenomenon and the convergence property of the coupling algorithm for viscoelastic fluid-structure interaction (VFSI). Simulations for two test cases, the flow through a two-dimensional channel with a flexible wall and lid-driven cavity flow with deformable bottom, are discussed in section 5.5.

5.1 Finite-element method for structural dynamics

The essential basics of FEM for structural dynamics is given in this section. The presentation is based on the works [160, 159, 151, 140].

The momentum equation for the solid, as shown in (2.57), reads

$$\rho^s \ddot{\mathbf{d}} - \nabla_X \cdot (\mathbf{F}\,\mathbf{S}) = 0 \quad \text{in} \quad \Omega^s. \tag{5.1}$$

Boundary conditions for the displacement and traction are

$$\mathbf{d} = \bar{\mathbf{d}} \quad \text{on} \quad \partial\Omega^s_d \quad \text{and} \quad \mathbf{F}\,\mathbf{S}\,\mathbf{n}_X = \bar{\mathbf{t}} \quad \text{on} \quad \partial\Omega^s_t. \tag{5.2}$$

where $\bar{\mathbf{d}}$ and $\bar{\mathbf{t}}$ are the prescribed displacement and traction, respectively.

The starting point of FEM is to transform equation (5.1) into the weak form.

When an approximation $\mathbf{d}_h$ of the exact solution $\mathbf{d}$ is substituted into equation (5.1), a residual R is produced:

$$\rho^s \ddot{\mathbf{d}}_h - \nabla_X \cdot \big(\mathbf{F}(\mathbf{d}_h)\,\mathbf{S}(\mathbf{d}_h)\big) = R, \tag{5.3}$$

because the approximate solution is usually not equal to the exact solution. The residual R denotes the error not fulfilling the momentum balance by $\mathbf{d}_h$. This residual will be reduced to zero in a weak sense when we multiply the residual by a weighting function $\phi = \{\phi | \phi = 0 \text{ on } \partial\Omega^s_d\}$ and integrate the residual over the whole domain, i.e.

$$\int\limits_{\Omega^s} \rho^s \ddot{\mathbf{d}}_h \cdot \phi \,\mathrm{d}V - \int\limits_{\Omega^s} \nabla_X \cdot \big(\mathbf{F}(\mathbf{d}_h)\,\mathbf{S}(\mathbf{d}_h)\big) \cdot \phi \,\mathrm{d}V = 0,$$

which also holds for the exact solution $\mathbf{d}$

$$\int\limits_{\Omega^s} \rho^s \ddot{\mathbf{d}} \cdot \phi \,\mathrm{d}V - \int\limits_{\Omega^s} \nabla_X \cdot (\mathbf{F}\,\mathbf{S}) \cdot \phi \,\mathrm{d}V = 0, \tag{5.4}$$

This vector-valued function ϕ is usually called virtual displacement or test function. For the second term in (5.4), we make use of the partial integration, the divergence theorem and introduce the traction boundary condition. Consequently, equation (5.4) turns out to be

$$\int_{\Omega^s} \rho^s \ddot{\mathbf{d}} \cdot \phi \, \mathrm{d}V + \int_{\Omega^s} (\mathbf{FS}) : \nabla \phi \, \mathrm{d}V - \int_{\partial \Omega_t^s} \bar{\mathbf{t}} \cdot \phi \, \mathrm{d}A = 0. \tag{5.5}$$

In addition, we have the following equation

$$(\mathbf{FS}) : \nabla_X \phi = \mathbf{S} : (\mathbf{F}^\mathsf{T} \nabla_X \phi) = \mathbf{S} : \frac{1}{2} \left(\mathbf{F}^\mathsf{T} \nabla_X \phi + \nabla_X \phi^\mathsf{T} \mathbf{F} \right) = \mathbf{S} : \delta \mathbf{E}, \tag{5.6}$$

where the fact has been used that the scalar product of the symmetric tensor $\mathbf{S}$ with the antisymmetric part of the tensor $\mathbf{F}^\mathsf{T} \nabla_X \phi$ is zero. The term $\delta \mathbf{E} = \frac{1}{2} (\nabla_X \phi^\mathsf{T} \mathbf{F} + \mathbf{F}^\mathsf{T} \nabla_X \phi)$ denotes the variation of the Green-Lagrange strain tensor. Therefore, equation (5.5) is rewritten as

$$\underbrace{\int_{\Omega^s} \rho^s \ddot{\mathbf{d}} \cdot \phi \, \mathrm{d}V}_{\text{inertial term}} + \underbrace{\int_{\Omega^s} \delta \mathbf{E} : \mathbf{S} \, \mathrm{d}V}_{\text{stress divergence term}} - \underbrace{\int_{\partial \Omega_t^s} \bar{\mathbf{t}} \cdot \phi \, \mathrm{d}A}_{\text{loading term}} = 0. \tag{5.7}$$

With a finite element discretization, the problem domain is divided into finite elements by

$$\Omega^s \approx \Omega_h^s = \sum_{e=1}^{ne} \Omega_e^s, \tag{5.8}$$

where ne is the number of element, Ω_e^s is the domain of element e, Ω_h^s is the domain covered by all the elements. Figure 5.1 shows an example of the discretization of a two-dimensional problem. The solution within one finite element is approximated as

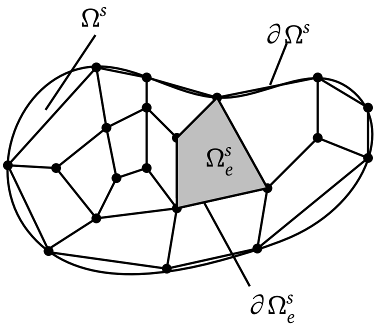

Figure 5.1.: An example of finite element discretization of a two-dimensional problem. In style of [151].

$$\mathbf{d}(\xi) = \sum_{I=1}^{n} N_I(\xi) \mathbf{d}_I, \tag{5.9}$$

where $\xi = (\xi_1, \xi_2, \xi_3)$ is the local coordinate for the element, n is the number of nodes in an element, $N_I(\xi)$ are the shape functions and $\mathbf{d}_I$ are the unknown nodal displacements. The isoparametric concept is employed, i.e. not only the variables but also the geometry are interpolated by the same shape function. Therefore, we have

$$\mathbf{X}(\xi) = \sum_{I=1}^{n} N_I(\xi) \mathbf{X}_I. \tag{5.10}$$

With this approximation the integrals in the weak form can be approximated as

$$\int_{\Omega^s} (\cdot)\,\mathrm{d}V \approx \int_{\Omega^s_h} (\cdot)\,\mathrm{d}V = \sum_{e=1}^{ne} \int_{\Omega^s_e} (\cdot)\,\mathrm{d}V. \tag{5.11}$$

In the weak form (5.7) there are three terms: inertial term, stress divergence term and loading term. They are calculated as follows:

- Inertial term $\int_{\Omega^s} \rho^s \ddot{\mathbf{d}} \cdot \phi \,\mathrm{d}V$

  The accelerations needed in the inertia term within an element Ω^s_e are approximated by

  $$\ddot{\mathbf{d}}_e(\mathbf{X}, t) = \sum_{K=1}^{n} N_K(\xi) \ddot{\mathbf{d}}_K.$$

  Thus the inertial term is computed as

  $$\int_{\Omega^s} \rho^s \ddot{\mathbf{d}} \cdot \phi \,\mathrm{d}V = \sum_{e=1}^{ne} \int_{\Omega_e} \phi^{\mathsf{T}} \rho^s \ddot{\mathbf{d}}_e \mathrm{d}V = \sum_{e=1}^{ne} \sum_{I=1}^{n} \sum_{K=1}^{n} \phi_I^{\mathsf{T}} \int_{\Omega^s_e} N_I \rho^s N_K \mathrm{d}V \ddot{\mathbf{d}}_K. \tag{5.12}$$

  Introducing the mass matrix

  $$\mathbf{M}_{IK} = \int_{\Omega^s_e} \rho^s N_I N_K \,\mathrm{d}V \mathbf{I} \tag{5.13}$$

  the inertial term has the form

  $$\int_{\Omega^s} \rho^s \ddot{\mathbf{d}} \cdot \phi \,\mathrm{d}V = \sum_{e=1}^{ne} \sum_{I=1}^{n} \sum_{K=1}^{n} \phi_I^{\mathsf{T}} M_{IK} \ddot{\mathbf{d}}_K = \phi^{\mathsf{T}} \mathbf{M} \ddot{\mathbf{d}}, \tag{5.14}$$

- Stress divergence term $\int_{\Omega^s} \delta \mathbf{E} : \mathbf{S} \,\mathrm{d}V$

  To formulate this term, the variation of the Green-Lagrange strain tensor must be discretized within an element Ω^s_e according to

  $$\delta \mathbf{E}_e = \frac{1}{2} \sum_{I=1}^{n} \left(\mathbf{F}_e^{\mathsf{T}} (\phi_I \nabla_X N_I) + (\nabla_X N_I \phi_I) \mathbf{F}_e \right). \tag{5.15}$$

  The finite element approximation of the deformation gradient is $\mathbf{F}_e = \sum\limits_{K=1}^{n} (\mathbf{x}_K \nabla_X N_K)$.

  For formulating the finite element form, it is convenient to derive the matrix formulation. Therefore, we go back to index notation which yields for (5.15)

  $$\delta E_{AB} = \frac{1}{2} \sum_{I=1}^{n} (F_{Ak} N_{I,B} + N_{I,A} F_{kB}) \phi_{kI},$$

  where the components of the deformation gradient are $F_{kB} = \sum\limits_{J=1}^{n} x_{kJ} N_{J,B}$.

  With the matrix formulation, vector form of the Green-Lagrange strain tensor within a element is written as

  $$\delta \hat{\mathbf{E}}_e = (\delta E_{11}, \delta E_{22}, \delta E_{33}, 2\delta E_{12}, 2\delta E_{23}, 2\delta E_{13})^{\mathsf{T}} = \sum_{I=1}^{n} \mathbf{B}_{LI} \phi_I,. \tag{5.16}$$

where the matrix $\mathbf{B}_{LI}$ has the components

$$\mathbf{B}_{LI} = \begin{pmatrix} F_{11}N_{I,1} & F_{21}N_{I,1} & F_{31}N_{I,1} \\ F_{12}N_{I,2} & F_{22}N_{I,2} & F_{32}N_{I,2} \\ F_{13}N_{I,3} & F_{23}N_{I,3} & F_{33}N_{I,3} \\ F_{11}N_{I,2}+F_{12}N_{I,1} & F_{21}N_{I,2}+F_{22}N_{I,1} & F_{31}N_{I,2}+F_{32}N_{I,1} \\ F_{12}N_{I,3}+F_{13}N_{I,2} & F_{22}N_{I,3}+F_{23}N_{I,2} & F_{32}N_{I,3}+F_{33}N_{I,2} \\ F_{11}N_{I,3}+F_{13}N_{I,1} & F_{21}N_{I,3}+F_{23}N_{I,1} & F_{31}N_{I,3}+F_{33}N_{I,1} \end{pmatrix}. \tag{5.17}$$

The index L denotes that the matrix $\mathbf{B}_{LI}$ depends linearly from the displacements, because the deformation gradient can be formulated as $\mathbf{F} = \mathbf{I} + \nabla \mathbf{d}$.

Due to the symmetry of the second Piola-Kirchhoff stress tensor, only six independent components are in the vector form which reads

$$\hat{\mathbf{S}}_e = (S_{11}, S_{22}, S_{33}, S_{12}, S_{23}, S_{13})^\mathsf{T}. \tag{5.18}$$

Then the term $\int_{\Omega^s} \delta\mathbf{E} : \mathbf{S}\,\mathrm{d}V$ is calculated as

$$\int_{\Omega^s} \delta\mathbf{E} : \mathbf{S}\,\mathrm{d}V = \sum_{e=1}^{ne} \int_{\Omega^s_e} \delta\hat{\mathbf{E}}_e^\mathsf{T} \hat{\mathbf{S}}_e \mathrm{d}V = \sum_{e=1}^{ne} \sum_{I=1}^{n} \phi_I^\mathsf{T} \int_{\Omega^s_e} \mathbf{B}_{LI}^\mathsf{T} \hat{\mathbf{S}}_e \mathrm{d}V. \tag{5.19}$$

Defining the vector

$$\mathbf{R}_I(\mathbf{d}_e) = \int_{\Omega^s_e} \mathbf{B}_{LI}^\mathsf{T} \hat{\mathbf{S}}_e \mathrm{d}V, \tag{5.20}$$

we obtain

$$\int_{\Omega^s} \delta\mathbf{E} : \mathbf{S}\,\mathrm{d}V = \sum_{e=1}^{ne} \sum_{I=1}^{n} \phi_I^\mathsf{T} \mathbf{R}_I(\mathbf{d}_e) = \phi^\mathsf{T} \mathbf{R}(\mathbf{d}). \tag{5.21}$$

Within this formulation, ϕ is the virtual displacement and $\mathbf{R}(\mathbf{d})$ denotes the force. Their inner product is the virtual internal work after assembly.

- Loading term $\int_{\Omega^s_t} \bar{\mathbf{t}} \cdot \phi \,\mathrm{d}A_t$

  Applying the finite element approximation for the virtual displacement, the discretization of the loading term in the weak form reads

$$\int_{\Omega^s_t} \bar{\mathbf{t}} \cdot \phi \mathrm{d}A_t = \sum_{r=1}^{n_r} \sum_{I=1}^{n} \phi_I^\mathsf{T} \int_{\Gamma_r} N_I \bar{\mathbf{t}} \mathrm{d}A_r, \tag{5.22}$$

  where n_r is the number of element boundaries where loads are applied and Γ_r is the surface of an element subjected to the traction $\bar{\mathbf{t}}$. We introduce a compact notation for the load term

$$\mathbf{P}_I = \int_{\Gamma_r} N_I \bar{\mathbf{t}} \mathrm{d}A_r. \tag{5.23}$$

  Hence the loading terms in the weak form is

$$\int_{\Omega^s_t} \bar{\mathbf{t}} \cdot \phi \mathrm{d}A_t = \sum_{e=1}^{nr} \sum_{I=1}^{n} \phi_I^\mathsf{T} \mathbf{P}_I = \phi^\mathsf{T} \mathbf{P}, \tag{5.24}$$

  where the vector $\mathbf{P}$ stands for the applied loads acting on the structure

Summarizing the above illustrated three terms (5.14), (5.21) and (5.24), equation (5.7) is rewritten as

$$\phi^{\mathsf{T}}(\mathbf{M}\ddot{\mathbf{d}} + \mathbf{R}(\mathbf{d}) - \mathbf{P}) = 0. \tag{5.25}$$

Because the virtual displacement ϕ is arbitrary, we have a non-linear system of ordinary differential equations

$$\mathbf{M}\ddot{\mathbf{d}} + \mathbf{R}(\mathbf{d}) - \mathbf{P} = 0. \tag{5.26}$$

To solve the transient problem, the Newmark algorithm [99] is used. It is based on the approximation for displacement and velocity for the time level $n+1$ by

$$\begin{aligned} \mathbf{d}^{n+1} &= \mathbf{d}^n + \Delta t \dot{\mathbf{d}}^n + \frac{1}{2}(1-\beta_2)\Delta t^2 \ddot{\mathbf{d}}^n + \frac{1}{2}\beta_2 \Delta t^2 \ddot{\mathbf{d}}^{n+1}, \\ \dot{\mathbf{d}}^{n+1} &= \dot{\mathbf{d}}^n + (1-\beta_1)\Delta t \ddot{\mathbf{d}}^n + \beta_1 \Delta t \ddot{\mathbf{d}}^{n+1}. \end{aligned} \tag{5.27}$$

The factor β_1 provides for weighting contribution of the influence of the initial and the final accelerations on the change of velocity. The factor β_2 gives a linearly varying weighting between initial and final accelerations on the change of displacement. Equations (5.27) and (5.26) allow the three unknowns $\mathbf{d}$, $\dot{\mathbf{d}}$ and $\ddot{\mathbf{d}}$ to be determined.

5.2 Grid movement methods

In the FSI problems the fluid domain varies due to the deformation or movement of the solid. Hence the mesh is modified in every iteration of the coupling algorithm. The method for grid movement in the fluid solver plays an important role in the FSI solution procedure, typically in the case where large structural deformation occurs. The basic requirements for grid movement technique are: no grid folding occurs and the mesh fits the moving boundaries exactly. Besides these two requirements, the grid movement technique has to fulfil that the distortions of control volumes are minimum, in order to decrease the risk of deterioration of discretization accuracy and the efficiency of the solver.

In the present fluid solver the grid movement proceeds in three steps, in which several methods are available: *1*) distortion of edges, where linear and cubic spline interpolation can be chosen; *2*) distortion of faces, where linear interpolation, transfinite interpolation (TFI) and elliptic method are optional; *3*) distortion of blocks, where linear interpolation, TFI and elliptic method can be employed. In the present work cubic spline interpolation is employed in the distortion of edges and TFI is used in the distortions of face and block due to their moderate accuracy computational cost. Therefore, these methods are briefly illustrated in the following sections. The elliptic method is the most robust but also the most expensive method compared to the other methods, cf. [158]. Detailed description of the elliptic method can be found in the works of Pironkov [117], Yigit et al. [158] and Thompson et al. [142].

We consider a block in three-dimension. The indices of the structured grid nodes are $i = 1, 2, \ldots, N_i$, $j = 1, 2, \ldots, N_j$ and $k = 1, 2, \ldots, N_k$. Every node in this block has coordinate $\mathbf{x}_{i,j,k}$ for every i, j, k.

Distortion of edges

Let us consider the edge along the i-direction with j and k being fixed to 1. The points on this edge have coordinates $\mathbf{x}_{i,1,1}$ with $i = 1, 2, \ldots, N_i$. The end points on the edge $\mathbf{x}_{1,1,1}$ and $\mathbf{x}_{N_i,1,1}$ have been distorted.

With linear interpolation the internal points are calculated by

$$\mathbf{x}_{i,1,1} = (\mathbf{x}_{N_i,1,1} - \mathbf{x}_{1,1,1})k_i + \mathbf{x}_{1,1,1}, \tag{5.28}$$

with

$$k_i = \frac{1}{\bar{l}} \sum_{m=2}^{i} ||\mathbf{x}_{m,1,1} - \mathbf{x}_{m-1,1,1}|| \quad \text{and} \quad \bar{l} = \sum_{i=2}^{N_i} ||\mathbf{x}_{i,1,1} - \mathbf{x}_{i-1,1,1}||. \tag{5.29}$$

By cubic spine method the internal points are distorted according to

$$\mathbf{x}_{i,1,1} = \mathbf{x}_{1,1,1} + \mathbf{a}_2 k_i^3 + \mathbf{a}_1 k_i^2 + \mathbf{T}_1 k_i \tag{5.30}$$

with

$$\begin{aligned} \mathbf{a_1} &= -3\mathbf{x}_{1,1,1} + 3\mathbf{x}_{N_i,1,1} - 2\mathbf{T}_1 + \mathbf{T}_2, \\ \mathbf{a_2} &= 2\mathbf{x}_{1,1,1} - 3\mathbf{x}_{N_i,1,1} + \mathbf{T}_1 - \mathbf{T}_2. \end{aligned} \tag{5.31}$$

The vectors $\mathbf{T}_1$ and $\mathbf{T}_2$ are two vectors at the end points. They are chosen, such that the angles between the edge and connected faces remain the same as in the initial geometry. The detailed calculation of these two vectors can be read in [117].

Distortion of faces and blocks

When linear interpolation is chosen in grid movement, equation (5.28) is used along one of the parameter directions. When TFI is chosen, we build a one-to-one mapping $\mathbf{x}(\xi,\eta,\zeta) = (x(\xi,\eta,\zeta), y(\xi,\eta,\zeta), z(\xi,\eta,\zeta))$ of the physical coordinate $\mathbf{x} = (x,y,z)$ to computational coordinates $\xi = (\xi,\eta,\zeta)$, where $0 \leqslant \xi \leqslant 1$, $0 \leqslant \eta \leqslant 1$ and $0 \leqslant \zeta \leqslant 1$, see figure 5.2.

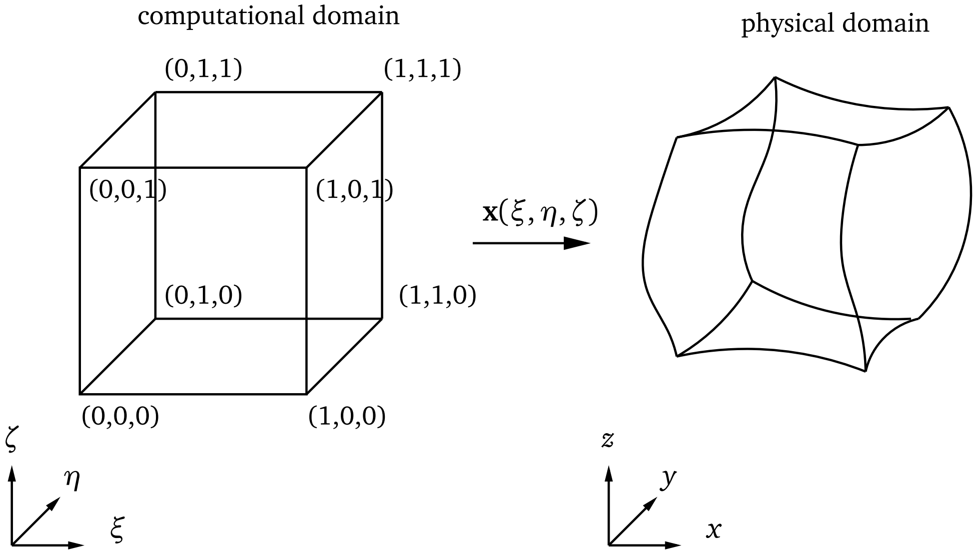

Figure 5.2.: Map between computational domain and physical domain for transfinite interpolation. In style of [142].

The internal grid points are computed from the given boundary point coordinates according to

$$\mathbf{x}(\xi,\eta,\zeta) = \mathbf{U} + \mathbf{V} + \mathbf{W} - \mathbf{UV} - \mathbf{VW} - \mathbf{UW} + \mathbf{UVW}, \tag{5.32}$$

where

$$\begin{aligned}
\mathbf{U} &= (1-\xi)\mathbf{x}(0,\eta,\zeta) + \xi\mathbf{x}(1,\eta,\zeta) \\
\mathbf{V} &= (1-\eta)\mathbf{x}(\xi,0,\zeta) + \eta\mathbf{x}(\xi,1,\zeta) \\
\mathbf{W} &= (1-\zeta)\mathbf{x}(\xi,\eta,0) + \zeta\mathbf{x}(\xi,\eta,1) \\
\mathbf{UV} &= (1-\xi)(1-\zeta)\mathbf{x}(0,\eta,0) + (1-\xi)\zeta\mathbf{x}(0,\eta,1) \\
&\quad + \xi(1-\xi)\mathbf{x}(1,\eta,0) + \mathbf{x}(1,0,\zeta) + \xi\eta\mathbf{x}(1,1,\zeta) \\
\mathbf{UV} &= (1-\xi)(1-\eta)\mathbf{x}(0,0,\zeta) + \xi\zeta\mathbf{x}(1,\eta,1) \\
&\quad + \xi(1-\eta)\mathbf{x}(1,\eta,0) + \mathbf{x}(1,0,\zeta) + \xi\eta\mathbf{x}(1,1,\zeta) \\
\mathbf{VW} &= (1-\eta)(1-\eta)\mathbf{x}(\xi,0,0) + (1-\eta)\zeta\mathbf{x}(\xi,1,0) \\
&\quad + \eta(1-\eta)\mathbf{x}(\xi,01,1) + \eta\zeta\mathbf{x}(\xi,1,1) \\
\mathbf{UVW} &= (1-\xi)(1-\eta)(1-\zeta)\mathbf{x}(0,0,0) \\
&\quad + (1-\xi)(1-\eta)\zeta\mathbf{x}(0,0,1) + (1-\xi)\eta(1-\zeta)\mathbf{x}(0,1,0) \\
&\quad + (1-\xi)\eta\zeta\mathbf{x}(1,0,1) + \xi\eta(1-\zeta)\mathbf{x}(1,1,0) \\
&\quad + \xi\eta\zeta\mathbf{x}(1,1,1)
\end{aligned} \tag{5.33}$$

5.3 Coupling algorithm

The coupling algorithm between the fluid and structural domains can be classified into two classes according to the way of data exchange: the monolithic and the partitioned approaches.

With monolithic approach the fluid and structure problems are solved simultaneously by a single solver at each time level, see figure 5.3. A single system of equations is created for the entire problem, taking the boundary conditions on the interface into account. This approach can achieve high accuracy and stability, but it also requires substantially more effort on development and maintenance of a specialized code and modification for different FSI problems.

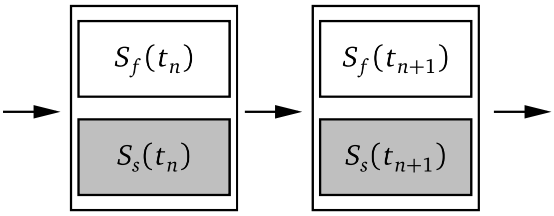

Figure 5.3.: Monolithic fluid-structure interaction coupling. S_s and S_f denote the solution of the structural and the fluid problem, respectively.

Contrarily, with partitioned approach the fluid and structural problems are solved separately with different solvers, see figure 5.4. The advantage of this approach is that both the fluid and structural problems can be solved with the efficient techniques in the individual domain. The developed program can be applied in a wide range of applications.

In order to satisfy the interface conditions, data exchange between the solvers is required. The approach is considered to be explicit, when the data is exchanged once per time step. In this coupling way, stability problem (e.g. the added mass problem) may arise, even though in each solver implicit method is used.

An improvement in the partitioned approach is done by exchanging the data more than once per time step, which forms the implicit partitioned approach. To compute the i-th iteration, the solution at time level t_n and the last approximation $S(t_{n+1})_f^{i-1}$ and $S(t_{n+1})_s^{i-1}$ are considered. Due to the outer iteration, stability is improved, even though the stability problem is not removed.

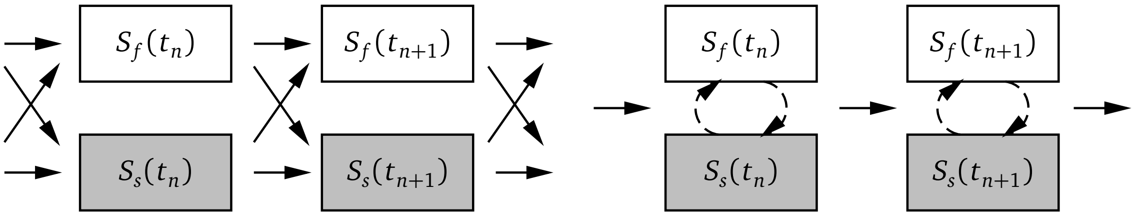

(a) Explicit (b) Implicit

Figure 5.4.: Partitioned fluid-structure interaction coupling

Implicit partitioned coupling algorithm for viscoelastic fluid-structure interaction

As mentioned in section 1.3, one of the difficulties in simulation of VFSI problems is the so-called High Weissenberg Number Problem (HWNP) in simulation of viscoelastic fluid flow. For simulation of VFSI problems, a partitioned coupling algorithm is attractive, because it is flexible to adapt modern techniques in the fluid and/or structural solver. Such an approach thus simplifies the work to integrate the techniques for HWNP into the VFSI simulation. Furthermore, with the implicit approach, the stability can be greatly improved. Therefore the implicit partitioned coupling algorithm is chosen in the present work for simulation of viscoelastic fluid-structure interaction problems.

The implicit partitioned coupling algorithm employed in the present work has been successfully applied to the Newtonian fluid-structure interaction (NFSI) problems, see [131]. The approach is also referred to as block Gauss-Seidel approach or Dirichlet-Neumann coupling approach, where the information flows as in a classical Gauss-Seidel procedure for the iterative solution, cf. [69]. In figure 5.5 a schematic view of the numerical algorithm is given.

After initialization the flow field is determined with the actual fluid mesh geometry. From this the forces exerted by the fluid on the interacting solid walls are computed. Compared to the NFSI problem, the polymer contribution of the extra stress should be additionally considered. These forces are passed to the structural solver as boundary conditions. The structural solver computes the deformations, with which the fluid mesh is then modified by one of the grid movement methods presented in section 5.2. After the modification of the fluid mesh the fluid solver computes the flow field again.

In the FSI simulation the momentum and constitutive equations for an Oldroyd-B fluid flow are transferred to the ALE form by

$$\rho^f \left.\frac{\partial \mathbf{u}}{\partial t}\right|_\chi + \rho^f(\mathbf{u}-\mathbf{u}^g)\cdot\nabla\mathbf{u} - 2\eta_s\nabla\cdot\mathbf{D} = -\nabla p + \nabla\cdot\tau_p, \tag{5.34}$$

$$\left.\frac{\partial \tau_p}{\partial t}\right|_\chi + (\mathbf{u}-\mathbf{u}^g)\cdot\nabla\tau_p = \tau_p\nabla\mathbf{u} + (\nabla\mathbf{u})^\mathsf{T}\tau_p + \frac{1}{\lambda}\left(2\eta_p\mathbf{D}-\tau_p\right), \tag{5.35}$$

where $\mathbf{u}^g$ is the velocity of the grid. When LCR is used, the transport equation for the log-conformation reads

$$\left.\frac{\partial \mathbf{s}}{\partial t}\right|_\chi + (\mathbf{u}-\mathbf{u}^g)\cdot\nabla\mathbf{s} = \Omega\mathbf{s} - \mathbf{s}\Omega + 2\mathbf{B} + \frac{1}{\lambda}(e^{-\mathbf{s}}-\mathbf{I})\,. \tag{5.36}$$

When SRCR is used, the transport equation for the square-root-conformation reads

$$\left.\frac{\partial \mathbf{A}}{\partial t}\right|_\chi + (\mathbf{u}-\mathbf{u}^g)\cdot\nabla\mathbf{A} = \mathbf{A}\nabla\mathbf{u} + \mathbf{M}\mathbf{A} + \frac{1}{2\lambda}(\mathbf{A}^{-\mathsf{T}}-\mathbf{A})\,. \tag{5.37}$$

The other equations for conformation tensor and their variant forms can be transform analogously.

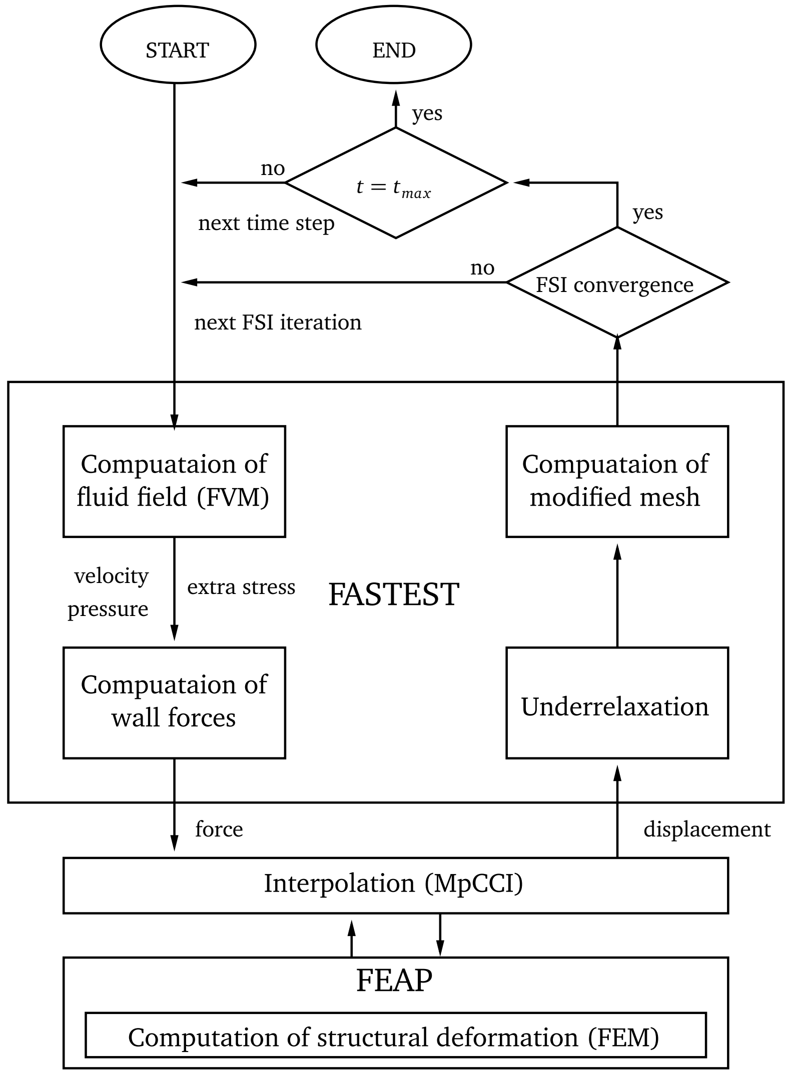

Figure 5.5.: Coupling algorithm for the viscoelastic fluid-structure interaction

For the ALE description, a discrete form of the space conservation law,

$$\frac{d}{dt}\int_{V_f} dV = \int_{S_f} \mathbf{u}^g \cdot \mathbf{n} dS, \tag{5.38}$$

is taken into account in order to compute the additional convective fluxes in equations for the blocks that are moving. This is done via the swept volumes δV_c of the control volume faces for which one has the relation, cf. [31],

$$\sum_c \frac{\delta V_c^n}{\Delta t_n} = \frac{V_f^n - V_f^{n-1}}{\Delta t_n} = \sum_c (\mathbf{u}^g \cdot \mathbf{n} S_f)_c^n, \tag{5.39}$$

where the summation index c runs over the faces of the control volume, the index n denotes the time level t_n and Δt_n is the time step size. In this way, interface displacements enter the fluid part in a manner which ensures strict mass conservation.

The fluid-structure interaction loop is repeated until the convergence criterion is reached which is defined by the change of the mean displacements as

$$\frac{1}{N}\sum_{k=1}^{N} \frac{||\mathbf{d}^{k,m-1} - \mathbf{d}^{k,m}||_\infty}{||\mathbf{d}^{k,m}||_\infty} < \varepsilon_{FSI}, \tag{5.40}$$

where m denotes the FSI iteration counter, N is the number of interface nodes, and $||\,.\,||_\infty$ denotes the maximum norm. The data transfer between the flow and solid solvers within the partitioned solution algorithm is performed via an interface, realized by the coupling software MpCCI [46]. which controls the data communication and also carries out the interpolations of the data from the fluid and solid grids. More details are given in [131]. For stabilizing the coupled solution algorithm, an under-relaxation is employed, where the actually computed displacements $\mathbf{d}^{act}$ are linearly weighted with the values $\mathbf{d}^{old}$ from the preceding iteration to give the new displacement $\mathbf{d}^{new}$ according to

$$\mathbf{d}^{new} = \alpha_{FSI}\mathbf{d}^{act} + (1 - \alpha_{FSI})\mathbf{d}^{old}, \tag{5.41}$$

where $0 < \alpha_{FSI} \leqslant 1$. The under-relaxation does not change the final converged result.

5.4 Mass-spring-dashpot model for the analysis of fluid-structure interaction problems

The mass-spring-dashpot model (MSD) is applied to qualitatively study the different dynamic behaviours of NFSI and VFSI and analyse the properties of the partitioned coupling algorithm for VFSI. The MSD model has been introduced by Joosten et al. [69] and employed in [70] and [33] for further investigation. In the following sections, the model for NFSI problems as proposed by Joosten et al [69] is first briefly reviewed, then the extension for VFSI problems is shown. Finally, the analysis of convergence property of the partitioned algorithm with the MSD is given.

Mass-spring-dashpot model for Newtonian fluids

For an NFSI problem the solid domain is represented by a point mass m^s and a spring with stiffness k, while the fluid domain is represented by a point mass m^f and a dashpot with viscosity c. The connection between these elements is displayed in figure 5.6.

The motions of the fluid and structure are described by

$$m^f \ddot{d}^f + c\dot{d}^f = -F^s, \tag{5.42}$$

$$m^s \ddot{d}^s + kd^s = F^f, \tag{5.43}$$

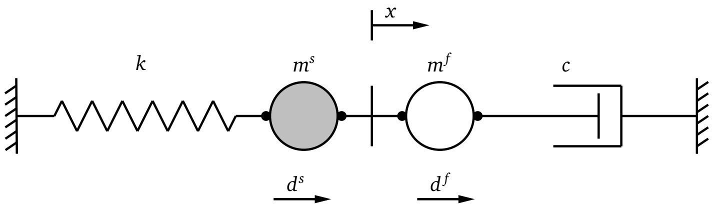

Figure 5.6.: Mass-spring-dashpot model for a Newtonian fluid-structure interaction problem

where $\ddot{d}$ and $\dot{d}$ represent the second and first time derivative of the displacement, respectively. F^f and F^s are the forces acting on the structure by the fluid and on the fluid by the structure, respectively. At the fluid-structure interface the condition of the continuity of velocities and the local balance of forces are imposed, i.e.

$$d^s = d^f = x \quad \text{and} \quad F^s - F^f = 0, \tag{5.44}$$

where x is the displacement of the interface. Summation of equations (5.42) and (5.43) yields a single equation for the motion of the interface according to

$$m\ddot{x} + c\dot{x} + kx = 0, \tag{5.45}$$

where $m = m^s + m^f$ is the total mass of the system. The solution of this system is well-known. The system does not oscillate if $c/2\sqrt{km} \leqslant 1$, else the system shows harmonic oscillation according to

$$x = Ae^{\frac{c}{2m}t}\cos(\omega_d t - \varphi), \tag{5.46}$$

where

$$\omega_d = \sqrt{\frac{k}{m} - \frac{c^2}{4m^2}} \tag{5.47}$$

is the frequency, φ is the phase shift and

$$A = \sqrt{x_0^2 + \frac{(\dot{x_0}^2 + \frac{c}{2m}x_0)^2}{\frac{k}{m} - \frac{c^2}{4m^2}}} \tag{5.48}$$

is the amplitude, where x_0 and $\dot{x_0}$ are the initial displacement and initial velocity, respectively.

Mass-spring-dashpot model for viscoelastic fluids

To model the viscoelastic fluid, the elastic effect of the fluid must be taken into account. One of the possibilities is to add a spring parallel to the dashpot, which constructs the so-called Kelvin-Voigt element as shown in [69]. But this element is suitable for solid but not for fluid, cf. [71], because this element is instantaneous viscous, since the deformation of the spring and dashpot occurs simultaneously. If a constant force is applied, the deformation will be damped by viscosity and the system will come to equilibrium as for an elastic solid. Therefore, in the fluid part the dashpot is substituted by the Jeffrey element as shown in figure 5.7, where a spring k^f is combined in parallel with the dashpot c_2 and then combined with the dashpot c_1 in series. The Jeffrey model is the mechanical prototype model in the derivation of the Oldroyd-B model with continuum approach, see chapter 3.

In the solid domain the force produced by the spring is

$$F_{ks} = k^s \Delta l_1, \tag{5.49}$$

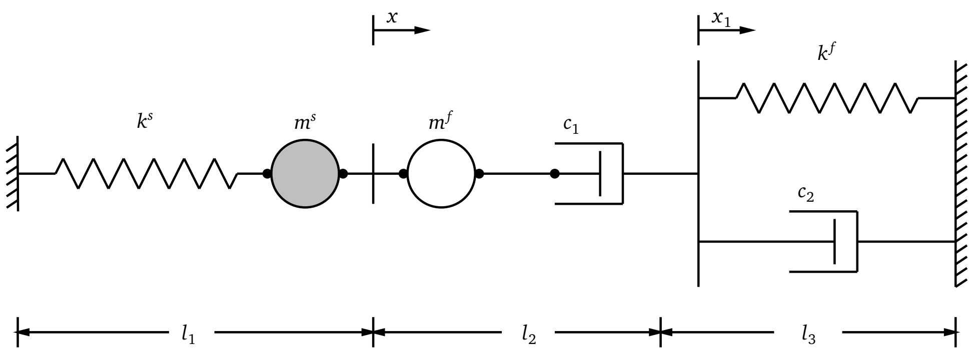

Figure 5.7.: Mass-spring-dashpot model for a viscoelastic fluid-structure interaction problem

where Δl_1 is the change of length of the spring. In this case $\Delta l_1 = x$.

If we rewrite equation (5.49) in terms of stress σ_1 and strain $\varepsilon_1 = \Delta l_1 / l_1$, we have

$$\sigma_1 = \frac{k^s L^s}{A^s} \varepsilon_1 = E^s \varepsilon_1, \tag{5.50}$$

where $L^s = l_1$ is the characteristic length of the solid, A^s is the cross-section area of the solid and

$$E^s = \frac{k^s L^s}{A^s} \tag{5.51}$$

is the modulus of elasticity.

The balance in the solid domain is

$$m^s \ddot{x} = -k^s x + F^f, \tag{5.52}$$

where F^f is the force from fluid exerted on the solid.

In the fluid domain, the force produced by the Jeffrey element is

$$F = c_1 \Delta\dot{l}_2 = c_1(\dot{x}_1 - \dot{x}). \tag{5.53}$$

From equation (5.53) we have

$$\dot{x}_1 = \dot{x} + F/c_1, \tag{5.54}$$

$$\ddot{x}_1 = \ddot{x} + \dot{F}/c_1. \tag{5.55}$$

On the other hand, taking time derivative on

$$F = k^f \Delta l_3 + c_2 \Delta\dot{l}_3 \tag{5.56}$$

yields

$$\dot{F} = k^f \Delta\dot{l}_3 + c_2 \Delta\ddot{l}_3 = k^f(-\dot{x}_1) + c_2(-\ddot{x}_1). \tag{5.57}$$

Inserting (5.54) and (5.55) into (5.57), after rearranging we have

$$\frac{c_1 + c_2}{k^f} \dot{F} + F = -c_1 \dot{x} - \frac{c_1 c_2}{k^f} \ddot{x}. \tag{5.58}$$

Written in terms of stress and strain, equation (5.58) has the form

$$\lambda \dot{\sigma} + \sigma = \eta \dot{\varepsilon} + \eta \lambda_2 \ddot{\varepsilon}, \tag{5.59}$$

where

$$\lambda = \frac{c_1 + c_2}{k^f} \tag{5.60}$$

is the fluid relaxation time,

$$\eta = \frac{c_1 L^f}{A^f} \tag{5.61}$$

is the total viscosity and

$$\lambda_2 = \frac{c_2}{k^f} \tag{5.62}$$

is the retardation time of the fluid and

$$\dot{\varepsilon} = \frac{\Delta \dot{l}_2 + \Delta \dot{l}_3}{l_2 + l_3} = -\frac{\dot{x}}{L^f}, \tag{5.63}$$

where $L^f = l_2 + l_3$ is the characteristic length of the fluid domain.

Relating to the solvent and polymer viscosities, we have the following relations:

$$\eta_s = \frac{c_1 c_2 L^f}{(c_1 + c_2) A^f} \quad \text{and} \quad \eta_p = \frac{c_1^2 L^f}{(c_1 + c_2) A^f}. \tag{5.64}$$

The viscosity ratio is

$$\beta = \frac{\eta_s}{\eta_s + \eta_p} = \frac{c_2}{c_1 + c_2}. \tag{5.65}$$

According to the balance of fluid body, we have

$$m^f \ddot{x} = F - F^s, \tag{5.66}$$

where F^s is the force from solid exerted on the fluid.

Since $F^f = F^s$, considering (5.52) and (5.66), we have

$$F = (m^f + m^s)\ddot{x} + k^s x. \tag{5.67}$$

and its time derivative

$$\dot{F} = (m^f + m^s)\dddot{x} + k^s \dot{x}. \tag{5.68}$$

Inserting (5.67) and (5.68) into (5.58) the differential equation for the whole system read as

$$\frac{(m^f + m^s)(c_1 + c_2)}{k^f}\dddot{x} + \left(m^f + m^s + \frac{c_1 c_2}{k^f}\right)\ddot{x} + \left(\frac{(c_1 + c_2)k^s}{k^f} + c_1\right)\dot{x} + k^s x = 0. \tag{5.69}$$

Equation (5.69) can be rewritten as

$$m\lambda \dddot{x} + \left(m + \frac{\beta \eta \lambda A^f}{L^f}\right)\ddot{x} + \left(\frac{E^s A^s \lambda}{L^s} + \frac{\eta A^f}{L^f}\right)\dot{x} + \frac{E^s A^s}{L^s} x = 0, \tag{5.70}$$

where $m = m^s + m^f$ is the total mass of the system. To make equation (5.70) dimensionless, we let $x = x_o x^*$ and $t = \lambda t^*$. Omitting the superscript $*$ in the following, the dimensionless form of equation (5.70) reads

$$\dddot{x} + \left(1 + \beta \frac{\eta \lambda A^f}{L^f m}\right)\ddot{x} + \left(\frac{E^s A^s \lambda^2}{L^s m} + \frac{\eta A^f \lambda}{L^f m}\right)\dot{x} + \frac{E^s A^s \lambda^2}{L^s m} x = 0. \tag{5.71}$$

We define the dimensionless elasticity number as

$$E = \frac{\mathrm{Wi}}{\mathrm{Re}} = \frac{\lambda U/L^f}{\rho^f U L^f/\eta} = \frac{\lambda\eta}{\rho^f (L^f)^2} = \frac{\lambda\eta A^f}{\rho^f L^f A^f L^f} = \frac{\lambda\eta A^f}{m^f L^f}. \tag{5.72}$$

Furthermore, we introduce the stiffness ratio of solid to fluid

$$K = \frac{k^s}{k^f} = (1-\beta)\frac{E^s A^s \lambda L^f}{\eta A^f L^s}, \tag{5.73}$$

and the mass ratio of the fluid mass to the total mass

$$\alpha_m = \frac{m^f}{m}. \tag{5.74}$$

Finally, the dimensionless MSD model reads

$$\dddot{x} + (1+\beta E\alpha_m)\ddot{x} + (\frac{K}{1-\beta}+1)E\alpha_m\dot{x} + \frac{K}{1-\beta}E\alpha_m x = 0. \tag{5.75}$$

Solution of the mass-spring-dashpot model for viscoelastic fluid-structure interaction

We are now looking for the solution of equation (5.75). For simplicity we rewrite equation (5.75) as

$$\dddot{x} + a\ddot{x} + b\dot{x} + cx = 0 \tag{5.76}$$

with

$$a = 1+\beta E\alpha_m, \quad b = (\frac{K}{1-\beta}+1)E\alpha_m \quad \text{and} \quad c = \frac{K}{1-\beta}E\alpha_m. \tag{5.77}$$

The characteristic equation of (5.76) is

$$r^3 + ar^2 + br + c = 0. \tag{5.78}$$

In order to express the solution of the above equation in a clear form we let

$$q = c - \frac{1}{3}ab + \frac{2}{27}a^3 \tag{5.79}$$

and

$$\Delta = c^2 + \frac{4}{27}b^3 - \frac{2}{3}abc - \frac{1}{27}a^2b^2 + \frac{4}{27}a^3c. \tag{5.80}$$

The type of solution of equation (5.78) depends on the discriminant Δ. The coefficients a, b and c are positive by the physics. The relation between Δ and the parameters a, b and c is shown in figure 5.8, where we can see a region of $\Delta \leqslant 0$. According to the cases $\Delta < 0$, $\Delta = 0$ and $\Delta > 0$, the solution of equation (5.76) can be divided into three types

- Solution Type 1 (ST1)

  If $\Delta < 0$, equation (5.78) has three different real roots

$$r_{k+1} = \sqrt[6]{16(q^2-\Delta)}\cos\frac{\arccos\frac{-q}{\sqrt{q^2-\Delta}} + 2k\pi}{3} - \frac{a}{3} \quad , \quad k = 0,1,2 \tag{5.81}$$

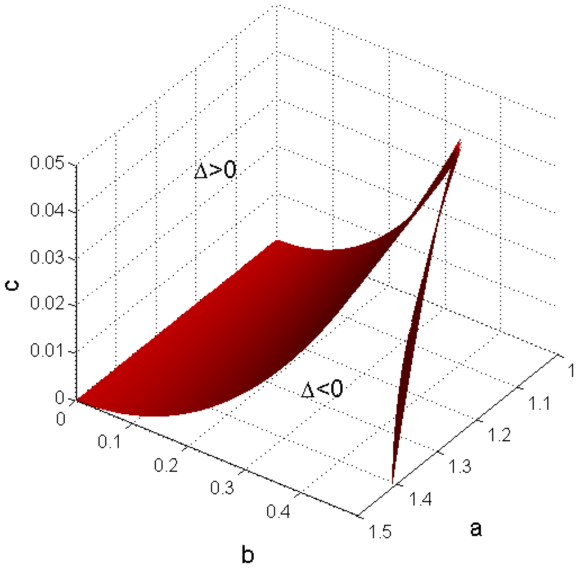

Figure 5.8.: a, b and c fields where $\Delta > 0$ and $\Delta \leqslant 0$. The surface in red is $\Delta = 0$.

and all these three roots are negative. The proof of negativity of all these roots is described in the following: Denoting r_1, r_2 and r_3 the three roots of the characteristic equation

$$r^3 + ar^2 + br + c = 0, \tag{5.82}$$

the characteristic equation can be rewritten as

$$(r - r_1)(r - r_2)(r - r_3) = r^3 - (r_1 + r_2 + r_3)r^2 + (r_1r_2 + r_1r_3 + r_2r_3)r - r_1r_2r_3 = 0 \tag{5.83}$$

Comparing the coefficients of equations (5.82) and (5.83), we have

$$-(r_1 + r_2 + r_3) = a > 0 \tag{5.84}$$

$$r_1r_2 + r_1r_3 + r_2r_3 = b > 0 \tag{5.85}$$

$$-r_1r_2r_3 = c > 0 \tag{5.86}$$

Without loss of generality we have

case 1 if $r_1, r_2, r_3 > 0$, condition (5.84) is violated.

case 2 if $r_1 > 0$ and $r_2, r_3 < 0$ then $r_1r_2r_3 > 0$ and (5.86) is violated.

case 3 if $r_1, r_2 > 0$ and $r_3 < 0$, knowing from (5.84) $r_3 = -a - r_1 - r_2$ and substitution into (5.85) we get

$$r_1r_2 + r_2(-a - r_1 - r_2) + r_1(-a - r_1 - r_2) = -ar_2 - r_2^2 - ar_1 - r_1^2 - r_1r_2 < 0, \tag{5.87}$$

hence condition (5.85) is violated.

Therefore, all the roots must be negative.

The solution of equation (5.76) for this case is

$$x(t) = A_1e^{r_1t} + A_2e^{r_2t} + A_3e^{r_3t} \tag{5.88}$$

where the coefficients A_1, A_2 and A_3 depend on the initial conditions. This solution represents a fully exponential damping.

- Solution Type 2 (ST2)

  If $\Delta = 0$, equation (5.78) has three real roots, where one has multiplicity two, i.e.

$$r_1 = -2\sqrt[3]{\frac{q}{2}} - \frac{a}{3} \quad , \quad r_2 = r_3 = \sqrt[3]{\frac{q}{2}} - \frac{a}{3}. \tag{5.89}$$

  The solution for equation (5.76) for this case is

$$x(t) = A_1 e^{r_1 t} + (A_2 + A_3 t) e^{r_2 t}. \tag{5.90}$$

- Solution Type 3 (ST3)

  If $\Delta > 0$, equation (5.78) has one real root $r_1 = -g$ and two complex conjugate roots $r_2 = -\alpha + i\omega$ and $r_3 = -\alpha - i\omega$ with non-vanishing imaging parts, where g, α and ω are real positive and have the following forms:

$$g = -\sqrt[3]{\frac{-q-\sqrt{\Delta}}{2}} - \sqrt[3]{\frac{-q+\sqrt{\Delta}}{2}} + \frac{a}{3}, \tag{5.91}$$

$$\alpha = \frac{1}{2}\left(\sqrt[3]{\frac{-q-\sqrt{\Delta}}{2}} + \sqrt[3]{\frac{-q+\sqrt{\Delta}}{2}}\right) + \frac{a}{3}, \tag{5.92}$$

  and

$$\omega = \frac{\sqrt{3}}{2}\left(\sqrt[3]{\frac{-q-\sqrt{\Delta}}{2}} - \sqrt[3]{\frac{-q+\sqrt{\Delta}}{2}}\right). \tag{5.93}$$

  The solution of equation (5.76) for this case is

$$x = e^{-\alpha t}(A_1 \cos(\omega t) + A_2 \sin(\omega t)) + A_3 e^{-gt}, \tag{5.94}$$

  or can be written as

$$x = C_1 e^{-\alpha t} \sin(\omega t + \varphi) + C_2 e^{-gt} \tag{5.95}$$

  with $C_1 = \sqrt{A_1^2 + A_2^2}$, $\varphi = \arctan\frac{A_2}{A_1}$ and $C_2 = A_3$. The parameters C_1, C_2 and φ are determined by the initial conditions.

  Equation (5.95) consists of two parts: one is a periodic part with exponentially damped amplitude, the other is a decaying exponential without oscillation. If $\alpha > g$ the periodic term damps out more rapidly than the pure exponential term. We denote this type of solution as ST3EXP. An example of ST3EXP is shown in figure 5.9 (a). In contrast, if $\alpha < g$, the pure exponential term vanishes more rapidly than the periodic term. We denote this type of solution as ST3PER. An example of ST3PER is shown in figure 5.9 (b).

To investigate the influence of the elasticity number E on the solution, a parameter study is here performed. We investigate the influence of E on discriminant Δ and the parameters α, g and ω in equation (5.95). As default values we set $K = 1.0$, $\alpha_m = 0.5$ and $\beta = 0.5$. When one of the parameters is changed, the other two are set to the default values. The study is done as follows:

i Influence on Δ

  The discriminant Δ determines the type of solution. Figure 5.10 shows Δ as a function of E for different K, α_m and β. As the elasticity number increases, the value of discriminant, which is positive, first increases then decreases and falls below zero, i.e. the solution type is first ST3 and remains for a range of E then changes to ST1.

  We denote the value of $E > 0$ at which $\Delta = 0$ as the critical value E_{cr}. From figure 5.10 we see *a)* as the stiffness ratio K increases, the critical elasticity number E_{cr} increases; *b)* as the mass ratio α_m increases, the critical elasticity number E_{cr} decreases; *c)* as the viscosity ratio β increases, the critical elasticity number E_{cr} first decreases until $\beta = 0.7$ then increases.

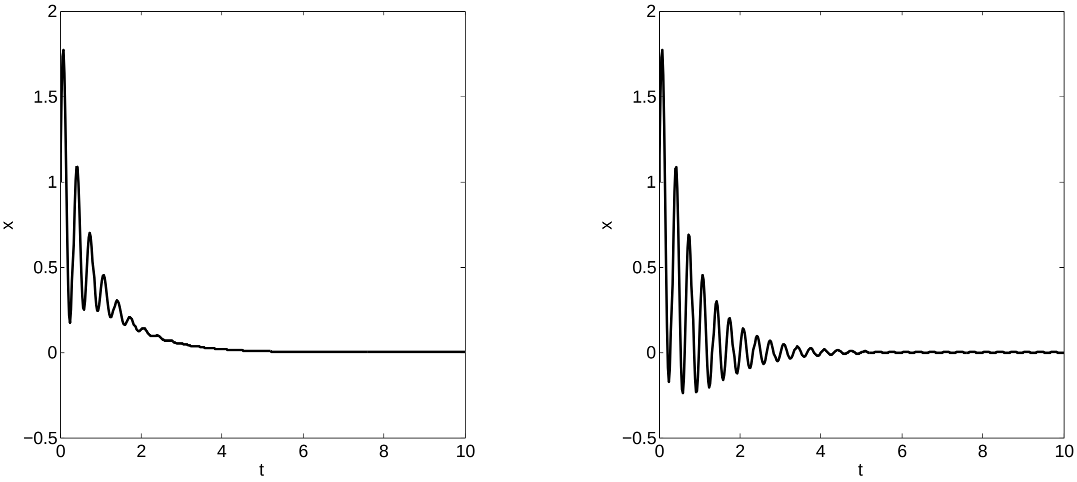

(a) ST3EXP $\alpha > g$ (b) ST3PER $\alpha < g$

Figure 5.9.: Example of solution type ST3EXP and ST3PER

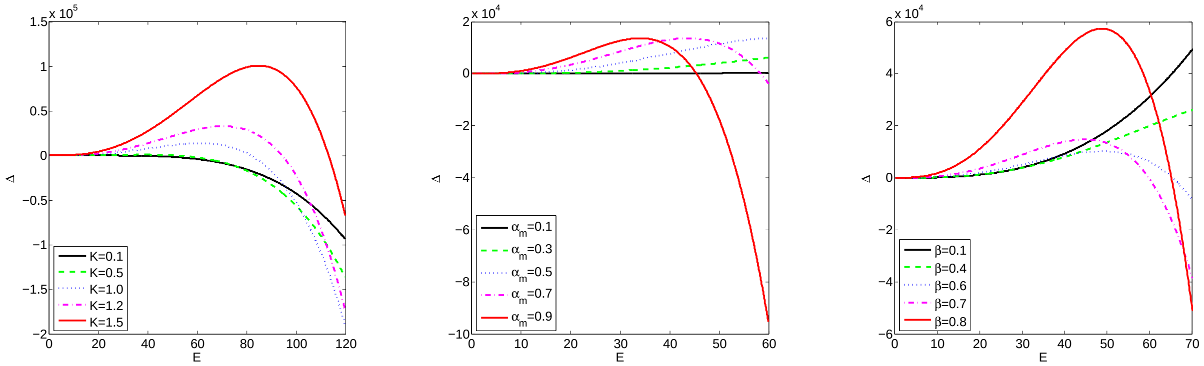

(a) (b) (c)

Figure 5.10.: Influence of E on Δ

ii Influence on α

The value of α determines how fast the periodic term vanishes in the solution of ST3. Figure 5.11 shows α as a function of E for different K, α_m and β. As the elasticity number increases, the value of α also increases, i.e. the periodic term vanishes faster for larger elasticity number.

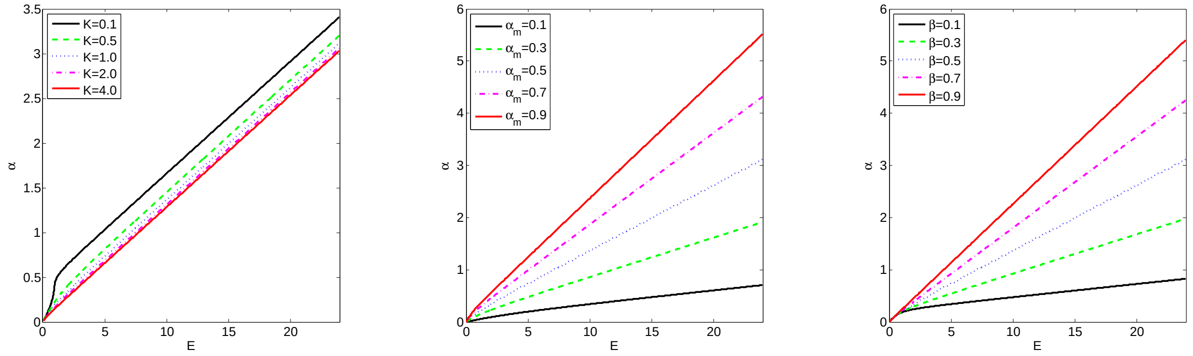

(a) (b) (c)

Figure 5.11.: Influence of E on α

iii Influence on g

The value of g determines how fast the exponential term vanishes in the solution of ST3. Figure 5.12 shows g as a function of E for different K, α_m and β. As the elasticity number increases, the value of g decrease, i.e. the exponential term vanishes more slowly for larger elasticity number. Since α increases and g decrease for increasing E, the solution type can be changed form ST3PER to ST3EXP, if the initially the solution type is ST3PER.

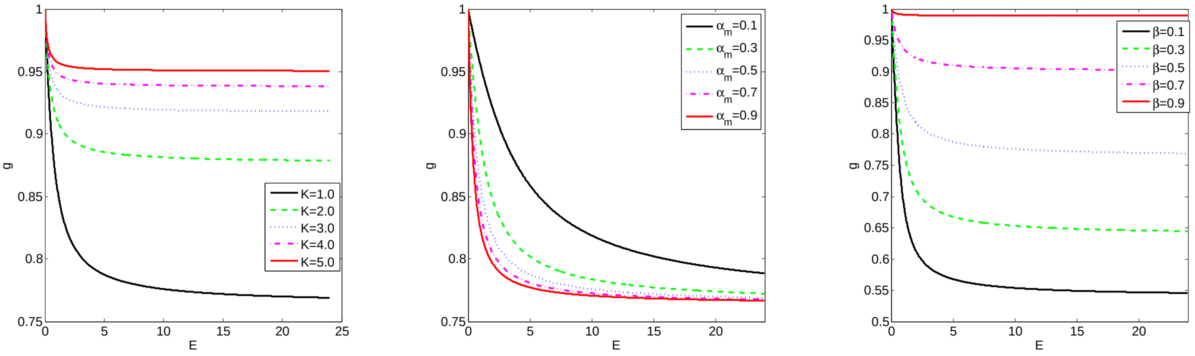

(a) (b) (c)

Figure 5.12.: Influence of E on g

iv Influence on ω

The value of ω determines the frequency of the periodic term in the solution of ST3. Figure 5.13 shows ω as a function of E for different K, α_m and β. In Figure 5.13 (b) and (c) the stiffness ratio is chosen as $K = 0.5$. As the elasticity number increases, the frequency first increases then decreases. The peak of ω is different for different value of K, α_m and β.

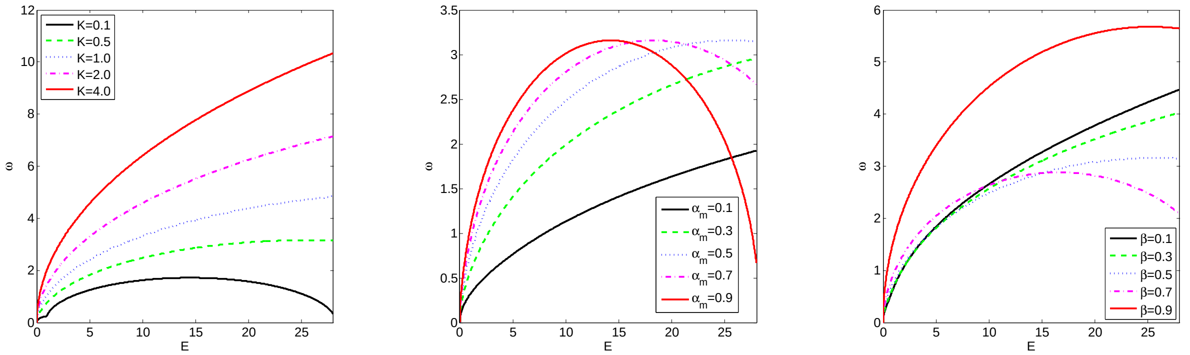

(a) (b) (c)

Figure 5.13.: Influence of E on ω

Based on the above discussion, we see that the dynamic behaviour of a VFSI problem is more complicated than the one of an NFSI problem. In addition, the proposed MSD model provides an opportunity to qualitatively analyse the dynamic behaviour of the VFSI problem for different physical parameters. This qualitative analysis of the dynamic behaviour by means of the MSD model together with the simulation results will be shown in section 5.5.

Convergence property of the partitioned algorithm

Besides for analysis of the dynamic behaviour, it is also convenient to use the MSD model to analyse the convergence properties of the coupling algorithm, as it is shown in [69]. Following the approaches in [69] we now use the above model to investigate the convergence properties of our proposed coupling algorithm for VFSI problems.

Equations for the separated corresponding fluid and solid domain are considered. Given the solution at time level t_n, the block Gauss-Seidel procedure for the MSD model can be described by the following algorithm:

```
input  : the solution at time level $t_n$
output: the solution at time level $t_{n+1}$
estimate the structural displacement $x^s_{n+1}$;
repeat
    set $x^f_{n+1} = x^s_{n+1}$;
    solve the system in the fluid domain for $F^f$;
    set $F^s = F^f$;
    solve the system in the structural domain for $x^s_{n+1}$;
until $\frac{||x^s_{n+1} - x^f_{n+1}||}{||x^f_{n+1}||} < \varepsilon$;
```

Algorithm 1: Block Gauss-Seidel algorithm for the mass-spring-dashpot model

Owing to the linearity of the problem, the expression of the solution has the following form

$$x^{s,i+1}_{n+1} = Ax^{s,i}_{n+1} + \mathbf{b} \cdot \mathbf{x}_n, \tag{5.96}$$

where the superscript i and $i+1$ denote the Gauss-Seidel procedure iteration counter and the scalar coefficient A is known as the convergence factor of the iteration. Scalar A and vector $\mathbf{b}$ depend exclusively on the time step size and the problem parameters. The vector $\mathbf{x}_n$ contains all solution variables of the previous time level t_n. For convergence of a system which can be described by equation (5.96), only the value of A is important. Convergence is obtained if and only if $|A| < 1$.

If we apply the backward Euler scheme for time integration, we have

$$\dot{x}_{n+1} = \frac{1}{\Delta t}(x_{n+1} - x_n), \tag{5.97}$$

$$\ddot{x}_{n+1} = \frac{1}{\Delta t^2}(x_{n+1} - x_n) - \frac{1}{\Delta t}\dot{x}_n. \tag{5.98}$$

Applying equation (5.97) and equation (5.98) to all solution variables, the governing equation can be formulated at the time level t_{n+1} with the displacements and forces at t_{n+1} as the only unknowns.

Following the procedure previously shown we can compute the coefficient A for the MSD model for VFSI having the form

$$A = -\frac{m^f(c_1 + c_2 + k^f\Delta t) + (c_1c_2 + c_1k^f\Delta t)\Delta t}{(c_1 + c_2 + k^f\Delta t)(m^s + k^s\Delta t^2)}. \tag{5.99}$$

The coefficient A depends on all the physical parameters in the MSD model including the fluid stiffness k^f. Since small time steps are needed to ensure a certain accuracy of the simulations, we determine the limit of A as Δt tends to zero. Then we obtain the simple expression

$$\lim_{\Delta t \to 0} A = -\frac{m^f}{m^s}. \tag{5.100}$$

Therefore, we see that for extreme small time steps the block Gauss-Seidel scheme does not converge if $\frac{m^f}{m^s} > 1$. This is the 'added mass effect' as encountered in NFSI problems. The larger $\frac{m^f}{m^s}$ is, the slower the algorithm converges. If under-relaxation α_{FSI} is employed, equation (5.96) is transformed to

$$x^{s,i+1}_{n+1} = (1 - \alpha_{FSI})(Ax^{s,i}_{n+1} + \mathbf{b} \cdot \mathbf{x}_n) + \alpha_{FSI}x^{s,i}_{n+1} \tag{5.101}$$

$$= ((1 - \alpha_{FSI})A + \alpha_{FSI})x^{s,i}_{n+1} + (1 - \alpha_{FSI})\mathbf{b} \cdot \mathbf{x}_n. \tag{5.102}$$

The criterion for convergence now reads

$$|(1 - \alpha_{FSI})A + \alpha_{FSI}| < 1. \tag{5.103}$$

For a fixed coefficient $A \neq 1$, there is an optimal value of α_{FSI} such that $(1 - \alpha_{FSI})A + \alpha_{FSI} = 0$.

The above analysis shows that applying the implicit partitioned coupling algorithm for a VFSI problem we are facing the same problem as for an NFSI problem, i.e. as Δt is decreased, the convergence behaviour often deteriorates, the block Gauss-Seidel scheme without under-relaxation is convergent only if $\frac{m^f}{m^s} < 1$, i.e. the fluid mass is less than the solid mass. In addition, we can see that the convergence behaviour depends also on the fluid stiffness k^f, which is directly related to the fluid relaxation time.

5.5 Computation of prototype problems for viscoelastic fluid-structure interaction

In this section we investigate the VFSI problem via simulation applying the coupling algorithm proposed in section 5.3. The first test case “flow through a two-dimensional channel with a flexible wall” is employed to study the steady problem, whereas the second case “lid-driven cavity with flexible bottom” is employed to study the time-dependent problem. The investigation of the partition coupling algorithm for VFSI is done within the latter test case. For all the simulations, the LCR is employed in the viscoelastic fluid flow solver. The results presented in this section is based on our paper [22].

5.5.1 Flow through a two-dimensional channel with a flexible wall

This test case is regarded as a simplified version of the flow in an elastic tube, which occurs naturally in several physiological applications. A number of numerical works have been performed for this test case for Newtonian fluids, e.g. [93, 91, 92], as well as for shear-dependent non-Newtonian fluids, e.g. [90] and [89]. Recently, Chakraborty et al. [19, 20] have investigated this test case considering the fluids as viscoelastic fluids modeled by Oldroyd-B, FENE-P and Owens models. The geometry parameters are set according to the dimensionless parameters proposed in [18] as shown in figure 5.14. The model consists of a steady flow in a channel in which a part of the upper wall is replaced by an elastic plate. The rigid channel has width D. An external pressure p_{ext} is exerted on the elastic plate. The upstream of the rigid channel has length $L_u = 5D$ and downstream has length $L_d = 30D$. Steady Poiseuille flow with average velocity $\bar{u}_{in}$ is assumed at the entrance. We first reproduce the results for an NFSI problem, then change the fluid relaxation time to simulate VFSI problems.

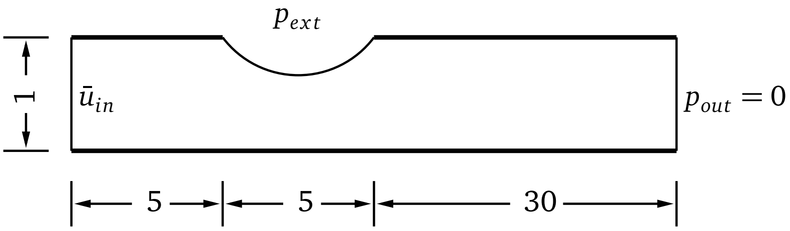

Figure 5.14.: Flow through a two-dimensional channel with a flexible wall

Computation for an NFSI problem

Luo et al. [92] have carried out extensive studies for this test case considering the fluid to be Newtonian and the flexible wall to be a plane-strained elastic beam that obeys Hooke's law. For the purpose of comparison, the dimensions of the channel and other parameters are chosen to be identical to the ones used in their work: $\bar{u}_{in} = 0.03\,\mathrm{m/s}$, $D = 0.01\,\mathrm{m}$, $\rho^f = 1000\,\mathrm{kg/m^3}$ and $\eta = 0.001\,\mathrm{Pa \cdot s}$. These parameters correspond to $\mathrm{Re} = 300$. The wall has Young's modulus $E^s = 35.9\,\mathrm{kPa}$ and Poison ratio $\nu^s = 0.45$. As external pressure $p_{ext} = 1.755\,\mathrm{Pa}$ and as outlet pressure $p_{out} = 0$ are employed. The flexible wall thickness is varied in the range from $0.01D$ to $0.1D$. The trilinear 8 nodes elements with Saint Venant-Kirchhoff material law are employed in the structural solver. We have done a mesh refinement study for the case $b = 0.01D$ (the smallest wall thickness), for selecting the mesh in the fluid solver for further simulations. The results are shown in Figure 5.15, in which the deformations of the upper plate for different meshes are compared. The employed meshes are 100 × 20 for M1, 200 × 40 for M2, 400 × 80 for M3, and 800 × 160 for M4. It is shown that mesh M3 is fine enough to produce accurate results. The results are calculated for zero beam pre-tension. The computed plate deformation for different plate thickness are shown in Figure 5.16 together with the results from [92]. Most of our results agree to the ones from [92] except for the smallest plate thickness $b = 0.01D$ and $b = 0.02D$ which depart a little. This is expected, since the beam obeys Hooke's law in [92], while the non-linear Saint Venant-Kirchhoff constitutive law is employed in our simulation.

Computation for a VFSI problem

The same parameters are chosen as in the NFSI simulation, except that the fluid relaxation time is larger than zero. The relaxation times we have chosen for the simulation are 0.05 s, 0.1 s and 0.2 s. The corresponding Weissenberg numbers are 0.15, 0.3 and 0.6, respectively. The viscosity ratio of solvent to total viscosity is $\beta = 0.5$, i.e. $\eta_s = \eta_p = 0.0005\,\mathrm{Pa \cdot s}$. The plate thickness is $b = 0.01D$. Figure 5.17 shows the plate deformations for different Weissenberg numbers. We see that the displacement of the bottom part of the plate are different for different fluid relaxation times (Weissenberg numbers). As the Weissenberg number increases, the lowest point of the wall moves upwards gradually.

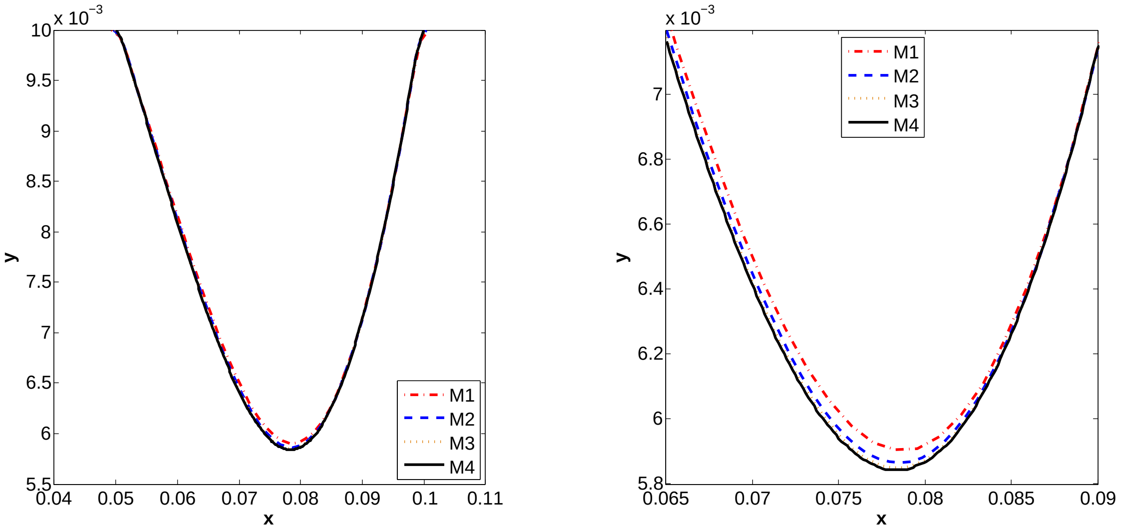

(a) Deformation of the whole plate

(b) A zoom in at the bottom part

Figure 5.15.: Plate deformation for plate thickness $b = 0.01D$ computed with different meshes

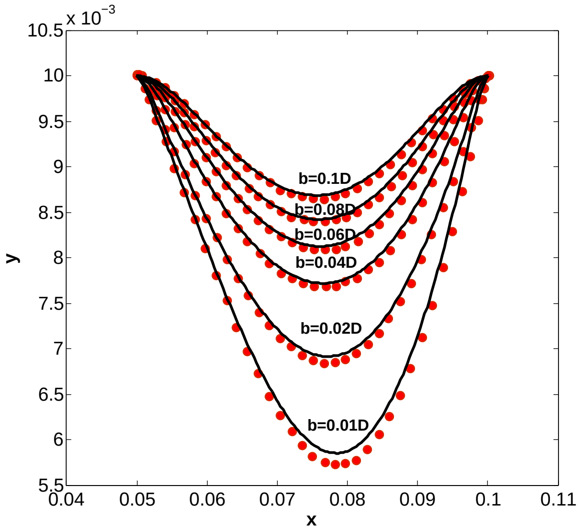

Figure 5.16.: Plate deformation for different plate thickness. Shape obtained from [92] (red points) and present solver (solid line)

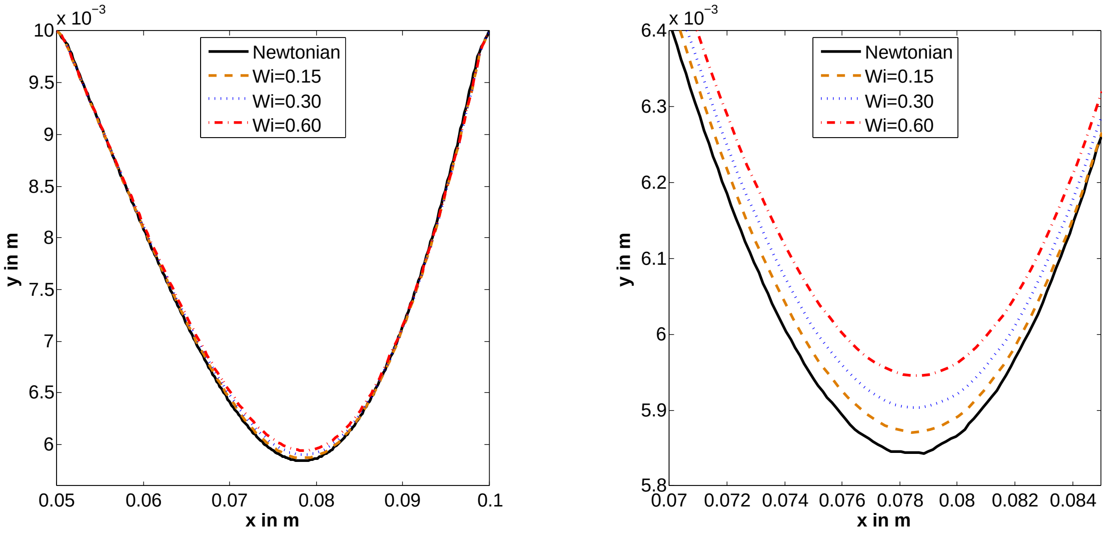

(a) Deformation of the whole plate (b) A zoom in at the bottom part

Figure 5.17.: Plate deformation for plate thickness $b = 0.01D$ for Oldroyd-B fluids with different Weissenberg numbers

A mesh convergence study is performed for the results of these three Weissenberg numbers. The results are shown in table 5.1. Three characteristic quantities are chosen for analysis:

- the maximum vertical displacement of the elastic plate;
- the average kinetic energy $\frac{1}{V}\int_V \frac{1}{2}(u^2+v^2)\,\mathrm{d}V$ in the fluid domain;
- the average elastic energy $\frac{1}{V}\int_V (c_{11}+c_{22})\,\mathrm{d}V$ in the fluid domain,

where u_1 and u_2 are the components of the velocity vector $\mathbf{u}$, c_{11} and c_{22} are the diagonal components of the conformation tensor $\mathbf{c}$. The rate of convergence is evaluated from

$$R = \log\left(\frac{\phi^{M1}-\phi^{M2}}{\phi^{M2}-\phi^{M3}}\right)/\log 2, \tag{5.104}$$

where ϕ is one of the above mentioned characteristic quantities and the superscripts M1, M2 and M3 indicate the value of ϕ for the corresponding successively refined mesh.

For larger Weissenberg numbers, i.e. Wi > 0.6, the solver can still run stably but the simulation results do not show mesh converge any more. Nevertheless, with LCR, we are able to obtain convergent result with larger Weissenberg numbers than the one (Wi $= 0.15$) that we obtain without applying LCR.

Next we study the reason for the change of plate deformation in the cases of different Weissenberg numbers. For this purpose, we investigate the stress acting on the plate. This stress can be separated to normal and tangential components on the plate surface. We first study the normal stress and then the tangential stress.

The normal stress consists of the pressure p and the solvent contribution $\tau_{1,n}$ and polymer contribution $\tau_{2,n}$ of the normal extra stress. These components along the plate are plotted in figure 5.18 for the case of Wi $= 0.60$. We can clearly see that the only contribution to the normal forces which results in the wall moving upwards is the pressure, because the solvent and polymer contributions of the normal extra stress are zero. This result has been addressed in [19] and analysed analytically by Patankar et al. [110]. The conclusion can be briefly proofed as follows:

Wi = 0.15	M1	M2	M3	Rate
Maximum displacement (10^{-3}m)	4.050	4.090	4.106	1.378
Kinetic energy (10^{-4}m^2/s^2)	9.175	9.076	9.041	1.504
Elastic energy	6.184	5.905	5.774	1.088
Wi = 0.30				
Maximum displacement (10^{-3}m)	4.015	4.057	4.075	1.271
Kinetic energy (10^{-4}m^2/s^2)	9.168	9.069	9.034	1.509
Elastic energy	9.924	9.482	9.250	0.935
Wi = 0.60				
Maximum displacement (10^{-3}m)	3.978	4.012	4.033	0.713
Kinetic energy (10^{-4}m^2/s^2)	9.161	9.062	9.033	1.784
Elastic energy	24.847	23.534	22.928	1.114

Table 5.1.: Mesh convergence study for the test case flow through a two-dimensional channel with a flexible wall

Consider an orthogonal coordinate system (ξ_1, ξ_2, ξ_3) such that ξ_1 and ξ_2 are along the surface of the rigid body and ξ_3 is normal to it. Since no-slip boundary conditions are employed on the surface, we have

$$\mathbf{u} = 0, \quad \frac{\partial \mathbf{u}}{\partial \xi_1} = \mathbf{0} \quad \text{and} \quad \frac{\partial \mathbf{u}}{\partial \xi_2} = \mathbf{0}. \tag{5.105}$$

Let u, v, w be the velocity components in the curvilinear coordinates. Because of the divergence condition $\nabla \cdot \mathbf{u} = 0$, we obtain

$$\frac{\partial w}{\partial \xi_3} = 0. \tag{5.106}$$

The velocity gradient tensor with respect to the curvilinear coordinate system reads

$$\mathbf{L} = \begin{pmatrix} 0 & 0 & 0 \\ 0 & 0 & 0 \\ \frac{1}{h_3}\frac{\partial u}{\partial \xi_3} & \frac{1}{h_3}\frac{\partial v}{\partial \xi_3} & 0 \end{pmatrix}, \tag{5.107}$$

where h_3 is a scale factor for the curvilinear coordinate ξ_3. Substituting $\mathbf{L}$ into the extra stress equation for an Oldroyd-B fluid

$$\tau + \lambda \overset{\nabla}{\tau} = \eta(\mathbf{D} + \lambda_2 \overset{\nabla}{\mathbf{D}}) \tag{5.108}$$

we obtain

$$\tau_{33} + \lambda \frac{\partial \tau_{33}}{\partial t} = 0, \tag{5.109}$$

where τ_{33} is the normal extra stress component in the curvilinear coordinate. This equation implies that $\tau_{33} = 0$ at all time if its initial value is zero. If the initial value is not zero, τ_{33} decays exponentially to zero with a time constant λ.

Let $\mathbf{n}^*$ and $\mathbf{n}$ be the unit normal vectors on the surface of the rigid body at a given point with respect to a new observer and an observer moving with the rigid body, respectively. The relations between τ^* and τ and between $\mathbf{n}^*$ and $\mathbf{n}$ are

$$\tau^* = \mathbf{Q}\tau\mathbf{Q}^{\mathsf{T}} \quad \text{and} \quad \mathbf{n}^* = \mathbf{Q}\mathbf{n}, \tag{5.110}$$

where $\mathbf{Q}$ is the rotation tensor. Let τ^* be the extra stress tensor with respect to the new observer. The normal component of stress with respect to this observer is

$$\tau_N^* = (\mathbf{n}^*)^{\mathsf{T}} \tau^* \mathbf{n}^* = \mathbf{n}^{\mathsf{T}} \mathbf{Q}^{\mathsf{T}} \mathbf{Q} \tau \mathbf{n} = \mathbf{n} \tau \mathbf{n} = \tau_{33}. \tag{5.111}$$

Therefore, the value of the normal component of stress in any frame is the same as the one by the observer moving with the rigid body.

Patankar et al. [110] show that any incompressible fluid with a constitutive model of the form

$$a_1\mathbf{D} + a_2 \overset{\triangledown}{\mathbf{D}} + a_3\tau + a_4 \overset{\triangledown}{\tau} = 0 \tag{5.112}$$

will have a zero normal component of extra stress on a rigid body surface, where a_1, a_2, a_3, a_4 are constants or some scalar functions of the invariants of $\mathbf{D}$ and τ is the total extra stress tensor.

Figure 5.19 shows the pressure on the plate for different Weissenberg numbers. We see that as the Weissenberg number increases, the pressure on the major part, especially on the central part, of the plate increases correspondingly, which causes the deflection of the plate to decreases.

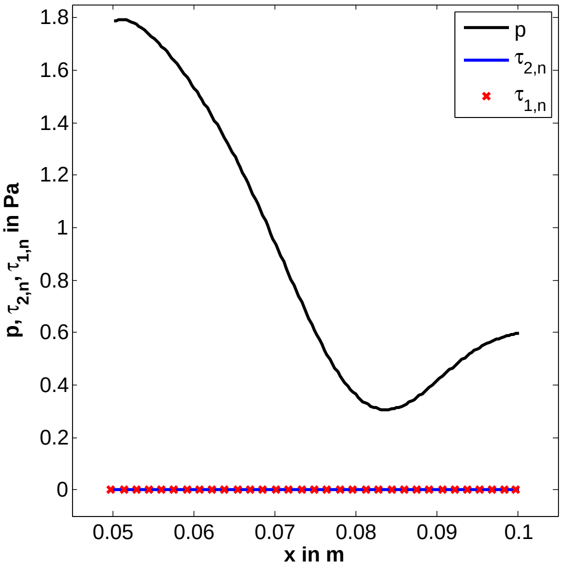

Figure 5.18.: Pressure p, solvent contribution $\tau_{1,n}$ and polymer contribution $\tau_{2,n}$ of the normal extra stress on the flexible wall at Wi $= 0.6$

The tangential stress $\tau_t = \tau_{1,t} + \tau_{2,t}$ consists of the solvent contribution $\tau_{1,t}$ and polymer contribution $\tau_{2,t}$ of the tangential extra stress. This tangential stress on the plate is plotted in figure 5.20 for the cases at different Weissenberg numbers. The tangential stress may influence the horizontal displacement of the material point of the plate. In order to see this influence, we plot this displacement of the material point along the plate in figure 5.21 which shows the small differences between Newtonian and viscoelastic flows at different Weissenberg numbers. Since the differences for both normal and tangential stresses are small, we do not observe large differences in the deformation of the plate between Newtonian and viscoelastic fluid flows.

The dynamic behaviour of the plate for this test case was originally intended to study, but it was found that in the start-up phase the plate oscillated with the amplitude close to or even larger than the channel height. The simulation broke down in these cases. Note that, for the Oldroyd-B model, even in a fixed domain, there is no global existence result for weak solutions. In the case of VFSI no theoretical results are available, too. Therefore, another test case is employed to investigate the dynamic behaviour of VFSI problems.

5.5.2 Computation of lid driven cavity flow with deformable bottom

Because of its simple geometry, this configuration is a favourite test case not only for fluid dynamics but also for FSI. For FSI simulations, the bottom of the cubic cavity is replaced by an elastic plate whose edges are fixed. Two-

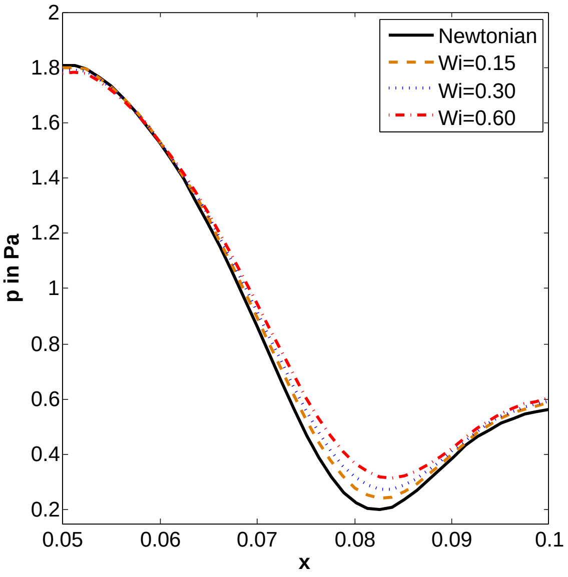

Figure 5.19.: Pressure on the plate at different Weissenberg numbers

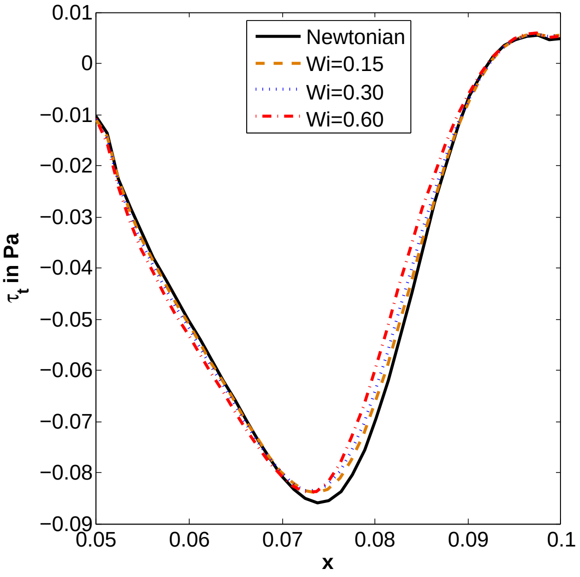

Figure 5.20.: Tangential stress on the plate at different Weissenberg numbers

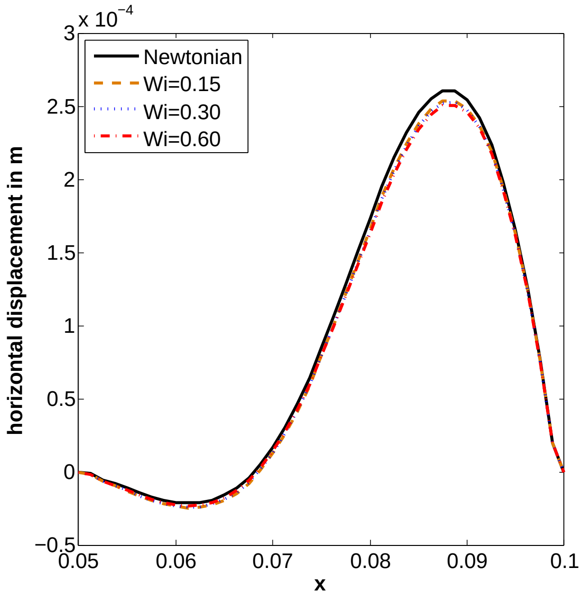

Figure 5.21.: Horizontal displacement of the material point along the plate at different Weissenberg numbers

dimensional simulations of this test case have been investigated in, e.g. [79, 74]. Three-dimensional simulations have been studied in, e.g. [58]. In the following, the three-dimensional case is investigated.

The underlying geometry is illustrated in figure 5.22. The parameters are the same as in [79, 74]. The cavity has length $l = 1\,\mathrm{m}$, the inlet and outlet has height $h = 0.1\,\mathrm{m}$. The fluid has density $\rho^f = 1\,\mathrm{kg/m^3}$, total viscosity $\eta = 0.01\,\mathrm{Pa\cdot s}$, for which $\eta_s = \eta_p = 0.005\,\mathrm{Pa\cdot s}$. The bottom plate has a thickness of $d = 0.002\,\mathrm{m}$, Young's modulus $E^s = 250\,\mathrm{Pa}$ and density $\rho^s = 500\,\mathrm{kg/m^3}$. The plate is fixed at the edges. A time-dependent lid velocity $u_{lid} = 1 - \cos(2\pi t/5)\,\mathrm{m/s}$ or a time-independent lid velocity $u_{lid} = 1\,\mathrm{m/s}$ is used for different aims of study. When the time-dependent lid velocity is employed, the bottom plate exhibits a periodic oscillation which is reached after a short transition phase. When the time-independent lid velocity is employed, the bottom plate first oscillates then reaches a stationary state.

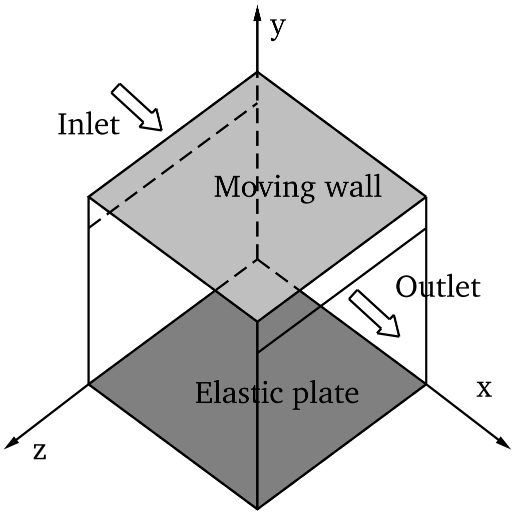

Figure 5.22.: Geometry of the lid-driven cavity flow with flexible bottom

Before investigation of the FSI dynamics process, we perform several mesh convergence studies for Computation Fluid Dynamics (CFD), Computational Structural Mechanics (CSM) in the separated domains, as well as FSI tests with time-independent lid velocity.

CFD test

In CFD test the bottom wall is rigid, i.e. the fluid domain is fixed. We choose *a*) the total vertical forces exerted by the fluid on the bottom plate, *b*) the average kinetic energy and *c*) the average elastic energy in the fluid domain as the objective quantities for study. Three successively refined meshes Mf1, Mf2 and Mf3 are employed to simulate the fluid flow at different Weissenberg numbers. The number of control volumes for these meshes are 16 × 16 × 16, 32 × 32 × 32 and 64 × 64 × 64, respectively. Weissenberg numbers are changed by varying the fluid relaxation time. For Weissenberg numbers $\mathrm{Wi} = 0.05$, 0.1 and 0.2, the fluid relaxation times are $\lambda = 0.05\,\mathrm{s}$, $0.1\,\mathrm{s}$ and $0.2\,\mathrm{s}$, respectively.

In the first test, a constant lid velocity $u_{lid} = 1\,\mathrm{m/s}$ is employed. The computed values of the objective quantities are shown in table 5.2. For the Weissenberg numbers under consideration all the simulations show convergence. For larger Weissenberg numbers ($\mathrm{Wi} > 0.2$), we observe that the solution does not reach the steady state and oscillation occurs in the vertical force. This oscillation becomes stronger as the Weissenberg number increases and mesh convergence is not observed. Therefore, we choose $\mathrm{Wi} = 0.2$ for the maximal Weissenberg number in the FSI test for investigation. Note that for $\mathrm{Wi} > 1.0$ the simulations are still stable with LCR.

$\mathrm{Wi} = 0.05$	Mf1	Mf2	Mf3	Rate
Vertical force (10^{-1}N)	−2.611	−3.961	−4.416	1.571
Kinetic energy ($10^{-2}\mathrm{m}^2/\mathrm{s}^2$)	7.394	5.405	4.910	2.005
Elastic energy	4.448	3.736	3.410	1.129
$\mathrm{Wi} = 0.10$				
Vertical force (10^{-1}N)	−2.487	−3.746	−4.133	1.700
Kinetic energy ($10^{-2}\mathrm{m}^2/\mathrm{s}^2$)	7.394	5.387	4.875	1.970
Elastic energy	4.654	3.943	3.624	1.155
$\mathrm{Wi} = 0.20$				
Vertical force(10^{-1}N)	−2.179	−3.334	−3.760	1.438
Kinetic energy ($10^{-2}\mathrm{m}^2/\mathrm{s}^2$)	7.431	5.421	4.870	1.867
Elastic energy	5.383	4.646	4.361	1.369

Table 5.2.: Mesh convergence study in CFD test for the test case lid-driven cavity flow with $u_{lid} = 1\,\mathrm{m/s}$

In the second test, the lid velocity is varying in time according to $u_{lid} = 1 - \cos(2\pi t/5)\,\mathrm{m/s}$. To check the time resolution we employ three time step sizes and compare the average forces and amplitudes. The fluid relaxation time in this test is $\lambda = 0.1\,\mathrm{s}$ which corresponds to $\mathrm{Wi} = 0.1$. The results are shown in table 5.3.

Δt (s)	0.025	0.05	0.1
Forces (10^{-1}N)	-6.477 ± 8.519	-6.478 ± 8.527	-6.508 ± 8.565

Table 5.3.: Vertical forces exerted by the fluid on the bottom wall in the CFD test with $u_{lid} = 1 - \cos(2\pi/5t)\,\mathrm{m/s}$

CSM test

In the CSM test we investigate the vertical displacements of the middle point of the plate under different pressure loads. The plate is discretized with trilinear 8-node solid hexahedral solid elements. Three successively refined meshes Ms1 (20 × 20 × 2), Ms2 (30 × 30 × 3) and Ms3 (40 × 40 × 4) are employed. In the first test, the values of the pressure are kept constant. Table 5.4 shows the results of the mesh convergence study. In the second test the pressure is varying periodically in time according to $p = 0.2 + 0.1\sin(2\pi t/5)\,\mathrm{Pa}$.

Different time step sizes with mesh Ms2 are checked. The calculated equilibrium position and amplitude of the oscillation are given in table 5.5.

Load (Pa)	Ms1	Ms2	Ms3
0.1	-1.838	-1.857	-1.858
0.5	-3.349	-3.363	-3.371

Table 5.4.: Vertical displacement (10^{-1}m) of the middle point of the plate in CSM test

Δt (s)	0.025	0.05	0.1
Equilibrium position (m)	-2.3069	-2.3067	-2.3072
Amplitude (m)	0.4557	0.4557	0.4557

Table 5.5.: Oscillation equilibrium position and amplitude of the middle point of the plate in CSM test for $p = 0.2 + 0.1\sin(2\pi t/5)\,\text{Pa}$

FSI test

Besides the above CFD and CSM tests we also perform a mesh convergence study for FSI. In the test the solid plate is discretized with mesh Ms2. The time step size is $\Delta t = 0.05\,\text{s}$. The lid velocity is set to $u_{lid} = 1\,\text{m/s}$. Simulations are done with meshes Mf1, Mf2 and M3 for the fluid domain. The objective variables for the investigation are *a*) the maximum displacement of the bottom plate, *b*) the average kinetic energy and *c*) the average elastic energy as they reach steady state. The results are shown in table 5.6.

Wi = 0.05	Mf1	Mf2	Mf3	Rate
Maximum displacement (10^{-1}m)	-2.502	-2.991	-3.276	0.779
Kinetic energy ($10^{-2}\text{m}^2/\text{s}^2$)	5.959	4.426	3.842	1.393
Elastic energy	3.8976	3.2111	3.0401	2.006
Wi = 0.10				
Maximum displacement (10^{-1}m)	-2.456	-2.914	-3.173	0.825
Kinetic energy ($10^{-2}\text{m}^2/\text{s}^2$)	5.972	4.411	4.053	2.124
Elastic energy	4.064	3.236	3.013	1.895
Wi = 0.20				
Maximum displacement (10^{-1}m)	-2.337	-2.771	-3.004	0.898
Kinetic energy ($10^{-2}\text{m}^2/\text{s}^2$)	7.468	5.405	4.785	1.736
Elastic energy	5.762	4.648	4.110	1.051

Table 5.6.: Mesh convergence study in the FSI test with $u_{lid} = 1\,\text{m/s}$

Investigation of FSI dynamics

For the following investigation mesh Mf2 and Ms2 are employed for the fluid and solid domain, respectively. The time step size of $\Delta t = 0.05\,\text{s}$ is chosen.

In the first test, we impose a time-dependent lid velocity $u_{lid} = 1 - \cos(2\pi t/5)\,\text{m/s}$ on the upper wall. Simulations with different Weissenberg numbers are executed. We change the Weissenberg number by varying the fluid relaxation time. Figure 5.23 shows the fields of velocity magnitude, the streamlines on the cross section $z = 0.5\,\text{m}$ and deformations of the bottom plate at Wi $= 0.1$ for one vibration period. The vertical positions of the middle point of the plate, originally located at $(0.5, 0, 0.5)$, during the whole simulation are shown in figure 5.24. We can see that the plate reaches a steady periodic oscillation after a transient phase. We say that the oscillation reaches

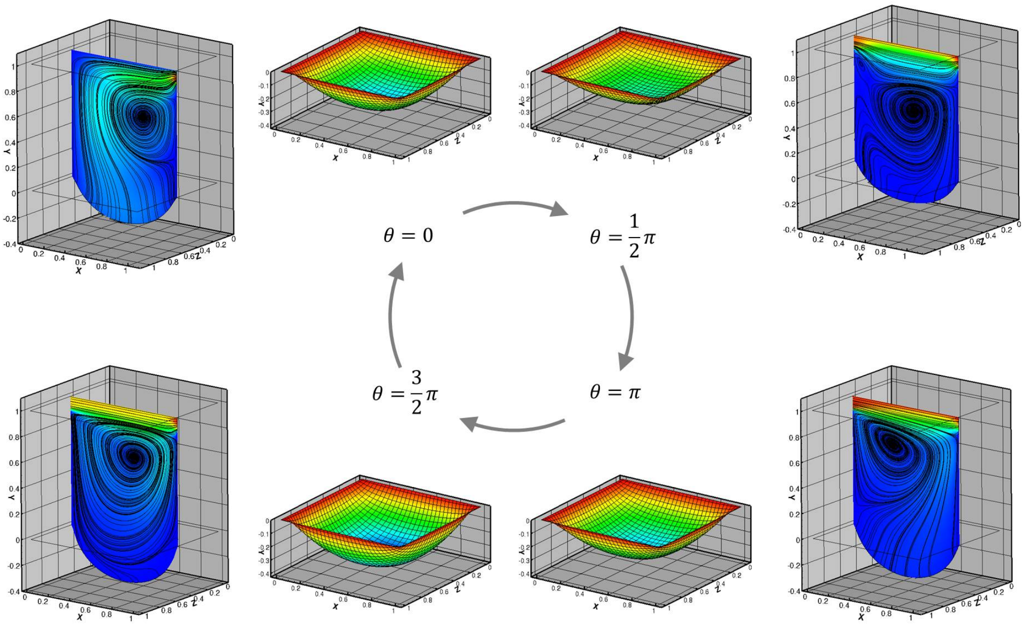

Figure 5.23.: The fields of velocity magnitude, streamlines for cross section $z = 0.5\,\mathrm{m}$ and deformations of the bottom plate for the vibration phase angles $\theta = 0, \pi/2, \pi$ and $3\pi/2$ in a whole vibration period in the case of lid-driven cavity flow with lid velocity $u_{lid} = 1 - \cos(2\pi t/5)\,\mathrm{m/s}$ at Wi $= 0.1$

steady when the relative difference of the amplitude fulfills $|A_t - A_s|/|A_s| \leqslant 0.5\%$, and the difference does not increase any more. Here A_t denotes the current amplitude and A_s is the amplitude at steady state. The equilibrium positions, oscillation amplitudes and times to reach steady state for different Weissenberg numbers are listed in table 5.7. Following phenomena have been observed as the Weissenberg number increases:

- The equilibrium position moves downwards from Wi $= 0$ (Newtonian) to Wi $= 0.05$, then moves upwards.
- The amplitude first increases until Wi $= 0.1$, then decreases for Wi $= 0.2$.
- The time to reach steady state first increases from Wi $= 0$ (Newtonian) to Wi $= 0.05$, then remains unchanged until Wi $= 0.1$, finally decreases for Wi $= 0.2$.

Wi	0 (Newtonian)	0.05	0.1	0.2
Equilibrium position (10^{-1}m)	-2.795	-3.003	-2.899	-2.717
Oscillation Amplitude (10^{-1}m)	0.660	0.898	0.961	0.466
Time to steady state (s)	24.80	46.20	46.20	40.95

Table 5.7.: Characteristic values of plate motion for at different Weissenberg numbers in the case lid driven cavity with $u_{lid} = 1 - \cos(2\pi/5t)\,\mathrm{m/s}$

In the second FSI test, we let the lid velocity to be constant, i.e. $u_{lid} = 1\mathrm{m/s}$. The vertical positions of the middle point of the bottom plate at different Weissenberg numbers are shown in figure 5.25. After a transient phase with oscillation the plate reaches stationary state. As the Weissenberg number increases, we have observed the following phenomena:

- The equilibrium position moves upwards.
- The plate needs longer time to reach the stationary state.
- The oscillation frequency first decreases from Wi $= 0$ (Newtonian) to Wi $= 0.01$, then increases.

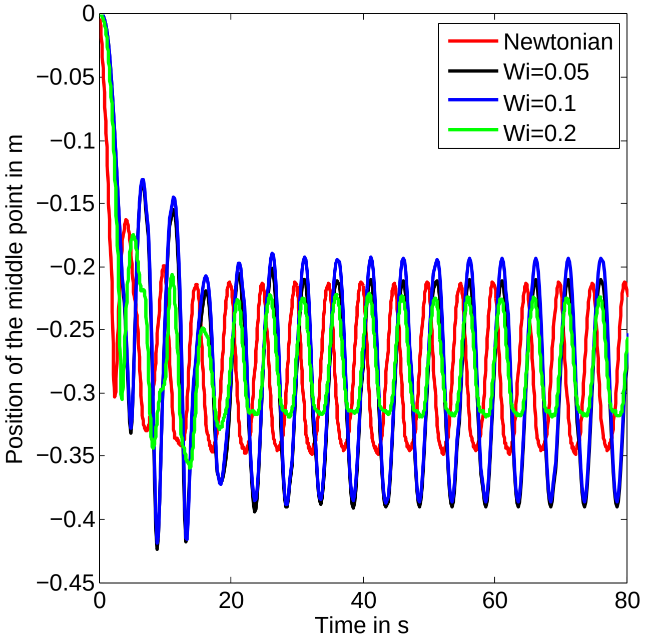

Figure 5.24.: Vertical position of the middle point of bottom plate in the case lid-driven cavity flow with lid velocity $u_{lid} = 1 - \cos(2\pi t/5)\,\mathrm{m/s}$

- The horizontal position of the vortex center shifts in the upstream direction as the Weissenberg number increases. The vertical position first moves upwards from Wi = 0 (Newtonian) to Wi = 0.01 then moves downwards. The streamlines for various Weissenberg number flows are shown in figure 5.26. The phenomenon of vortex center shifting in the upstream direction has also been observed in the case of the lid driven cavity with a rigid bottom wall. See e.g. [106] for an experimental work and [155] for a numerical work.

The values of the equilibrium position, the time to stationary state and the oscillation frequency are explicitly listed in table 5.8. The differences of the oscillation amplitude and phase shift are also observed. However, we do not see a trend for these quantities for increasing Weissenberg numbers.

Wi	0 (Newtonian)	0.01	0.05	0.1	0.2
Equilibrium position (10^{-1}m)	-3.163	-3.083	-2.991	-2.914	-2.771
Time to stationary state (s)	31.50	32.95	34.35	36.10	38.35
Oscillation frequency (Hz)	0.475	0.400	0.425	0.450	0.450
Vortex center location x (10^{-1}m)	5.611	5.605	5.604	5.563	5.468
Vortex center location y (10^{-1}m)	6.035	6.043	6.020	5.997	5.995

Table 5.8.: Characteristic values of plate motion at different Weissenberg numbers in the case lid driven cavity with $u_{lid} = 1.0\,\mathrm{m/s}$

Simultaneously we study the problem by means of the MSD model. We can calculate the parameters in the MSD model by means of equation (5.72), (5.73) and (5.74). As in the simulation, we investigate the influence of the Weissenberg number on the displacement of the fluid-solid interface. Therefore, we vary the fluid relaxation time to change the Weissenberg number. Note that varying the fluid relaxation time changes both the elasticity number E and the stiffness ratio K in the MSD model.

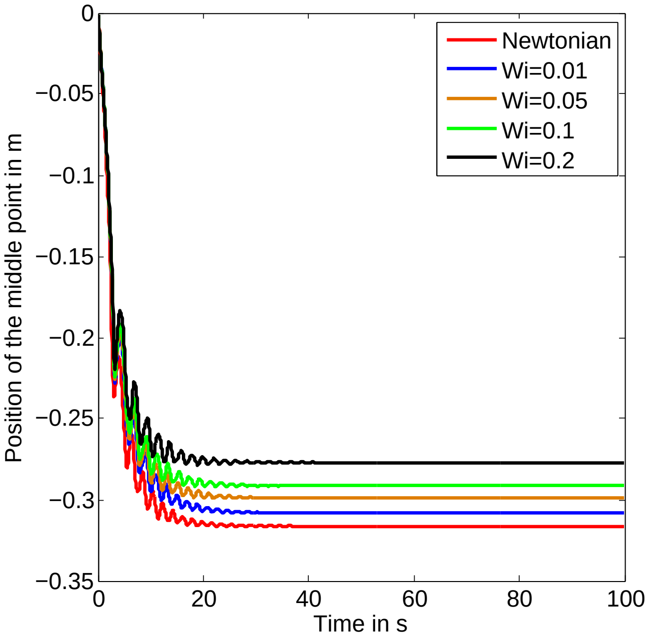

Figure 5.25.: Vertical position of the middle point of bottom plate at different Weissenberg numbers in the case lid-driven cavity flow with lid velocity $u_{lid} = 1\,\mathrm{m/s}$

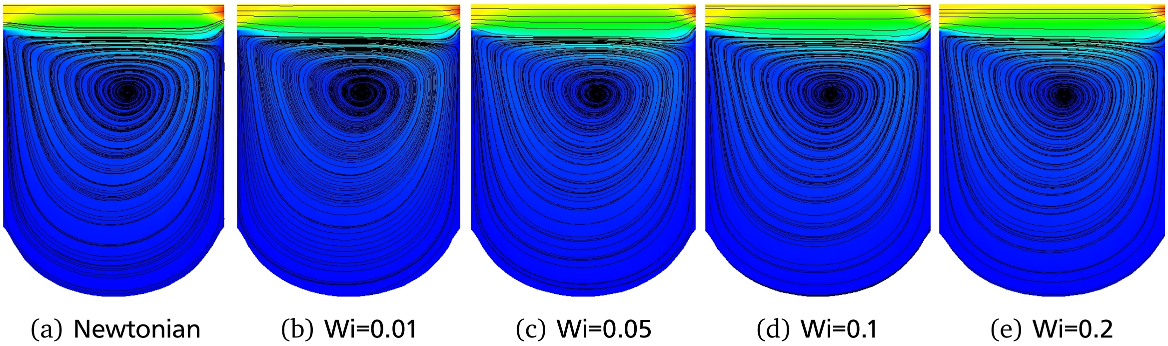
(a) Newtonian (b) Wi=0.01 (c) Wi=0.05 (d) Wi=0.1 (e) Wi=0.2

Figure 5.26.: Streamline on the cross section of $z = 0.5\,\mathrm{m}$ and the field of velocity magnitude in the case lid-driven cavity flow with lid velocity $u_{lid} = 1\,\mathrm{m/s}$

Figure 5.27 shows the determinant Δ of the characteristic equation (5.78) and parameter g, α and ω in equation (5.95) as functions of Wi. We see that in the range of Weissenberg numbers under consideration, the value of Δ is always positive, i.e. the solution type belongs to type ST3, for which the solution consists of a periodic part with exponentially damping amplitude and a decaying exponential part without oscillation. This fact is reflected in the simulations. Comparing the values of g and α we see that $\alpha < g$ is valid. It indicates that the exponential part vanishes faster than the periodic part, which belongs to solution type ST3PER in type ST3. Furthermore, the increasing value of ω indicates that the frequency of the oscillation increases. We can also see this fact in the simulations as we refer to table 5.8. The oscillation frequency for Newtonian flow is larger than the flow at $\text{Wi} = 0.01$ can also be explained by means of the MSD model. If we compute the frequency with the MSD model for Newtonian fluid, we obtain the value of $\omega_{Newtonian} = 0.4999$ which is larger than $\omega > \omega_{Wi=0.01} = 0.005$.

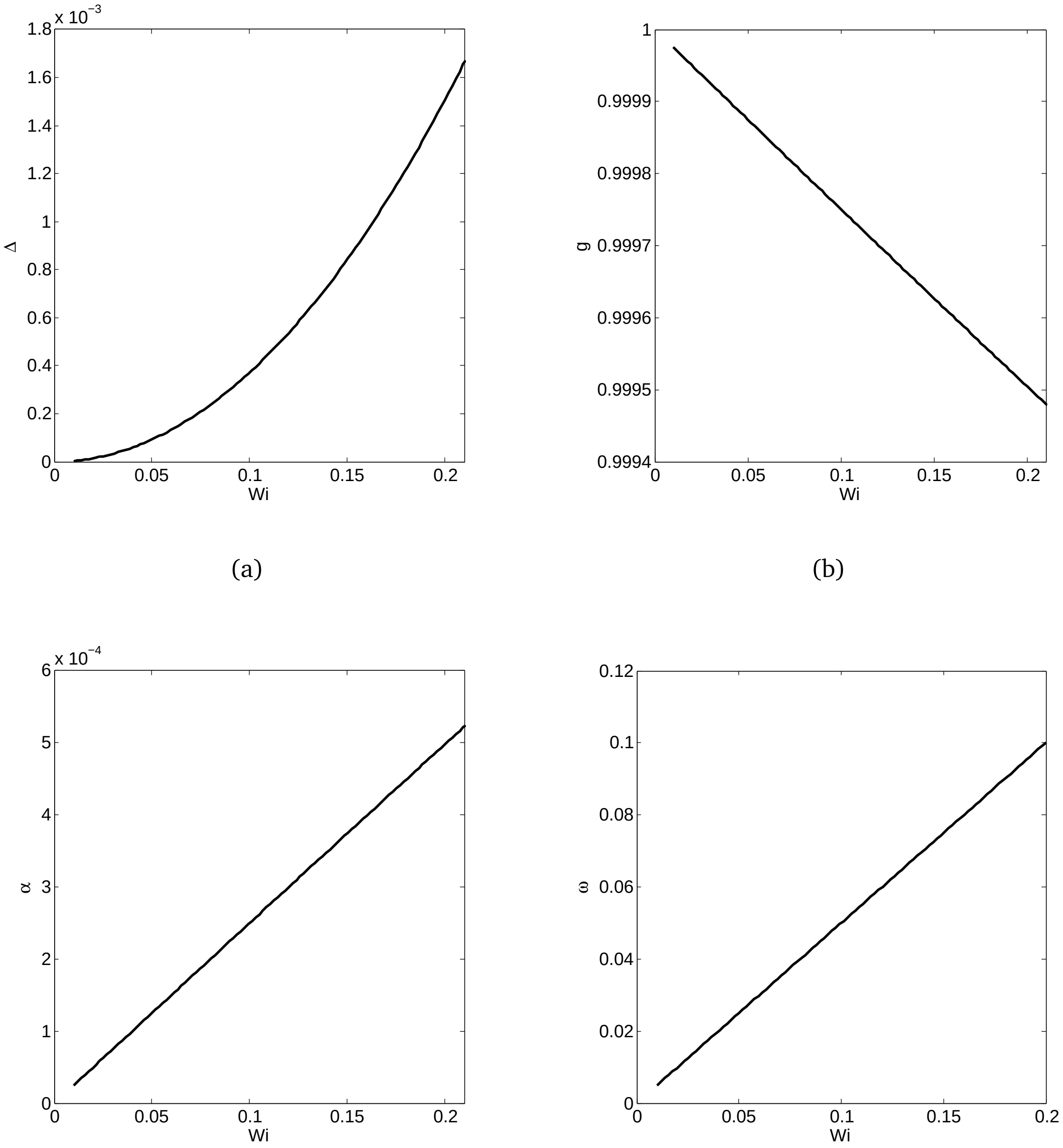

(a) (b)

(c) (d)

Figure 5.27.: MSD model parameters as a function of the Weissenberg number

Wi	Δ (10^{-6})	g	α (10^{-5})	ω
0.01	3.703	1.000	2.500	0.005
0.05	92.63	0.9999	12.50	0.025
0.1	371.5	0.9998	24.98	0.050
0.2	1500	0.9995	49.78	0.100

Table 5.9.: Values of MSD model for different Weissenberg numbers

Next we investigate the influence of the Reynolds number. In order to do so, we vary the viscosity of the fluid. The other parameters remain unchanged as in the last test. The lid velocity is $u_{lid} = 1\,\text{m/s}$. The fluids have relaxation time $\lambda = 0.2\,\text{s}$, which corresponds to $\text{Wi} = 0.2$. The evolution of the position of the middle point of the bottom plate is plotted in figure 5.28. We have observed the following phenomena as the Reynolds number increases:

- The equilibrium position moves upwards.
- The plate needs longer time to reach the stationary state.
- The oscillation frequency does not change obviously.
- The location of the vortex center moves right- and upwards as the Reynolds number increases. The streamlines for flows at various Reynolds numbers are shown in figure 5.29.

The values of the equilibrium position, the time to stationary state and the oscillation frequency for different Reynolds numbers are explicitly listed in table 5.10.

Re	33	50	100	200
Equilibrium position (10^{-1}m)	-2.862	-2.810	-2.771	-2.749
Time to stationary state (s)	25.90	27.35	38.35	76.20
Oscillation frequency (Hz)	0.400	0.400	0.433	0.433
Vortex center location x (10^{-1}m)	5.181	5.264	5.468	5.950
Vortex center location y (10^{-1}m)	5.930	5.934	5.995	6.159

Table 5.10.: Characteristic values of plate motion at different Reynolds numbers in the case lid driven cavity with $u_{lid} = 1.0\,\text{m/s}$

Again we analyse this test making use of the MSD model. Figure 5.30 shows the determinant Δ of the characteristic equation (5.78) and parameter g, α and ω in equation (5.95) as functions of Re. The calculated values of Δ, g, α and ω for different Reynolds numbers are listed in table 5.11. For all the Reynolds numbers the value of Δ are positive and $\alpha < g$. The solution type belongs to type ST3PER. The exponential part of the solution damps faster than the periodic term. The value of α decreases quickly as the Reynolds number increases, i.e. the periodic term damps more slowly with increasing Reynolds number. This fact is obviously reflected in the simulation. The values of ω does not change much, which is also observed by the oscillation frequency in the simulation.

Re	Δ (10^{-3})	g	α (10^{-4})	ω
33	1.495	0.9985	14.948	0.1001
50	1.501	0.9990	9.9602	0.1000
100	1.506	0.9995	4.9777	0.1000
200	1.509	0.9998	2.4882	0.1000

Table 5.11.: Values of MSD model for different Reynolds numbers

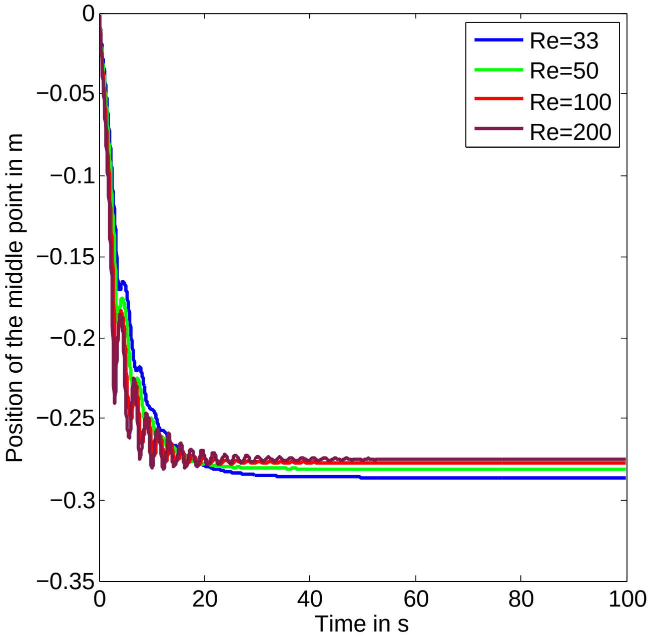

Figure 5.28.: Vertical position of the middle point of bottom plate for different Reynolds numbers at Wi $= 0.2$ in the case lid-driven cavity flow with $u_{lid} = 1\,\mathrm{m/s}$

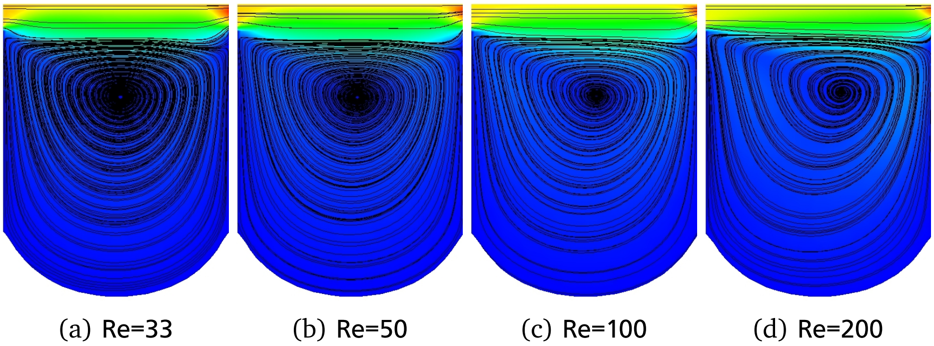
(a) Re=33 (b) Re=50 (c) Re=100 (d) Re=200

Figure 5.29.: Streamline on the cross section of $z = 0.5\,\mathrm{m}$ and the field of velocity magnitude in the case lid-driven cavity flow with lid velocity $u_{lid} = 1\,\mathrm{m/s}$

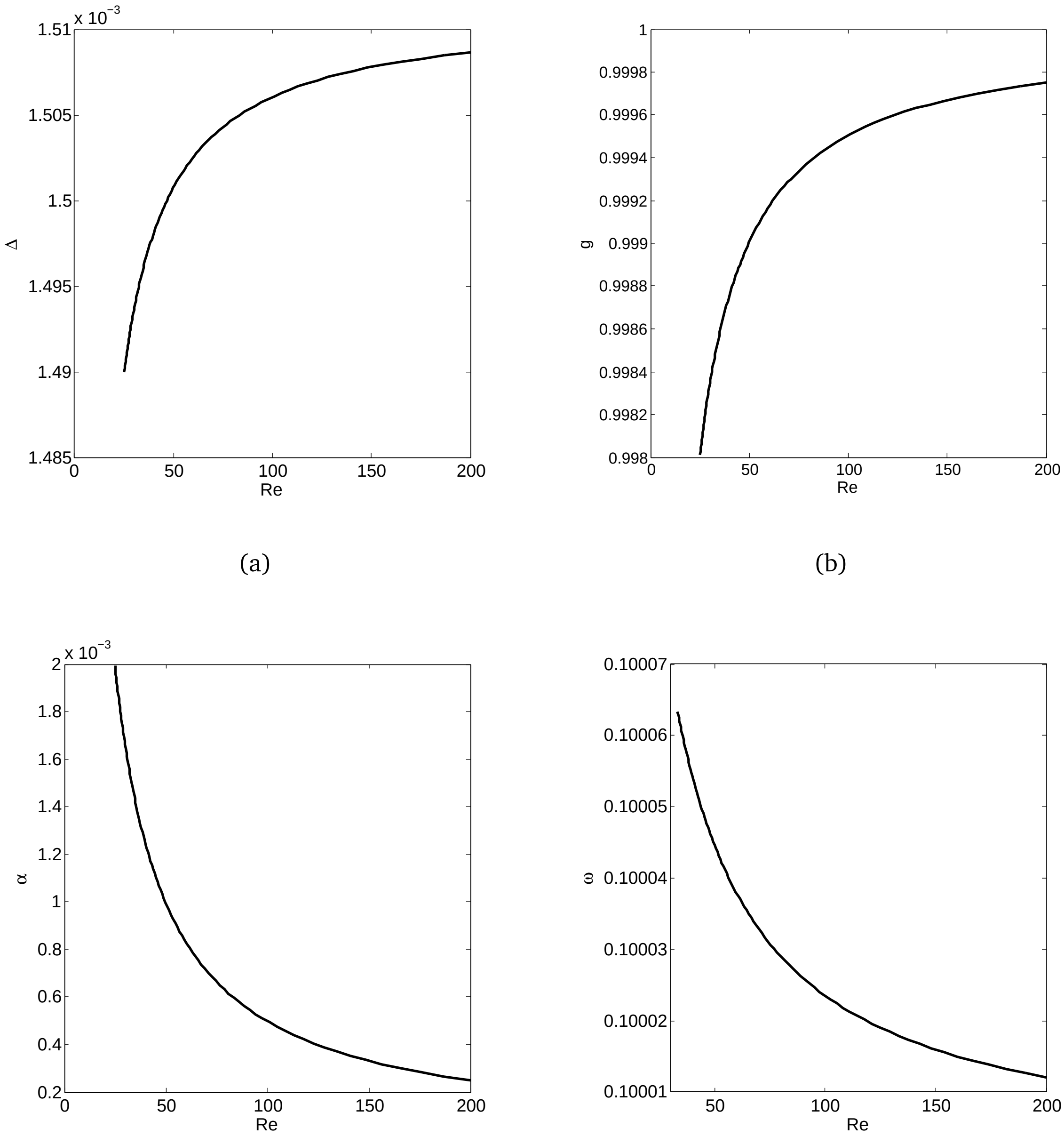

(a) (b)

(c) (d)

Figure 5.30.: MSD model parameters as a function of the Reynolds number

In the above tests, the value of the elasticity number E ranges from 10^{-4} to 6×10^{-3}, the stiffness ratio K ranges from 0.25 to 10, the mass ratio $\alpha_m = 0.5$ and the viscosity ratio $\beta = 0.5$. For these values the solution type belongs to ST3PER. The type ST3EXP occurs only if $\alpha > g$. It is not the case in the simulations in the present work. However, the trend of the transition from ST3PER to ST3EXP is observed. From the analysis in section 5.4 we know that the changing from solution type ST3PER to ST3EXP occurs when E is large, i.e. the Weissenberg number is large and/or the Reynolds number is small. But we did not consider these settings in the simulations. Based on the discussion of the second and third FSI test, we see that the simulation and the MSD model show consistency in the qualitative analysis of the dynamic behaviour in VFSI.

Investigation of the coupling algorithm

In the last part of the simulation experiments we study the influence of numerical and physical parameters on the convergence properties of the implicit partitioned coupling algorithm for VFSI. The number of total CFD iterations in the FSI simulation is employed to evaluate the influence. The investigated numerical parameters are the time step size Δt, the FSI under-relaxation factor α_{FSI}, whereas the physical parameters are the fluid relaxation time λ and the density ratio ρ^f/ρ^s. The simulations are carried out with lid velocity $u_{lid} = 1 - \cos(2\pi t/5)\,\mathrm{m/s}$. Totally 5 s of physical time are simulated in every simulation run.

Four groups of tests are done:

a) Influence of λ and ρ^f/ρ^s by setting $\lambda = 0.05\,\mathrm{s}, 0.1\,\mathrm{s}$ and $0.2\,\mathrm{s}$ and $\rho^f/\rho^s = 1/500, 1/375$ and $1/250$ with $\alpha_{FSI} = 0.5$ and $\Delta t = 0.05\,\mathrm{s}$ (see figure 5.31 (a))

b) Influence of λ and α_{FSI} by setting $\lambda = 0.05\,\mathrm{s}, 0.1\,\mathrm{s}$ and $0.2\,\mathrm{s}$ with $\rho^f/\rho^s = 1/500$ and $\Delta t = 0.05\,\mathrm{s}$ (see figure 5.31 (b))

c) Influence of α_{FSI} and ρ^f/ρ^s by setting $\rho^f/\rho^s = 1/500, 1/375$ and $1/250$ with $\lambda = 0.1\,\mathrm{s}$ and $\Delta t = 0.05\,\mathrm{s}$ (see figure 5.31 (c))

d) Influence of λ and Δt by setting $\rho^f/\rho^s = 1/500$ with $\lambda = 0.05\,\mathrm{s}, 0.1\,\mathrm{s}$ and $0.2\,\mathrm{s}$ and $\Delta t = 0.05\,\mathrm{s}$. (see figure 5.31 (d))

Figure 5.31 (a) shows that the number of CFD iterations increases as the fluid relaxation time increases. This trend is the same as for CFD simulations of viscoelastic fluid flow: as the Weissenberg number increases, more iterations are needed for convergence. Figure 5.31 (a) also shows that as the density ratio increases the simulation converges more slowly. It indicates that the added mass effect occurs, and this effect is more obvious by large density ratios, which has also been discussed for the MSD model in section 5.4.

In Figure 5.31 (b) we see the increasing number of CFD interactions for increasing fluid relaxation time. Comparing the results for different fluid relaxation times we see that there is an optimal FSI under-relaxation factor $\alpha_{FSI} = 0.5$. This factor does not vary in the considered range of fluid relaxation times.

The investigation of the influence of the FSI under-relaxation factor α_{FSI} and the density ratio ρ^f/ρ^s is given in Figure 5.31 (c). With different density ratios, the optimal FSI under-relaxation factor varies. The larger ρ^f/ρ^s, the smaller the optimal under-relaxation factor.

From Figure 5.31 (d) we know that time step size also influences the computation. As the time step size decreases, the number of CFD iteration increases dramatically.

The results of the above simulations is consistent with the conclusion drawn from the analysis of the MSD model. The convergence properties of the implicit partitioned algorithm for VFSI is greatly influenced by the density ratio between fluid and solid. The higher the density ratio, the more slowly the simulation converges. The fluid relaxation time also influences the convergence rate. The larger the fluid relaxation time, the more slowly the simulation converges.

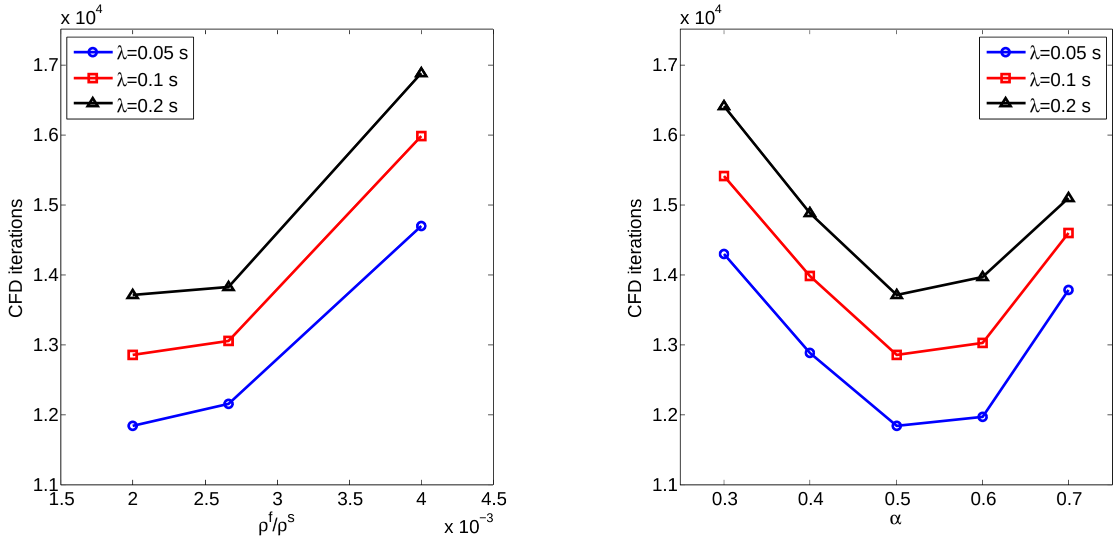

(a) Influence of λ and ρ^f/ρ^s

(b) Influence of λ and α_{FSI}

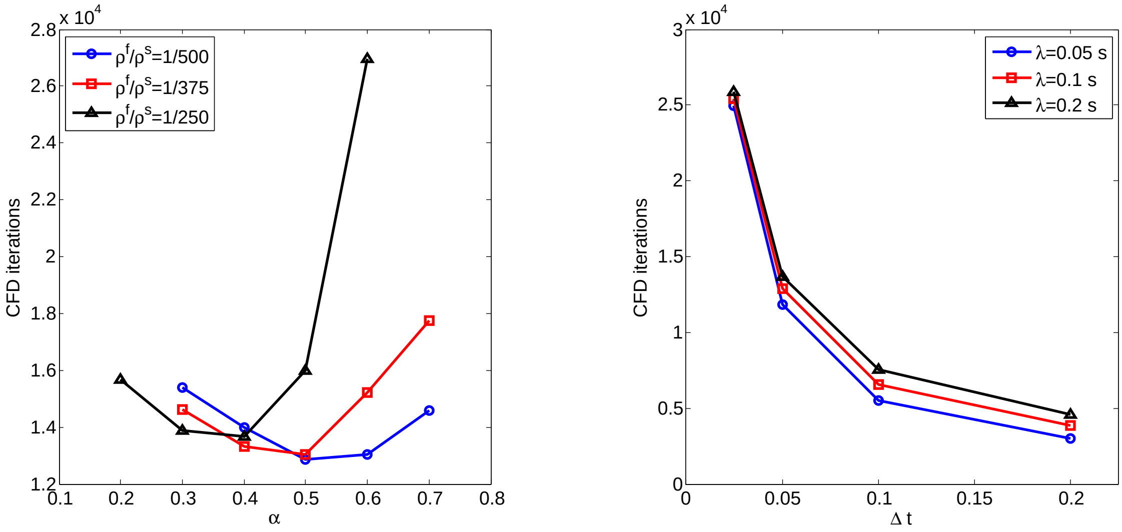

(c) Influence of α_{FSI} and ρ^f/ρ^s

(d) Influence of Δt and λ

Figure 5.31.: Influence of physical and numerical parameters on the implicit partitioned algorithm for viscoelastic fluid-structure interaction

Summary

In this chapter the log-conformation representation approach is employed in the fluid solver for simulation of viscoelastic fluid-structure interaction problems. The dynamic behaviour of VFSI systems is presented via simulations applying an implicit partitioned coupling algorithm.

Concerning the convergence properties of the proposed implicit partitioned coupling algorithm for VFSI, we have found:

- The implicit partitioned algorithm can be successfully applied for VFSI problems. However, similar to NFSI problems, there is the added mass effect, when the density ratio of fluid to solid is large.
- The fluid relaxation time influences the rate of convergence. The larger the fluid relaxation time, the more slowly the computation converges.

Besides simulations, the mass-spring-dashpot model is also employed to investigate the solution of VFSI problems. The results from the simulation and the MSD model are consistent in the qualitative analysis of the dynamic behaviour in VFSI and the convergence properties of the coupling algorithm. The MSD model can be regarded as an alternative effective tool for qualitative analysis for VFSI systems.

The significant dynamic behaviours of VFSI systems are summarized as follows:

- The solution of a VFSI problem is more complicated than that of an NFSI problem. In free oscillation, the physical parameters determine the type of transient solution. There are three types of solution. The first (ST1) and second type (ST2) are fully exponential damped. The third type (ST3) is a combination of a periodic part with exponentially damped amplitude and an exponential decay without oscillation. For ST3, which motion damps faster depends on the physical parameters of the system.
- The solution of a VFSI problem is greatly influenced by the elasticity number of the flow which is the ratio of the Weissenberg number to the Reynolds number.
- The solid deformation is influenced by the Weissenberg number in the fluid flow in both forced and free oscillation. In forced oscillation, the amplitude, the equilibrium position, the phase shift and the time to reach steady state are different for different Weissenberg numbers, whereas in free oscillation the amplitude, the equilibrium position, the frequency, the time to reach stationary state and the phase shift are changed.
- With the employed physical parameters in the investigated test cases, the amplitude of oscillation first increases, then decreases as the Weissenberg number becomes larger in forced oscillation. In free oscillation, the system needs longer time to reach a stationary state, accompanied by an increasing oscillation frequency, when $\mathrm{Wi} > 0$ becomes larger for fixed Reynolds numbers. For fixed Weissenberg number but increasing Reynolds numbers, the system need longer time to reach stationary state.

Difficulties are encountered during the investigation by obtaining results at high Weissenberg numbers. Although we are able to obtain stable solutions at very high Weissenberg numbers with the log-conformation representation approach, we are still facing the problem of mesh convergence. Furthermore, the solution of the problem shows unsteadiness at high Weissenberg numbers. This results in difficulties for the investigation of high Weissenberg number VFSI problems.

6 Direct numerical simulation of a valveless micropump

In this chapter the implicit partitioned coupling algorithm for viscoelastic fluid-structure interaction is applied to simulate a valveless micropump pumping a viscoelastic fluid. In section 6.1, two semi-analytical models of the pumping flow rate for pumping Newtonian fluids are reviewed. Subsequently, the question of how to use these semi-analytical models to qualitatively analyse the pumping flow rate for pumping viscoelastic fluids is discussed. We will see that the diffuser efficiency plays an important role in control of pumping flow rate. Therefore, in section 6.2 an Oldroyd-B fluid flowing in a diffuser/nozzle element is simulated to investigate the influence of fluid viscoelasticity on the diffuser efficiency. In section 6.3 direct numerical simulation of the whole valveless micropump is presented and discussed.

6.1 Semi-analytical models for the pumping flow rate

The valveless micropump was first proposed by E. Stemme and G. Stemme [135]. They have also provided a simplified analytical model to estimate the pumping flow rate without considering the influence of the interaction between the pumping fluid and the oscillation plate. Nevertheless, this model has been the basis for further development. Since then, several semi-analytical models have been proposed considering the influence of the fluid-plate interaction see, e.g. [107, 108, 38, 10]. In this section, the model proposed by E. Stemme and G. Stemme [135] is reviewed. Subsequently, this model is extended taking the effect of FSI into account. The derivation follows the works of Pan et al. [107] and Azarbadegan et al. [10]. Discussion about the influence of fluid viscoelasticity on the model is given in the final part of this section.

Model without consideration of fluid-structure interaction

The components of a valveless micropump are shown in figure 6.1. A typical valveless micropump consists of a large chamber with an oscillating diaphragm, and two diffuser/nozzle elements at inlet and outlet. A diffuser is an expanding duct, while a nozzle is a converging one. The flow directing action in the pump is realized due to the fact that in a diffuser/nozzle element lower pressure loss occurs in the diffuser direction than in the nozzle direction for the same flow velocity.

In the supply mode, the chamber volume increases, so the fluid flows into the chamber through both inlet and outlet. However, the inlet element acts as a diffuser, which has lower pressure loss, while the outlet element acts as a nozzle having higher pressure loss. Thus the overall volume flux flows from inlet to outlet. Analogously, in the pump mode the chamber volume decreases, inlet acts as a nozzle, outlet acts as a diffuser and larger volume flux is transported through the outlet than the inlet. As a result, for a complete pump cycle, a net volume is transported from the inlet side to the outlet side, although the diffuser/nozzle elements convey fluid in both directions.

To model the pumping flow rate, the following assumptions are made:

- The total pressure loss inside the pump is caused by the local pressure loss of the flow through diffuser and nozzle.
- The pressure inside the chamber is uniform.
- The pressures at inlet and outlet are $P_{in} = P_{out} = 0$.
- The inlet and outlet elements have identical geometry.

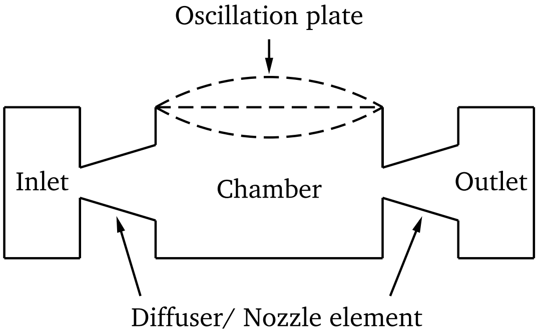

Figure 6.1.: Elements in a valveless micropump

As given in the classical fluid dynamics textbooks, e.g. [149], the pressure losses through a diffuser and a nozzle can be estimated by

$$\Delta P_d = \frac{1}{2}\rho^f u_d^2 \xi_d \quad \text{and} \quad \Delta P_n = \frac{1}{2}\rho^f u_n^2 \xi_n, \tag{6.1}$$

where ρ^f is the density of the fluid, u_d and u_n are the average fluid flow velocities in the narrowest parts of the diffuser and nozzle, respectively. The coefficients ξ_d and ξ_n are the pressure loss coefficients of the diffuser and nozzle.

The fluid volumetric flow rate through the diffuser and nozzle are calculated by the product of the mean velocity and the cross section area according to

$$Q_d = A_d u_d \quad \text{and} \quad Q_n = A_n u_n, \tag{6.2}$$

where A_d and A_n are the cross-sectional areas of the narrowest part of the diffuser and nozzle, respectively. From equation (6.1) we can obtain the expression for u_d and u_n. Substituting u_d and u_n into equation (6.2) the flow rates are obtained as

$$Q_d = A_d \sqrt{\frac{2\Delta P_d}{\rho^f \xi_d}} \quad \text{and} \quad Q_n = A_d \sqrt{\frac{2\Delta P_n}{\rho^f \xi_n}}. \tag{6.3}$$

Since the inlet and outlet elements have the same geometry, they have the identical cross-sectional throat area $A_d = A_n = A$. In addition, under the assumption of the pressures at inlet and outlet $P_{in} = P_{out} = 0$, we have $\Delta P_d = \Delta P_n = |P|$, where P is the pressure in the chamber. Defining the coefficient

$$C = A\sqrt{\frac{2|P|}{\rho^f}}, \tag{6.4}$$

the flow rates can then be expressed as

$$Q_d = \frac{C}{\sqrt{\xi_d}} \quad \text{and} \quad Q_n = \frac{C}{\sqrt{\xi_n}}. \tag{6.5}$$

Since the effect of FSI is not taken into account, we suppose that the chamber volume varies according to

$$V = V_m \sin(2\pi f t) = V_m \sin(\omega t), \tag{6.6}$$

where $f = \omega/2\pi$ is the pumping frequency and V_m is the volume variation amplitude. Thus we can obtain the net flow rate as

$$Q_i - Q_o = \dot{V} = V_m \omega \cos(\omega t), \tag{6.7}$$

where Q_i and Q_o are the flow rate at inlet and outlet, respectively, and $\dot{V}$ is the time derivative of the chamber volume.

During the supply mode the chamber volume increases, i.e $\dot{V} > 0$. In this mode the inlet element acts as a diffuser and the outlet element acts as a nozzle. Hence we obtain the flow rates at inlet and outlet by

$$Q_i = Q_d = \frac{C}{\sqrt{\xi_d}} \quad \text{and} \quad Q_o = -Q_n = -\frac{C}{\sqrt{\xi_n}}. \tag{6.8}$$

The net flow rate is

$$Q_i - Q_o = C\left(\frac{1}{\sqrt{\xi_d}} + \frac{1}{\sqrt{\xi_n}}\right) = V_m \omega \cos(\omega t). \tag{6.9}$$

Consequently, the coefficient C can be calculated with the above equation according to

$$C = V_m \omega \cos(\omega t) \frac{\sqrt{\xi_d \xi_n}}{\sqrt{\xi_d} + \sqrt{\xi_n}} \tag{6.10}$$

with which the flow rate at outlet in the supply mode is obtained as

$$Q_s = \frac{-V_m \omega \cos(\omega t)}{1 + \sqrt{\xi_n/\xi_d}}. \tag{6.11}$$

During the pump mode the chamber volume decreases, i.e. $\dot{V} < 0$, which gives a net flow out of the chamber with the inlet element acting as a nozzle and the outlet element acting as a diffuser. Similarly, we obtain the inlet and outlet flow rate by

$$Q_i = -Q_n = -\frac{C}{\sqrt{\xi_n}} \quad \text{and} \quad Q_o = Q_d = \frac{C}{\sqrt{\xi_d}}. \tag{6.12}$$

The flow rate at outlet for the pump mode is

$$Q_p = -\frac{-V_m \omega \cos(\omega t)}{1 + \sqrt{\xi_d/\xi_n}}. \tag{6.13}$$

Let $T = 1/f$ be the period. In the time span from $-T/4$ to $T/4$ the chamber volume increases, i.e. $\dot{V} > 0$, thus the pump is in the supple mode. In the time span from $T/4$ to $3T/4$ the chamber volume decreases, i.e. $\dot{V} < 0$, thus the pump is in the pump mode. Since the pressure loss coefficients are assumed to be constant throughout the pump cycle, the total pump volume during one complete pump stroke through outlet is obtained by

$$V_o = \int\limits_{-T/4}^{T/4} Q_s \, \mathrm{d}t + \int\limits_{T/4}^{3T/4} Q_p \, \mathrm{d}t = 2V_m \frac{\sqrt{\eta_{nd}} - 1}{\sqrt{\eta_{nd}} + 1}, \tag{6.14}$$

where

$$\eta_{nd} = \xi_n/\xi_d \tag{6.15}$$

is the diffuser efficiency.

Therefore, the average flow rate at outlet is given by

$$Q = \frac{V_o}{T} = \frac{V_m}{\pi} \frac{\sqrt{\eta_{nd}} - 1}{\sqrt{\eta_{nd}} + 1} \omega. \tag{6.16}$$

Equation (6.16) shows that η_{nd} must be larger than 1.0 in order to have a pump action. The pumping flow rate depends on the diffuser efficiency η_{nd}, volume variation amplitude V_m and the pumping frequency ω.

Model with consideration of fluid-structure interaction

In the last section, the model is derived based on the assumption that the chamber volume varies ideally according to a sine function. However, in practice, the fluid is driven by the plate vibration and the fluid in turn resists this vibration, which is a typical FSI problem.

Let us consider a circular plate with radius R_a and use the polar coordinates r and φ in solving the bending problems. According to the bending theory of thin plate (see e.g. [145]), the displacement $W(r, \varphi, t)$ can be described by

$$h\rho^s \frac{\partial^2 W}{\partial t^2} + \frac{Eh^3}{12(1-\nu^2)} \nabla^4 W = f_e - P, \tag{6.17}$$

where h is the thickness, ρ^s is the density, E is the elastic modulus, ν is Poisson's ratio, f_e is the period external excited force per unit area and P is the pressure exerted by the fluid on the plate. The symbol ∇^4 is the two-dimensional double Laplacian operator. The plate is clamped along its edge, i.e. the boundary conditions are

$$W = 0\Big|_{r=R_a} \quad \text{and} \quad \frac{\partial W}{\partial r} = 0\Big|_{r=R_a}. \tag{6.18}$$

The volume variation of the chamber can be calculated as the integral of the plate displacement over the plate area according to

$$V = \int_0^{R_a} W 2\pi r \mathrm{d}r. \tag{6.19}$$

The rate of volume variation fulfils the continuity condition, thus we have

$$\dot{V} = Q_d + Q_n. \tag{6.20}$$

The pressure losses in equation (6.1) can be rewritten in terms of the flow rate according to

$$\Delta P_d = \frac{\rho^f}{2A^2} \xi_d Q_d^2 \quad \text{and} \quad \Delta P_n = \frac{\rho^f}{2A^2} \xi_d Q_n^2. \tag{6.21}$$

Taking equations (6.20) and (6.21) into account, the pressure inside the chamber can be obtained by

$$P = \frac{\rho^f}{2A^2} \frac{|\dot{V}|\dot{V}}{(1/\sqrt{\xi_d} + 1/\sqrt{\xi_n})^2}. \tag{6.22}$$

Substituting the expression (6.22) of P into equation (6.17) we obtain the coupled equation

$$h\rho^s \ddot{W} + \frac{Eh^3}{12(1-\mu^2)} \nabla^4 W + \frac{\rho^f |\dot{V}|}{2A^2(1/\sqrt{\xi_n} + 1/\sqrt{\xi_d})^2} \dot{V} = f_e, \tag{6.23}$$

and the mean flow rate though the outlet

$$Q = \frac{1}{T} \int_T Q_o \mathrm{d}t = \frac{1}{T(\sqrt{\xi_n} + \sqrt{\xi_d})} \int_T \left(\sqrt{\xi_n} H(\dot{V}) + \sqrt{\xi_d} H(-\dot{V}) \right) \dot{V} \mathrm{d}t, \tag{6.24}$$

where T is the period of the excitation force and $H(x)$ is the *Heaviside* function defined by

$$H(x) = \begin{cases} 1 & \text{if } x > 0 \\ 0 & \text{if } x \leqslant 0 \end{cases}. \tag{6.25}$$

From equation (6.24) we know that in order to obtain the mean flow rate, we need to know the value of $\dot{V}$ which is related to the plate displacement W. Therefore, we are looking for an approximate solution to equation (6.23).

For convenience we rewrite the coefficients in equation (6.23) as

$$D = \frac{Eh^3}{12(1-\nu^2)} \quad \text{and} \quad \alpha = \frac{1}{2A^2(1/\sqrt{\xi_n} + 1/\sqrt{\xi_d})^2}. \tag{6.26}$$

Thus we have

$$h\rho^s \ddot{W} + D\nabla^4 W + \alpha|\dot{V}|\dot{V} = f_e. \tag{6.27}$$

Moreover, it is more helpful to rewrite equation (6.27) in terms of the mean displacement of the plate which is defined as

$$X = \frac{1}{A_c}\int_0^{Ra} W 2\pi r \mathrm{d}r, \tag{6.28}$$

where $A_c = \pi R_a^2$ is the area of the plate. Equation (6.27) is integrated over the plate surface area with the individual terms calculated according to

$$\int_0^{R_a} D\nabla^4 W 2\pi r\,\mathrm{d}r = \lambda_E D X/R_a^2, \qquad \int_0^{R_a} \rho\alpha|\dot{V}|\dot{V} 2\pi r\,\mathrm{d}r = A_c\rho\alpha|\dot{V}|\dot{V},$$

$$\int_0^{R_a} h\rho^s \ddot{W} 2\pi r\,\mathrm{d}r = A_c\rho^s h\ddot{X}, \qquad \int_0^{R_a} f_e 2\pi r\,\mathrm{d}r = F_a \sin(\omega t),$$

where F_a is the amplitude of the applied force and λ_E gives the information about how the plate is loaded and the boundary conditions applied to the edge, cf. [10]. Consequently, the coupling equation (6.23) is rewritten as

$$A_c\rho^s h\ddot{X} + \frac{\lambda_E D}{R_a^2} X + A_c\rho^f \alpha|\dot{V}|\dot{V} = F_a \sin(\omega t). \tag{6.29}$$

The volume variation rate can also be expressed as the rate of mean displacement according to $\dot{V} = A_c\dot{X}$.

With the definitions

$$\omega_N^2 = \frac{\lambda_E D/R_a^2}{h\rho^s A_c}, \tag{6.30}$$

$$\beta_m = \frac{A_c^2 \xi_n \xi_d}{2A^2 h(\sqrt{\xi_n} + \sqrt{\xi_d})^2}\frac{\rho^f}{\rho^s} \tag{6.31}$$

and

$$F\omega_N^2 = \frac{F_a}{h\rho^s A_c}, \tag{6.32}$$

equation (6.29) becomes

$$\ddot{X} + \omega_N^2 X + \beta_m|\dot{X}|\dot{X} = F\omega_N^2 \sin(\omega t) \tag{6.33}$$

The above equation shows that the vibration motion of the plate depends on *a*) the first term for the inertia of the membrane; *b*) the second term for the elastic deformation and *c*) the third term for the FSI effect. The parameter β_m can be regarded as the FSI coupling parameter.

In the next step we define $\tau = \omega t$ and rewrite equation (6.33) as

$$\omega^2 \frac{\mathrm{d}^2 X}{\mathrm{d}\tau^2} + \omega_N^2 X + \omega^2 \beta_m \left| \frac{\mathrm{d}X}{\mathrm{d}\tau} \right| \frac{\mathrm{d}X}{\mathrm{d}\tau} = F \omega_N^2 \sin(\tau). \tag{6.34}$$

An approximate solution to equation (6.34) can be constructed with the form

$$X = X_m \sin(\tau - \theta), \tag{6.35}$$

where X_m is the amplitude and θ is the phase shift between the applied force and the response of the plate. Inserting (6.35) into (6.34) we obtain the equation

$$(\omega_N^2 - \omega^2) X_m \sin(\tau - \theta) + X_m^2 \beta_m \omega^2 |\cos(\tau - \theta)| \cos(\tau - \theta) = \omega_N^2 F \sin\tau. \tag{6.36}$$

The first-order harmonic of the non-linear term can be estimated by making use of the Fourier series, i.e.

$$|\cos(\tau - \theta)| \cos(\tau - \theta) \approx \frac{8}{3\pi} \cos(\tau - \theta) + \text{higher order harmonics}. \tag{6.37}$$

In addition, applying the trigonometric identities

$$\begin{aligned} \sin(\tau - \theta) &= \sin\tau \cos\theta - \cos\tau \sin\theta, \\ \cos(\tau - \theta) &= \cos\tau \cos\theta + \sin\tau \sin\theta, \end{aligned} \tag{6.38}$$

equation (6.36) is rewritten as

$$\begin{aligned} &\left((\omega_N^2 - \omega^2) X_m \cos\theta + X_m^2 \beta_m \omega^2 \frac{8}{3\pi} \sin\theta - \omega_N^2 F \right) \sin\tau \\ + &\left((\omega^2 - \omega_N^2) X_m \sin\theta + X_m^2 \beta_m \omega^2 \frac{8}{3\pi} \cos\theta \right) \cos\tau = 0 \end{aligned} \tag{6.39}$$

which yields the following two equations

$$(\omega_N^2 - \omega^2) X_m \cos\theta + X_m^2 \beta_m \omega^2 \frac{8}{3\pi} \sin\theta - \omega_N^2 F = 0, \tag{6.40}$$

$$(\omega^2 - \omega_N^2) X_m \sin\theta + X_m^2 \beta_m \omega^2 \frac{8}{3\pi} \cos\theta = 0. \tag{6.41}$$

Furthermore, we define $R_\omega = \omega / \omega_N$ and rewrite the two equations as

$$(1 - R_\omega^2) X_m \cos\theta + X_m^2 \beta_m R_\omega^2 \frac{8}{3\pi} \sin\theta - \omega_N^2 F = 0, \tag{6.42}$$

$$(R_\omega^2 - 1) X_m \sin\theta + X_m^2 \beta_m R_\omega^2 \frac{8}{3\pi} \cos\theta = 0. \tag{6.43}$$

With equations (6.42) and (6.43), the solutions of X_m and θ are obtained as

$$X_m = \frac{F}{\left(0.5(1 - R_\omega^2)^2 + \sqrt{64 F^2 \beta_m^2 R_\omega^4 / 9\pi^2 + 0.25(1 - R_\omega^2)^4} \right)^{1/2}}, \tag{6.44}$$

$$\theta = \arcsin\left(\frac{F}{\sqrt{F^2 + ((3\pi/16)(1 - R_\omega^2)^2 / \beta_m R_\omega^2)^2} + (3\pi/16)(1 - R_\omega^2)^2 / \beta_m R_\omega^2} \right). \tag{6.45}$$

Substituting $V = X_m \cos(\omega t - \theta) A_c$ into equation (6.24), we obtain the mean flow rate through the micropump as

$$Q = \frac{\sqrt{\xi_n} - \sqrt{\xi_d}}{\sqrt{\xi_n} + \sqrt{\xi_d}} \frac{A_c}{\pi} X_m \omega. \tag{6.46}$$

From equation (6.46) we can see:

- The influence of FSI on the mean flow rate is reflected in the term X_m. According to equation (6.44), X_m increases with decreasing β_m. The FSI coupling parameter β_m has the form

  $$\beta_m = \frac{A_c^2}{2A^2 h(\sqrt{1/\xi_d} + \sqrt{1/\xi_n})^2} \frac{\rho^f}{\rho^s}.$$

  Hence we can increase the flow rate by reducing β_m in the following ways: *a*) reducing the geometry coefficient $A_c^2/(2A^2h)$; *b*) reducing the density ratio ρ^f/ρ^s and *c*) change the pressure loss coefficients such that the value of $\sqrt{1/\xi_d} + \sqrt{1/\xi_n}$ increases.

- If the effect of FSI is weak, i.e. β_m is small, we obtain the relation

  $$Q \propto \frac{\sqrt{\xi_n} - \sqrt{\xi_d}}{\sqrt{\xi_n} + \sqrt{\xi_d}} = \frac{\sqrt{\xi_n/\xi_d} - 1}{\sqrt{\xi_n/\xi_d} + 1} = \frac{\sqrt{\eta_{nd}} - 1}{\sqrt{\eta_{nd}} + 1}. \tag{6.47}$$

  Therefore, the larger diffuser efficiency η_{nd}, the larger the mean flow. It coincides with the conclusion drawn from the model without consideration of FSI.

- Increasing the chamber radius, the pumping frequency and external pressure amplitude on the plate can increase the pumping flow rate.

- Fluid properties, such as viscoelasticity, can influence the pressure loss coefficient ξ_n and ξ_d in diffuser and nozzle and thus the mean flow rate. Therefore, it is worth investigating the viscoelastic fluid flow in a diffuser/nozzle element.

6.2 Simulation of the viscoelastic fluid flow in a diffuser/nozzle element

From the above discussion we know that the diffuser efficiency plays a vital role in the pumping performance. Although the geometry of the diffuser/nozzle element is simple, the fluid flow inside is complicated. There is no good analytical expression for the flow-pressure characteristics in a diffuser flow, cf. [104]. The diffuser efficiency η_{nd} defined in (6.15) is usually investigated via experiments and simulations. For Newtonian fluids, numerical investigation has been done in, e.g. [104, 134, 12]. It has been found that the diffuser efficiency η_{nd} depends on the geometry of the diffuser element and the flow Reynolds number. It is interesting and important to know how this coefficient is influenced by different Weissenberg numbers for the viscoelastic fluid flow. Therefore, the diffuser efficiency is investigated in this section. Both two-dimensional and three-dimensional diffuser/nozzle elements are studied.

Two-dimensional diffuser/nozzle element

The geometry of the investigated two-dimensional diffuser/nozzle element is shown in figure 6.2. The width of the narrow side is $W_1 = 8.0 \times 10^{-5}\,\mathrm{m}$. The narrow channel and wide channel have the same length as the convergent(divergent) channel with $L = 0.001\,\mathrm{m}$. Opening angle α varies from 1° to 11°.

The investigated fluid has density $\rho^f = 998\,\mathrm{kg/m^3}$, solvent viscosity $\eta_s = 0.003\,\mathrm{pa \cdot s}$, polymer viscosity $\eta_p = 0.0045\,\mathrm{pa \cdot s}$. A constant volume flux is given at the narrow side for the diffuser direction or at the wide side for the nozzle direction. With these parameters the Reynolds number with respect to the velocity and width at the narrow side is $\mathrm{Re} = 50$. The fluid relaxation time is varied from $8.51 \times 10^{-7}\,\mathrm{s}$ to $8.51 \times 10^{-6}\,\mathrm{s}$. The correspondent Weissenberg numbers are varied from 0.1 to 1.0.

The pressure loss is measured along the whole length of the element. In every single simulation the pressure loss coefficients ξ_d and ξ_n are calculated according to equation (6.1) by

$$\xi_d = \frac{2\Delta P_d}{\rho^f u_d^2} \quad \text{and} \quad \xi_n = \frac{2\Delta P_n}{\rho^f u_n^2},$$

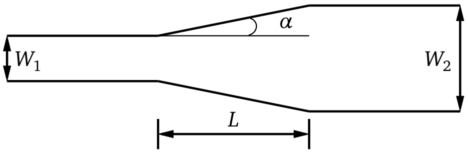

Figure 6.2.: Geometry of a two-dimensional diffuser/nozzle element

where u_d and u_n are the mean velocities at the narrow side for the differ and nozzle direction, respectively. The diffuser efficiency is obtained by

$$\eta_{nd} = \xi_n / \xi_d. \tag{6.48}$$

The values of diffuser efficiency for different Weissenberg numbers and opening angles are listed in table 6.1. These values are also plotted in figure 6.3. It is evident that for all the concerned opening angles the diffuser efficiency decreases with increasing Weissenberg number. In addition, for a fixed Weissenberg number the diffuser efficiency has a maximum as depicted in figure 6.3 (b). The maximum occurs at the opening angle 7°.

Wi	1°	3°	5°	7°	9°	11°
0.1	1.3100	1.8133	2.0812	2.1924	2.1648	2.0976
0.2	1.3026	1.7945	2.0564	2.1656	2.1412	2.0758
0.3	1.2951	1.7760	2.0321	2.1393	2.1180	2.0542
0.4	1.2876	1.7578	2.0083	2.1136	2.0953	2.0330
0.5	1.2803	1.7399	1.9849	2.0883	2.0728	2.0120
0.6	1.2729	1.7225	1.9619	2.0634	2.0505	1.9910
0.7	1.2656	1.7049	1.9392	2.0388	2.0285	1.9703
0.8	1.2585	1.6877	1.9170	2.0146	2.0066	1.9496
0.9	1.2513	1.6708	1.8949	1.9906	1.9848	1.9290
1.0	1.2441	1.6540	1.8732	1.9669	1.9631	1.9084

Table 6.1.: Diffuser efficiency for different Weissenberg numbers and opening angles

Three-dimensional diffuser/nozzle element

The three-dimensional diffuser/nozzle element has thickness $8. \times 10^{-5}\,\mathrm{m}$. Other geometry parameters of the elements, fluid property and inlet volume flux is the same as the two-dimensional one, i.e. the investigated fluid has density $\rho^f = 998\,\mathrm{kg/m^3}$, solvent viscosity $\eta_s = 0.003\,\mathrm{pa \cdot s}$, polymer viscosity $\eta_p = 0.0045\,\mathrm{pa \cdot s}$. A constant volume flux is given at the narrow side for the diffuser direction or at the wide side for the nozzle direction. With these parameters the Reynolds number with respect to the velocity and width at the narrow side is $\mathrm{Re} = 50$. The fluid relaxation time is varied from $8.51 \times 10^{-7}\,\mathrm{s}$ to $8.51 \times 10^{-6}\,\mathrm{s}$. The correspondent Weissenberg numbers are 0.1 to 1.0.

The simulation results are shown in table 6.2 and figure 6.4. From figure 6.4 (a) we see that the diffuser efficiency decreases as the Weissenberg number increases, which is the same phenomenon as observed in the two-dimensional case. At a fixed Weissenberg number the diffuser efficiency increases as the opening angle increases. However, there is not significant change when the angle is larger than 13°, see figure 6.4 (a). The maximum occurs at an opening angle of 15°.

6.3 Simulation of a valveless micropump pumping viscoelastic fluids

In this section the simulation techniques for FSI presented in chapter 5 is applied to simulate a valveless micropump. As for a preliminary study, a two-dimensional pump is first investigated. Thereafter, a three-dimensional

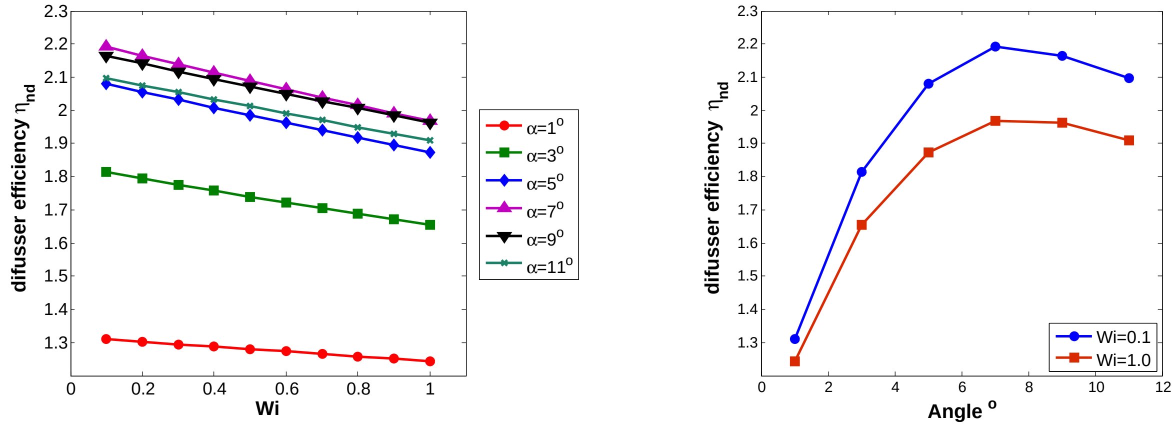

(a) (b)

Figure 6.3.: Diffuser efficiency for different Weissenberg numbers and opening angles

Wi	1°	3°	5°	7°	9°	11°	13°	15°	17°
0.1	1.0862	1.1808	1.2242	1.2458	1.2569	1.2624	1.2647	1.2654	1.2652
0.2	1.0847	1.1783	1.2212	1.2428	1.2539	1.2595	1.2620	1.2628	1.2627
0.3	1.0837	1.1765	1.2193	1.2408	1.2520	1.2577	1.2603	1.2612	1.2612
0.4	1.0827	1.1750	1.2177	1.2392	1.2505	1.2563	1.2590	1.2599	1.2599
0.5	1.0818	1.1737	1.2163	1.2379	1.2493	1.2551	1.2579	1.2588	1.2587
0.6	1.0811	1.1725	1.2151	1.2368	1.2483	1.2542	1.2569	1.2578	1.2576
0.7	1.0803	1.1715	1.2142	1.2359	1.2474	1.2534	1.2561	1.2569	1.2566
0.8	1.0797	1.1706	1.2133	1.2351	1.2467	1.2527	1.2554	1.2561	1.2557
0.9	1.0791	1.1698	1.2126	1.2345	1.2461	1.2521	1.2548	1.2554	1.2548
1.0	1.0785	1.1691	1.2119	1.2339	1.2456	1.2516	1.2543	1.2548	1.2541

Table 6.2.: Diffuser efficiency for different Weissenberg numbers and opening angles in a three-dimensional diffuser/nozzle element

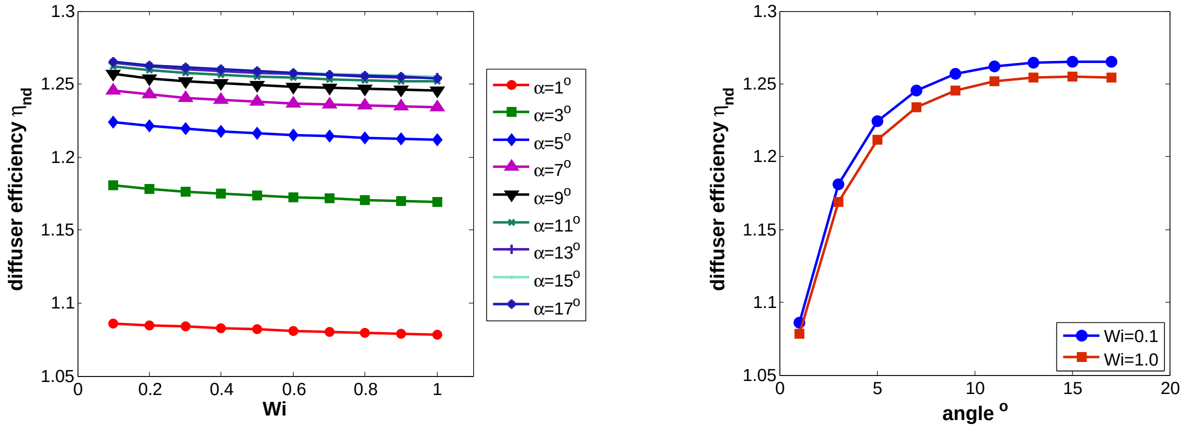

(a) (b)

Figure 6.4.: Diffuser efficiency for different Weissenberg numbers and opening angles in a three-dimensional diffuser/nozzle element

pump is simulated. We investigate the pumping flow rate influenced by the fluid relaxation time of the viscoelastic fluid.

Two-dimensional valveless micropump

The geometry of the micropump is shown in figure 6.5 and table 6.3. The physical properties of the pumping fluid and the elastic plate are displayed in table 6.4. The pressures at inlet and outlet are set to zero, whereas the pressure exerted on the elastic plate is $p_e = p\sin(2\pi f t)$. Different values of amplitude and frequency are chosen in the simulation.

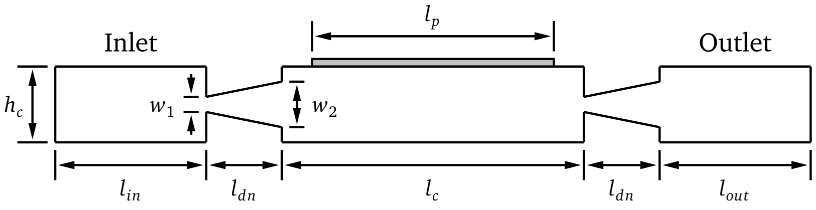

Figure 6.5.: Geometry of a two-dimensional valveless micropump

Element	Item	Size
Chamber	length l_c	7.0×10^{-3} m
	height h_c	1.0×10^{-3} m
Diffuser/nozzle element	length l_{dn}	1.0×10^{-3} m
	height at narrow side w_1	4.0×10^{-5} m
	height at wide side w_2	5.0×10^{-4} m
	Opening angle α	12.95°
Elastic plate	length l_p	5.0×10^{-3} m
	height h_p	1.0×10^{-4} m

Table 6.3.: Geometrical parameters of a two-dimensional valveless micropump

Pumping fluid	density ρ^f	1.0×10^{3} kg/m^3
	viscosity η	1.0×10^{-3} pa · s
	relaxation time λ^f	0 s, 0.01 s, 0.1 s and 1.0 s
Elastic plate	density ρ^s	8.0×10^{3} kg/m^3
	Elastic modulus E	1.0×10^{11} Pa
	Poisson's ratio ν	0.495

Table 6.4.: Physical properties of the pumping fluid and the elastic plate in the two-dimensional pump

Firstly, simulation is done with the pumping medium of a Newtonian fluid. The mean flow direction can be measured by $Q_{net} = Q_{inlet} + Q_{outlet}$. This quantity is shown in figure 6.6 for *a*) different pumping frequencies f = 5 Hz, 10 Hz and 15 Hz and fixed external pressure amplitude $p = 2$ kPa; *b*) different external pressure amplitudes $p = 2$ kPa and 3 kPa and fixed pumping frequency 10 Hz. For all the cases, the mean flow direction is from inlet to outlet. The net flow rate increases with increasing pumping frequency and external pressure.

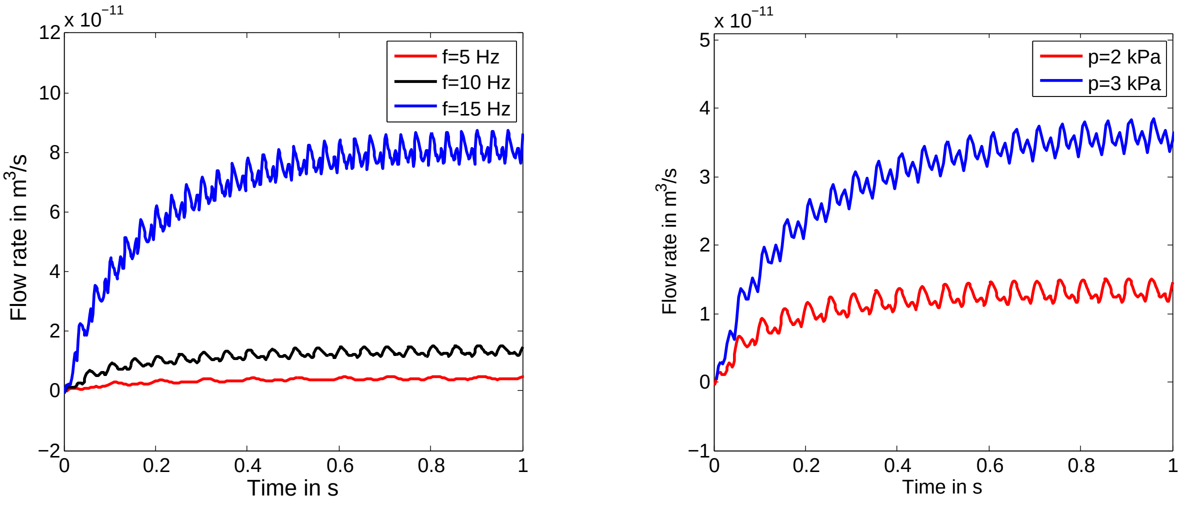

(a) (b)

Figure 6.6.: Net flow rates $Q_{net} = Q_{inlet} + Q_{outlet}$ for a Newtonian fluid with (a) different pumping frequencies and (b) different external pressure amplitudes

In particular, we observe the mean flow rate at outlet. Figure 6.7 shows, e.g., the outlet flow rate with pumping frequencies 10 Hz and external pressure amplitudes 2 kPa. We calculate the mean outlet flow rates for different pumping frequencies with fixed external pressure amplitude $p = 2\,\text{kPa}$. They are

$$\begin{aligned} Q &= 0.1115 \times 10^{-10}\,\text{m}^3/\text{s} &&\text{for}\quad f = 5\,\text{Hz},\\ Q &= 0.8670 \times 10^{-10}\,\text{m}^3/\text{s} &&\text{for}\quad f = 10\,\text{Hz},\\ Q &= 3.5273 \times 10^{-10}\,\text{m}^3/\text{s} &&\text{for}\quad f = 15\,\text{Hz}. \end{aligned}$$

When the pumping frequency is fixed at 10 Hz, the flow rates for different external pressure amplitude are

$$\begin{aligned} Q &= 0.8670 \times 10^{-10}\,\text{m}^3/\text{s} &&\text{for}\quad p = 2\,\text{kPa},\\ Q &= 1.3848 \times 10^{-10}\,\text{m}^3/\text{s} &&\text{for}\quad p = 3\,\text{kPa}. \end{aligned}$$

The results show that the flow rate increases with increasing pumping frequency and external pressure amplitude, which agrees with the conclusion drawn from the semi-analytical model (6.46) and from the observation in experiments, see e.g. [153]

Secondly, we consider Oldroyd-B fluid as the pumping medium. The external pressure amplitude and the pumping frequency are set to $p = 2\,\text{kPa}$ and $f = 10\,\text{Hz}$, respectively. The fluid relaxation time is changed from 0.01 s to 1 s. The outlet flow rates for these different fluid relaxation times are shown in figure 6.8. The computed mean outlet flow rates for these fluid relaxation times are

$$\begin{aligned} Q &= 12.978 \times 10^{-11}\,\text{m}^3/\text{s} &&\text{with}\quad \lambda = 0.01\,\text{s},\\ Q &= 8.065 \times 10^{-11}\,\text{m}^3/\text{s} &&\text{with}\quad \lambda = 0.1\,\text{s},\\ Q &= 5.624 \times 10^{-11}\,\text{m}^3/\text{s} &&\text{with}\quad \lambda = 1.0\,\text{s}. \end{aligned}$$

We can clearly see that the mean outlet flow rate decreases as the fluid relaxation time increases. A two dimensional diffuser/nozzle element has been studied in the previous section. We have learned that the diffuser efficiency η_{nd} decreases as the fluid relaxation time increases. The change of the diffuser efficiency influences the outlet flow rate.

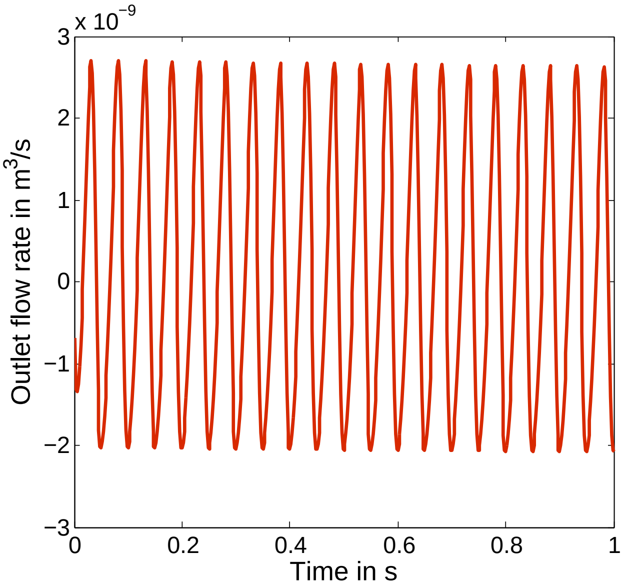

Figure 6.7.: Outlet flow rate for a Newtonian fluid with pumping frequencies $10\,\mathrm{Hz}$ and external pressure amplitudes $2\,\mathrm{kPa}$

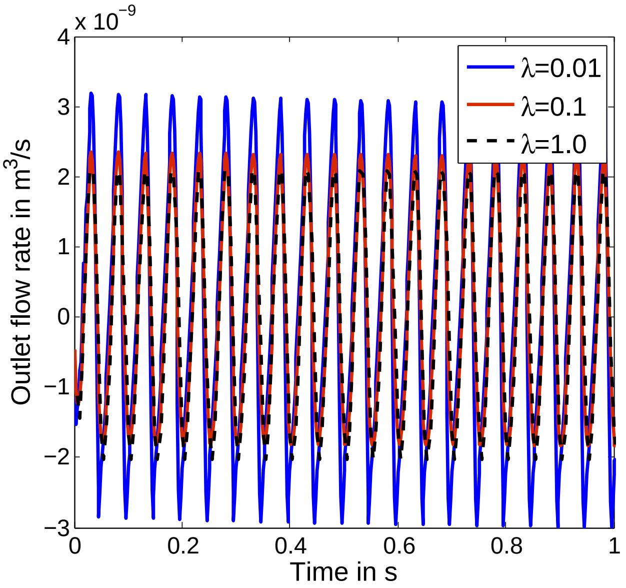

Figure 6.8.: Outlet flow rates for an Oldroyd-B fluid with different fluid relaxation time

Three-dimensional valveless micropump

A three-dimensional valveless micropump is here studied. We employ the same geometrical parameters of the pump and physical parameters of the pumping fluid and the vibrating plate as used in [87]. In [87] experiments have been done for a valveless micropump pumping ethanol, a Newtonian fluid. We compare the simulation results with the experiment ones for Newtonian fluid, then investigate viscoelastic fluid by increasing the fluid relaxation time.

The investigated micropump consists of a chamber, two tapered diffuser/nozzle elements for the inlet and outlet and a Polyimide (PI) thin plate, see figure 6.9. The thickness of PI plate is 2.1 μm, the diameter of the chamber is 2 mm, and the depth of the chamber is 60 μm. The diffuser/nozzle elements have throat widths 40 μm and 145 μm for the narrow side and wide side, respectively. The length of the diffuser is 600 μm. The diffuser angle 2θ is 10°. The PI film has Young's modulus 2.6 GPa and Poisson's ratio 0.34. In the experiment in [87] ethanol is employed for the pumping fluid which has density 789 kg/m^3 and viscosity 1.2 mPa $\cdot$ s. These parameters are listed in table 6.5 and 6.6.

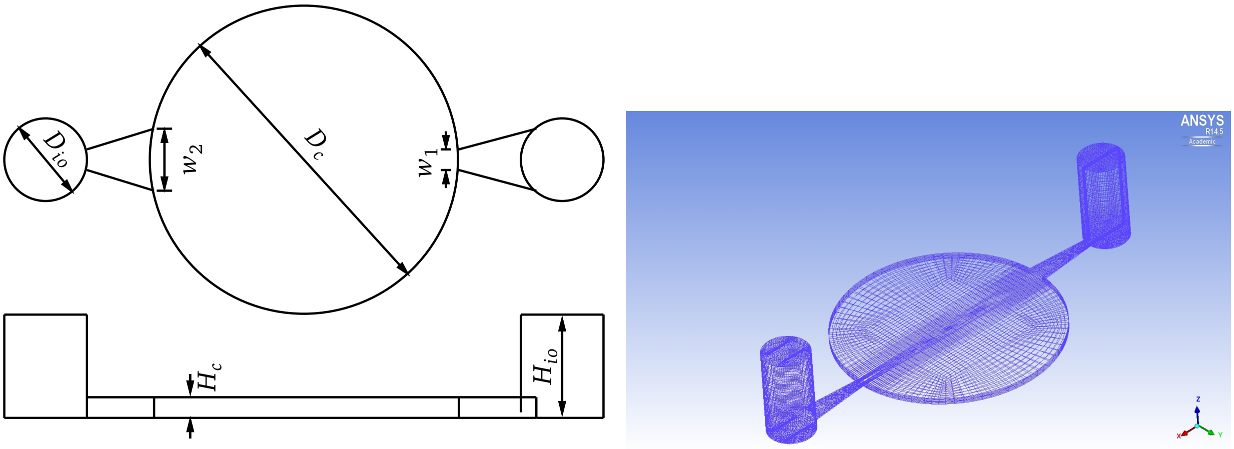

(a)

(b)

Figure 6.9.: Geometry of the three-dimensional valveless micropump

Element	Item	Size
Chamber	diameter D_c	2.0×10^{-3} m
	height H_c	6.0×10^{-5} m
Inlet/outlet	diameter D_{io}	4.0×10^{-4} m
	height H_{io}	8.13×10^{-4} m
Diffuser/nozzle element	length l_{dn}	6.0×10^{-4} m
	width at narrow side w_1	4.0×10^{-5} m
	width at wide side w_2	1.45×10^{-4} m
	Opening angle α	5°
Elastic plate	length l_p	2.0×10^{-3} m
	thickness h_p	2.1×10^{-6} m

Table 6.5.: Geometrical parameters of a three-dimensional micropump

In the following we first study the plate characterization and the diffuser efficiency of the diffuser/nozzle element separately, then simulate the whole pump to investigate the outlet flow rate.

Pumping fluid	density ρ^f	789 kg/m^3
	viscosity η	1.2×10^{-3} pa · s
	relaxation time λ^f	0 s, 0.01 s, 0.1 s and 1.0 s
Elastic plate	density ρ^s	1430 kg/m^3
	Elastic modulus E	2.6×10^9 Pa
	Poisson's ratio ν	0.34

Table 6.6.: Physical parameters of the pumping fluid and the elastic plate in the three-dimensional pump

Plate characterization

We investigate the plate deformation without interaction with the fluid. The natural frequencies of a clamped circular plate can be determined by

$$f_N = \frac{\alpha^2}{2\pi R_a^2}\sqrt{\frac{D}{\rho^s h_p}}, \tag{6.49}$$

where $D = Eh_p^3/(12(1-\nu^2))$ and α is determined by solving the equation

$$J_0(\alpha)I_1(\alpha) + I_0(\alpha)J_1(\alpha) = 0,$$

where J_0 and J_1 are the Bessel functions of first kind of order zero and order one, respectively. I_0 and I_1 are the modified Bessel functions of first kind of order zero and order one, respectively. The derivation and description of equation (6.49) can found in, e.g. [145]. The frequencies of the first three modes are: $f_{N1} = 1413\,\text{Hz}$, $f_{N2} = 5502\,\text{Hz}$ and $f_{N3} = 123270\,\text{Hz}$. The applied pressure frequency $f = 2.5\,\text{Hz}$ is significantly lower than the natural frequency of any mode.

To investigate the deformation of the plate under applied pressure $p = 5000\sin(2\pi \cdot 2.5t)\,\text{Pa}$, we use the FEM solver FEAP and discretize the plate with 900 hexahedral grids. The deformation of the plate in one period is shown in figure 6.10 (a). The largest deflection is located at the center point. The displacement of the center point is shown in figure 6.10 (b). The amplitude is 4.1733×10^{-5} m. This value is smaller than the height of the chamber, which prevents the plate from touching the bottom of the chamber.

Diffuser efficiency of the diffuser/nozzle element

According to the experiment data of the average outlet flow rate given in [87], we estimate the average velocity flowing through the narrow side of the diffuser/nozzle element as $\bar{u} = 2.778 \times 10^{-3}$ m/s. The corresponding Reynolds number is Re $= 0.073$. The computation of the diffuser efficiency is done with this Reynolds number following the procedure shown in section 6.2. We choose the fluid relaxation time ranging from 0.001 s to 0.05 s. The results are shown in table 6.7 and figure 6.11.

We can clearly see that the diffuser efficiency decreases as the relaxation time decreases. Moreover, the diffuser efficiency falls below 1.0 when $\lambda \geqslant 0.04$ s. We know from section 6.1 that the diffuser efficiency is required to be larger than 1.0 in order to achieve pump action. In the next section we choose the fluid relaxation time ranging from 0.001 s to 0.01 s to investigate the outlet flow rate.

Outlet flow rate

First of all, we use a Newtonian fluid as the pumping medium and compare the simulated result with the experimental one. The computed average outlet flow rate is 5.8255×10^{-12} m^3/s. Compared with the experimental result of 6.6667×10^{-12} m^3/s, the relative error is 12.61%, which is acceptable for such a complex problem where also in the experiment many sources for possible errors are present.

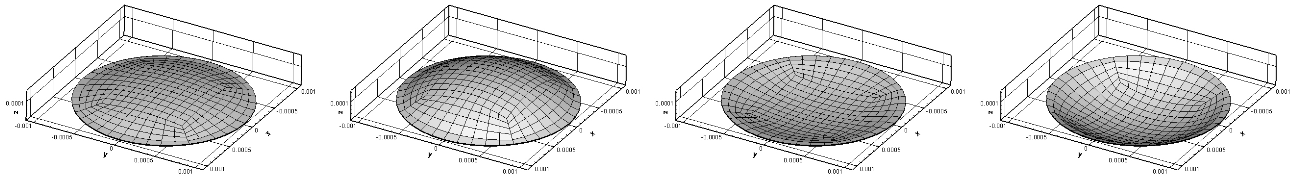

(a) Deformation of the whole plate in one period

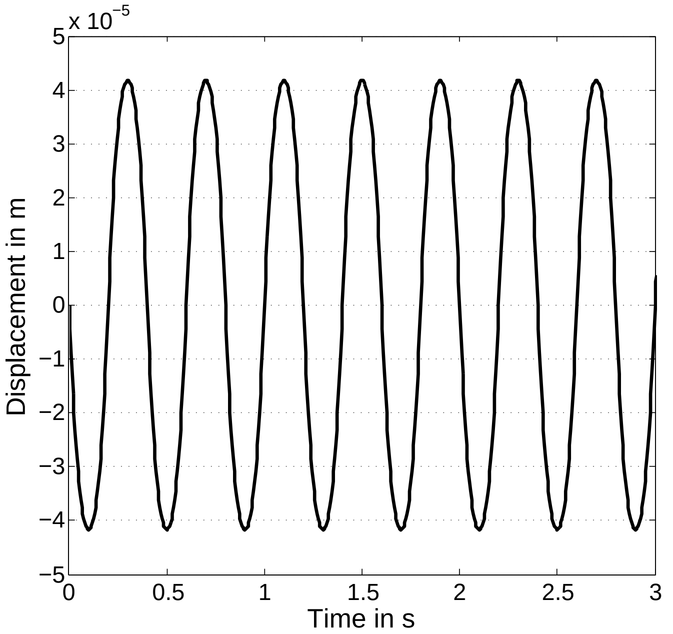

(b) Deflection of the middle point

Figure 6.10.: Deformations of the plate

λ in s	ξ_d	ξ_n	η_{nd}
0.001	10702.47	10719.73	1.001612
0.002	10702.60	10719.37	1.001567
0.003	10702.73	10719.05	1.001524
0.004	10702.86	10718.69	1.001479
0.005	10702.99	10718.33	1.001433
0.006	10703.12	10717.98	1.001388
0.007	10703.25	10717.65	1.001345
0.008	10703.38	10717.29	1.001300
0.009	10703.55	10716.97	1.001254
0.01	10703.68	10716.61	1.001208
0.02	10705.17	10713.33	1.000762
0.03	10706.68	10710.24	1.000316
0.04	10708.65	10707.28	0.999873
0.05	10710.79	10704.52	0.999414

Table 6.7.: Pressure loss coefficients ξ_d (diffuser) and ξ_n (nozzle) and diffuser efficiency η_{nd} for different fluid relaxation times λ

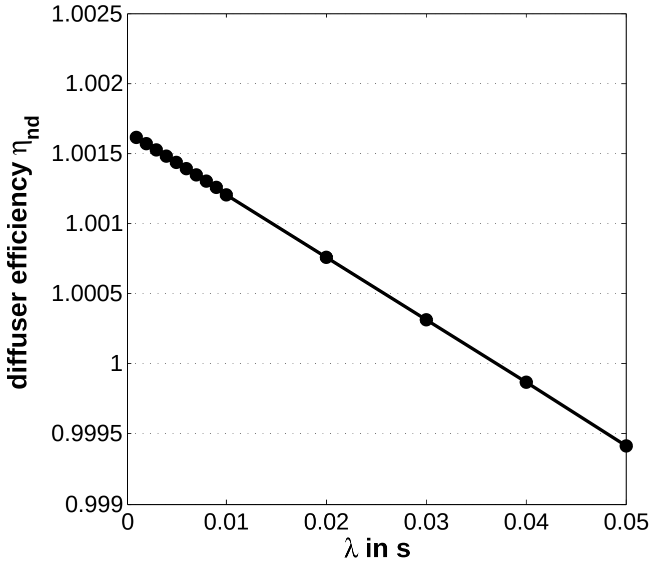

Figure 6.11.: Diffuser efficiency for different fluid relaxation times

Next, we set the fluid relaxation time to $\lambda = 0.002\,\mathrm{s}$, $0.004\,\mathrm{s}$, $0.006\,\mathrm{s}$, $0.008\,\mathrm{s}$ and $0.01\,\mathrm{s}$. Figure 6.12 shows the outlet flow rates for different fluid relaxation times. For all these relaxation times there is a transition interval (about two periods) before the flow rate reaches steady state. When the flow reaches steady state, the mean outlet flow rates for various fluid relaxation times are:

$$\begin{aligned}
Q &= 6.0976 \times 10^{-12}\,\mathrm{m^3/s} && \text{for} \quad \lambda = 0.002\,\mathrm{s},\\
Q &= 6.0937 \times 10^{-12}\,\mathrm{m^3/s} && \text{for} \quad \lambda = 0.004\,\mathrm{s},\\
Q &= 6.0899 \times 10^{-12}\,\mathrm{m^3/s} && \text{for} \quad \lambda = 0.006\,\mathrm{s},\\
Q &= 6.0862 \times 10^{-12}\,\mathrm{m^3/s} && \text{for} \quad \lambda = 0.008\,\mathrm{s},\\
Q &= 6.0826 \times 10^{-12}\,\mathrm{m^3/s} && \text{for} \quad \lambda = 0.01\,\mathrm{s}.
\end{aligned}$$

The above results show that the outlet flow rate decreases when the fluid relaxation time increases from 0.002 s to 0.01 s. This trend can also be predicted with the semi-analytical model (6.46). We substitute the physical parameters into the model (6.46). The values of the pressure loss coefficient are taken from the simulation results shown in table 6.7. The calculated results are shown in figure 6.13 (b). Although these values have deviation from the simulation, they predict the same trend of change of the outlet flow rate with different fluid relaxation times. Since the deviation is large, it is strongly needed to consider the fully VFSI to improve the model.

Summary

A two-dimensional as well as a three-dimensional valveless micropump is investigated via VFSI simulations. The outlet flow rates with different pumping frequencies, external pressure amplitudes are investigated in the two-dimensional case. The flow rate increases with increasing pumping frequency and external pressure amplitude. This trend agrees with the conclusion drawn from the semi-analytical model and the observation in experiments. When the pumping medium is an Oldroyd-B fluid, the outlet flow rate decreases with increasing fluid relaxation time.

The investigation of a three-dimensional micropump starts with the comparison of the outlet flow rate obtained from simulation and experiment using a Newtonian fluid as pumping medium. The deviation of the simulated result is in an acceptable range. Using an Oldroyd-B fluid as pumping medium, the outlet flow rates with different fluid

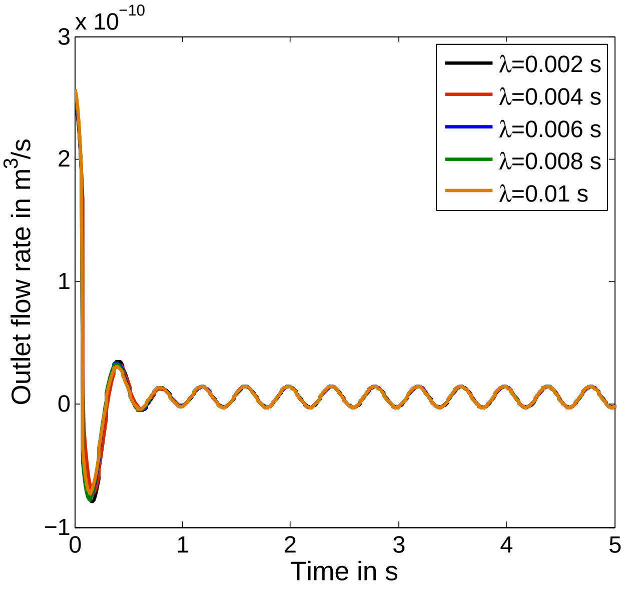

Figure 6.12.: Outlet flow rates for an Oldroyd-B fluid with different fluid relaxation times

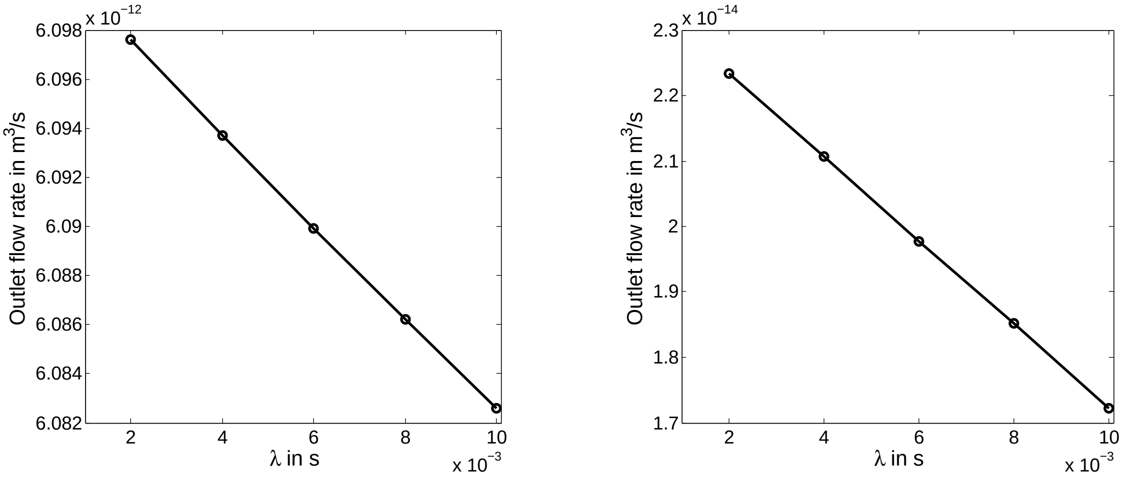

(a) Simulation

(b) Semi-analytical model

Figure 6.13.: Outlet flow rates for Oldroyd-B fluids with different fluid relaxation times (a) Result from simulation (b) Result from semi-analytical model

relaxation times are studied. For the investigated fluid relaxation times, the flow rate decreases with increasing relaxation time. This trend is also predicted with the semi-analytical model, but deviation of the predicted valued compared to simulation is found. An improvement of the semi-analytical model is required in the future work.

7 Summary and outlook

In the present work a framework for numerical modeling of the interaction between viscoelastic fluids and elastic solids is developed and implemented. The phenomenon of viscoelastic fluid-structure interaction (VFSI) is studied via numerical modeling. The aim of the work is to gain deeper insight into the VFSI problem which is an interdisciplinary research topic based on computational rheology and fluid-structure interaction (FSI).

An implicit partitioned coupling algorithm is employed for fluid-structure coupling. For the fluid part the in-house finite-volume program FASTEST is used. In order to simulate viscoelastic fluid flows, the solver for such flows is developed within FASTEST. The finite-element program FEAP is employed for the solid part. The data transfer between the fluid and solid part within the partitioned solution algorithm is performed via an interface, realized by the coupling software MpCCI.

Three main topics are discussed in the present work: *1*) numerical modeling of viscoelastic fluid flow; *2*) numerical modeling of viscoelastic fluid-structure interaction and *3*) direct numerical simulation of a valveless micropump.

Since numerical modeling of viscoelastic fluid flow is the most important and difficult part within a VFSI problem, the present work begins with this topic. The question of how to choose suitable stable and accurate numerical schemes for practical simulation is deeply discussed.

The stability problem in simulation of viscoelastic fluid flow is referred to as the so-called *High Weissenberg Number Problem* (HWNP) which is identified by the difficulty of convergence of iterative algorithms in numerical simulation when the Weissenberg number is above certain values. In order to cope with the problem, preserving the positive definiteness of the conformation tensor is crucial in the simulation. In the present work four approaches to cope with the HWNP are compared and discussed. These are the *both-sides diffusion* (BSD), the *positive definiteness preserving scheme* (PDPS), the *log-conformation representation* (LCR) and the *square root-conformation representation* (SRCR). The most important conclusions drawn from the comparison are:

- LCR and SRCR are the most stable schemes for high Weissenberg number flow. PDPS preserves the positive definiteness of the conformation tensor, while BSD can not. Yet, an additional attractive advantage of BSD is that it can well solve the stability problem caused by small viscosity ratios.
- LCR has a higher convergence rate than the other approaches.
- SRCR provides the advantage of shorter computation time compared to LCR. At moderate Weissenberg numbers SRCR is an optimal choice in computation.

A detailed description of the features and capabilities of the stabilization approaches is given in table 4.14. This table can be regarded as a guide to choose suitable stabilization approaches in simulation of viscoelastic fluid flow.

The accuracy problem in simulation of viscoelastic fluid flow stems from the fact that the constitutive equation is advection-dominated. In order to achieve accurate and oscillation-free results, *high resolution scheme* (HRS) must be applied for the advection. Three treatments have been proposed to adapt HRS in the program FASTEST:

- Using Normalized Variable and Space Formulation (NVSF) for non-uniform grids.
- Construction of virtual upwind points to deal with the data transferring between block boundaries.
- Using deferred correction representation to decrease the implementation effort.

In the second main topic, numerical modeling of viscoelastic fluid-structure interaction, we discuss the question of what are the different behaviours between VFSI and Newtonian fluid-structure interaction (NFSI).

Besides simulations, a *mass-spring-dashpot* (MSD) model is employed to investigate the solution of VFSI problems. The simulation and the MSD model are consistent in the qualitative analysis of the dynamic behaviour in VFSI. Thus the MSD model can be used alternatively as an effective tool for qualitative analysis for VFSI systems. Significant dynamic behaviours of VFSI systems are summarized as follows:

- The solution of a VFSI problem is more complicated than that of an NFSI problem. In free oscillation there are three types of solution. The first (ST1) and second type (ST2) are fully exponential damped. The third type (ST3) is a combination of a periodic part with exponentially damped amplitude and an exponential decay without oscillation.
- The solid deformation is influenced by the Weissenberg number in both forced and free oscillation. In forced oscillation, the amplitude, the equilibrium position and the phase shift are different for different Weissenberg numbers, whereas in free oscillation the amplitude, the equilibrium position, the frequency and the phase shift are changed.

Regarding the convergence properties of the proposed implicit partitioned coupling algorithm for VFSI, we have found:

- The implicit partitioned algorithm can be well applied for VFSI problems. However, similar to NFSI problems, there is the added mass effect, when the density ratio of fluid to solid is large.
- The fluid relaxation time also influences the rate of convergence. The larger the fluid relaxation time, the more slowly the computation converges.

As for an example of application of the developed viscoelastic fluid flow solver and the implicit partitioned coupling algorithm for VFSI, the third main topic is direct numerical simulation of a valveless micropump. We focus on the question of how does the volumetric flow rate vary with different relaxation times of the pumping fluid.

The discussion starts with the construction of a semi-analytical model with which we use for qualitative analysis. We have simulated a three-dimensional valveless micropump using a Newtonian fluid as pumping medium. The deviation of the simulated result is in an acceptable range compared with the experiment. Using an Oldroyd-B fluid as pumping medium, the outlet flow rate with different fluid relaxation times is studied. For the investigated fluid relaxation times, the flow rate decreases with increasing relaxation time. Qualitatively, this trend is also predicted with the semi-analytical model.

The solver development and phenomenon investigation in the present work is only a beginning of the research for VFSI. They have limitations. The solver is required to be extended and the further investigation should be done.

In this work only Oldroyd-B fluid is investigated. The reason for choosing this model for investigation is that it has the simplest form and poses the most severe numerical difficulties. Once the Oldroyd-B model is implemented and the numerical difficulties are overcome, the implementation and investigation of other models are direct forward. In order to simulate practical applications, other models, such as PTT and Giesekus models, are usually required. Therefore, investigation of other models is required in the future work.

Four stabilization approaches for simulation of viscoelastic fluid flow are applied for the simulations and comprehensively compared in the present work. However, the High Weissenberg Number Problem has not been completely solved. The stabilization techniques are still being developed. New approaches appeared in recent years, e.g. the kernel conformation representation by Afonso et al. [4]. It is worth testing these new approaches in the future to optimize the computation for practical usage.

The influence of temperature has not been considered in the present work. In practical applications a thermal fluid-structure interaction usually occurs as well. Therefore, it is reasonable to extend the current framework of VFSI to thermal VFSI.

As for another potential application of VFSI, we can merge the simulation techniques of multiphase flow into the VFSI numerical framework to simulate the stirred tank in mixing process. The proposed VFSI numerical framework can also be used for investigation of micro-organism and micro-robot swimming in viscoelastic fluids which is currently a hot interdisciplinary research topic.

A Derivation of objective time derivative

The derivation follows the work of Joseph [71].

To facilitate the presentation of the body-fixed frames, one of the possibilities is that we cover the body with a convected coordinate system ξ^i. A convected coordinate system deforms with the body so that the coordinates (ξ^1, ξ^2, ξ^3) associated with a particular material point do not change with time. Base vector $\mathbf{g}_i$ at a material point are defined by

$$\mathbf{g}_i(\xi^1,\xi^2,\xi^3,t) = \frac{\partial}{\partial \xi^i}\mathbf{x}(\xi^1,\xi^2,\xi^3,t), \tag{A.1}$$

where $\mathbf{x}(\xi^1,\xi^2,\xi^3,t)$ is the position vector at time t of the material point with convected coordinates (ξ^1,ξ^2,ξ^3). A three-dimensional tensor, taking the example of the stress tensor σ, can be expressed with respect to the basis $\mathbf{g}_i\mathbf{g}_j$ according to

$$\sigma(\xi,t) = \sigma^{ij}(\xi,t)\mathbf{g}_i(\xi,t)\mathbf{g}_j(\xi,t), \tag{A.2}$$

where ξ is shorthand for the convected label (ξ^1,ξ^2,ξ^3) of the material point.

The frame at the material point with basis g_1, g_2, g_3 rotates and deforms with the neighbourhood of the point. As a first choice of invariant tensor rate, we define the rate of tensor σ to be the time derivative of σ with respect to this body fixed frame, i.e.

$$\frac{\mathrm{D}\sigma}{\mathrm{D}t} = \left(\frac{\partial}{\partial t}\sigma^{ij}(\xi,t)\right)\mathbf{g}_i(\xi,t)\mathbf{g}_j(\xi,t). \tag{A.3}$$

The rate defined in equation is different from the material derivative $\mathrm{d}\sigma/\mathrm{d}t$, because it ignores the change of the base vectors $\mathbf{g}_i$ with time. We remove the dependence on convected coordinates from the rate definition. Taking the material derivative it yields

$$\begin{aligned}\frac{\mathrm{d}\sigma}{\mathrm{d}t} &= \left(\frac{\partial}{\partial t}\sigma^{ij}(\xi,t)\right)\mathbf{g}_i(\xi,t)\mathbf{g}_j(\xi,t)\\ &\quad+\sigma^{ij}(\xi,t)\left(\frac{\partial}{\partial t}\mathbf{g}_i(\xi,t)\right)\mathbf{g}_j(\xi,t)+\sigma^{ij}(\xi,t)\mathbf{g}_i(\xi,t)\left(\frac{\partial}{\partial t}\mathbf{g}_j(\xi,t)\right).\end{aligned} \tag{A.4}$$

Considering

$$\begin{aligned}\frac{\mathrm{d}\mathbf{g}_i}{\mathrm{d}t} &= \frac{\partial}{\partial t}\mathbf{g}_i(\xi,t)\\ &= \frac{\partial}{\partial t}\left(\frac{\partial}{\partial \xi^i}\mathbf{x}(\xi,t)\right) = \frac{\partial}{\partial \xi^i}\left(\frac{\partial}{\partial t}\mathbf{x}(\xi,t)\right)\\ &= \frac{\partial}{\partial \xi^i}\mathbf{u}(\xi,t) = \frac{\partial}{\partial \mathbf{x}}\mathbf{u}(\xi,t)\frac{\partial}{\partial \xi^i}\mathbf{x}(\xi,t) = \nabla\mathbf{u}^{\mathsf{T}}\mathbf{g}_i\end{aligned} \tag{A.5}$$

we obtain

$$\begin{aligned}\frac{\mathrm{D}\sigma}{\mathrm{D}t} &= \frac{\mathrm{d}\sigma}{\mathrm{d}t} - \sigma^{ij}\nabla\mathbf{u}^{\mathsf{T}}\mathbf{g}_i\mathbf{g}_j - \sigma^{ij}\mathbf{g}_i\nabla\mathbf{u}^{\mathsf{T}}\mathbf{g}_j\\ &= \frac{\mathrm{d}\sigma}{\mathrm{d}t} - \nabla\mathbf{u}^{\mathsf{T}}(\sigma^{ij}\mathbf{g}_i\mathbf{g}_j) - (\sigma^{ij}\mathbf{g}_i\mathbf{g}_j)\nabla\mathbf{u}\\ &= \frac{\mathrm{d}\sigma}{\mathrm{d}t} - \nabla\mathbf{u}^{\mathsf{T}}\sigma - \sigma\nabla\mathbf{u} = \overset{\triangledown}{\sigma}\,.\end{aligned} \tag{A.6}$$

We call $\overset{\triangledown}{\sigma}$ upper convected derivative:

$$\overset{\triangledown}{\sigma} = \frac{\partial\sigma}{\partial t} + \mathbf{u}\cdot\nabla\sigma - \nabla\mathbf{u}^{\mathsf{T}}\sigma - \sigma\nabla\mathbf{u} \tag{A.7}$$

Other body-fixed frames can be defined. Reciprocal base vector $\mathbf{g}^i$ are defined by

$$\mathbf{g}^i \cdot \mathbf{g}_j = \delta^i_j. \tag{A.8}$$

Then the tensor σ can be expressed as

$$\sigma(\xi, t) = \sigma_{ij}(\xi, t)\mathbf{g}^i(\xi, t)\mathbf{g}^j(\xi, t), \tag{A.9}$$

And the rate of the tensor σ is expressed as

$$\frac{\mathrm{D}\sigma}{\mathrm{D}t} = \left(\frac{\partial}{\partial t}\sigma_{ij}(\xi, t)\right)\mathbf{g}^i(\xi, t)\mathbf{g}^j(\xi, t). \tag{A.10}$$

Using the transformation

$$\frac{\mathrm{d}\mathbf{g}^i}{\mathrm{d}t} = -\nabla\mathbf{u}\,\mathbf{g}^i, \tag{A.11}$$

and following the procedure by derivation of the upper convected derivative, the lower convected derivative $\overset{\triangle}{\sigma}$ is obtained :

$$\overset{\triangle}{\sigma} = \frac{\partial\sigma}{\partial t} + \mathbf{u}\cdot\nabla\sigma + \nabla\mathbf{u}\,\sigma + \sigma\nabla\mathbf{u}^{\mathsf{T}}. \tag{A.12}$$

The co-rotational derivative $\overset{\circ}{\sigma}$ is defined by

$$\overset{\circ}{\sigma} = \frac{1}{2}(\overset{\triangledown}{\sigma} + \overset{\triangle}{\sigma}) = \frac{\partial\sigma}{\partial t} + (\mathbf{u}\cdot\nabla)\sigma - \sigma\mathbf{W} + \mathbf{W}\sigma, \tag{A.13}$$

where

$$\mathbf{W} = \frac{1}{2}(\nabla\mathbf{u} - \nabla\mathbf{u}^{\mathsf{T}}). \tag{A.14}$$

B Loss of evolution in the flow of an Oldroyd-B fluid

The analysis follows the work of Owen and Phillips [105].

The loss of evolution is an instability of Hadamard type in which short waves will dramatically increase in amplitude, cf [72]. The two-dimensional form of the Oldroyd-B system (3.96) is used as an example for illustration. Writing the variables in a vector

$$\phi = (p, u, v, \tau_{p,xx}, \tau_{p,yy}, \tau_{p,xy})^{\mathsf{T}} \tag{B.1}$$

the set of the partial differential equations can be reformulated in a quasilinear system:

$$\mathbf{A}_0 \frac{\partial \phi}{\partial t} + \mathbf{A}_1 \frac{\partial \phi}{\partial x} + \mathbf{A}_2 \frac{\partial \phi}{\partial y} + \mathbf{A}_3 \left(\frac{\partial^2 \phi}{\partial x^2} + \frac{\partial^2 \phi}{\partial y^2} \right) + \mathbf{S}\phi = 0, \tag{B.2}$$

with the coefficients

$$\mathbf{A}_0 = \begin{pmatrix} 0 & 0 & 0 & 0 & 0 & 0 \\ 0 & \rho & 0 & 0 & 0 & 0 \\ 0 & 0 & \rho & 0 & 0 & 0 \\ 0 & 0 & 0 & \lambda & 0 & 0 \\ 0 & 0 & 0 & 0 & \lambda & 0 \\ 0 & 0 & 0 & 0 & 0 & \lambda \end{pmatrix},$$

$$\mathbf{A}_1 = \begin{pmatrix} 0 & 1 & 0 & 0 & 0 & 0 \\ 1 & \rho u & 0 & -1 & 0 & 0 \\ 0 & 0 & \rho u & 0 & 0 & -1 \\ 0 & -2(\lambda\tau_{p,xx} + \eta_p) & 0 & \lambda u & 0 & 0 \\ 0 & 0 & -2\lambda\tau_{p,xx} & 0 & \lambda u & 0 \\ 0 & 0 & -2(\lambda\tau_{p,xx} + \eta_p) & 0 & 0 & \lambda u \end{pmatrix},$$

$$\mathbf{A}_2 = \begin{pmatrix} 0 & 0 & 1 & 0 & 0 & 0 \\ 0 & \rho v & 0 & 0 & 0 & -1 \\ 0 & 0 & \rho v & 0 & -1 & 0 \\ 0 & -2\lambda\tau_{p,xy} & 0 & \lambda v & 0 & 0 \\ 0 & 0 & -2(\lambda\tau_{p,yy} + \eta_p) & 0 & \lambda v & 0 \\ 0 & -(\lambda\tau_{p,yy} + \eta_p) & 0 & 0 & 0 & \lambda v \end{pmatrix},$$

$$\mathbf{A}_3 = \begin{pmatrix} 0 & 0 & 0 & 0 & 0 & 0 \\ 0 & -\eta_s & 0 & 0 & 0 & 0 \\ 0 & 0 & -\eta_s & 0 & 0 & 0 \\ 0 & 0 & 0 & 0 & 0 & 0 \\ 0 & 0 & 0 & 0 & 0 & 0 \\ 0 & 0 & 0 & 0 & 0 & 0 \end{pmatrix} \quad \text{and} \quad \mathbf{S} = \begin{pmatrix} 0 & 0 & 0 & 0 & 0 & 0 \\ 0 & 0 & 0 & 0 & 0 & 0 \\ 0 & 0 & 0 & 0 & 0 & 0 \\ 0 & 0 & 0 & 1 & 0 & 0 \\ 0 & 0 & 0 & 0 & 1 & 0 \\ 0 & 0 & 0 & 0 & 0 & 1 \end{pmatrix}.$$

We consider a wave solution of the system propagating in $\xi = \xi_1 \mathbf{e}_x + \xi_2 \mathbf{e}_y$ direction:

$$\begin{aligned} \phi(\mathbf{x}, t) &= \phi_0 \exp(-i\omega t + i(\xi_1 x + \xi_2 y)) \\ &= \phi_0 \exp(\mathfrak{I}(\omega) t) \exp(-i\mathfrak{R}(\omega) t + i(\xi_1 x + \xi_2 y)), \end{aligned} \tag{B.3}$$

where $\Im(\omega)$ and $\Re(\omega)$ are the imagine and real parts of ω. If $\Im(\omega) \leqslant 0$ then for all direction ξ all waves damp exponentially in time. The fulfilment of this condition prevents the onsets of Hadamard instability.

Substituting the this wave solution into the system (B.2) we obtain

$$i(-\omega \mathbf{A}_0 + \xi_1 \mathbf{A}_1 + \xi_2 \mathbf{A}_2 + i(\xi_1^2 + \xi_2^2)\mathbf{A}_3)\phi_0 + \mathbf{S}\phi_0 = 0. \tag{B.4}$$

There exist a non-trivial solution for all ξ if

$$\det(-\omega \mathbf{A}_0 + \xi_1 \mathbf{A}_1 + \xi_2 \mathbf{A}_2 + i(\xi_1^2 + \xi_2^2)\mathbf{A}_3 - i\mathbf{S}) = 0 \tag{B.5}$$

which can be written explicitly

$$\begin{vmatrix} 0 & \xi_1 & \xi_2 & 0 & 0 & 0 \\ \xi_1 & \rho\nu - i\eta_s(\xi_1^2+\xi_2^2) & 0 & -\xi_1 & 0 & -\xi_2 \\ \xi_2 & 0 & \rho\nu - i\eta_s(\xi_1^2+\xi_2^2) & 0 & -\xi_2 & -\xi_1 \\ 0 & m_1 & 0 & \lambda\nu - i & 0 & 0 \\ 0 & 0 & m_2 & 0 & \lambda\nu - i & 0 \\ 0 & m_3 & m_4 & 0 & 0 & \lambda\nu - i \end{vmatrix} = 0, \tag{B.6}$$

where

$$\begin{aligned} \nu &= \omega + \xi \cdot u, \\ m_1 &= -2\xi_1(\lambda\tau_{p,xx} + \eta_p) - 2\xi_2\lambda\tau_{p,xy}, \\ m_2 &= -2\xi_2(\lambda\tau_{p,yy} + \eta_p) - 2\xi_1\lambda\tau_{p,xy}, \\ m_3 &= -\xi_2(\lambda\tau_{p,yy} + \eta_p), \\ m_4 &= -\xi_1(\lambda\tau_{p,xx} + \eta_p). \end{aligned}$$

In terms of ν the stability condition is $\Im(\nu) \geqslant 0$ and the determinant reads

$$\begin{gathered} -(\xi_1^2+\xi_2^2)(\lambda\nu - i)^2((\rho\nu - i\eta_s(\xi_1^2+\xi_2^2))(\lambda\nu - i) \\ -(\lambda\tau_{p,xx}+\eta_p)\xi_1^2 + 2\lambda\tau_{p,xy}\xi_1\xi_2 + (\lambda\tau_{p,yy}+\eta_p)\xi_2^2) = 0. \end{gathered} \tag{B.7}$$

This equation has a double root $\nu = i/\lambda$. With this solution a wave solution has an exponential rate of decay $-1/\lambda$. The other root of equation (B.7) are

$$\nu = \frac{i}{2}\left(\frac{\eta_s|\xi|^2}{\rho} + \frac{1}{\lambda}\right) \pm \sqrt{\frac{\xi^\mathsf{T}\tau_A\xi}{\rho} + \frac{\eta_s|\xi|^2}{\rho\lambda} - \frac{1}{4}\left(\frac{\eta_s|\xi|^2}{\rho} + \frac{1}{\lambda}\right)^2} \tag{B.8}$$

where $\tau_\mathbf{A} = \tau_p + \frac{\eta_p}{\lambda}\mathbf{I}$ is the configuration tensor. It has a linear relation to the conformation tensor according to

$$\mathbf{c} = \frac{\lambda}{\eta_p}\tau_A. \tag{B.9}$$

If all the waves damp exponentially in time it is required $\Im(\nu) \geqslant 0$ which is equivalent to

$$\xi^\mathsf{T}\tau_A\xi \geqslant -\frac{\eta_s|\xi|^2}{\lambda}. \tag{B.10}$$

We can clearly see that if τ_A is positive definite the condition (B.10) is always fulfilled. Otherwise the allowed range of τ_A depends on the factor η_s/λ.

C Analytical solution for two-dimensional Poiseuille flow of an Oldroyd-B fluid

An Oldroyd-B fluid flows in a channel with height $2h$. The flow is driven by a constant pressure gradient. No-slip boundary conditions are set at the upper and bottom wall.

- Solution for steady state
  Components of velocity $\mathbf{u}$:

$$u = \frac{\partial p}{\partial x}\frac{y^2 - h^2}{2(\eta_s + \eta_p)}$$
$$v = 0.$$

  Components of polymeric contribution of extra stress τ_p:

$$\tau_{p,xx} = \left(\frac{\partial p}{\partial x}\right)^2 \frac{2\lambda\eta_p}{(\eta_s+\eta_p)^2} y^2$$
$$\tau_{p,xy} = \frac{\partial p}{\partial x}\frac{\eta_p}{\eta_s+\eta_p} y$$
$$\tau_{p,yy} = 0$$

- Solution for start-up state
  The solution is given in dimensionless form by Walters and Kind [147]. The dimensionless variables are defined as

$$Y = \frac{y}{h}, \quad T = \frac{t}{\lambda}, \quad U = \frac{u}{\bar{u}} \quad \text{and} \quad \beta = \frac{\eta_s}{\eta_s+\eta_p},$$

  and

$$\mathrm{Wi} = \frac{\lambda\bar{u}}{h}, \quad \mathrm{Re} = \frac{\rho\bar{u}h}{\eta_s+\eta_p}, \quad \mathrm{E} = \frac{\mathrm{Wi}}{\mathrm{Re}},$$

  where $\bar{u} = -\frac{h^2}{3(\eta_s+\eta_p)}\frac{\partial p}{\partial x}$.
  The solution of U is

$$U(T,Y) = 1.5(1.0 - Y^2) - 48\sum_{n'=1}^{\infty}\left(n^{-3}\sin(0.5n(1+Y))e^{-0.5\alpha_n T}G(T)\right),$$

  where

$$G(T) = \cosh(0.5\beta_n T) + \frac{\gamma_n}{\beta_n}\sinh(0.5\beta_n T),$$

  and

$$n = (2n'-1)\pi, \quad \alpha_n = 1 + \frac{1}{4}\beta n^2, \quad \gamma = 1 - 0.25(2-\beta)\mathrm{E}n^2.$$

  If $\alpha_n^2 - \mathrm{E}n^2 \geqslant 0$ then

$$\beta_n = \sqrt{\alpha_n^2 - \mathrm{E}n^2},$$
$$G(T) = \cosh(0.5\beta_n T) + \frac{\gamma_n}{\beta_n}\sinh(0.5\beta_n T).$$

If $\alpha_n^2 - \mathrm{E}n^2 < 0$ then

$$\beta_n = \sqrt{\mathrm{E}n^2 - \alpha_n^2},$$
$$G(T) = \cos(0.5\beta_n T) + \frac{\gamma_n}{\beta_n}\sin(0.5\beta_n T).$$

D Derivation of the log-conformation representation

The conformation tensor $\mathbf{c}$ can be diagonalized as

$$\mathbf{c} = \mathbf{R}\Lambda\mathbf{R}^{\mathsf{T}}, \tag{D.1}$$

where $\mathbf{R}$ is the eigenvector matrix fulfilling $\mathbf{R}\mathbf{R}^{\mathsf{T}} = \mathbf{R}^{\mathsf{T}}\mathbf{R} = \mathbf{I}$ and Λ is the diagonal matrix containing the eigenvalues of $\mathbf{c}$. The logarithm of $\mathbf{c}$ is given by

$$\mathbf{s} = \log \mathbf{c} = \mathbf{R} \log \Lambda \, \mathbf{R}^{\mathsf{T}}, \tag{D.2}$$

where $\log \Lambda = \operatorname{diag}(\log \Lambda_i)$ for $\Lambda = \operatorname{diag}(\Lambda_i)$. Defining $\mathbf{L} := \nabla \mathbf{u}$ and substituting (D.1) into

$$\frac{\mathrm{d}\mathbf{c}}{\mathrm{d}t} = \mathbf{c}\mathbf{L} + \mathbf{L}^{\mathsf{T}}\mathbf{c} + \frac{1}{\lambda}(\mathbf{I} - \mathbf{c}) \tag{D.3}$$

yields

$$\frac{\mathrm{d}\mathbf{R}}{\mathrm{d}t}\Lambda\mathbf{R}^{\mathsf{T}} + \mathbf{R}\frac{\mathrm{d}\Lambda}{\mathrm{d}t}\mathbf{R}^{\mathsf{T}} + \mathbf{R}\Lambda\frac{\mathrm{d}\mathbf{R}^{\mathsf{T}}}{\mathrm{d}t} = \mathbf{R}\Lambda\mathbf{R}^{\mathsf{T}}\mathbf{L} + \mathbf{L}^{\mathsf{T}}\mathbf{R}\Lambda\mathbf{R}^{\mathsf{T}} + \frac{1}{\lambda}\mathbf{I} - \frac{1}{\lambda}\mathbf{R}\Lambda\mathbf{R}^{\mathsf{T}}, \tag{D.4}$$

where $\mathrm{d}/\mathrm{d}t$ denotes the material derivative operator.

Multiplying Equation (D.4) from the left by $\mathbf{R}^{\mathsf{T}}$ and from the right by $\mathbf{R}$ yields

$$\mathbf{R}^{\mathsf{T}}\frac{\mathrm{d}\mathbf{R}}{\mathrm{d}t}\Lambda + \frac{\mathrm{d}\Lambda}{\mathrm{d}t} + \Lambda\frac{\mathrm{d}\mathbf{R}^{\mathsf{T}}}{\mathrm{d}t}\mathbf{R} = \Lambda\mathbf{R}^{\mathsf{T}}\mathbf{L}\mathbf{R} + \mathbf{R}^{\mathsf{T}}\mathbf{L}^{\mathsf{T}}\mathbf{R}\Lambda + \frac{1}{\lambda}\mathbf{I} - \frac{1}{\lambda}\mathbf{R}\Lambda\mathbf{R}^{\mathsf{T}}. \tag{D.5}$$

Defining $\tilde{\Omega} := \mathbf{R}^{\mathsf{T}}\frac{\mathrm{d}\mathbf{R}}{\mathrm{d}t}$ and $\tilde{\mathbf{L}} := \mathbf{R}^{\mathsf{T}}\mathbf{L}\mathbf{R}$ we can reformulate Equation (D.5) as

$$\tilde{\Omega}\Lambda + \frac{\mathrm{d}\Lambda}{\mathrm{d}t} + \Lambda\tilde{\Omega}^{\mathsf{T}} = \Lambda\tilde{\mathbf{L}} + \tilde{\mathbf{L}}^{\mathsf{T}}\Lambda + \frac{1}{\lambda}\mathbf{I} - \frac{1}{\lambda}\Lambda. \tag{D.6}$$

Since

$$\tilde{\Omega}^{\mathsf{T}} + \tilde{\Omega} = \frac{\mathrm{d}\mathbf{R}^{\mathsf{T}}}{\mathrm{d}t}\mathbf{R} + \mathbf{R}^{\mathsf{T}}\frac{\mathrm{d}\mathbf{R}}{\mathrm{d}t} = \frac{\mathrm{d}(\mathbf{R}^{\mathsf{T}}\mathbf{R})}{\mathrm{d}t} = \frac{\mathrm{d}\mathbf{I}}{\mathrm{d}t} = \mathbf{0}, \tag{D.7}$$

$\tilde{\Omega}$ is anti-symmetric. Using the chain rule we can express the material derivative of $\mathbf{s}$ as

$$\begin{aligned} \frac{\mathrm{d}\mathbf{s}}{\mathrm{d}t} &= \frac{\mathrm{d}\mathbf{R}}{\mathrm{d}t}\log\Lambda\,\mathbf{R}^{\mathsf{T}} + \mathbf{R}\frac{\mathrm{d}\log\Lambda}{\mathrm{d}t}\mathbf{R}^{\mathsf{T}} + \mathbf{R}\log\Lambda\frac{\mathrm{d}\mathbf{R}^{\mathsf{T}}}{\mathrm{d}t} \\ &= \mathbf{R}\left(\tilde{\Omega}\log\Lambda + \frac{\mathrm{d}\Lambda}{\mathrm{d}t}\Lambda^{-1} + \log\Lambda\,\tilde{\Omega}^{\mathsf{T}}\right)\mathbf{R}^{\mathsf{T}}. \end{aligned} \tag{D.8}$$

What remains to be done is express the term $\frac{\mathrm{d}\Lambda}{\mathrm{d}t}\Lambda^{-1}$ and $\tilde{\Omega}\log\Lambda + \log\Lambda\,\tilde{\Omega}^{\mathsf{T}}$ with the help of Equation (D.6). From Equations (D.6) and (D.7) we know that the diagonal terms in $\tilde{\Omega}\Lambda + \Lambda\tilde{\Omega}^{\mathsf{T}}$ vanish, and that $\frac{\mathrm{d}\Lambda}{\mathrm{d}t}$ is diagonal. Therefore, we have

$$\left(\frac{\mathrm{d}\Lambda}{\mathrm{d}t}\right)_{ii} = \left(\Lambda\tilde{\mathbf{L}} + \tilde{\mathbf{L}}^{\mathsf{T}}\Lambda + \frac{1}{\lambda}\mathbf{I} - \frac{1}{\lambda}\Lambda\right)_{ii} = 2\Lambda_{ii}\tilde{L}_{ii} + \frac{1}{\lambda} - \frac{1}{\lambda}\Lambda_{ii}. \tag{D.9}$$

Since $\frac{\mathrm{d}\Lambda}{\mathrm{d}t}\Lambda^{-1}$ is also a diagonal matrix, we have

$$\left(\frac{\mathrm{d}\Lambda}{\mathrm{d}t}\Lambda^{-1}\right)_{ii} = 2\tilde{L}_{ii} + \frac{1}{\lambda\Lambda_{ii}} - \frac{1}{\lambda}. \tag{D.10}$$

The off-diagonal components of $\left(\tilde{\Omega}\Lambda + \Lambda\tilde{\Omega}^{\mathsf{T}}\right)_{ij} = \tilde{\Omega}_{ij}(\Lambda_{jj} - \Lambda_{ii})$ are equal to the off-diagonal components of the right hand side of Equation (D.6), namely

$$\tilde{\Omega}_{ij}(\Lambda_{jj} - \Lambda_{ii}) = \left(\Lambda\tilde{\mathbf{L}} + \tilde{\mathbf{L}}^{\mathsf{T}}\Lambda\right)_{ij} = \Lambda_{ii}\tilde{L}_{ij} + \tilde{L}_{ji}\Lambda_{jj} \tag{D.11}$$

which yields

$$\tilde{\Omega}_{ij} = \frac{\Lambda_{ii}\tilde{L}_{ij} + \tilde{L}_{ji}\Lambda_{jj}}{\Lambda_{jj} - \Lambda_{ii}}. \tag{D.12}$$

Then we have

$$\left(\tilde{\Omega}\log\Lambda + \log\Lambda\,\tilde{\Omega}^{\mathsf{T}}\right)_{ij} = \tilde{\Omega}_{ij}(\log\Lambda_{jj} - \log\Lambda_{ii}) = \frac{\Lambda_{ii}\tilde{L}_{ij} + \tilde{L}_{ji}\Lambda_{jj}}{\Lambda_{jj} - \Lambda_{ii}}(\log\Lambda_{jj} - \log\Lambda_{ii}). \tag{D.13}$$

Defining the diagonal matrix $\tilde{\mathbf{B}}$ with $\tilde{B}_{ii} = \tilde{L}_{ii}$ and $\mathbf{B} = \mathbf{R}\tilde{\mathbf{B}}\mathbf{R}^{\mathsf{T}}$, $\Omega = \mathbf{R}\tilde{\Omega}\mathbf{R}^{\mathsf{T}}$, substituting (D.10) and (D.13) into equation (D.8) we obtain the final form of LCR

$$\frac{\mathrm{d}\mathbf{s}}{\mathrm{d}t} = \Omega\mathbf{s} - \mathbf{s}\Omega + 2\mathbf{B} + \frac{1}{\lambda}(e^{-\mathbf{s}} - \mathbf{I}) \,. \tag{D.14}$$

E Derivation of the square root-conformation representation

The derivation utilizes the property that a symmetry positive definite matrix has the unique positive symmetric square root $\mathbf{A} = \mathbf{c}^{\frac{1}{2}}$.

Substituting $\mathbf{c} = \mathbf{A}^{\mathsf{T}}\mathbf{A}$ into the evolution equation of the conformation tensor

$$\frac{\mathrm{d}\mathbf{c}}{\mathrm{d}t} = \mathbf{cL} + \mathbf{L}^{\mathsf{T}}\mathbf{c} + \frac{1}{\lambda}(\mathbf{I} - \mathbf{c}) \tag{E.1}$$

yields

$$\frac{\mathrm{d}\mathbf{A}^{\mathsf{T}}}{\mathrm{d}t}\mathbf{A} + \mathbf{A}^{\mathsf{T}}\frac{\mathrm{d}\mathbf{A}}{\mathrm{d}t} = \mathbf{A}^{\mathsf{T}}\mathbf{AL} + \mathbf{L}^{\mathsf{T}}\mathbf{A}^{\mathsf{T}}\mathbf{A} + \frac{1}{\lambda}(\mathbf{I} - \mathbf{A}^{\mathsf{T}}\mathbf{A})\,, \tag{E.2}$$

where $\mathbf{L} = \nabla\mathbf{u}$. After multiplying equation (E.2) from the left by $\mathbf{A}^{-\mathsf{T}}$ and rearranging we have

$$\frac{\mathrm{d}\mathbf{A}}{\mathrm{d}t} = \mathbf{AL} + \mathbf{A}^{-\mathsf{T}}\left(-\frac{\mathrm{d}\mathbf{A}^{\mathsf{T}}}{\mathrm{d}t} + \mathbf{L}^{\mathsf{T}}\mathbf{A}^{\mathsf{T}} + \frac{1}{2\lambda}(\mathbf{A}^{-1} - \mathbf{A}^{\mathsf{T}})\right)\mathbf{A} + \frac{1}{2\lambda}(\mathbf{A}^{-\mathsf{T}} - \mathbf{A})\,. \tag{E.3}$$

Defining

$$\mathscr{F} := \frac{\mathrm{d}\mathbf{A}}{\mathrm{d}t} - \mathbf{AL} - \frac{1}{2\lambda}(\mathbf{A}^{-\mathsf{T}} - \mathbf{A}) \tag{E.4}$$

equation (E.3) can be rewritten as

$$\mathscr{F}\mathbf{A}^{-1} = -\mathbf{A}^{-\mathsf{T}}\mathscr{F}^{\mathsf{T}} \tag{E.5}$$

Defining $\mathbf{M} := \mathbf{A}^{-\mathsf{T}}\mathscr{F}^{\mathsf{T}}$, this shows

$$\mathbf{M}^{\mathsf{T}} = -\mathbf{M}. \tag{E.6}$$

So $\mathbf{M}$ is anti-symmetric with components

$$\mathbf{M} = \begin{pmatrix} 0 & m_{12} & m_{13} \\ -m_{12} & 0 & m_{23} \\ -m_{13} & -m_{23} & 0 \end{pmatrix}. \tag{E.7}$$

The evolution equation for $\mathbf{A}$ turns out to be

$$\frac{\partial\mathbf{A}}{\partial t} + \mathbf{u}\cdot\nabla\mathbf{A} = \mathbf{AL} + \mathbf{MA} + \frac{1}{2\lambda}\left(\mathbf{A}^{-\mathsf{T}} - \mathbf{A}\right)\,, \tag{E.8}$$

To preserve the symmetry of $\mathbf{A}$, the right-hand side of equation (E.8) should be symmetric. For this reason the matrix

$$\mathbf{K} = \mathbf{AL} + \mathbf{MA} \tag{E.9}$$

with components k_{ij} is required to be symmetric. The entries of the tensor $\mathbf{M}$ depend on $\mathbf{L}$ and the symmetric tensor $\mathbf{A}$. They are calculated by computing the right hand side of Equation (E.9) and solving the equations $k_{ij} = k_{ji}$ for

$i \neq j$. In the three-dimensional case, there are three such equations. In matrix notation, the system of these equations reads

$$\begin{pmatrix} a_{11}+a_{22} & a_{23} & -a_{13} \\ a_{23} & a_{11}+a_{33} & a_{12} \\ -a_{13} & a_{12} & a_{22}+a_{33} \end{pmatrix} \begin{pmatrix} m_{12} \\ m_{13} \\ m_{23} \end{pmatrix} = \begin{pmatrix} r_1 \\ r_2 \\ r_3 \end{pmatrix}, \tag{E.10}$$

where

$$\begin{aligned} r_1 &= (a_{12}l_{11} - a_{11}l_{12}) + (a_{22}l_{21} - a_{12}l_{22}) + (a_{23}l_{31} - a_{13}l_{32}) \,, \\ r_2 &= (a_{13}l_{11} - a_{11}l_{13}) + (a_{33}l_{31} - a_{13}l_{33}) + (a_{23}l_{21} - a_{12}l_{23}) \,, \\ r_3 &= (a_{13}l_{12} - a_{12}l_{13}) + (a_{23}l_{22} - a_{22}l_{23}) + (a_{33}l_{32} - a_{23}l_{33}) \,. \end{aligned} \tag{E.11}$$

By swapping the first and the third columns of the coefficient matrix and subsequently swapping the first and the third rows of the resulting coefficient matrix, and finally multiplying the second row and the second column of the resulting matrix by -1, equations (E.10) can be transformed into

$$(\mathrm{tr}(\mathbf{A})\mathbf{I} - \mathbf{A})\,\tilde{\mathbf{m}} = \tilde{\mathbf{w}}, \tag{E.12}$$

where

$$\tilde{\mathbf{m}} = (m_{23}, -m_{13}, m_{12})^{\mathsf{T}} \,, \tilde{\mathbf{w}} = (w_3, -w_2, w_1)^{\mathsf{T}}. \tag{E.13}$$

If **A** is symmetric, there is an orthogonal matrix **P** such that

$$\mathbf{A} = \mathbf{P}^{\mathsf{T}} \Lambda \mathbf{P}, \tag{E.14}$$

where Λ is diagonal with the corresponding three eigenvalues Λ_i of **A**. The left side of equation (E.12) can be transformed according to

$$\begin{aligned} \mathrm{tr}(\mathbf{A})\mathbf{I} - \mathbf{A} &= \mathrm{tr}(\mathbf{A})\mathbf{I} - \mathbf{P}^{\mathsf{T}}\Lambda\mathbf{P} = \mathbf{P}^{\mathsf{T}}(\mathrm{tr}(\mathbf{A})\mathbf{I} - \Lambda)\mathbf{P} \\ &= \mathbf{P}^{\mathsf{T}}(\mathrm{diag}(\Lambda_2 + \Lambda_3, \Lambda_1 + \Lambda_3, \Lambda_1 + \Lambda_2))\mathbf{P}. \end{aligned} \tag{E.15}$$

Therefore, one can uniquely solve for **A** in such a way that the evolution equation (E.8) is symmetric. The above arguments for this fact follow those given in [11].

Bibliography

[1] Aboubacar, M. and M.F. Webster: *A cell-vertex finite volume/element method on triangles for abrupt contraction viscoelastic flows*. Journal of Non-Newtonian Fluid Mechanics, 98(2-3):83 – 106, 2001.

[2] Afonso, A., P.J. Oliveira, F.T. Pinho and M.A. Alves: *The log-conformation tensor approach in the finite-volume method framework*. Journal of Non-Newtonian Fluid Mechanics, 157(1-2):55 – 65, 2009.

[3] Afonso, A. M., P. J. Oliveira, Pinho F. T. and M. A. Alves: *Dynamics of high-Deborah-number entry flows: a numerical study*. Journal of Fluid Mechanics, 677:272–304, 5 2011.

[4] Afonso, A.M., F.T. Pinho and M.A. Alves: *The kernel-conformation constitutive laws*. Journal of Non-Newtonian Fluid Mechanics, 167¨C168(0):30 – 37, 2012.

[5] Alves, M. A., P. J. Oliveira and F. T. Pinho: *A convergent and universally bounded interpolation scheme for the treatment of advection*. International Journal for Numerical Methods in Fluids, 41(1):47–75, 2003.

[6] Alves, M. A., F. T. Pinho and P. J. Oliveira: *Effect of a high-resolution differencing scheme on finite-volume predictions of viscoelastic flows*. Journal of Non-Newtonian Fluid Mechanics, 93(2-3):287 – 314, 2000.

[7] Alves, MA, FT Pinho and PJ Oliveira: *The flow of viscoelastic fluids past a cylinder: finite-volume high-resolution methods*. Journal of Non-Newtonian Fluid Mechanics, 97(2-3):207–232, 2001.

[8] Alves, Manuel A., Paulo J. Oliveira and Fernando T. Pinho: *Benchmark solutions for the flow of Oldroyd-B and PTT fluids in planar contractions*. Journal of Non-Newtonian Fluid Mechanics, 110(1):45 – 75, 2003.

[9] Amoreira, L. J. and P. J. Oliveira: *Comparison of Different Formulations for the Numerical Calculation of Unsteady Incompressible Viscoelastic Fluid Flow*. Advance in Applied Mathematics and Mechanics, 2(4):483–502, AUG 2010.

[10] Azarbadegan, A, I Eames and A Wojcik: *Fluid-Structure coupling in valveless micropumps*. Journal of Micromechanics and Microengineering, 21(8):085033, 2011.

[11] Balci, Nusret, Becca Thomases, Michael Renardy and Charles R. Doering: *Symmetric factorization of the conformation tensor in viscoelastic fluid models*. Journal of Non-Newtonian Fluid Mechanics, 166(11):546 – 553, 2011.

[12] Ben-Mansour, Rached and Ahmet Z. Sahin: *Optimization of Conical Micro-Diffusers and Micro-Nozzles Considering Entropy Generation*. Arabian Journal for Science and Engineering, 38(11):3161–3170, 2013.

[13] Beris, Antony N. and Kostas D. Housiadas: *Computational Viscoelastic Fluid Mechanics and Numerical Studies of Turbulent Flows of Dilute Polymer Solutions*. In *Modeling and Simulation in Polymers*, pages 1–36. Wiley-VCH Verlag GmbH & Co. KGaA, 2010.

[14] Bernstein, B; Kearsley, EA; Zapas LJ: *A study of stress relaxation with finite strain*. Transactions of the Society of Rheology, 7:391–410, 1963.

[15] Bird, R. Byron: *Kinetic theory of polymeric liquids*. Accounts of Chemical Research, 18(12):364–371, 1985.

[16] Bird, R.B. and O. Hassager: *Dynamics of Polymeric Liquids: Fluid mechanics*. Dynamics of Polymeric Liquids. Wiley, 1987.

[17] Brown, Robert A. and Gareth H. McKinley: *Report on the VIIIth international workshop on numerical methods in viscoelastic flows*. Journal of Non-Newtonian Fluid Mechanics, 52(3):407 – 413, 1994.

[18] Cai, Z.X. and X.Y. Luo: *A fluid-beam model for flow in a collapsible channel*. Journal of Fluids and Structures, 17(1):125 – 146, 2003.

[19] Chakraborty, Debadi, Mohit Bajaj, Leslie Yeo, James Friend, Matteo Pasquali and J. Ravi Prakash: *Viscoelastic flow in a two-dimensional collapsible channel*. Journal of Non-Newtonian Fluid Mechanics, 165:1204 – 1218, 2010.

[20] Chakraborty, Debadi, J. Ravi Prakash, James Friend and Leslie Yeo: *Fluid-structure interaction in deformable microchannels*. Physics of Fluids (1994-present), 24(10):–, 2012.

[21] Chen, Xingyuan, Holger Marschall, Michael Schäfer and Dieter Bothe: *A comparison of stabilisation approaches for finite-volume simulation of viscoelastic fluid flow*. International Journal of Computational Fluid Dynamics, 27(6-7):229–250, 2013.

[22] Chen, Xingyuan, Michael Schäfer and Dieter Bothe: *Numerical modeling and investigation of viscoelastic fluid-structure interaction applying an implicit partitioned coupling algorithm*. Journal of Fluids and Structures. Submitted.

[23] Chen, Xingyuan, Michael Schäfer and Dieter Bothe: *Numerical modeling of viscoelastic fluid-structure interaction and its application for a valveless micropump*. In *Proceeding of European Conference on Numerical Mathematics and Advanced Applications 2013*, Lecture Notes in Computational Science and Engineering. Springer, 2014. Accepted.

[24] Chilcott, M.D. and J.M. Rallison: *Creeping flow of dilute polymer solutions past cylinders and spheres*. Journal of Non-Newtonian Fluid Mechanics, 29(0):381 – 432, 1988.

[25] Claus, Susanne: *Numerical Simulation of Complex Viscoelastic Flows using Discontinuous Galerkin Spectral/hp Element Methods*. PhD thesis, Cardiff University, May 2013.

[26] Damanik, H., J. Hron, A. Ouazzi and S. Turek: *A monolithic FEM approach for the log-conformation reformulation (LCR) of viscoelastic flow problems*. Journal of Non-Newtonian Fluid Mechanics, 165(19¨C20):1105 – 1113, 2010.

[27] Darwish, M. S. and F. H. Moukalled: *Normalized variable and space formulation methodology for high-resolution schemes*. Numerical Heat Transfer, Part B: Fundamentals, 26(1):79–96, 1994.

[28] Darwish, Marwan: *Development and testing of a robust free-surface finite volume method*. Faculty of Engineering and Architecture, American University of Beirut, 2003.

[29] Darwish, M.S. and F. Moukalled: *TVD schemes for unstructured grids*. International Journal of Heat and Mass Transfer, 46(4):599 – 611, 2003.

[30] Dealy, J.M.: *Weissenberg and Deborah Numbers – Their Definition and Use*. Rheoloy Bulletin, 79(2):14–18, 2010.

[31] Demirdžić, I. and M. Perić: *Space conservation law in finite volume calculations of fluid flow*. Int. J. Numer. Meth. Fluids, 8(9):1037–1050, 1988.

[32] Denn, Morton M.: *Fifty years of non-Newtonian fluid dynamics*. AIChE J., 50(10):2335–2345, 2004.

[33] Dettmer, Wulf G. and Djordje Perić: *A new staggered scheme for fluid-structure interaction*. Int. J. Numer. Meth. Engng, 93(1):1–22, 2013.

[34] Deville, M. and T.B. Gatski: *Mathematical Modeling for Complex Fluids and Flows*. Springer, 2012.

[35] Doi, Masao and S. F. Edwards: *Dynamics of concentrated polymer systems. Part 1.-Brownian motion in the equilibrium state*. J. Chem. Soc., Faraday Trans. 2, 74:1789–1801, 1978.

[36] Donea, Jean, Antonio Huerta, J.-Ph. Ponthot and A. Rodriguez-Ferran: *Arbitrary Lagrangian-Eulerian Methods*. In *Encyclopedia of Computational Mechanics*. John Wiley & Sons, Ltd, 2004.

[37] Doraiswamy, D.: *The Origins of Rheology: A Short Historical Excursion*. Rheology Bulletin, 71(1), 2002.

[38] Eames, I., A. Azarbadegan and M. Zangeneh: *Analytical Model of Valveless Micropumps*. Microelectromechanical Systems, Journal of, 18(4):878–883, 2009.

[39] Edussuriya, S.S, A.J Williams and C Bailey: *A cell-centred finite volume method for modelling viscoelastic flow*. Journal of Non-Newtonian Fluid Mechanics, 117(1):47 – 61, 2004.

[40] Edwards, S F: *The statistical mechanics of polymerized material*. Proceedings of the Physical Society, 92(1):9, 1967.

[41] Eggleton, C.D., T.H. Pulliam and J.H. Ferziger: *Numerical simulation of viscoelastic flow using flux difference splitting at moderate Reynolds numbers*. Journal of Non-Newtonian Fluid Mechanics, 64(2-3):269 – 298, 1996.

[42] Fan, Yurun, R.I. Tanner and N. Phan-Thien: *Galerkin/least-square finite-element methods for steady viscoelastic flows*. Journal of Non-Newtonian Fluid Mechanics, 84(2¨C3):233 – 256, 1999.

[43] Fattal, Raanan and Raz Kupferman: *Time-dependent simulation of viscoelastic flows at high Weissenberg number using the log-conformation representation*. Journal of Non-Newtonian Fluid Mechanics, 126(1):23 – 37, 2005.

[44] Favero, J.L., A.R. Secchi, N.S.M. Cardozo and H. Jasak: *Viscoelastic flow analysis using the software OpenFOAM and differential constitutive equations*. Journal of Non-Newtonian Fluid Mechanics, 165(23¨C24):1625 – 1636, 2010.

[45] Ferziger, J.H. and M. Perić: *Computational Methods for Fluid Dynamics*. Springer London, Limited, 2002.

[46] Fraunhofer: *MpCCI–Mesh-Based Parallel Code Coupling Interface. User Guid V2.0*. Fraunhofer SCAI, 2004.

[47] Gaskell, P. H. and A. K. C. Lau: *Curvature-compensated convective transport: SMART, A new boundedness-preserving transport algorithm*. Int. J. Numer. Meth. Fluids, 8(6):617–641, 1988.

[48] Gennes, P. G. de: *Reptation of a Polymer Chain in the Presence of Fixed Obstacles*. The Journal of Chemical Physics, 55(2):572–579, 1971.

[49] Giesekus, Hanswalter: *Die Elastizität von Flüssigkeiten*. Rheologica Acta, 5(1):29–35, 1966.

[50] Glaister, P.: *A TVD finite difference scheme with non-uniform meshes and without upstream weighting*. Computers & Mathematics with Applications, 22(3):45 – 58, 1991.

[51] Godunov, S.K.: *A difference method for numerical calculation of discontinuous solutions of the equations of hydrodynamics*. Mathematicheskii Sbornik, 47(89):271–306, 1959.

[52] Gonzalez, O. and A.M. Stuart: *A First Course in Continuum Mechanics*. Cambridge texts in applied mathematics. Cambridge University Press, 2008.

[53] Green, M. S. and A. V. Tobolsky: *A New Approach to the Theory of Relaxing Polymeric Media*. The Journal of Chemical Physics, 14(2):80–92, 1946.

[54] Grillet, Anne M., Bin Yang, Bamin Khomami and Eric S.G. Shaqfeh: *Modeling of viscoelastic lid driven cavity flow using finite element simulations*. Journal of Non-Newtonian Fluid Mechanics, 88(1-2):99 – 131, 1999.

[55] Guénette, Robert and Michel Fortin: *A new mixed finite element method for computing viscoelastic flows*. Journal of Non-Newtonian Fluid Mechanics, 60(1):27 – 52, 1995.

[56] Harten, Ami: *High resolution schemes for hyperbolic conservation laws*. Journal of Computational Physics, 49(3):357 – 393, 1983.

[57] Harten, Ami and Peter D. Lax: *On a Class of High Resolution Total-Variation-Stable Finite-Difference Schemes*. SIAM Journal on Numerical Analysis, 21(1):pp. 1–23, 1984.

[58] Heck, M., D.C. Sternel, M. Schäfer and S. Yigit: *Influence of numeical and physical paramters on an Implicit partitioned fluid-structure solver*. In Wesseling, P., Oñate E. and Périaux (editors): *ECCOMAS CFD*, The Netherlands, 2006.

[59] Hinch, E.J.: *The flow of an Oldroyd fluid around a sharp corner*. Journal of Non-Newtonian Fluid Mechanics, 50(2-3):161 – 171, 1993.

[60] Hirsch, C.: *Numerical Computation of Internal and External Flows: The Fundamentals of Computational Fluid Dynamics: The Fundamentals of Computational Fluid Dynamics*. Number v. 1. Elsevier Science, 2007.

[61] Holmes, Lori, Jovani Favero and Tim Osswald: *Numerical simulation of three-dimensional viscoelastic planar contraction flow using the software OpenFOAM*. Computers & Chemical Engineering, 37(0):64 – 73, 2012.

[62] Hoogstraten, Peter A. A. van, Paul M. A. Slaats and Frank P. T. Baaijens: *A Eulerian approach to the finite element modelling of neo-Hookean rubber material*. Applied Scientific Research, 48:193–210, 1994. 10.1007/BF02027967.

[63] Hou, Gene, Jin Wang and Anita Layton: *Numerical methods for fluid-structure interaction - a review*. Commun. Comput. Phys, 12(2):337–377, 2012.

[64] Huilgol, R.R. and N. Phan-Thien: *Fluid Mechanics of Viscoelasticity: General Principles, Constitutive Modelling, Analytical and Numerical Techniques*. Rheology Series. Elsevier Science, 1997.

[65] Hulsen, Martien A., Raanan Fattal and Raz Kupferman: *Flow of viscoelastic fluids past a cylinder at high Weissenberg number: Stabilized simulations using matrix logarithms*. Journal of Non-Newtonian Fluid Mechanics, 127(1):27 – 39, 2005.

[66] Jameson, Antony and Peter D. Lax: *Conditions for the construction of multi-point total variation diminishing difference schemes*. Applied Numerical Mathematics, 2:335 – 345, 1986. Special Issue in Honor of Milt Rose's Sixtieth Birthday.

[67] Jasak, H.: *Error Analysis and Estimation for the Finite Volume Method with Application to Fluid Flows*. PhD thesis, Imperial College, 1996.

[68] Jasak, H., H.G. Weller and A.D. Gosman: *High resolution NVD differencing scheme for arbitrarily unstructured meshes*. Int. J. Numer. Meth. Fluids, 31(2):431–449, 1999.

[69] Joosten, M. M., W. G. Dettmer and D. Perić: *Analysis of the block Gauss-Seidel solution procedure for a strongly coupled model problem with reference to fluid-structure interaction*. Int. J. Numer. Meth. Engng., 78(7):757–778, 2009.

[70] Joosten, M. M., W. G. Dettmer and D. Perić: *On the temporal stability and accuracy of coupled problems with reference to fluid-structure interaction*. Int. J. Numer. Meth. Fluids, 64(10-12):1363–1378, 2010.

[71] Joseph, D.D.: *Fluid Dynamics of Viscoelastic Liquids*. Number v. 84 in *Applied Mathematical Sciences*. Springer, 1990.

[72] JOSEPH, D.D. and J.C. SAUT: *Change of type and loss of evolution in the flow of viscoelastic fluids*. Journal of Non-Newtonian Fluid Mechanics, 20(0):117 – 141, 1986.

[73] JR., M.W. JOHNSON and D. SEGALMAN: *A model for viscoelastic fluid behavior which allows non-affine deformation*. Journal of Non-Newtonian Fluid Mechanics, 2(3):255 – 270, 1977.

[74] KASSIOTIS, CHRISTOPHE, ADNAN IBRAHIMBEGOVIC, RAINER NIEKAMP and HERMANNG. MATTHIES: *Nonlinear fluid-structure interaction problem. Part I: implicit partitioned algorithm, nonlinear stability proof and validation examples*. Computational Mechanics, 47(3):305–323, 2011.

[75] KAYE, A: *An equation of state for non-Newtonian fluids*. British Journal of Applied Physics, 17(6):803, 1966.

[76] KHOSLA, P.K. and S.G. RUBIN: *A diagonally dominant second-order accurate implicit scheme*. Computers & Fluids, 2(2):207 – 209, 1974.

[77] KRAMERS, H. A.: *The Behavior of Macromolecules in Inhomogeneous Flow*. The Journal of Chemical Physics, 14(7):415–424, 1946.

[78] KUHN, WERNER: *Über die Gestalt fadenförmiger Moleküle in Lösungen*. Kolloid-Zeitschrift, 68(1):2–15, 1934.

[79] KÜTTLER, ULRICH and WOLFGANGA. WALL: *Fixed-point fluid-structure interaction solvers with dynamic relaxation*. Computational Mechanics, 43(1):61–72, 2008.

[80] LANEY, C. and D. CAUGHEY: *Extremum control. II - Semidiscrete approximations to conservation laws*. In *Aerospace Sciences Meetings*, pages –. American Institute of Aeronautics and Astronautics, January 1991.

[81] LEE, JOO SUNG, REBECCA DYLLA-SPEARS, NERAYO P. TECLEMARIAM and SUSAN J. MULLER: *Microfluidic four-roll mill for all flow types*. Applied Physics Letters, 90(7):–, 2007.

[82] LEE, YOUNG-JU and JINCHAO XU: *New formulations, positivity preserving discretizations and stability analysis for non-Newtonian flow models*. Computer Methods in Applied Mechanics and Engineering, 195(9-12):1180 – 1206, 2006.

[83] LEER, BRAM VAN: *Towards the ultimate conservative difference scheme. II. Monotonicity and conservation combined in a second-order scheme*. Journal of Computational Physics, 14(4):361 – 370, 1974.

[84] LEONARD, B. P.: *Simple high-accuracy resolution program for convective modelling of discontinuities*. International Journal for Numerical Methods in Fluids, 8(10):1291–1318, 1988.

[85] LEVEQUE, R.J.: *Numerical Methods for Conservation Laws*. Lectures in Mathematics ETH Zürich, Department of Mathematics Research Institute of Mathematics. Springer, 1992.

[86] LIU, I-S.: *On Euclidean objectivity and the principle of material frame-indifference*. Continuum Mechanics and Thermodynamics, 16(1-2):177–183, 2004.

[87] LIU, YINGWEI, HIROKI KOMATSUZAKI, ZONGFAN DUAN, SATOMITSU IMAI and YASUHIRO NISHIOKA: *Diffuser Micropump Structured with Extremely Flexible Diaphragm of 2-μm-thick Polyimide Film*. Japanese Journal of Applied Physics, 50(5):04DK15, 2011.

[88] LODGE, A. S.: *A network theory of flow birefringence and stress in concentrated polymer solutions*. Trans. Faraday Soc., 52:120–130, 1956.

[89] LUKÁČOVÁ-MEDVID'OVÁ, G. RUSNÁKOVÁ and A. ZAUŠKOVÁ: *Kinematic splitting algorithm for fluid-structure interaction in hemodynamics*. Computer Methods in Applied Mechanics and Engineering, 265(0):83 – 106, 2013.

[90] LUKÁČOVÁ-MEDVID'OVÁ, M. and A. ZAUŠKOVÁ: *Numerical modelling of shear-thinning non-Newtonian flows in compliant vessels*. Int. J. Numer. Meth. Fluids, 56(8):1409–1415, 2008.

[91] Luo, X. Y. and T. J. Pedley: *A numerical simulation of unsteady flow in a two-dimensional collapsible channel*. Journal of Fluid Mechanics, 314:191–225, 5 1996.

[92] Luo, Xiaoyu, Ben Calderhead, Haofei Liu and Wenguang Li: *On the initial configurations of collapsible channel flow*. Computers & Structures, 85:977 – 987, 2007. <ce:title>Fourth {MIT} Conference on Computational Fluid and Solid Mechanics</ce:title>.

[93] Luo, X.Y. and T.J. Pedley: *A Numerical Simulation of Steady Flow in a 2-D Collapsible Channel*. Journal of Fluids and Structures, 9(2):149 – 174, 1995.

[94] McLeish, T. C. B. and R. G. Larson: *Molecular constitutive equations for a class of branched polymers: The pom-pom polymer*. Journal of Rheology (1978-present), 42(1):81–110, 1998.

[95] Meng, S, XK Li and G Evans: *Numerical simulation of Oldroyd-B fluid in a contraction channel*. Journal of Supercomputing, 22(1):29–43, MAY 2002.

[96] Metzner, A. B., J. L. White and M. M. Denn: *Constitutive equations for viscoelastic fluids for short deformation periods and for rapidly changing flows: Significance of the deborah number*. AIChE J., 12(5):863–866, 1966.

[97] Mok, Daniel Pinyen: *Partitionierte Lösungsansätze in der Strukturdynamik und der Fluid-Struktur-Interaktion*. PhD thesis, Institut für Baustatik der Universität Stuttgart, 2001.

[98] Muniz, A. R., A. R. Secchi and N. S. M. Cardozo: *High-order finite volume method for solving viscoelastic fluid lows*. Brazilian Journal of Chemical Engineering, 25:153 – 166, 03 2008.

[99] Newmark, N.: *A method of computation for structural dynamics*. Journal of the Engineering Mechanics Division, 85:67–94, 1959.

[100] Ng, K. C., M. Z. Yusoff and E. Y. K. Ng: *Higher-order bounded differencing schemes for compressible and incompressible flows*. Int. J. Numer. Meth. Fluids, 53(1):57–80, 2007.

[101] Oldroyd, J. G.: *On the Formulation of Rheological Equations of State*. Proceedings of the Royal Society of London. Series A. Mathematical and Physical Sciences, 200(1063):523–541, 1950.

[102] Oliveira, P. J. and F. T. Pinho: *Plane contraction flows of upper convected Maxwell and Phan-Thien-Tanner fluids as predicted by a finite-volume method*. Journal of Non-Newtonian Fluid Mechanics, 88(1-2):63 – 88, 1999.

[103] Oliveira, P.J., F.T. Pinho and G.A. Pinto: *Numerical simulation of non-linear elastic flows with a general collocated finite-volume method*. Journal of Non-Newtonian Fluid Mechanics, 79(1):1 – 43, 1998.

[104] Olsson, Anders, Göran Stemme and Erik Stemme: *Numerical and experimental studies of flat-walled diffuser elements for valve-less micropumps*. Sensors and Actuators A: Physical, 84:165 – 175, 2000.

[105] Owens, R.G. and T.N. Phillips: *Computational Rheology*. Imperial College Press, 2002.

[106] Pakdel, Peyman, Stephen H. Spiegelberg and Gareth H. McKinley: *Cavity flows of elastic liquids: Two-dimensional flows*. Physics of Fluids (1994-present), 9(11):3123–3140, 1997.

[107] Pan, L.S., T.Y. Ng, G.R. Liu, K.Y. Lam and T.Y. Jiang: *Analytical solutions for the dynamic analysis of a valveless micropump – a fluid-membrane coupling study*. Sensors and Actuators A: Physical, 93(2):173 – 181, 2001.

[108] Pan, L.S., T.Y. Ng, X.H. Wu and H.P. Lee: *Analysis of valveless micropumps with inertial effects*. Journal of Micromechanics and Microengineering, 13(3):390, 2003.

[109] Pan, Tsorng-Whay, Jian Hao and Roland Glowinski: *On the simulation of a time-dependent cavity flow of an Oldroyd-B fluid*. International Journal for Numerical Methods in Fluids, 60(7):791–808, 2009.

[110] Patankar, N. A., P. Y. Huang, H. H. Hu and D. D. Joseph: *Normal Stresses on the Surface of a Rigid Body in an Oldroyd-B Fluid*. Journal of Fluids Engineering, 124(1):279–280, August 2001.

[111] Patankar, S.V and D.B Spalding: *A calculation procedure for heat, mass and momentum transfer in three-dimensional parabolic flows*. International Journal of Heat and Mass Transfer, 15(10):1787 – 1806, 1972.

[112] Perera, M.G.N. and K. Walters: *Long-range memory effects in flows involving abrupt changes in geometry: Part I: flows associated with I-shaped and T-shaped geometries*. Journal of Non-Newtonian Fluid Mechanics, 2(1):49 – 81, 1977.

[113] Perić, M.: *Analysis of pressure-velocity coupling on nonorthogonal grids*. Numerical Heat Transfer, Part B: Fundamentals, 17(1):63–82, 1990.

[114] Peterlin, A.: *Hydrodynamics of macromolecules in a velocity field with longitudinal gradient*. J. Polym. Sci. B Polym. Lett., 4(4):287–291, 1966.

[115] Phan-Thien, N.: *Understanding Viscoelasticity: An Introduction to Rheology*. Graduate Texts in Physics. Springer, 2012.

[116] Phan-Thien, Nhan and Hua-Shu Dou: *Viscoelastic flow past a cylinder: drag coefficient*. Computer Methods in Applied Mechanics and Engineering, 180(3¨C4):243 – 266, 1999.

[117] Pironkov, P.: *Numerial simulation of thermal fluid-structure interaction*. PhD thesis, Technische Universität Darmstadt, 2010.

[118] Poole, R.J.: *The Deborah and Weissenberg numbers*. The British Society of Rheology, Rheology Bulletin, 53(20):32–39, 2012.

[119] Quinzani, Lidia M., Robert C. Armstrong and Robert A. Brown: *Birefringence and laser-Doppler velocimetry (LDV) studies of viscoelastic flow through a planar contraction*. Journal of Non-Newtonian Fluid Mechanics, 52(1):1 – 36, 1994.

[120] Reiner, M.: *The Deborah number*. Physics Today, 17:62–62, 1964.

[121] Reiner, Markus and R. Schoenfeld-Reiner: *Viskosimetrische Untersuchungen an Lösungen hochmolekularer Naturstoffe. I. Mitteilung. Kautschuk in Toluol*. Kolloid-Zeitschrift, 65(1):44–62, 1933.

[122] Renardy, M.: *Mathematical Analysis of Viscoelastic Flows*. CBMS-NSF Regional Conference Series in Applied Mathematics. Society for Industrial and Applied Mathematics, 2000.

[123] Rhie, C. M. and W. L. Chow: *Numerical study of the turbulent flow past an airfoil with trailing edge separation*. AIAA Journal, 21(11):1525–1532, November 1983.

[124] Richter, Thomas: *Numerical methods for fluid-structure interaction problems*. 2010.

[125] Roe, P. L.: *Some contributions to the modelling of discontinuous flows*. In Engquist, B. E., S. Osher and R. C. J. Somerville (editors): *Large-Scale Computations in Fluid Mechanics*, pages 163–193, 1985.

[126] Roe, P. L. and M. J. Baines: *Algorithms for advection and shock problems*. In Viviand, H. (editor): *Numerical Methods in Fluid Mechanics*, pages 281–290, 1982.

[127] Sahin, Mehmet: *Parallel large-scale numerical simulations of purely-elastic instabilities behind a confined circular cylinder in a rectangular channel*. Journal of Non-Newtonian Fluid Mechanics, 195(0):46 – 56, 2013.

[128] Sahin, Mehmet and Helen J. Wilson: *A semi-staggered dilation-free finite volume method for the numerical solution of viscoelastic fluid flows on all-hexahedral elements*. Journal of Non-Newtonian Fluid Mechanics, 147:79 – 91, 2007.

[129] Sarkar, Kausik and William R. Schowalter: *Deformation of a two-dimensional viscoelastic drop at non-zero Reynolds number in time-periodic extensional flows*. Journal of Non-Newtonian Fluid Mechanics, 95(2000):315 – 342, 2000.

[130] Schäfer, M: *Computational Engineering-Introduction to Numerical Methods*. Springer Verlag, Berlin, 2006.

[131] Schäfer, Michael, Marcus Heck and Saim Yigit: *An Implicit Partitioned Method for the Numerical Simulation of Fluid-Structure Interaction*. In Bungartz, Hans-Joachim and Michael Schäfer (editors): *Fluid-Structure Interaction*, volume 53 of *Lecture Notes in Computational Science and Engineering*, pages 171–194. Springer Berlin Heidelberg, 2006.

[132] Schieber, J. D. and Hans Christian Öttinger: *The effects of bead inertia on the Rouse model*. The Journal of Chemical Physics, 89(11):6972–6981, 1988.

[133] Scovazzi, Guglielmo and Thomas JR Hughes: *Lecture notes on continuum mechanics on arbitrary moving domains*. Technical Report, Technical Report SAND-2007-6312P, Sandia National Laboratories, 2007.

[134] Singhal, Vishal, Suresh V. Garimella and Jayathi Y. Murthy: *Low Reynolds number flow through nozzle-diffuser elements in valveless micropumps*. Sensors and Actuators A: Physical, 113(2):226 – 235, 2004.

[135] Stemme, Erik and Goran Stemme: *A valveless diffuser/nozzle-based fluid pump*. Sensors and Actuators A: Physical, 39(2):159 – 167, 1993.

[136] Sternel, D.(ed.): *FASTEST User Manual*. Institute of Numerical Methods in Mechanical Engineering, Technische Universität Darmstadt, 2006.

[137] Stewart, P. A., N. Lay, M. Sussman and M. Ohta: *An improved sharp interface method for viscoelastic and viscous two-phase flows*. Journal of Scientific Computing, 35(1):43–61, APR 2008.

[138] Stone, Herbert L.: *Iterative Solution of Implicit Approximations of Multidimensional Partial Differential Equations*. SIAM Journal on Numerical Analysis, 5(3):530–558, 1968.

[139] Sweby, P.: *High Resolution Schemes Using Flux Limiters for Hyperbolic Conservation Laws*. SIAM Journal on Numerical Analysis, 21(5):995–1011, 1984.

[140] Taylor, RL: *FEAP, A Finite Element Analysis Program. Version 7.4 User Manual*. University of California at Berkeley, 2002.

[141] Thien, Nhan Phan and Roger I. Tanner: *A new constitutive equation derived from network theory*. Journal of Non-Newtonian Fluid Mechanics, 2(4):353 – 365, 1977.

[142] Thompson, J.F., B.K. Soni and N.P. Weatherill: *Handbook of Grid Generation*. Taylor & Francis, 1998.

[143] Truesdell, C.: *The elements of continuum mechanics*. Springer-Verlag New York, 1967.

[144] Truesdell, C. and K.R. Rajagopal: *An Introduction to the Mechanics of Fluids*. Modeling and simulation in science, engineering & technology. Springer, 2000.

[145] Ventsel, E. and T. Krauthammer: *Thin Plates and Shells: Theory: Analysis, and Applications*. Taylor & Francis, 2001.

[146] Wang, J.C.T. and G.F. Widhopf: *A high-resolution {TVD} finite volume scheme for the Euler equations in conservation form*. Journal of Computational Physics, 84(1):145 – 173, 1989.

[147] Waters, N. D. and M. J. King: *Unsteady flow of an elastico-viscous liquid*. Rheologica Acta, 9:345–355, 1970. 10.1007/BF01975401.

[148] Waterson, N.P. and H. Deconinck: *Design principles for bounded higher-order convection schemes - a unified approach*. Journal of Computational Physics, 224(1):182 – 207, 2007. Special Issue Dedicated to Professor Piet Wesseling on the occasion of his retirement from Delft University of Technology.

[149] White, F.M.: *Fluid Mechanics*. McGraw-Hill international editions. McGraw-Hill, 2003.

[150] White, James Lindsay: *Dynamics of viscoelastic fluids, melt fracture, and the rheology of fiber spinning*. J. Appl. Polym. Sci., 8(5):2339–2357, 1964.

[151] Wriggers, P.: *Nonlinear Finite Element Methods*. Springer, 2008.

[152] Xue, S.-C., R.I. Tanner and N. Phan-Thien: *Numerical modelling of transient viscoelastic flows*. Journal of Non-Newtonian Fluid Mechanics, 123(1):33 – 58, 2004.

[153] Yamahata, C., C. Lotto, E. Al-Assaf and M.A.M. Gijs: *A PMMA valveless micropump using electromagnetic actuation*. Microfluidics and Nanofluidics, 1(3):197–207, 2005.

[154] Yamamoto, Misazo: *The Visco-elastic Properties of Network Structure I. General Formalism*. Journal of the Physical Society of Japan, 11(4):413–421, 1956.

[155] Yapici, Kerim, Bulent Karasozen and Yusuf Uludag: *Finite volume simulation of viscoelastic laminar flow in a lid-driven cavity*. Journal of Non-Newtonian Fluid Mechanics, 164(1-3):51 – 65, 2009.

[156] Yee, H. C. and A. Harten: *Implicit TVD schemes for hyperbolic conservation laws in curvilinearcoordinates*. AIAA Journal, 25(2):266–274, February 1987.

[157] Yee, H.C, R.F Warming and A Harten: *Implicit total variation diminishing (TVD) schemes for steady-state calculations*. Journal of Computational Physics, 57(3):327 – 360, 1985.

[158] Yigit, S., M. Schäfer and M. Heck: *Grid movement techniques and their influence on laminar fluid-structure interaction computations*. Journal of Fluids and Structures, 24(6):819 – 832, 2008.

[159] Zienkiewicz, O.C. and R.L. Taylor: *The Finite Element Method: Solid mechanics*. Number v. 2 in *Referex collection.Mecánica y materiales*. Butterworth-Heinemann, 2000.

[160] Zienkiewicz, O.C., R.L. Taylor and R.L. Taylor: *The Finite Element Method: The basis*. Referex Engineering. Butterworth-Heinemann, 2000.

Curriculum Vitae

Personal information

Name	Xingyuan Chen
Place of birth	Guangdong, China
Date of birth	04 October 1984

Education

Oct.2007– Dec.2009	**Master of Science**, *Technische Universität Darmstadt*. Computational Mechanical and Process Engineering
Sep.2003– Jun.2007	**Bachelor of Science**, *Tongji University*, Shanghai, China. Machinery Design, Manufacturing and Automation Industrial Engineering
Sep.1997– Jun.2003	**Middle School**, *Guangzhou No.6 Middle School*, Guangzhou, Guangdong, China. Main subjects: Mathematics, Physic, English, Chinese
Sep.1991– Jun.1997	**Primary School**, *Tongfuzhong Road No.1 Primary School*, Guangzhou, Guangdong, China.

Experience

since Apr.2014	**Research assistant**, *Center of Smart Interfaces*, Technische Universität Darmstadt. Research topic: Direct numerical simulation of binary viscoelastic droplet collisions
Jun.2010– Mar.2014	**Research assistant**, *Center of Smart Interfaces*, Technische Universität Darmstadt. Research topic: Numerical modeling of complex fluid-structure interaction